ANALYSES OF GRAVITY GRAIN FLOWS

by

Ahmed Samy A. Elzaher Kamis

A Dissertation

Submitted to the Department of Civil Engineering

and Applied Mechanics

of McGill University

In Partial Fulfillment of the Requirements

for the Degree of

DOCTOR OF PHILOSOPHY

March 1985

To my parents

and to my family

ACKNOWLEDGEMENTS

The author wishes to express his deepest gratitude to Professor Stuart B. Savage for his continual guidance, constant encouragement and generous help throughout the course of this study.

Occasional discussions with Professor V.H. Chu were very helpful and are greatly appreciated. Thanks are due to Dr. D.L. Wilkinson for his suggestion of the back lighting which was used in the experiments. Some discussions with Dr. Ganoulis on the computational work were very beneficial and are greatly appreciated. I owe a debt of gratitude to Dr. N. Chepurniy for his help in the task of proofreading the manuscript.

Special thanks are due to Mr. D. Bauer for his valuable assistance during the design of the water tank used in the experiments. The technical assistance of C. Navas, B. Cockayne and R. Sheppard during the construction of the water tank is gratefully acknowledged. I would like to thank Ms. B. Basik for help in developing the computer programs used for data reduction.

I am indebted to numerous persons in the Department of Civil Engineering and Applied Mechanics, McGill University for their help and kind support.

The support of the Ministry of Education of the Arab Republic of Egypt in granting the author a study leave for Ph. D. studies is gratefully acknowledged.

Finally, I would like to acknowledge the financial support provided by the Natural Sciences and Engineering Research Council of Canada (NSERC).

ANALYSES OF GRAVITY GRAIN FLOWS

ABSTRACT

This investigation consists of two separate parts. In the first part the subaqueous flow of a cloud of coarse particles down an inclined bed was investigated experimentally and theoretically. This work is relevant to the mechanics of transportation of ocean bed sediment in the form of submarine grain flows. It was found experimentally that after an initial growth period, the cloud collapsed as a result of sedimentation. A theoretical analysis for the development of a two-dimensional cloud was derived based upon the overall conservation equations; the sediment mass balance equation, the ambient fluid entrainment equation and the linear momentum equation along the bed.

The second part of the thesis is a study of the flow and spreading of a finite mass of dry cohesionless granular material released from rest on rough inclines. Firstly, a two-dimensional depth - averaged model which describes both the longitudinal and the lateral spreading during flow down a rough inclined plane was developed. From the results of the numerical studies, it was concluded that the lateral spreading is insignificant relative to the longitudinal spreading. Therefore, a depth- averaged model which describes the one-dimensional longitudinal spreading down rough, curved beds was developed. It was concluded that the traveling distance and velocity of the center of mass of a rock pile can be approximately predicted by a simple analysis of a point mass sliding down the same incline. The long runout distance of the leading edge of the slide debris can result from extreme spreading of the pile as it accelerates down the slope after initial release.

RESUME

L'écoulement sous-aqueux d'un nuage de grosses particules le long d'un lit incliné a été étudié expérimentalement et théoriquement. Ces travaux sont applicables aux mécanismes de charriage de sédiment au fond des océans sous la forme d'écoulements de grains sous-marins. Il a été trouvé qu'après une période de croissance initiale, le nuage s'affaisait à cause de la sédimentation. Une analyse théorique pour le développement d'un nuage bidimensionnel a été dérivée à partir des équations de conservation globale: l'équation de balance de la masse du sédiment, l'équation d'entraînement du fluide ambient, et l'équation de force la d'impulsion linéairé le long du lit.

Une etude de l'écoulement et de la propagation d'une masse finie d'un matériau sec granuleux sans cohésion lachée du repos sur des pentes rugeuses est presentée. Premièrement, un modèle bidimensionnel à profondeur moyenne décrivant la propagation longitudinale et latérale durant l'écoulement le long d'un plan rugueux incliné est développé. D'après les résultats de les études numériques, il est conclu que la propagation laterale est sans importance en comparaison à la propagation longitudinale. Ainsi, un modèle à profondeur moyenne décrivant la propagation longitudinale unidimensionnelle le long de lits rugueux courbes est developpé. Il est conclu que la distance parcourue et la vitesse du centre de masse du tas de rochers peuvent être predites par une analyse simple d'une masse ponctuelle glissant le long de la même pente. La longue portée du bord d'attaque du tas de débris d'avalanche peut être le résultat d'une propagation extrême du tas lorsqu'il accélère le long de la pente après le lâchage initial.

TABLE OF CONTENTS

GENERAL INTRODUCTION

This thesis contains the results of two studies which are distinctly different but are nevertheless related; both deal with problems of a geotechnical nature related to the motion of discrete geological materials down slopes. In both cases the discrete nature of the materials is taken into account, but continuum 'fluid-like' models are used to model the flow behaviour. Both deal with unsteady, developing flows resulting from the initial release of a finite mass of particulate materials on rough inclined beds. The investigations examine the flows from the time of initiation until the collapse phase when all motion ceases. The main focus is on the mechanics of the flow processes.

The first study, Part I, deals with the flow of relatively small particles which are suspended in a fluid, where sedimentation and turbulent mixing of the fluid are important. Examples of such flows are submarine debris flows which might be initiated by underwater earthquakes, and powder snow avalanches. Submarine debris flows are of current interest in connection with oil exploration on the continental shelf regions.

The study of Part I corresponds to one limit of the general particulate flow problem in which the presence of the interstitial fluid plays an essential role in the flow mechanics. In this sense, we regard the particles to be 'small' and/or the mass density of the particles to be not too different from that of the surrounding fluid.

On the other hand, the second study, Part II, deals with the other limit in which the interstitial fluid effects are negligible. Attention is directed to the mechanics of rockfalls that initiate on steep slopes, 'flow' down the slope and eventually come to rest on a shallower slope or a horizontal region. Rockfalls of very large masses have been observed to exhibit extremely long runout distances. This phenomenon has puzzled geophysicists for many years and numerous hypotheses, based upon unusual constitutive behaviour of the discrete rock material, have been proposed to explain it. At best, all are controversial. Furthermore no detailed calculations of flow events based upon these hypotheses have been performed. Part II contains a numerical study of the rockfall problem using constitutive equations which are commonly accepted in quasi-static flows.

The main body of the presentation has been divided up into two separate sections, Part I and Part II, which discuss each of the separate problems in detail.

PART I

SUBAQUEOUS FLOW OF A CLOUD OF COARSE PARTICLES DOWN AN INCLINED BED

SUBAQUEOUS FLOW OF A CLOUD OF COARSE PARTICLES DOWN AN INCLINED BED

ABSTRACT

The subaqueous flow of a cloud of coarse particles down an inclined bed was investigated experimentally and theoretically. This work is relevant to the mechanics of transportation of ocean bed sediment in the form of submarine grain flows. These flows are of current interest in connection with oil exploration on the continental shelf regions.

Following a set of preliminary experiments, large scale experiments were carried out in a 4 m long tilting water tank using suspensions of sand particles and polystyrene beads. It was found that after an initial growth period, the cloud collapsed as a result of sedimentation. This was in strong contrast with the previous studies involving only fluids by Beghin, et al. (23) which showed the cloud would continue to grow without bound. Dimensional arguments and experimental observations suggested that the entrainment coefficient might be expressed as a function of both the Richardson number and the ratio of the particle net fall velocity to the cloud center of mass velocity.

A theoretical analysis for the development of a two-dimensional cloud was derived based upon the overall conservation equations; the sediment mass balance equation, the ambient fluid entrainment equation and the linear momentum equation along the bed. The mass diffusion coefficient involved in the model was taken as a multiple of the eddy viscosity; it then was related to the shear stress distribution within the cloud. The predicted behaviour of the flow was found to agree well with the experimental results.

TABLE OF CONTENTS

LIST OF FIGURES

LIST OF SYMBOLS

A	area
A_1, A_2, D_1	coefficients of equation (3.33)
A_3, A_4, D_2	coefficients of equation (3.34)
A_4, A_5, A_6, D_3	coefficients of equation (3.35)
b	width of the jet (equation (3.11))
C	characteristic concentration
C_D	drag coefficient
c	mean volumetric concentration
c'	concentration at position y
c_o	initial mean volumetric concentration
E	enterainment concentration
g	gravitational acceleration
g'	reduced gravitational acceleration ($= g\ c\ \Delta\rho\ /\ \rho_a$)
g'_o	initial reduced gravitational acceleration
H	characteristic height
h	maximum height of the cloud
K	aspect ratio (h / l)
k_v	added mass coefficient
L	mixing length
l	maximum length of the cloud
P	perimeter of the cloud
P_{av}	averaged perimeter of the cloud
R	Richardson number $= \dfrac{g' \cos \zeta\ H}{U^2}$
r^2	correlation coefficient
S_1	shape factor (equation (3.4))

S_2	shape factor (equation (3.5))
t	time
U	characteristic velocity
u	center of mass velocity
v	velocity at position y
w	particle fall velocity
w_o	particle free fall velocity
$\tilde{W}$	particle net fall velocity
x	streamwise cartesian coordinate
y	normal to the bed cartesian coordinate
Z_1 , Z_2 , Z_3	defined in equations (3.48), (3.49) and (3.50)
α	exponent in equation (3.8)
β	constant in equation (3.8)
Δt	time interval between two consecutive slides
$\Delta\rho$	density difference (= $\rho_p - \rho_a$)
ϵ	kinematic eddy viscosity
ϵ_s	mass diffusion coefficient
ζ	bed angle of inclination
ρ_a	mass density of the ambient fluid
ρ_p	mass density of the particle
ϕ	angle of repose of the material

CHAPTER 1
INTRODUCTION

Ocean bed sediment can be transported in the form of subaqueous grain flows moving down slopes under the action of gravity. The development and maintenance of such flows and the forces generated when they strike and flow around underwater objects are of interest in connection with oil exploration on the continental shelf regions. We may classify the flows broadly as 'two-dimensional' or 'three-dimensional'. Two-dimensional flows which are confined in a channel-like path of approximately uniform width have received the most attention. Three-dimensional flows, such as those characteristic of a current spreading in fan-like fashion over a surface, are important to the geologist, but little is known about their hydraulic or sedimentological properties.

Among two-dimensional subaqueous flows, two distinct types may be distinguished: surges involving a finite volume of dispersed particles and uniform flows or currents. Surges (alternatively called negatively buoyant clouds) are nonuniform, unsteady phenomena. They may be formed in nature by events such as a large slump or an underwater earthquake which creates a large volume of dispersed sediment. Gravity currents of these kinds occur in many different natural situations, and knowledge of their properties is of importance in many scientific disciplines. For example, powder snow avalanches which take place in an aerial environment are analogous to subaqueous debris flows. In fact, model studies of snow avalanches have been carried out in the laboratory (1,2) using solid particles released in water.

The mechanics of subaqueous grain flows and related kinds of gravity currents is poorly understood, despite the frequent occurrence of and the serious damage caused by these flows. The present study is an attempt to further our understanding of these complex flows. After a brief literature review presented in the next subsection, attention is directed to two-dimensional flows which involve the underwater release of a cloud of solid particles and the subsequent flow of the cloud down an inclined surface. Two sets of laboratory experiments (small and large scale) and an analysis of the growth and collapse of the sedimenting cloud are presented.

1.1 Review of Previous Work

A gravity current or density current is the flow of a fluid within another caused by a density difference between the two fluids. The difference in specific weight that provides the driving force may be due to either dissolved or suspended material or to temperature differences. At the leading edge of a gravity current there is a head which is characterized by a higher depth than the rest of the current. The head is followed by the body of the current which moves, in general, as a steady flow. The shape of a buoyant cloud resembles the head of a gravity current. In this review, attention is directed toward the subaqueous gravity currents which are composed of particle suspensions originating from continuous sources or instantaneous sources.

1.1.1 Gravity Currents and Related Phenomena

In the ocean, gravity currents of interest to this study consist of suspended mud, silt or sand. Examples of the damage that can be caused by this type of mass movement are the breaks in submarine telephone cables in 1966 and 1968 that were due to earthquake-triggered turbidity currents (3). Studies of turbidity currents have been performed mainly in two contexts, the geological context and the hydrodynamics context.

In geology, the concept of turbidity currents first attracted great interest after the suggestion by Daly (4) that turbidity currents produced by wave action might flow down the continental shelves and erode submarine canyons. Kuenen (5) performed experimental studies to test this hypothesis and his results supported the idea. However, the interest in turbidity currents was changed from considering them as an erosive agent to their capacity to transport sediments into deep water and to form graded beds. Kuenen (6) produced graded beds in laboratory experiments with mixture of sand and mud. Kuenen and Migliorini (7) also used laboratory experiments to explain graded beds in the Apennines in Italy. Hezzen and Ewing (8) used their experimental results to explain cable breaks and sand layers in the Atlantic Ocean. Middleton, in his classical papers (9,10,11), reviewed in length both the geological and the hydrodynamical aspects of the subject. In his first paper, Middleton studied experimentally the flow at the head of density currents, including the nature of the motion around and within the head using a saline water beneath fresh water. In the second paper, the laws of uniform flow of the density currents were studied and in the third paper, deposition of the sediment from the turbidity current and the formation of graded beds were discussed. Lengthy reviews on the history of the studies of the turbidity currents were presented by Middleton (12) and Simpson (13).

Hydrodynamic investigations of gravity currents can be classified under two main categories, the flow of the current along horizontal boundaries and the motion of the current flowing down a slope. It was found that when a current flowed along a horizontal boundary, the head was a controlling feature of the flow. The dynamics of the head was investigated thoroughly by Britter and Simpson (14,15). They showed how mixing occurring immediately behind the head determined the rate of advance of the current. A semi-empirical analysis was presented to describe the experimental results. Nevertheless, the flow of gravity currents on horizontal boundaries is often not the case in practical situations. The continental shelves over which turbidity currents flow are not flat and the motion of avalanches is essentially from one level to another.

The motion of a gravity current flowing down a slope has received some attention. Recently, Hopfinger and Tochon-Danguy (1,2) studied the flow of powder snow avalanches experimentally. Powder snow avalanches correspond to gravity currents in the limit where the density difference is small. A common salt solution was used by Hopfinger and Tochon-Danguy to model the avalanche and a simple theoretical analysis was proposed to predict the velocity and the development of the avalanche. From the experimental results they concluded that, the entrainment coefficient is only a function of the angle of inclination. Britter and Linden (16) presented results of an experimental study of gravity currents traveling down an incline. In these tests the slopes ranged between 0 and 90 degrees, in contrast with the previous experiments which covered only a limited range of the angle of bed inclination. The emphasis in these experiments was on the behaviour of the head of the current. The experiments provided evidence of considerable mixing and entrainment of the ambient fluid. It was concluded that, on small slopes (less than 5 degrees) the velocity of the head decreased with distance as the component of buoyancy force was insufficient to overcome the friction at the lower boundary. Also, they found that the head velocity was constant over the whole range of slopes from 5 to 90 degrees. They explained these results by stating that the increase of buoyancy force was counteracted by the increase in the entrainment as the angle of inclination increased.

Ellison and Turner (17), on the other hand, were interested in the flow behind the head. They studied the properties of this steady flow and showed that the mean velocity down the slope was independent of the distance downstream from the source. However, the thickness of the current increased downstream at a constant rate due to the entrainment of the ambient fluid.

The gravity currents mentioned above were modeled experimentally using a common salt water solution. This corresponds in real situations to either of two categories, non-particulate material gravity currents or equilibrium turbidity currents where the rate of erosion is equal to the rate of deposition. The first case includes most of the atmospheric gravity currents or oceanic gravity currents (river plumes at the surface and salt wedges on a river bed). However, in the case of powder snow avalanches (subaerial gravity currents) and non-equilibrium turbidity currents, sedimentation and erosion play a crucial role in the development of the flow. Evidence of fan formation and canyon erosion were found and discussed by Daly (4) and Kuenen (5); these are instances where erosion is a dominant factor. Erosion of the snow cover was discussed in References (1,2). An example where sedimentation is dominant is described by Kuenen (6); the formation of a graded bed was evident from both field observations and experimental studies.

Several disadvantages of attempting to model turbidity currents by using fluids can be identified by discussing the following three features of the flow: the entrainment coefficient, the lower boundary resistance and the form drag forces.

Entrainment implies a flow of ambient fluid into a turbulent flow. In the case where a gravity current is modeled using a dense fluid , the degree of turbulence is the major factor to be considered in evaluating the entrainment coefficient. Based on this concept, the entrainment coefficient has been expressed as a function of the Richardson number (the inverse square of the densimetric Froude number). Experimental observations of the nonhomogeneous flows, jets, plumes and mixing layers in References (16,17,19,20) show that the entrainment coefficient may vary significantly for the various types of flows. A comparison of the entrainment coefficient values for different types of flows of miscible fluids as a function of the Richardson number was presented by Turner (21). While correlations are possible for each type of flow, there are differences in entrainment coefficient values between the various types of flow. In cases like the present study which involve discrete solid particles and a fluid (instead of two miscible fluids) we must generalize the entrainment concept to account for the possibility of sedimentation. This can be clearly seen if we consider a turbidity current which is composed of a suspension of large particles having high fall velocities which flows on an incline of small slope. A subsiding current due to sedimentation and no entrainment are to be expected. In fact, only negative entrainment (or "detrainment") is possible in this situation.

Typically (16), the stress at the lower boundary has been considered in analyses of density currents only for the case of small bed slopes. The effects of bed friction have been assumed negligible for large slopes (16). These assumptions are appropriate for the case of a dense fluid flowing adjacent to a smooth bed boundary. A current consisting of particle suspensions flowing down a rough bed composed of particles is a quite different situation since the interaction between the particle suspensions and the bed particles has to be considered. Bed friction due to particle interactions can be much larger than that due to a fluid alone.

The form drag of the density currents involving only fluids typically has been neglected since it is small compared to the (negative) buoyancy force during flow down steep slopes. However, in the present case in which the lower boundary resistance force is significant, the form drag is no longer negligible in the streamwise force balance equation.

Semi-empirical descriptions of density currents have been proposed in References (1,9,10,14,15,16). Parker (22) recently introduced a simple model to analyze a continuous turbidity current, considering the sedimentation as well as the erosion. However, he only considered the case where erosion is just equal to sedimentation. Moreover, he neglected the entrainment and both the form drag and the lower boundary resistance so that a steady state flow was obtained. The analysis provides only qualitative results and no quantitative bounds for the case where either the sedimentation or the erosion is dominant.

1.1.2. Gravitational Convection from Instantaneous Sources

Morton et al. (19) studied both experimentally and theoretically the flow of a rising cloud of light fluid in another fluid. The idea of the entrainment coefficient was first introduced by them, and they made it the basis of their theory of plumes. Conservation laws of volume , momentum and buoyancy were the basis of the analysis which involved a constant entrainment coefficient. An exact solution of the governing equations was given to estimate the maximum height that a cloud might reach under a given set of conditions.

More recently, Beghin et al. (23) studied the flow of an 'inclined thermal' (negatively bouyant cloud in these experiments) which moves down a smooth inclined bed. Most of the experiments were performed using a common salt solution as the dense fluid. Some runs were made with a sand suspension. The sand used was graded to give grain sizes less than 20 um. Such small grains have a very small fall velocity in water; results of the tests with sand did not differ greatly from those obtained with the miscible fluids.

It was found that the spatial growth rates of the height and length of the cloud were linear functions of the angle of inclination. The height to length ratio was found to be constant for a given bed slope. The shape of the cloud was well approximated by half an ellipse. The entrainment coefficient was found to be constant for a given bed angle of inclination but increased linearly with the increase of bed slope.

A theoretical model based on the conservation laws of mass and linear momentum with the assumption of small density differences was developed (23). The theory predicted that the cloud would continue to grow linearly with the traveling distance, and the velocity would decay as the inverse of the square root of the traveling distance.

It may be concluded from the above review that, there is a lack of experimental data on density currents in which there are particles large and dense enough to play an important role in the flow dynamics. There is little available experimental or theoretical information on the entrainment, erosion and sedimentation processes in the context of gravity currents. The present study will focus on an idealization of the natural problem in an effort to gain some understanding of the mechanics involved in some of these questions.

CHAPTER 2
EXPERIMENTAL INVESTIGATION

The experiments were directed toward investigating the flow behaviour subsequent to the subaqueous release of a cloud of dense, coarse particles down a rough inclined bed. The emphasis of these experiments was on understanding how the tendency of the particles to sediment affects the entrainment process and the growth and collapse of the cloud. The bed resistance due to particle interactions and the form drag of the moving cloud were significant in these experiments. The results of some preliminary exploratory experiments performed in a small scale apparatus will be described first. These are followed by the presentation of results obtained in a larger apparatus designed on the basis of the preliminary experiments.

2.1 Preliminary Tests

Small scale laboratory experiments were carried out to determine the essential flow characteristics as a preliminary to the design of a larger scale tilting tank.

The small scale experiments were carried out in a plexiglass water tank a sketch of which is shown in Fig. 2.1. The tank was 2 m long, 0.12 m wide and 0.3 m deep. It could be capped and set to any angle of inclination from 0 to 45 degrees. A release gate spanning the width of the tank was positioned at the upper end of the tank. It was used to release a suspension of particles into the fresh water contained in the tank. A collection chamber was positioned at the lower end of the tank. Its bed level was lower than the bed level of the tank in order to both collect the particles which reached the end of the tank and to reduce the possibility of waves reflected from the end wall.

Some of the tests were performed with a suspension of sand having an average diameter of 0.1-0.2 mm, specific gravity of 2.5 and particle free fall velocity of 0.048 m/sec. Further runs were performed with a suspension composed of spherical polystyrene beads with an average diameter of 1-2 mm, specific gravity of 1.12 and particle free fall velocity of 0.036 m/sec. The angles of repose of the sand and the beads particles were determined to be 36 and 26 degrees respectively. The bed of the tank was covered with two sided sticky tape normally used for holding down floor carpets. Dry particles of the same type that were used in the flowing cloud experiments were placed in a pile on the top of the tape. A layer of particles became attached to the tape and the excess particles were removed leaving a rigid surface having a roughness corresponding to that of the individual particles. Note that while this creates a roughened bed, it does not permit the possibility of erosion which may be present in some natural flows. The experiments were performed at bed angles of inclination of 30, 34, 38 and 44 degrees. During the introduction of the beads behind the release gate prior to the test run, air bubbles sometimes became attached to the beads causing them to flocculate. To remedy this a small amount of Kodak 'Photo-Flo 200 Solution' was added to the suspension to reduce the surface tension of the water and minimize the development and attachment of the air bubbles.

The tank was adjusted to the required angle of inclination and then filled with fresh water. The required volume of material was then introduced behind the release gate. The initial volume per unit width (A_o) for both the sand and the bead suspensions was .003 m^2. The initial masses of sand and beads were .5 kg and .25 kg respectively. The gate was quickly withdrawn by hand and the suspension started to flow down the slope. Care was taken to release the cloud as smoothly as possible, consistent with a rapid release. The tank was repositioned to the horizontal just after the cloud collapsed so that the amount of solids which sedimented from the cloud during its travel could be determined as a function of the traveling distance.

The moving cloud was photographed at regular time intervals using a 35mm Canon A-1 camera with a high speed motor drive. The exposure time was (1/125) sec. A digital stop watch placed adjacent to the tank recorded the time each photograph was taken (within an accuracy of 1/100 sec). A 50mm x 50mm grid covering the back of the tank assisted in the determination of the cloud velocity and geometry. From the photographs, the following quantities were measured: the cloud's height and length, its area and circumference. By knowing the time between subsequent photographs the front velocity could be determined.

From the photograph, it was relatively easy to define the front position, but the bulgy nature of the contour made the determination of the cloud length somewhat subjective. A smooth curve was drawn by hand through the 'middle' of the irregular cloud boundary and was used to define the cloud geometry for the determination of its overall length l, maximum height h, area A and circumference P.

2.2 Results and Conclusions

All of the data presented in this section were obtained from slide-by-slide examination of the 35mm film of the flow. The observed cloud of particulate material was found to be similar in shape to the two-dimensional thermal on inclined boundaries studied by Beghin, et al. (23). The latter involved the flow of miscible fluids of fresh and salt water. However, the coarse particle cloud did not continue to grow without limit as was the case of the thermal, but it collapsed after an initial growth period. The shape of both kinds of clouds can be approximated by half an ellipse as will be later shown in Section 3.1. In the following discussion, the odd-numbered figures will refer to the sand suspension clouds and the even-numbered figures will refer to the bead suspension clouds. The ratio of the height to the length of the cloud ($K = h / l$) was found to be practically constant for a given angle of bed inclination as can be seen in Figs. 2.2 and 2.3. In these figures, the ratio K was varied somewhat with distance. Near the end of the cloud travel K dropped considerably during the final collapse phase. For the same angle of bed inclination, it can be noticed that the ratio K for the bead suspension cloud was somewhat higher than that of the sand suspension cloud. This can be attributed to the lower fall velocity of the beads which allowed for larger vertical growth of the cloud.

Figs. 2.4 and 2.5 show the length of the cloud normalized by the square root of the initial volume per unit width $\sqrt{A_o}$, versus the traveling distance normalized by the same factor. The general behaviour which is obvious from these figures is that the cloud initially grew in size, reached a maximum and then collapsed. Fig. 2.4 shows that at the largest angle of inclination (44 degrees), the sand cloud just reached its maximum size and started the collapse phase at the end of the tank. At the same bed inclination angle of 44 degrees, the plastic bead cloud had achieved its maximum size but had not completed its collapse phase by the end of the tank.

Figs. 2.6 and 2.7 show the cloud mean volumetric concentration against the traveling distance normalized by $\sqrt{A_o}$. The mean volumetric concentration was calculated for each slide by using the measured cloud area and the amount of material within the cloud at that particular time. The amount of particulate material within the cloud at a particular station was determined by subtracting the amount deposited on the bed up to that station from the total amount of material that was initially released. These figures show that the concentration initially decreased, due to the expansion of the cloud and the associated ambient fluid entrainment. During the final stage of the collapse of the cloud, the concentration increased again as a result of the detrainment of the cloud fluid.

Figs. 2.8 and 2.9 show the cloud front velocity normalized by the initial buoyancy $(g_o' A_o^{\frac{1}{2}})^{\frac{1}{2}}$ versus the traveling distance normalized by $A_o^{1/2}$, where $g_o' = g \frac{\Delta\rho}{\rho_a} c_o$ and g is the gravitational acceleration, $\Delta\rho$ is the density difference between the particle ρ_p and the ambient fluid ρ_a and c_o is the initial concentration before the release of the cloud. These figures show that the cloud reached a maximum velocity (which increased with the angle of bed inclination) and then decelerated until it finally collapsed.

Based on the above observations, the processes of growth and collapse could be described as follows. As the gate is withdrawn, the cloud starts to accelerate down the slope. The motion of the particles develops shear stresses between the different layers of the cloud which in turn create dispersive stresses (due to the collisions between the particles (24)) that cause the suspension to expand. Shear instabilities create turbulence within the cloud which, in addition to the high concentration, reduces the particle fall velocity which in turn enhances the growth of the cloud. Entrainment of the ambient fluid into the cloud decreases the solids concentration. As the cloud grows in size the streamwise mean flow velocity and mean flow shear rates decrease as a result of the decreased (negative) buoyancy forces, the form drag and the bed resistance. Particle sedimentation becomes increasingly important as the cloud slows down and the flow thereafter enters the collapse phase in which the cloud volume decreases. Finally all of the particles are deposited on the bed and motion ceases.

2.3. Large Scale Experiments

The design of the large scale apparatus was based on the experience gained by the preliminary experiments which were described in the previous section. One apparent problem with the preliminary experiments was the small size of the apparatus. It was noted that the length of the tank was insufficient for the complete initiation, growth and collapse cycle at high angles of bed inclination. Therefore, the length of the new apparatus was doubled to be 4 m. It was also observed in the preliminary tests that the flow was not truly two-dimensional since the width of the small tank was small (0.12 m). Thus, the width of the new tank was increased to 0.3 m to reduce the side wall effects. Finally, since the initial volume of the suspension planned for the new experiments was larger than that used in the preliminary experiments, it was expected that the height of the cloud would be correspondingly increased. To avoid disturbances to the flow of the cloud due to the presence of the top wall (ceiling), the depth of the new tank was doubled and made equal to 0.6 m.

Another difficulty experienced with the small apparatus was the release of the cloud. If the gate was withdrawn too quickly, large disturbances were created in the water and the suspension tended to diffuse and then to sediment immediately without forming a traveling cloud. Therefore, a release mechanism was designed for the large tank that would not only minimize this disturbance during the release of the cloud but would also achieve consistent releases for all the experimental runs.

Fig. 2.10 shows a photograph of the water tank. The tank was 4 m in length, 0.3 m in width, 0.6 m in depth and could be capped and set at any angle of inclination from 0 to 45 degrees. Fig. 2.11 shows the detailed drawing of the tank. The tank was made of an aluminum frame with glass sides; the supports were made of steel. Without going through any of the structural details, it suffices to say that the design met the specification of the Canadian Code (CSA standard CAN3-S16.1 (37)). The tank was completely built in the Hydraulics Laboratory of the Department of Civil Engineering and Applied Mechanics, McGill University.

During the preliminary tests, the front lighting technique produced a shadow of the cloud which in some cases was confused with the cloud itself. In the new experiments, a different lighting technique was used. The back glass windows of the tank were covered with opaque Mylar sheets and spot lights were positioned behind the tank and directed towards the Mylar sheets. The opaque Mylar sheets effectively diffused the light to provide a uniform backlighting. The experimental runs were carried out at night with all the laboratory lights turned off so that the only source of light was the spot lamps. Thus, as the cloud flowed, it blocked the background light and a sharp dark image of the cloud could be seen (see Figs. 2.12 , 2.13 and 2.14). The photographic technique was the same as that explained previously for the preliminary tests. However, the negatives were underexposed by two stops and overdeveloped in order to increase the contrast.

The tests were performed with suspensions similar to those used in the preliminary experiments. However, the initial volumes per unit width (A_o) for both the sand and the bead suspensions were 0.018 m^2 and 0.0226 m^2 respectively. Initial masses of 7 kg and 4.5 kg of sand and beads respectively were used. The experimental procedures were similar to those of the preliminary tests.

2.4 Results

The results were obtained from slide-by-slide examination of the 35mm film of the flow. The data were reduced from the slides by an interactive program written for a Hewlett-Packard HP model 9816 microcomputer with a HP Graphics Tablet model 9111A. A photograph of the data acquisition setup shown in Fig. 2.15.

A slide projector was used to project the image from the slides towards a mirror inclined at 45 degrees to the graphics tablet. The outer boundary of the cloud was traced using the special graphics tablet pen (stylus). The graphics tablet recorded the coordinates of the traced points with respect to a predetermined point of reference. The computer program then used this input to calculate the cloud length and height, the circumference, the area of the cloud and the center of area position relative to a fixed origin. The mass of the particles and the distribution of the material deposited on the bed at the end of each experimental run was part of the input to the computer program. Hence the mean volumetric concentration of the cloud could be calculated for each slide. Also, the time of each slide was input to calculate the center of mass velocity between two consecutive slides. This calculation assumed that the particle concentration was distributed uniformly throughout the cloud. Several other parameters were calculated and these will be discussed later in Chapter 3. The collected data were stored on a disc and another program was used to retrieve the stored data and to plot it in the form which will be presented in the next Chapter.

The obtained results were in good agreement with the general trends observed in the preliminary tests. The problems encountered during the preliminary tests were eliminated to a great extent. However, another problem arose during the experimental runs with polystyrene beads. The presence of air in the water inside the tank caused the formation of air bubbles on the beads. The combined air bubble and the bead configuration was sometimes positively buoyant and instead of flowing down the slope under gravity, the beads rose to the ceiling of the tank! The problem was solved by heating the water, cooling it and then storing it in a storage tank for 24 hours prior to running the experiment. Detailed results of these tests will be presented and compared with the theoretical predictions in Section 3.4.

CHAPTER 3
THEORETICAL ANALYSIS

A two-dimensional model of the flow of a cloud of coarse particles down an inclined bed is presented in this Chapter. The analysis is based on the consideration of the overall conservation equations for the cloud instead of using a detailed infinitesimal element approach. An estimation of the parameters involved in the governing equations is presented. A new function to estimate the entrainment coefficient is proposed in Section 3.2.3. A comparison between the experimental results and the predictions obtained from the numerical solution of the governing equations is presented in Section 3.4.

3.1 The Governing Equations

The analysis considers a two-dimensional flow of a cloud down an inclined rough boundary and treats the cloud as a continuum. The particles are regarded as sufficiently large that electrostatic and other interparticle forces can be neglected in the continuum model. The flow Reynolds number is assumed to be sufficiently high such that the viscous effects can be neglected for the overall flow development. (Note that the Reynolds number associated with the particle fall velocity is not necessary large and the particle fall velocity is determined in an appropriate way.) Fig. 3.1 shows a sketch of the cloud and the considered control volume. The control surface is shown on Fig. 3.1 as a line which separates the ambient fluid from the body of the cloud. The shape of the control volume is taken to be a half elliptic form which, as will be seen later, is a good representation of the observed flow. The ambient fluid is assumed to be infinitely deep and unstratified. The bed is inclined at a constant angle of inclination. The motion of the cloud is referred to a rectangular Cartesian coordinate system in which the x-axis is directed downstream tangential to the bed and the y-axis is normal to the bed.

The governing equations of the motion are the sediment mass balance equation, the ambient fluid entrainment equation and the linear momentum equation along the bed. These are similar to but extended versions of equations presented by Beghin, et al. (23), Britter and Linden (16) and Ellison and Turner (17).

The mass balance equation is

$$\frac{d}{dt} [\rho_p \; c \; A] = - \rho_p [w \cos \zeta \; c + \epsilon_s \frac{dc'}{dy}] \; l \qquad (3.1)$$

where

ρ_p = particle mass density

c = volumetric mean concentration

A = area of the cloud

w = particle fall velocity

ζ = bed angle of inclination

ϵ_s = mass diffusion coefficient

$\frac{dc'}{dy}$ = concentration gradient at the bed

l = length of the cloud

Equation (3.1) relates the rate of increase of the mass solid particles within the cloud (ρ_p c A) to the difference between particle sedimentation and diffusion rates at the bottom of the cloud over the length l.

The ambient fluid entrainment equation is chosen to have a standard form

$$\frac{d}{dt}\,[\,\rho_a\,(\,1 - c\,)\,A\,] = \rho_a\,P\,u\,E \tag{3.2}$$

where

ρ_a = ambient fluid mass density

P = perimeter of the cloud

u = center of mass velocity

E = entrainment coefficient

The linear momentum equation along the bed is

$$\frac{d}{dt}\,[\,\rho_a\,(\,1 - c\,)\,A\,u + k_v\,\rho_a\,A\,u + \rho_p\,c\,A\,u\,] =$$

$$\Delta\rho\;c\;g\;A\,\sin\zeta - \Delta\rho\;c\;g\;A\,\cos\zeta\,\tan\phi - \frac{1}{2}\,\rho_a\,C_D\,h\,u^2 \tag{3.3}$$

where

k_v = added mass coefficient

$\Delta\rho = \rho_p - \rho_a$

g = gravitational acceleration

ϕ = bed friction angle for the solid particles chosen to be approximately equal to the angle of repose of the material

C_D = drag coefficient

h = height of the cloud

The first term in the square brackets on the left hand side of equation (3.3) is the momentum of the cloud fluid, the second term is the added mass contribution and the third term is the momentum of the solids. The first term on the right hand side is the net buoyant weight component, the second term is the bed friction force (assuming that the shear stress at the bed equals $\tan\phi$ times the normal stress) and the third term is the form drag force.

It was suggested by the experimental results that the shape of the cloud can be approximated by half an ellipse having major and minor axes l and 2h respectively (Fig. 3.1). In order to verify this assumption, the area and the perimeter of the cloud were expressed in these forms

$$A = S_1 \, h \, l \tag{3.4}$$

$$P = S_2 \sqrt{h \, l} \tag{3.5}$$

where S_1 and S_2 are shape factors. For the half elliptic shape, S_1 is equal to $\pi/4$ and S_2 can be expressed as (23)

$$S_2 = \frac{\pi}{2^{\frac{2}{3}}} \frac{(4K^2 + 1)^{\frac{1}{2}}}{K^{\frac{1}{2}}} \tag{3.6}$$

where K is the height to length ratio (h/l). Tables (3.1) and (3.2) show the average values of the shape factors S_1 and S_2 for both the sand suspension and the beads suspension respectively as calculated from the experimental data. The tables show a reasonable agreement between the theoretical values and the corresponding experimental values.

3.2 Estimation of Parameters

In this Section, all the parameters appearing in the governing equations (3.1), (3.2) and (3.3) will be presented.

For the added mass coefficient k_v in equation (3.3), it is reasonable to take the value of this coefficient for an elliptic cylinder as given by Batchelor (25)

$$K_v = \frac{2h}{l} \tag{3.7}$$

For the present study, the value of the form drag coefficient for the flow over an elliptic shaped body ($0.1 < h/l < 0.2$) was taken to be 0.05 based upon data from Heorner (26).

3.2.1 The Fall Velocity of the Particle

In the classical sediment transport literature, the concentration of the suspended sediment load is commonly small enough such that the fall velocity w on the right hand side of equation (3.1) is customarily taken as the free fall velocity. Also the bed angle of inclination is commonly very small such that the value of the fall velocity is used instead of its component normal to the bed. However, in the present study, the bed angle of inclination is high and the cosine of the angle of bed inclination can no longer be taken to be one. Also the cloud mean concentration is relatively high and the fall velocity of the particles within the suspension needs to be determined.

Maude and Whitmore (27) presented the following simple relation to express the particle fall velocity as a function of the concentration

$$w = w_o \, (1 - c)^{\alpha} \tag{3.8}$$

where w_o is the free fall velocity of a particle in still surroundings and the exponent α is a function of the Reynolds number. The range of α values are (2.5 - 4.5) corresponding to a range of the Reynolds number (1 - 1000). A reasonable value for the Reynolds number was chosen to give $\alpha = 3.25$.

3.2.2 The Mass Diffusion Coefficient

The mass diffusion coefficient ϵ_s can be written as

$$\epsilon_s = \beta \epsilon \tag{3.9}$$

where β is constant and ϵ is the kinematic eddy viscosity (the turbulent momentum diffusion coefficient). The reciprocal of β is often called the turbulent Schmidt number (Daily and Harleman (28)). The value of β apparently changes with the concentration, however, the variation is small (Vanoni (29)). The approximate value of the Schmidt number can be taken to be 0.7 (28). The kinematic eddy viscosity can be expressed considering the Prandtl mixing-length theory as

$$\epsilon = L^2 \left| \frac{dv}{dy} \right| \tag{3.10}$$

where L is the mixing length and v is the velocity at any position y. It is reasonable to assume that the bed boundary layer is sufficiently small that it can be neglected. This assumption suggests that the mixing length might be taken to be constant over the depth. Since the mixing process depends on the shear stress distribution which in turn depends on the velocity distribution across the flow, a flow which has a velocity distribution similar to that of a gravity current head was searched for. It was found that the wall jet flow has a velocity distribution (Guitton and Newman (30)) similar to the velocity distribution in gravity current heads for the cases where a salt water solution was used to generate the gravity currents (Hopfinger and Tochon-Danguy (1), Ellison and

Turner (17)). Recently, Hermann and Scheiwiller (31) have used an ultrasonic doppler technique to successfully measure mean particle velocity profiles in a steady current consisting of a suspension of polystyrene beads. The measured profiles resembled the ones measured for the wall jet flow. An expression given by Schlichting (32) for the mixing length for a wall jet is

$$L = 0.068\ b \tag{3.11}$$

where b is the width of the jet (taken equal to the height h of the cloud for the present work). Combining equations (3.10) and (3.11) and substituting into equation (3.9) yields a simple expression for the mass diffusion coefficient

$$\epsilon_s = \beta\ (\ 0.068\ h\ )^2 \left| \frac{dv}{dy} \right| \tag{3.12}$$

The right hand side of equation (3.1) should be evaluated at the bed level since mass leaves the control volume through sedimentation at the bed level. Thus, both the concentration derivative in the right hand side of equation (3.1) and the velocity derivative in equation (3.12) have to be evaluated at the bed level (again remembering that the bed boundary layer is being neglected in the present discussion). Since both the velocity and the concentration profiles were not available from the present experimental study, an approximation of the shape of these profiles was made based on the previously measured profiles for gravity current heads (1,18,31). Thus, an estimate of the required gradients of the velocity and concentration can be made.

3.2.2.1 Similarity Assumption

It was found from the preliminary experiments that, for a given angle of bed inclination, the ratio of the height to the length of the cloud K was approximately constant (Fig. 2.4 and Fig. 2.5). Also these observations were consistent with the results of the large scale experiments which can be seen clearly from Figs. 3.2 and 3.3 for the sand clouds and the bead clouds respectively. These results suggested that a similarity assumption regarding the profiles of both the velocity and concentration distribution across the cloud could be made. It is convenient and reasonable to assume that both the velocity and concentration ha.e similar profiles in the y-direction as the cloud flows downstream. Fig. 3.4 shows a sketch of the assumed profiles.

Let U, H and C be characteristic values of the velocity, height and concentration respectively; they are defined by the following relations

$$U\,H = \int_0^h v\,dy \qquad (3.13)$$

$$U^2\,H = \int_0^h v^2\,dy \qquad (3.14)$$

$$C\,H = \int_0^h c'\,dy \qquad (3.15)$$

where v and c' are the velocity and concentration at any position y. It can be easily shown that the characteristic velocity, height and concentration are equal to

$$U = \frac{2}{3}\,u_b = u \qquad (3.16)$$

$$H = \frac{3}{4} h \tag{3.17}$$

$$C = \frac{2}{3} c_b = c \tag{3.18}$$

where the subscript b refers to the bed value of the variable. Thus, both the velocity and the concentration derivatives at the bed level can be written as

$$\frac{dv}{dy} = - \frac{u_b}{h} = - \frac{9}{8} \frac{U}{H} \tag{3.19}$$

$$\frac{dc'}{dy} = - \frac{c_b}{h} = - \frac{9}{8} \frac{C}{H} \tag{3.20}$$

Therefore, the mass diffusion coefficient, in equation (3.9) can be expressed as

$$\epsilon_s = \beta \, (0.068)^2 \, (\frac{4}{3} H)^2 \, \frac{9}{8} \frac{U}{H} \tag{3.21}$$

or

$$\epsilon_s = 0.0132 \ H \ U \tag{3.22}$$

and the second term in the right hand side of equation (3.1) can be written as

$$\epsilon_s \frac{dc'}{dy} = - 0.0149 \ C \ U = - 0.0149 \ c \ u \tag{3.23}$$

3.2.3 The Entrainment Coefficient

As was mentioned earlier in the Introduction, all the available relevant studies on the entrainment coefficient were a result of the dense flow simulations of gravity currents and clouds using miscible fluids. In these investigations, the entrainment coefficient was usually expressed as a function of the Richardson number. However, for the present study, the Richardson number alone is insufficient to specify this coefficient since it does not reflect the role of the particle properties on the entrainment process.

Thus, a dimensional analysis was performed to seek the relevant dimensionless groups upon which the entrainment coefficient might depend. Consider the following parameters to be important; the cloud characteristic height H, the reduced gravitational acceleration perpendicular to the flow direction $g' \cos\zeta$ and $g' = g\, c \frac{\Delta\rho}{\rho_a}$, the cloud characteristics velocity U and the particle net fall velocity $\tilde{W}$.

The length of the cloud was not selected since the ratio of the height to the length of the cloud was found to be constant for a given angle of bed inclination. The particle net fall velocity can be evaluated from the right hand side of equation (3.1) as follows

$$\tilde{W} = w \cos\zeta - \frac{\epsilon_s}{c} \frac{dc'}{dy} \tag{3.24}$$

Substituting equations (3.8) and (3.23) into equation (3.24) yields

$$\tilde{W} = w_o \,(1 - c)^{\alpha} \cos\zeta - 0.0149\, u \tag{3.25}$$

The selected parameters can be written as

$$f\ (\ H\ ,\ g'\cos\zeta\ ,\ U\ ,\ \tilde{W}\ )\ =\ 0 \qquad (3.26)$$

By using the Buckingham Π theorem, the following dimensionless groups were obtained

$$f\ (\ \frac{g'\cos\zeta\ H}{U^2}\ ,\ \frac{\tilde{W}}{U}\ )\ =\ 0 \qquad (3.27)$$

The first term is, of course, the Richardson number R = $g'\cos\zeta\ H\ /\ U^2$. The second term is the ratio of the particle net fall velocity to the cloud characteristic velocity which is an important parameter upon which the entrainment coefficient depends. This can be seen clearly if we consider the case of a cloud which consists of a suspension of large particles having high fall velocities. Only a subsiding flow and a very small or even a negative entrainment coefficient might be expected. Therefore, we propose that the entrainment coefficient can be expressed as follows

$$E\ =\ f\ (\ R\ ,\ \frac{\tilde{W}}{U}\ ) \qquad (3.28)$$

The evaluation of the this function can be achieved by using the experimental results. The entrainment coefficient can be calculated from the experimental data by using equation (3.1) since it can be written in the following form

$$\Delta\ [\ A\ (\ 1\ -\ c\ )\ ]\ =\ P_{av}\ u\ E\ \Delta t \qquad (3.29)$$

where Δ means the difference in the magnitude of the variable between two consecutive slides, Δt is the time interval between the same two slides and P_{av} is the average of the cloud perimeter measured from both slides. The entrainment coefficient, the Richardson number and the velocity ratio $\tilde{W} / U$ were calculated from the data collected using the computer program mentioned in Section 2.4.

A multiple linear regression analysis was performed on the data and the following expressions were obtained for the sand cloud and the beads cloud respectively

$$E = 0.0792 - 0.0117\ R - 0.1087\ \frac{\tilde{W}}{U} \tag{3.30}$$

$$E = 0.0923 - 0.0127\ R - 0.1194\ \frac{\tilde{W}}{U} \tag{3.31}$$

with r^2, the correlation coefficient, equal to 0.95 and 0.97 respectively.

Figs. 3.5 and 3.6 show the entrainment coefficient versus the Richardson number for different values of the velocity ratio $\tilde{W} / U$ for sand clouds and bead clouds respectively. Figs. 3.7 and 3.8 show the entrainment coefficient versus the velocity ratio for different values of the Richardson number for both the sand clouds and the bead clouds respectively.

The good agreement between equations (3.30) and (3.31) and the experimental results suggested that, there might be only one functional relationship for the entrainment coefficient regardless of the particle type since the particle properties were involved in the dimensionless parameter $\tilde{W} / U$. Therefore, another regression analysis was performed on all the data collected from both the sand and the bead cloud experiments. The least square regression gave the following expression for the entrainment coefficient

$$E = 0.0882 - 0.0149\,R - 0.0679\,\frac{\tilde{W}}{U} \qquad (3.32)$$

with $r^2 = 0.94$ which shows strong support for the proposed expression for the entrainment coefficient. Note, that the entrainment coefficient increases with the decrease in the velocity ratio $\tilde{W} / U$ and at the limit where $\tilde{W}$ vanishes, the expression shows reasonable agreement with the salt solution experiments which were reported by Beghin, et al. (23). Figs. 3.9 and 3.10 show the same trend observed in the individual cloud shown in Figs. 3.5, 3.6, 3.7 and 3.8. Equation (3.32) was used to evaluate the entrainment coefficient in the numerical solution of the governing equations which will be presented in the next Section.

3.3 Numerical Solution

The governing equations (3.1), (3.2) and (3.3) can be written, considering the obtained expressions for the parameters in the previous Section, as follows

$$A_1 \frac{dl}{dt} + A_2 \frac{dc}{dt} = D_1 \qquad (3.33)$$

$$A_3 \frac{dl}{dt} - A_2 \frac{dc}{dt} = D_2 \qquad (3.34)$$

$$A_4 \frac{du}{dt} + A_5 \frac{dl}{dt} + A_6 \frac{dc}{dt} = D_3 \qquad (3.35)$$

where

$$A_1 = 2\ S_1\ K\ c \tag{3.36}$$

$$A_2 = S_1\ K\ l \tag{3.37}$$

$$A_3 = 2\ S_1\ K\ (\ 1 - c\ ) \tag{3.38}$$

$$A_4 = S_1\ l\ [\ \rho_a\ (\ 1 + k_v\ ) + \Delta\rho\ c\ ] \tag{3.39}$$

$$A_5 = 2\ S_1\ u\ [\ \rho_a\ (\ 1 + k_v\ ) + \Delta\rho\ c\ ] \tag{3.40}$$

$$A_6 = S_1\ u\ l \tag{3.41}$$

$$D_1 = -\ [\ w_o\ \cos\zeta\ c\ (\ 1 - c\ )^{\alpha} - 0.0194\ c\ u\ ] \tag{3.42}$$

$$D_2 = S_2\ \sqrt{K}\ u\ E \tag{3.43}$$

$$D_3 = S_1\ l\ c\ g\ (\ \sin\zeta - \cos\zeta\ \tan\phi\ ) - \frac{1}{2}\ \rho_a\ C_D\ u^2 \tag{3.44}$$

Equations (3.33), (3.34) and (3.35) can be solved together to give three ordinary differential equations in l, c and u as follows

$$\frac{dl}{dt} = Z_1 \tag{3.45}$$

$$\frac{dc}{dt} = Z_2 \tag{3.46}$$

$$\frac{du}{dt} = Z_3 \tag{3.47}$$

where

$$Z_1 = \frac{D_1 + D_2}{A_1 + A_3} \tag{3.48}$$

$$Z_2 = \frac{A_3 Z_1 - D_2}{A_2} \tag{3.49}$$

$$Z_3 = \frac{D_3 - A_5 Z_1 - A_6 Z_2}{A_4} \tag{3.50}$$

A fourth ordinary differential equation was added to the system of equations (3.45), (3.46) and (3.47) in order to obtain the results as functions of the downstream distance as well as functions of the time

$$\frac{dx}{dt} = u \tag{3.51}$$

The governing ordinary differential equations (3.45), (3.46), (3.47) and (3.51) were integrated numerically using the Runge-Kutta method. Initial values were needed to start the integrations, these values were taken from the experimental data. The starting position was selected at the position where the cloud was fully developed. This position was a small distance downstream the release gate.

3.4 Predictions and Comparison with Experimental Results

The results of the numerical integration of the governing differential equations are presented and compared with the experimental data obtained from the large scale experiments (the even-numbered figures will refer to sand clouds and the odd-numbered figures will refer to bead clouds).

Figs. 3.11 and 3.12 show the predicted length of the cloud normalized by the square root of the initial volume of the cloud per unit width ($A_o^{1/2}$) versus the traveling distance normalized by the same factor for different bed inclinations. In Fig. 3.11 numerical solutions only for bed angles of inclination of 44 and 38 degrees are presented. Since the angle of repose of the sand was taken to be 36 degrees, the numerical solutions for the angles of bed inclination 34 and 30 degrees show an immediate collapse of the cloud which contradicts the experimental observation. It is believed that, as the suspension was released the shear stress which was created between the different layer of the cloud due to the sudden motion created a dispersive stress (24) which might have mobilized the cloud for a short distance. Then the retarding forces (the bed friction and the form drag) dominated and the cloud collapsed.

Figs. 3.13 and 3.14 show the cloud mean volumetric concentration versus the non-dimensional traveling distance. The graphs show that the model accounts well for the increase of the cloud mean concentration at the final collapse phase.

Figs. 3.15 and 3.16 show the non-dimensional center-of-mass velocity versus the non-dimensional traveling distance. Figs. 3.17 and 3.18 show the entrainment coefficient versus the non-dimensional traveling distance. These figures show that, the entrainment coefficient increased during the acceleration phase of the flow then it decreased through the deceleration phase. At the final stage of the deceleration phase, the entrainment coefficient became negative, i.e. fluid was detrained from the cloud.

In general, the numerical solution slightly overestimated the experimental results. The discrepancy might be attributed to the estimation of the parameters as well as the experimental data measurements. Also another possible reason is that, the model did not include the effect of particle interactions which may play an important role at high concentrations in the processes of growth and collapse of the cloud.

CHAPTER 4

SUMMARY AND CONCLUSIONS

Although there have been many studies of flows generated by density differences, most of these have involved different fluids (either miscible or immiscible) or temperature differences to create the density differences that drive the flow. On the other hand, there are instances in which the density differences arise because of the presence of solids suspended in the fluid. Some examples of density currents of this kind are turbidity currents in the ocean, the discharge of mine tailings into oceans and lakes, the 'silting up' of water supply reservoirs, powder snow avalanches and dust laden atmospheric gravity currents such as the Sudanese 'haboobs'. Subaqueous grain flows and the forces generated when they strike and flow around underwater objects are of current interest in connection with oil exploration on the continental shelf regions.

The presence of particle sedimentation and bed erosion can cause unsteady or developing density currents to behave in very different ways than density currents involving only fluids. Surprisingly, there have been very few fundamental studies of the mechanics of such flows. As an initial attempt to gain some insight into these flows, the present investigation has concentrated on the effects of finite particle size on the subaqueous flow of a cloud of particles down a rough inclined bed. The flow is analogous to one which might be initiated by a submarine earthquake.

Preliminary small scale laboratory experiments were carried out in a 2 m long tilting water tank to determine essential flow characteristics and variables. Suspensions of particles were released by a gate positioned at the upper end of the tank and the growth and collapse of the ensuing cloud was measured as it moved down the roughened bed of the tank. Two sets of tests were performed using suspensions of a) fine sand particles and b) polystyrene beads. The results of these experiments in which sedimentation and cloud collapse occurred were quite different from those carried out by Beghin, et al. using fresh water and salt water in which the clouds continued to grow without bound. Based on the experience gained by these preliminary tests, a large scale tilting tank was designed and a second series of tests was performed. The results obtained from the new experiments were consistent with those of the preliminary tests.

It was found that the shape of the particles cloud could be approximated by half an ellipse having major and minor axes l and 2h. The aspect ratio $K = h/l$ was found to be approximately constant during the flow for each bed inclination. It was observed that the cloud initially grew in size, reached a maximum and then collapsed. The distance of travel from initiation to collapse increased with an increase in the bed inclination. After the entry of the particulate material at the upper end of the tank, the cloud accelerated from rest, its velocity reached a maximum and then decayed to zero at the final collapse time. The peak center-of-mass velocity for a given bed slope increased with bed slope.

A theory to describe these two-dimensional flows was developed based upon three overall conservation equations; the sediment mass balance equation, the ambient fluid entrainment equation and the linear momentum equation along the bed. The sediment mass balance equation involved the tendency of the dense particles to settle and the opposite tendency for them to disperse as a result of turbulent mixing. The mass diffusion coefficient involved in the equation was taken as a multiple of the eddy viscosity which in turn could be related to the shear stress distribution within the cloud. An expression for this coefficient was devised by assuming that the shear stress distribution is similar to that of the wall jet.

Previous experimental observations of the dense fluid simulation of gravity currents and clouds involving only fluids showed that the entrainment coefficient which appears in the ambient fluid entrainment equation was only a function of the Richardson number and was constant for each bed slope. The present study, in which the cloud was made up of particulate solids, revealed that the entrainment coefficient not only varied along the flow path but could become negative after a particular station. Through dimensional analysis, the entrainment coefficient was expressed as a function of both the Richardson number and the ratio of the particle net fall velocity to the cloud center of mass velocity. A multiple regression analysis was performed using the experimental data, and the least square regression gave support for the proposed functional form entrainment coefficient.

The rate of change of the linear momentum of the cloud is due to the combination of the component of the net buoyancy force along the bed as a driving force and both the bed friction and the cloud form drag as a retardant forces. In the present study, the bed friction arising from particle interactions was found to be very significant. In previous studies by Beghin, et al. which involved only fluids, both the bed friction and the form drag were taken to be negligible.

The set of overall conservation equations was integrated numerically using a Runge-Kutta method and it was found that the present simple model predicted the main features of the development of the sedimenting cloud and was in good quantitative agreement with the laboratory experiments.

The experimental results obtained in the present experiments, the proposed law for the entrainment coefficient, the identification of the importance of particle bed friction and form drag, etc. can be applied in further investigations of density currents involving sedimenting particles. Detailed measurements of the distributions of particle velocities and concentration would make a significant contribution to our understanding of these flows. Acquisition of such data awaits the development of instrumentation capable of making measurements in a sufficiently short time for these time dependent flows. A theory to predict the detailed particle velocity and concentration distributions requires an appropriate constitutive equation for the fluid-particle mixture; this also is not presently available. The effects of erosion of bed materials of various kinds on the flows should be investigated. Finally the flows around and the forces developed on submerged bodies by density currents of suspensions should be investigated.

Table 3.1

Sand Suspension Cloud

Angle of bed inclination	44°	38°	34°	30°
$K = h/l$	.215	.170	.135	.103
S_1 (experiments)	.792	.814	.809	.817
S_1 (for ellipse)	.7854	.7854	.7854	.7854
S_2 (experiments)	2.892	2.876	2.953	3.241
S_2 (Eq. 3.6) (for ellipse)	2.608	2.813	3.131	3.534

Table 3.2

Bead Suspension Cloud

Angle of bed inclination	44°	38°	34°	30°
$K = h/l$	.299	.22	.145	.12
S_1 (experiments)	.783	.801	.793	.781
S_1 (for ellipse)	.7854	.7854	.7854	.7854
S_2 (experiments)	2.425	2.873	2.981	3.214
S_2 (Eq. 3.6) (for ellipse)	2.367	2.587	3.037	3.297

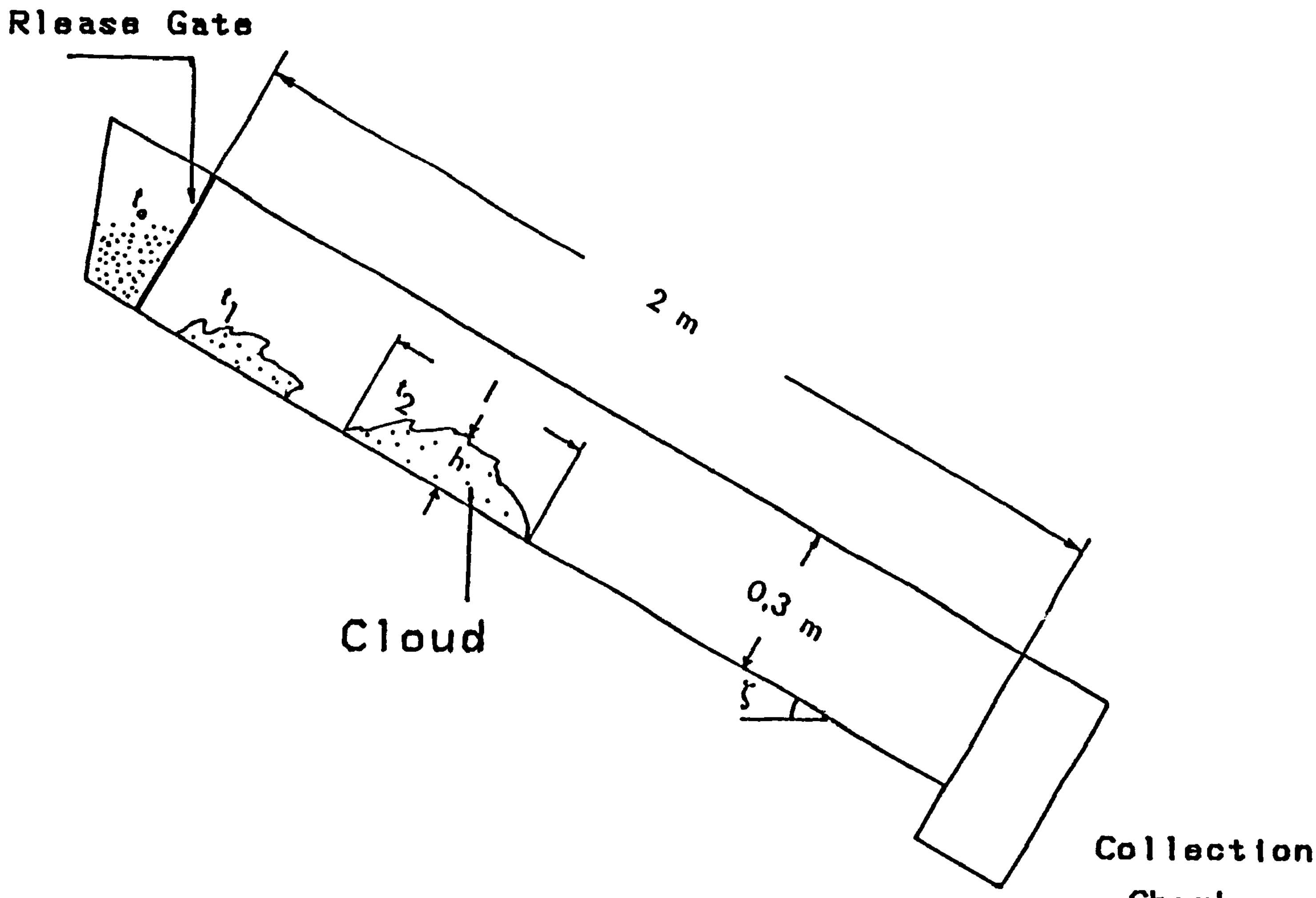

Fig. 2.1 Sketch of the small scale water tank

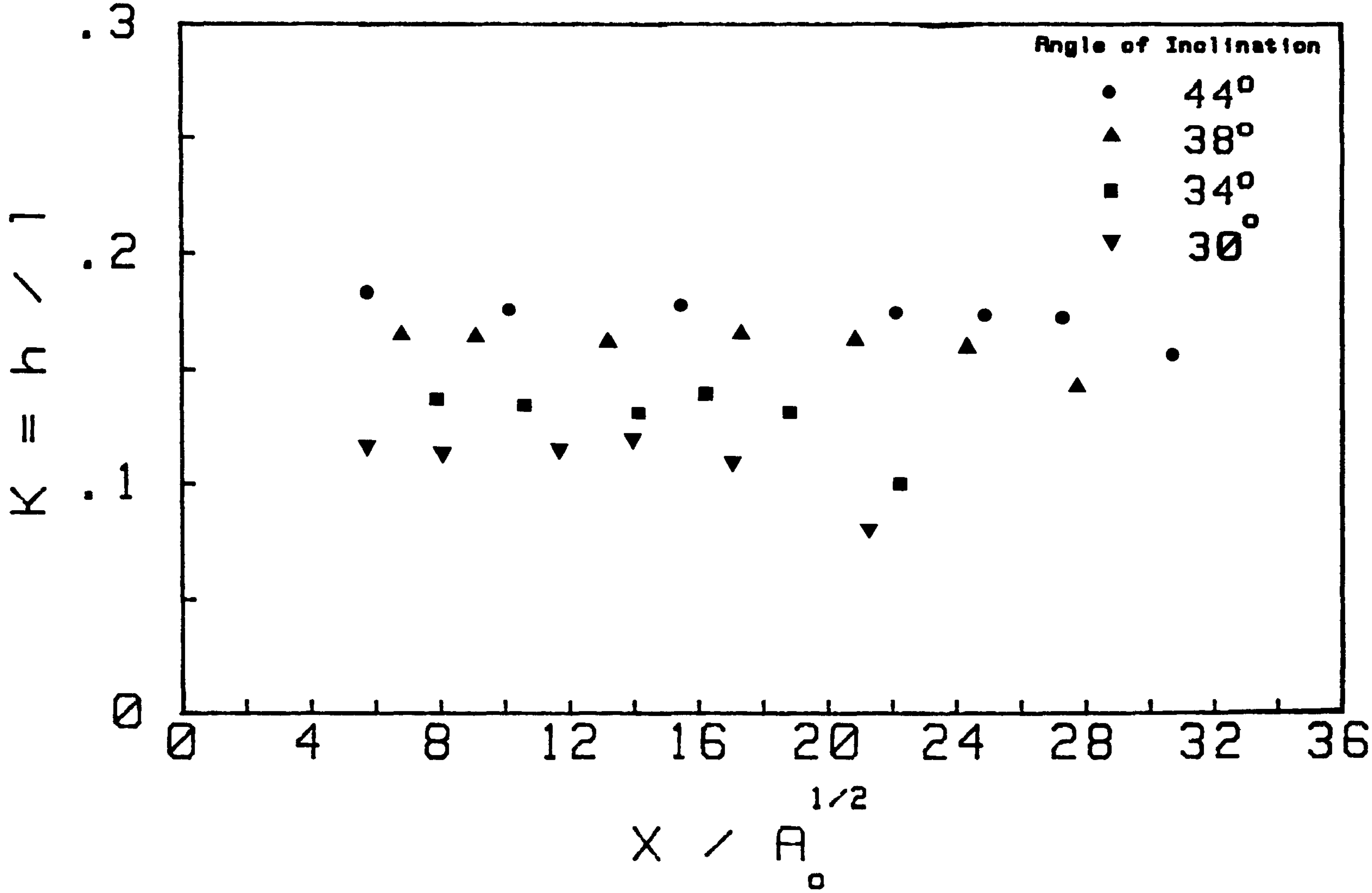

Fig.2.2 Aspect ratio of cloud versus traveling distance normalized by $A_o^{1/2}$ for sand suspension

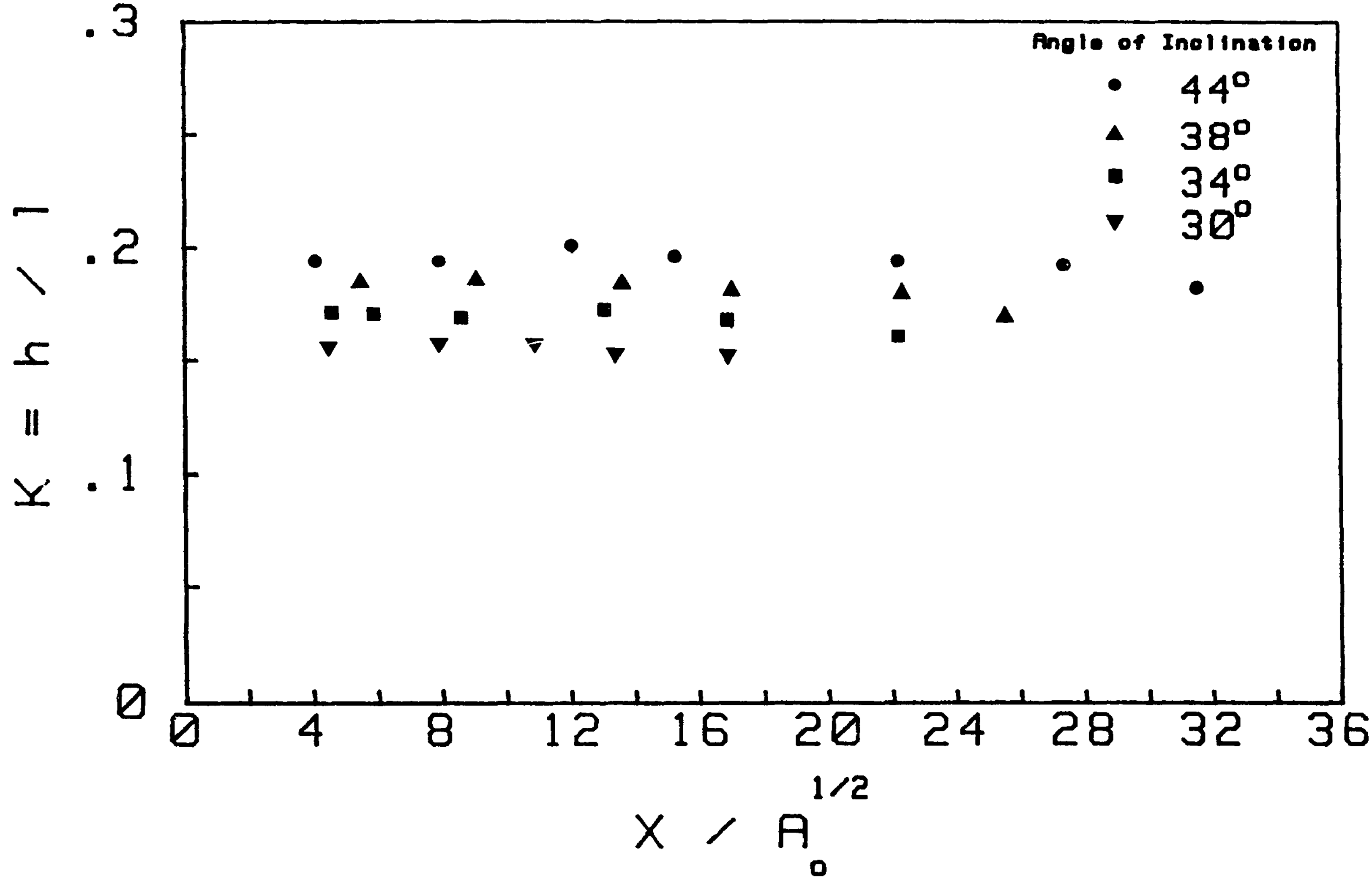

Fig.2.3 Aspect ratio of cloud versus traveling distance normalized by $A_o^{1/2}$ for bead suspension

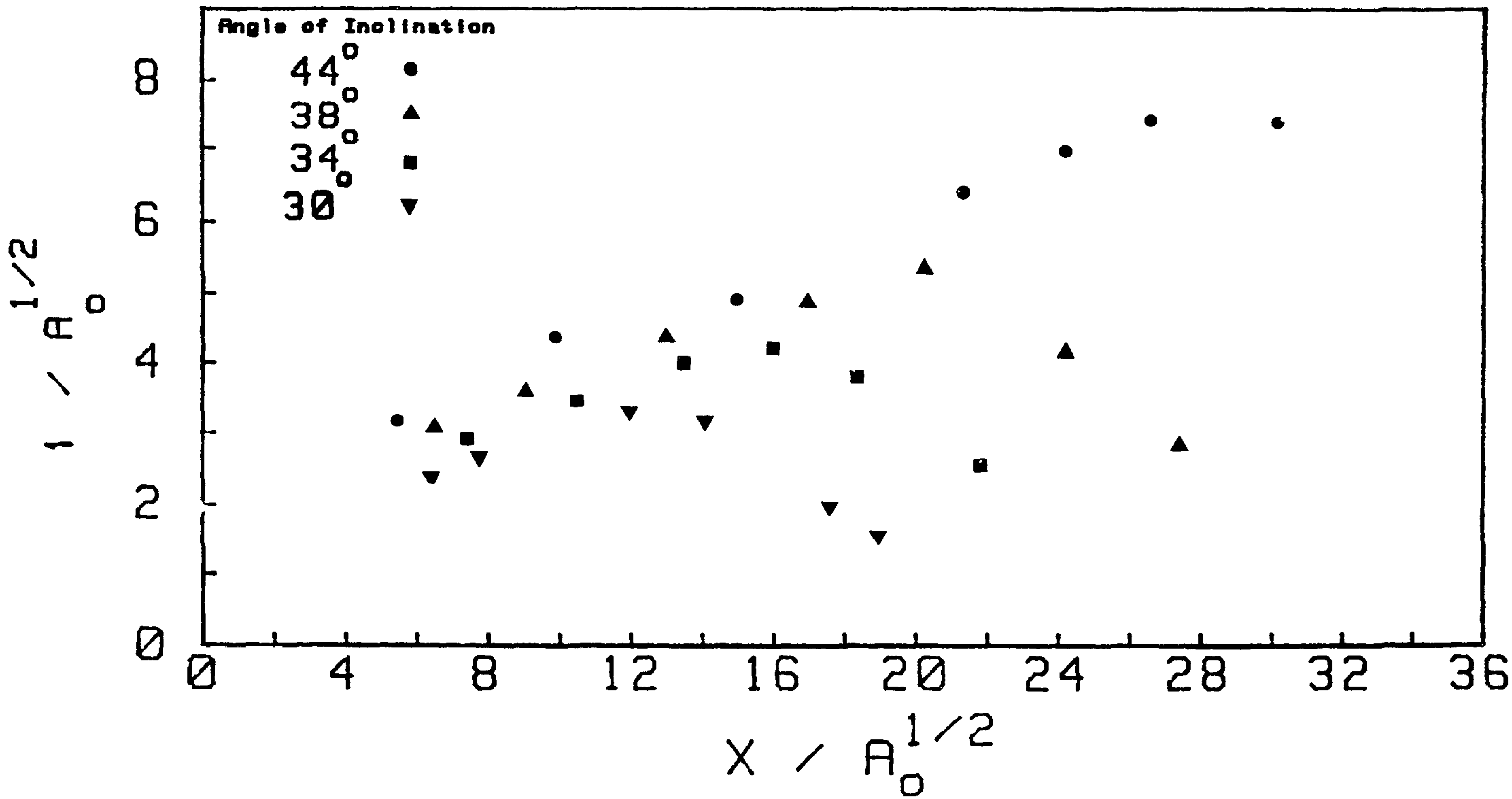

Fig.2.4 Length of the cloud versus traveling distance, both normalized by $A_o^{1/2}$ for sand suspension

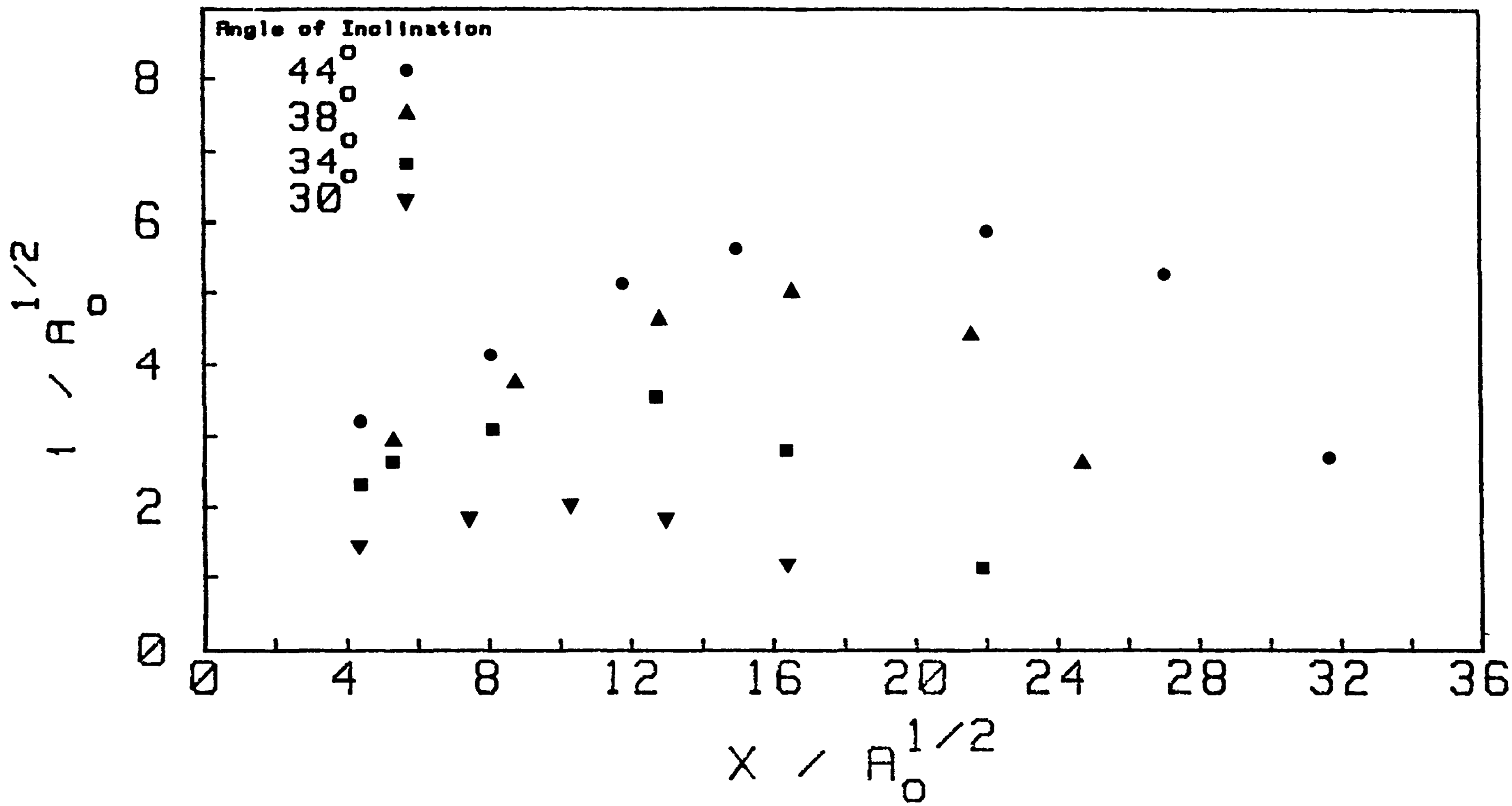

Fig.2.5 Length of the cloud versus traveling distance, both normalized by $A_o^{1/2}$ for bead suspension

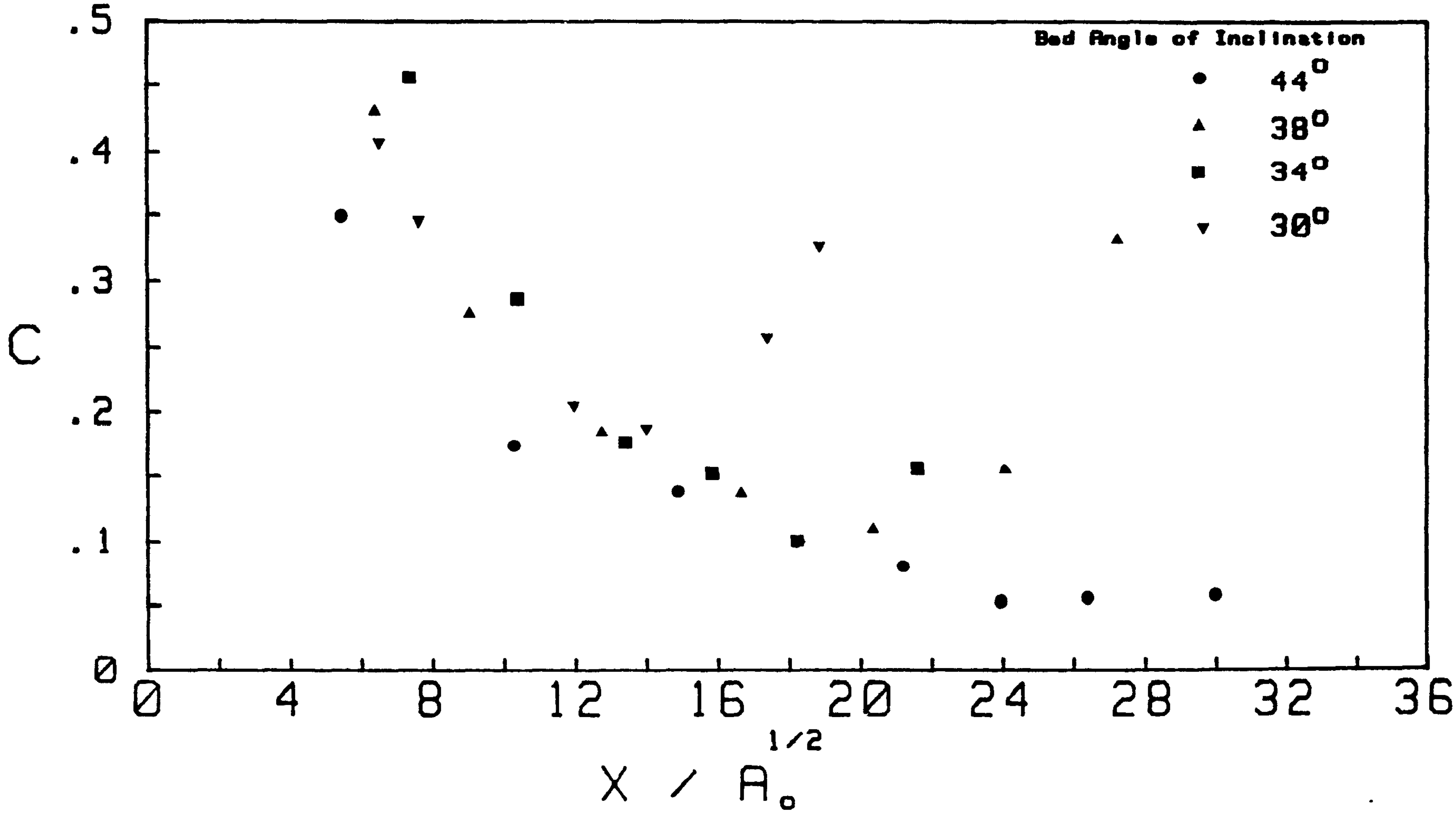

Fig.2.6 Cloud mean volumetric concentration versus traveling distance normalized by $A_o^{1/2}$ for sand suspension

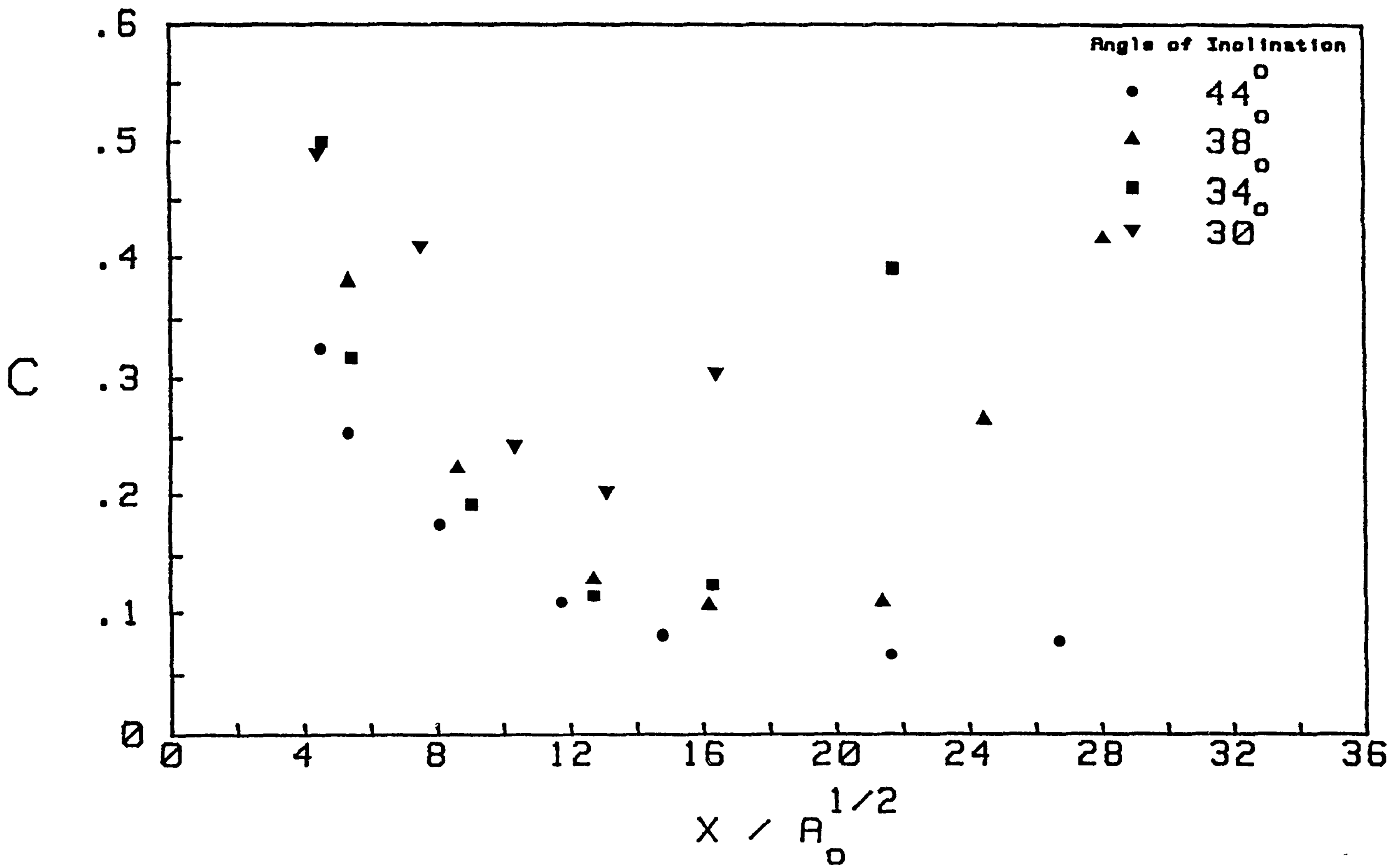

Fig.2.7 Cloud mean volumetric concentration versus traveling distance normalized by $A_o^{1/2}$ for bead suspension

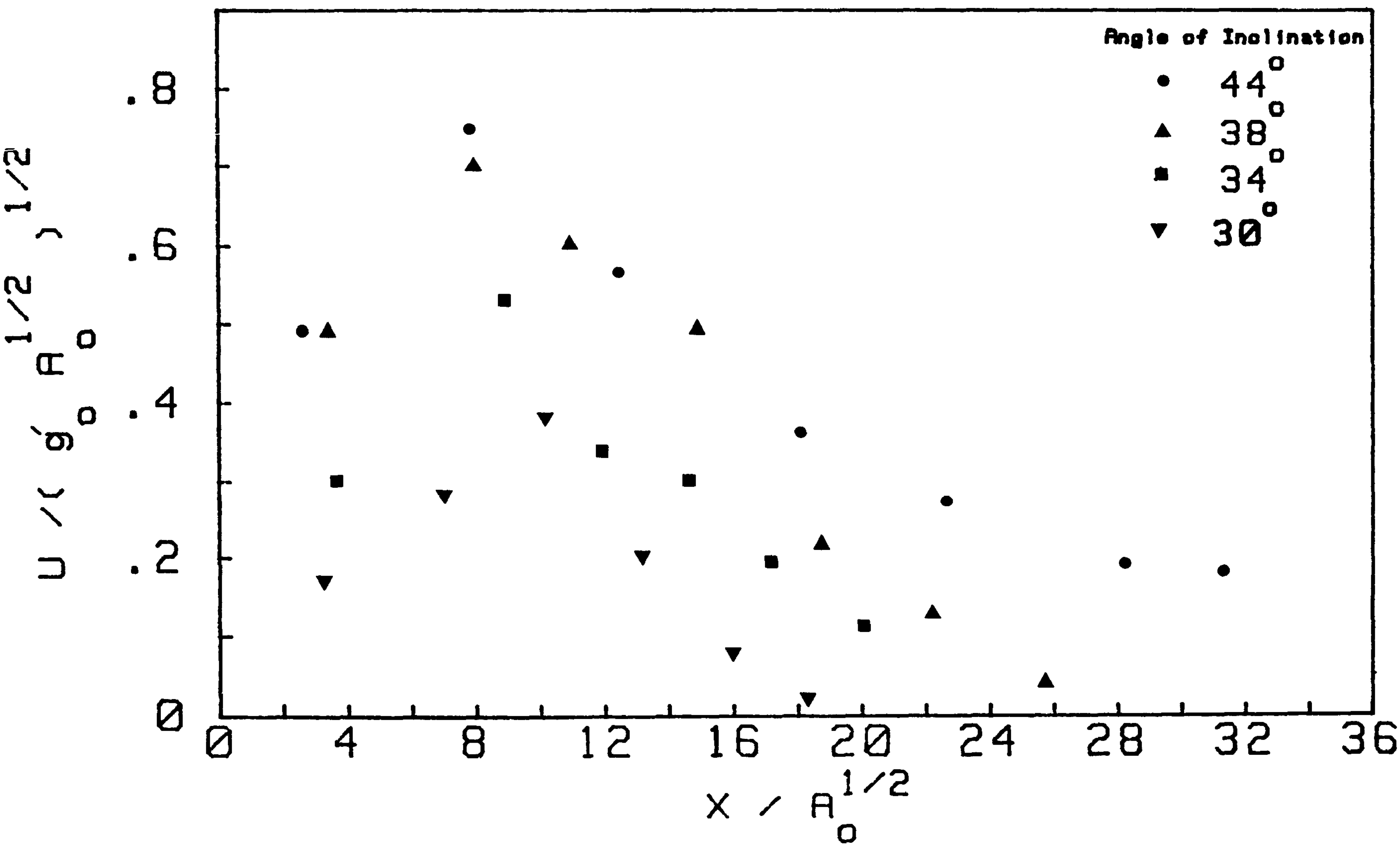

Fig.2.8 Non-dimensional front velocity versus non-dimensional traveling distance for sand suspension

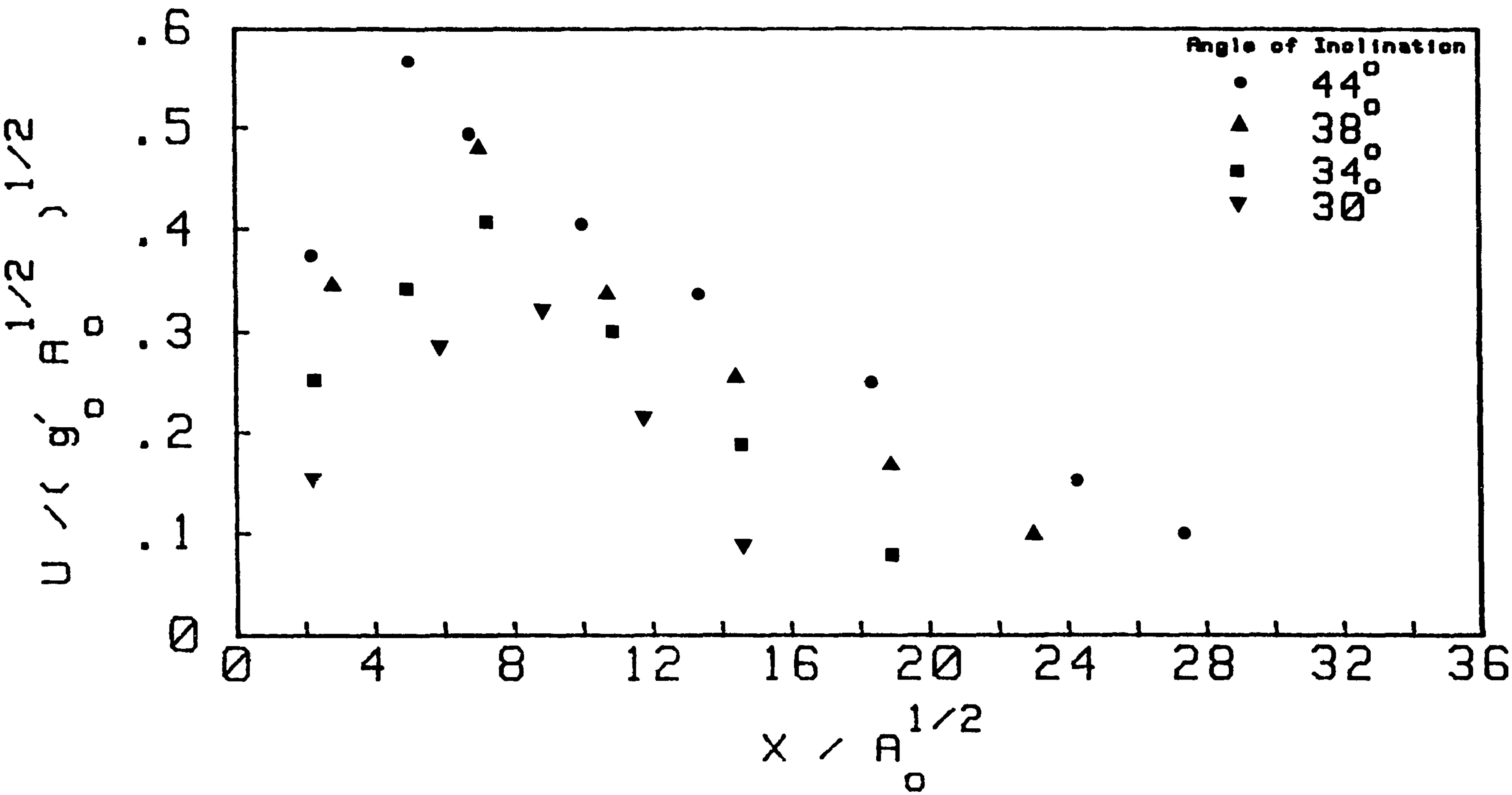

Fig.2.9 Non-dimensional front velocity versus non-dimensional traveling distance for bead suspension

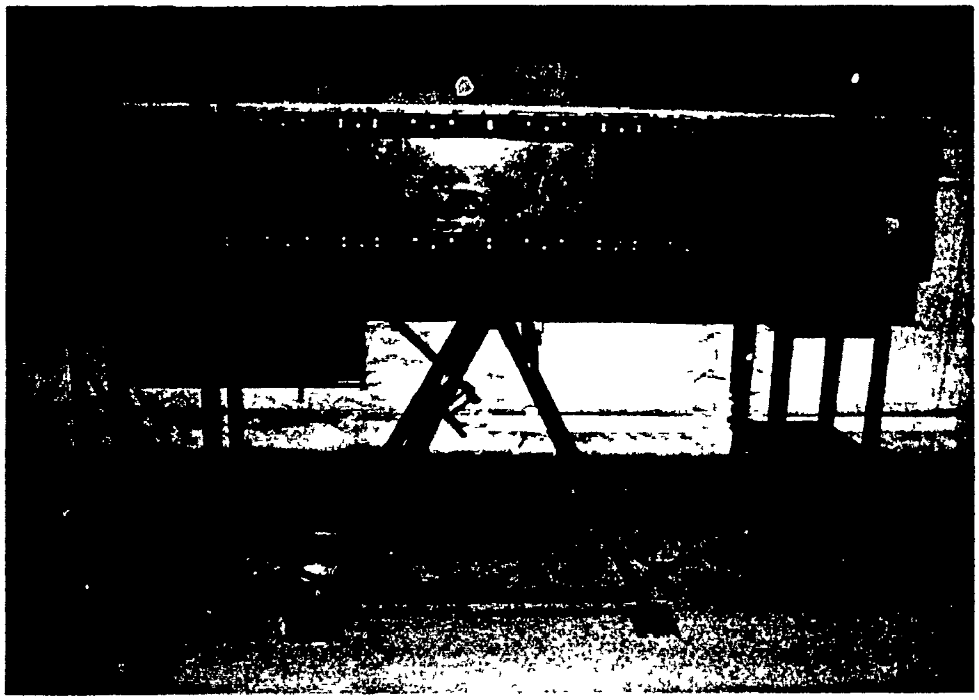

Fig.2.10 Photograph of the large scale water tank

Fig.2.12 Typical photograph from the large scale experiments

(a)

(b)

(c)

(d)

Fig.2.13 The sand cloud on slopes of (a) 30, (b) 34, (c) 38 and (d) 44 degrees respectively

(a)

(b)

(c)

(d)

Fig.2.14 The bead cloud on slopes of (a) 30, (b) 34, (c) 38 and (d) 44 degrees respectively

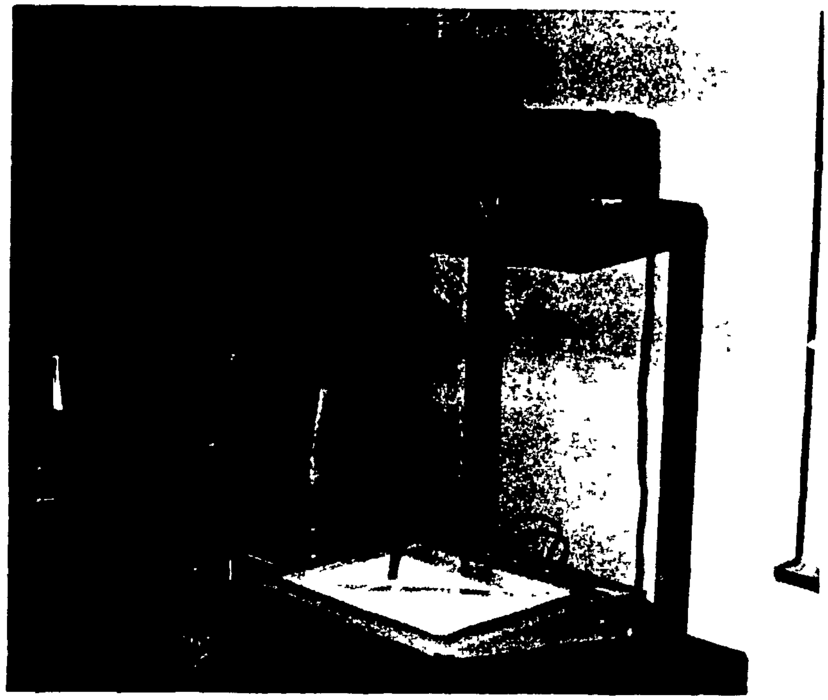

Fig.2.15 Photograph of the data acquisition system

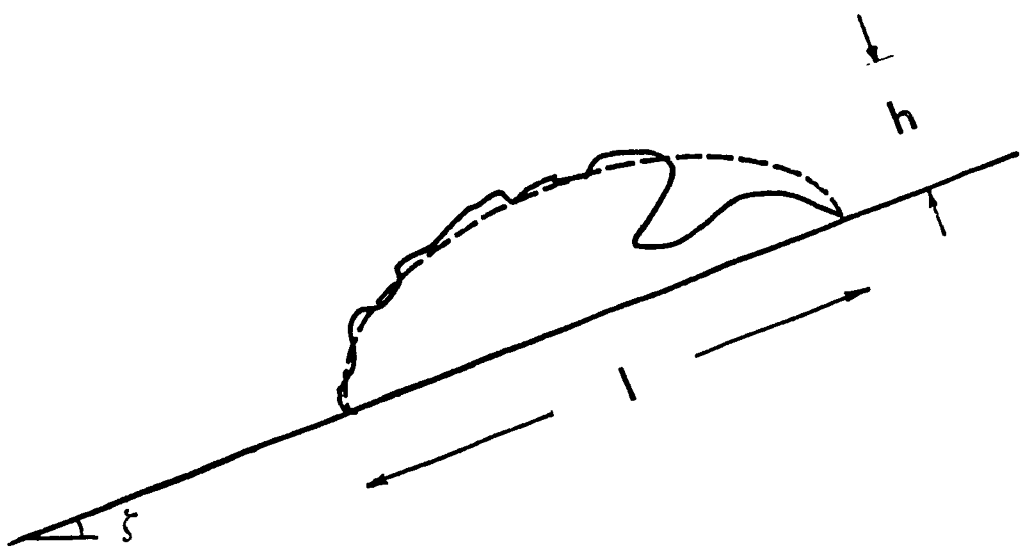

Fig.3.1 Sketch of the cloud and the assumed half elliptic shape

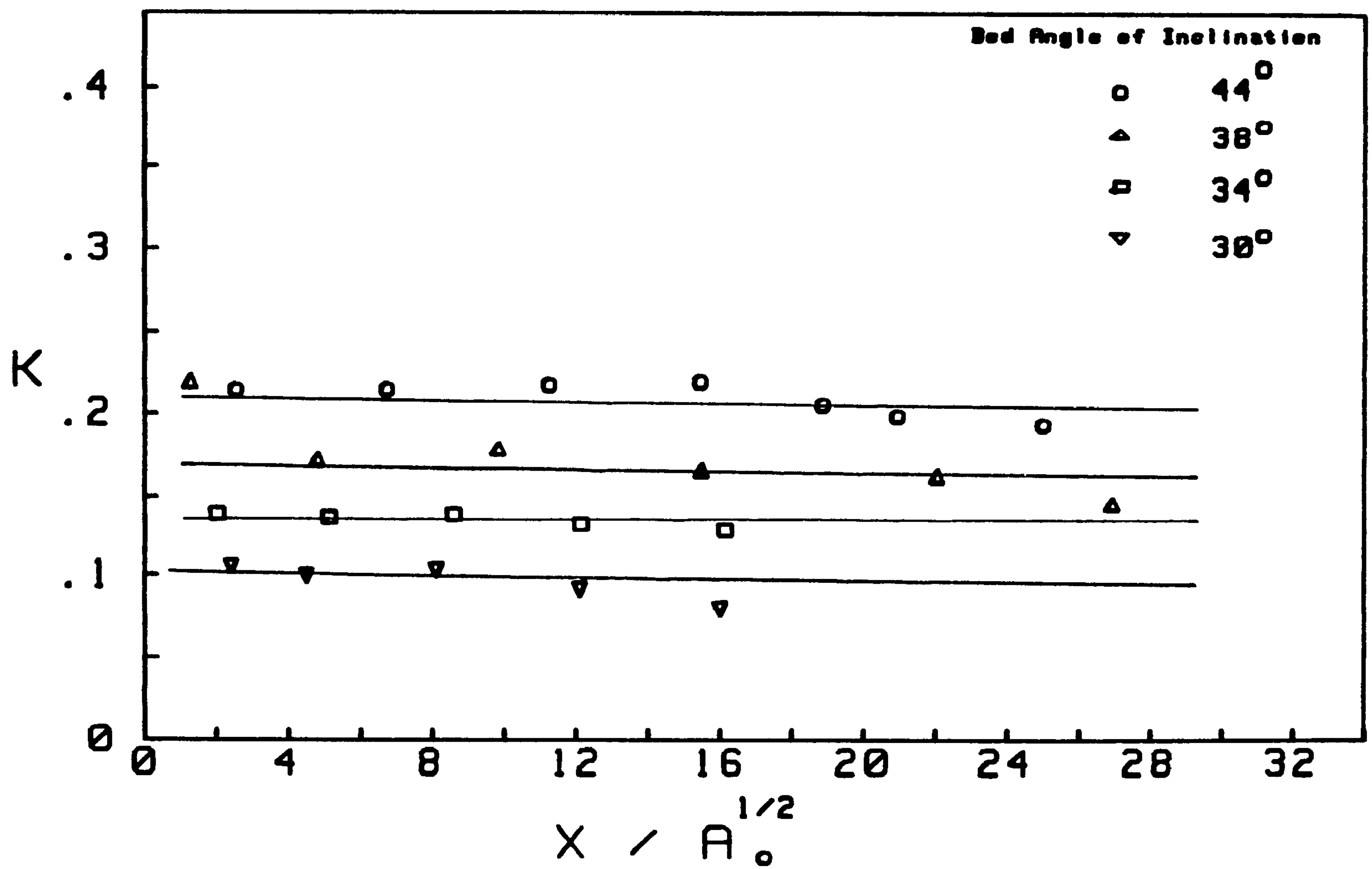

Fig.3.2 Aspect ratio of cloud versus traveling distance normalized by $A_o^{1/2}$ for sand suspension

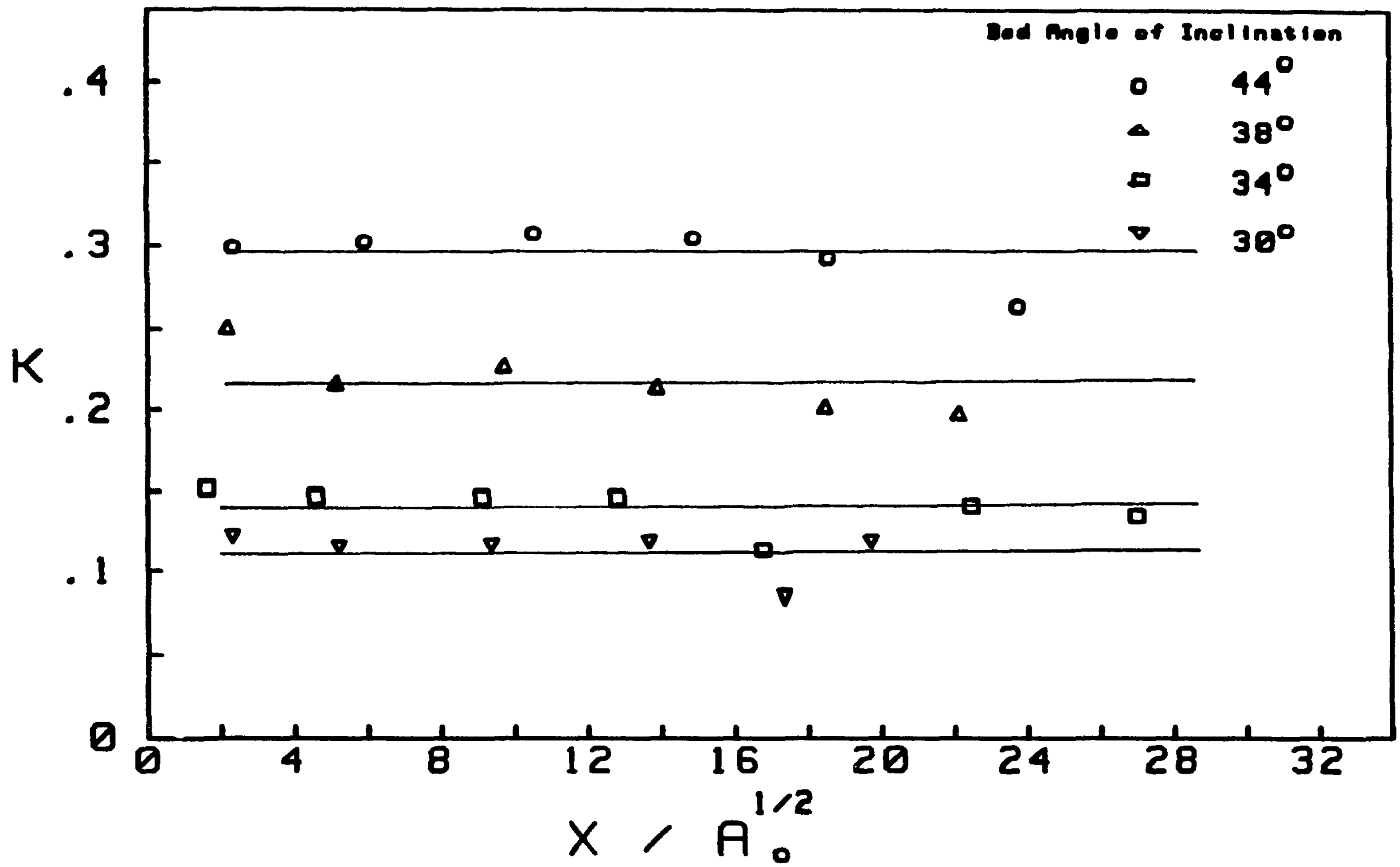

Fig.3.3 Aspect ratio of cloud versus traveling distance normalized by $A_o^{1/2}$ for bead suspension

c mean cloud concentration

u center of mass velocity

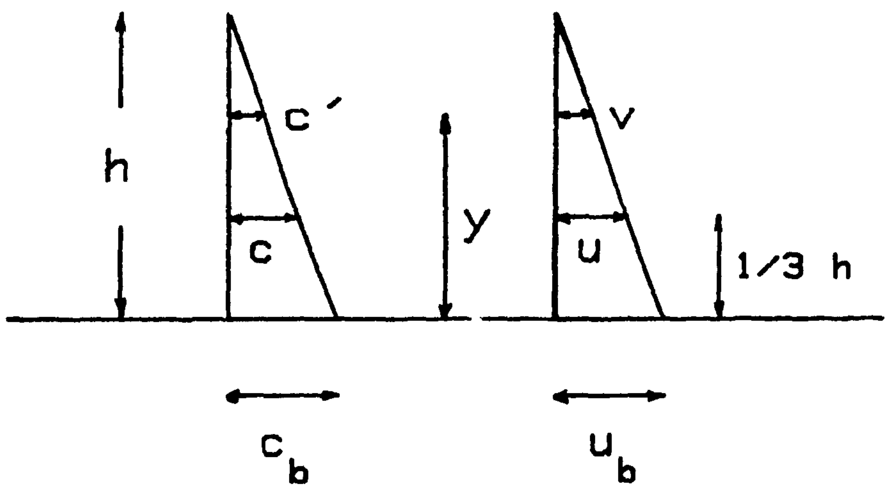

Fig.3.4 The assumed profiles of the velocity and concentration distribution

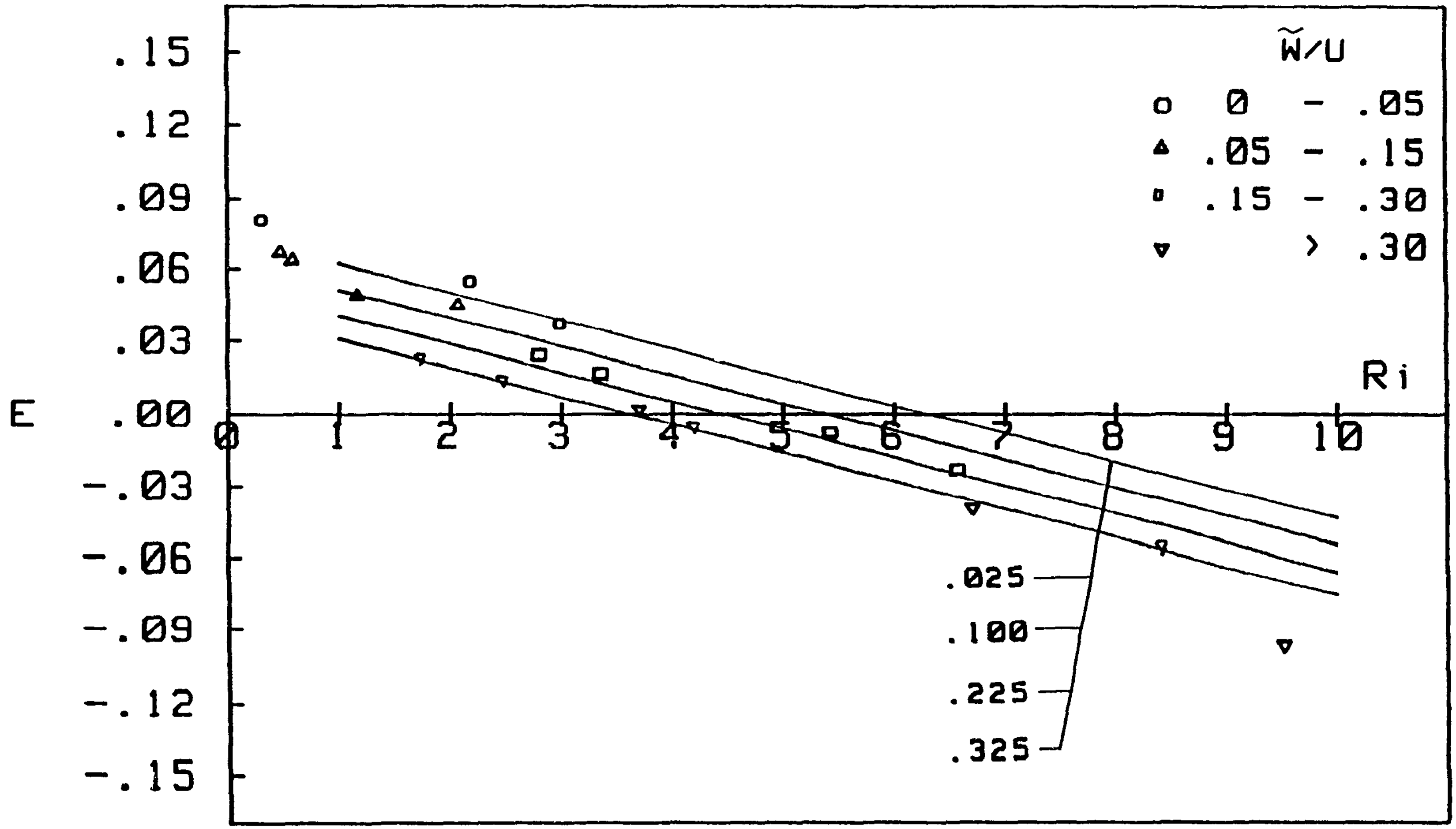

Fig.3.5 Entrainment coefficient versus Richardson number for different values of the velocity ratio $\widetilde{W}/U$ for sand suspension

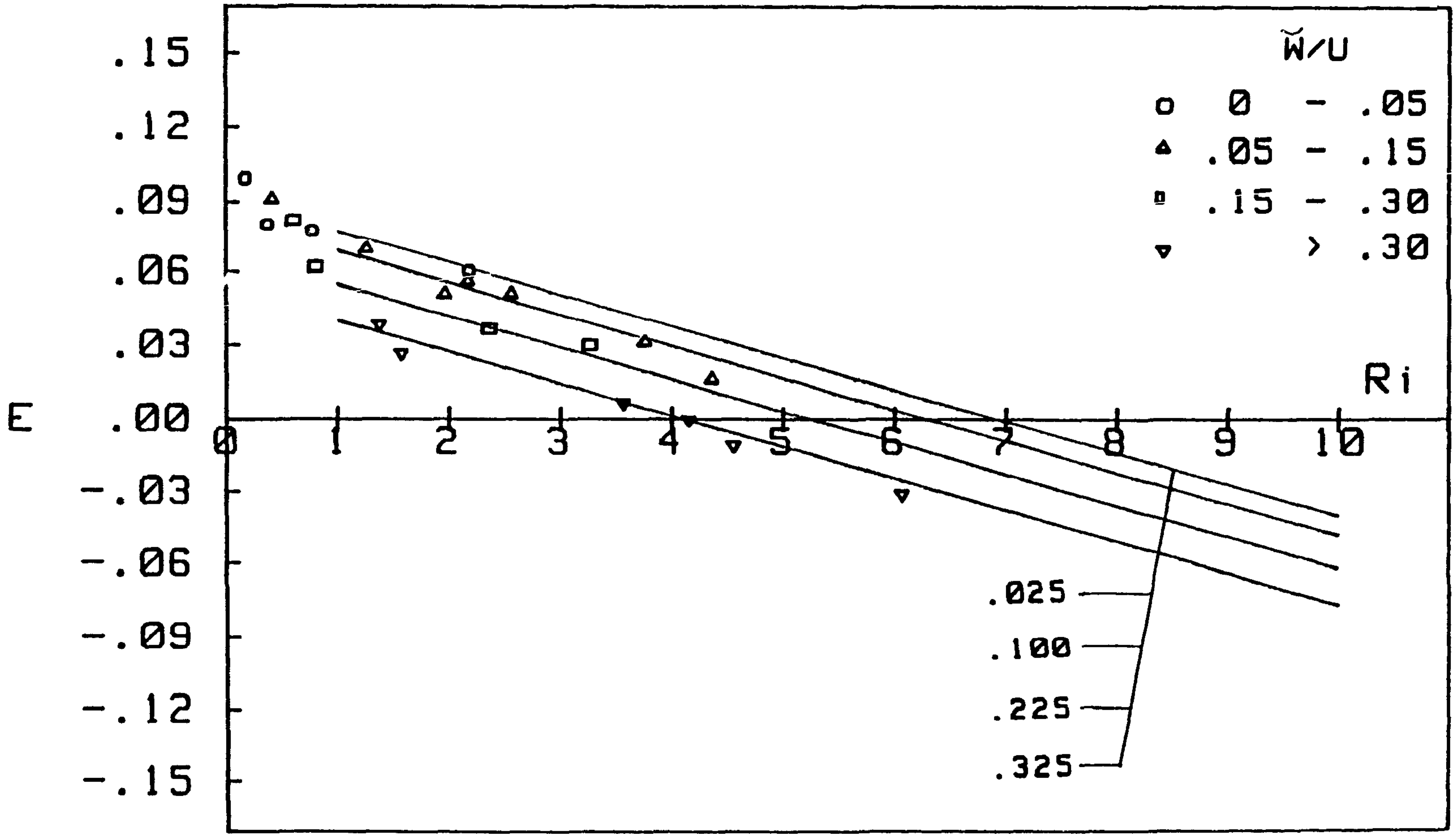

Fig.3.6 Entrainment coefficient versus Richardson number for different values of the velocity ratio $\widetilde{W}/U$ for bead suspension

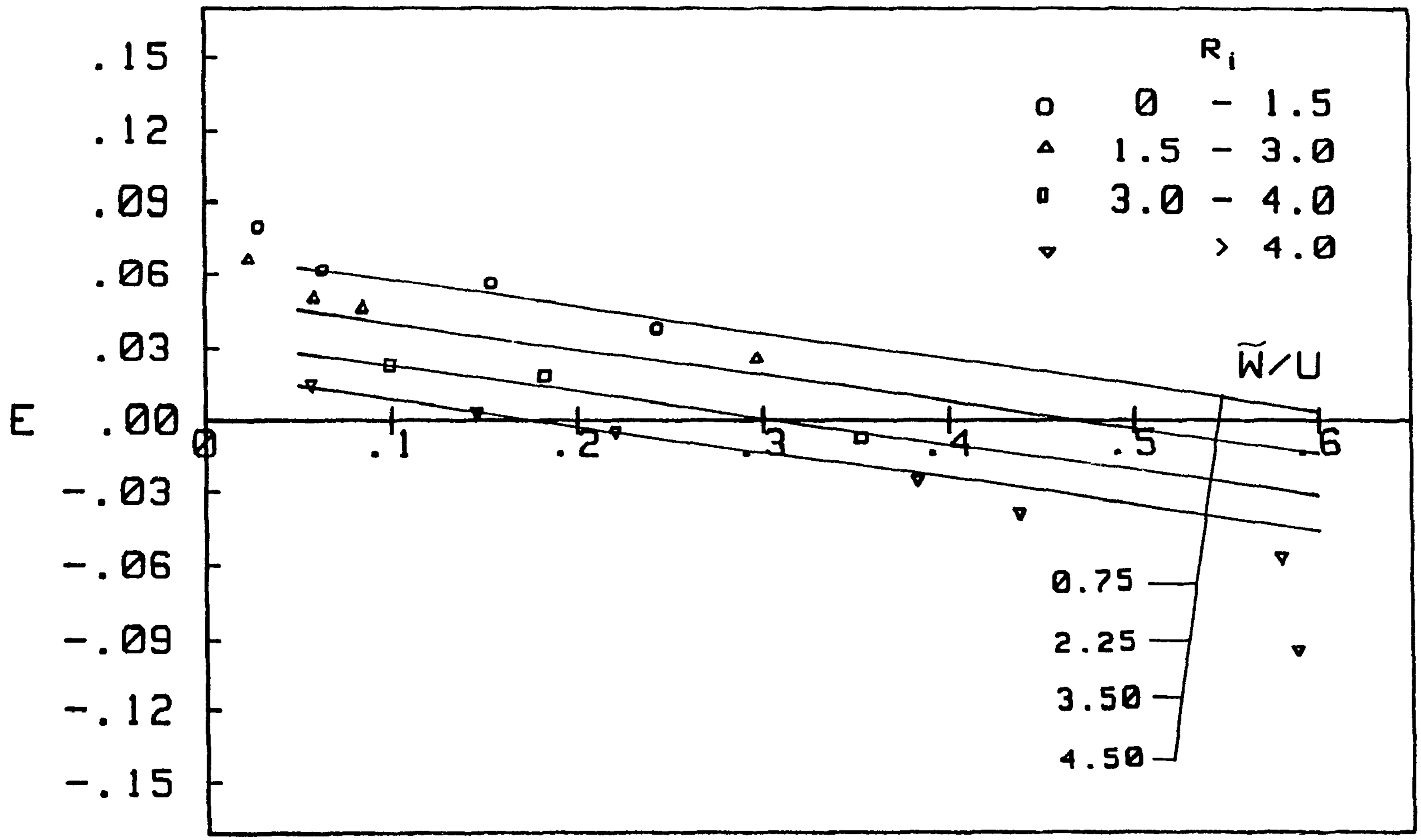

Fig.3.7 Entrainment coefficient versus velocity ratio $\widetilde{W}/U$ for different values of Richardson number for sand suspension

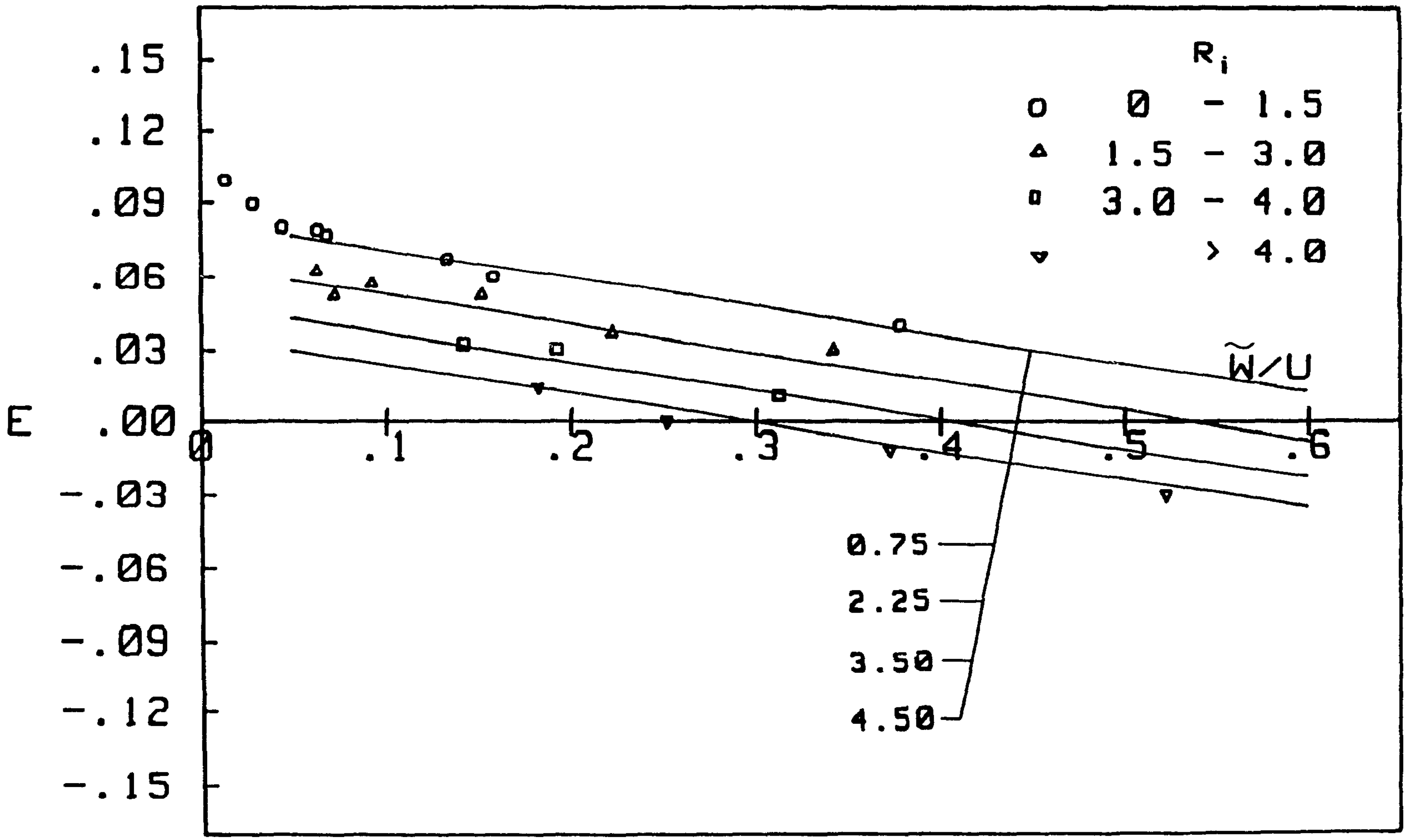

Fig.3.8 Entrainment coefficient versus velocity ratio $\widetilde{W}/U$ for different values of Richardson number for bead suspension

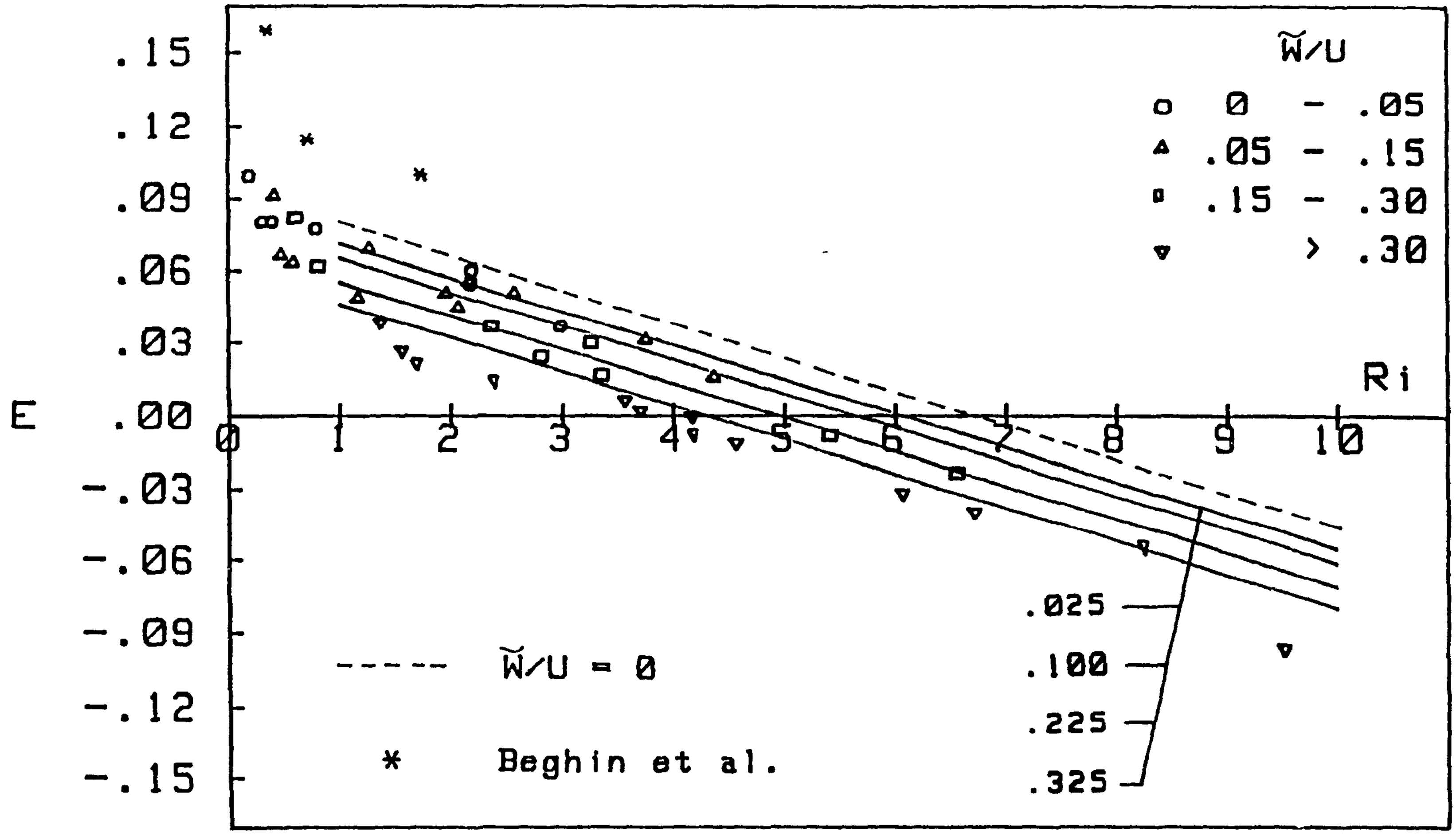

Fig.3.9 Entrainment coefficient versus Richardson number for different values of the velocity ratio $\tilde{W}/U$ for combined data from sand and bead suspensions

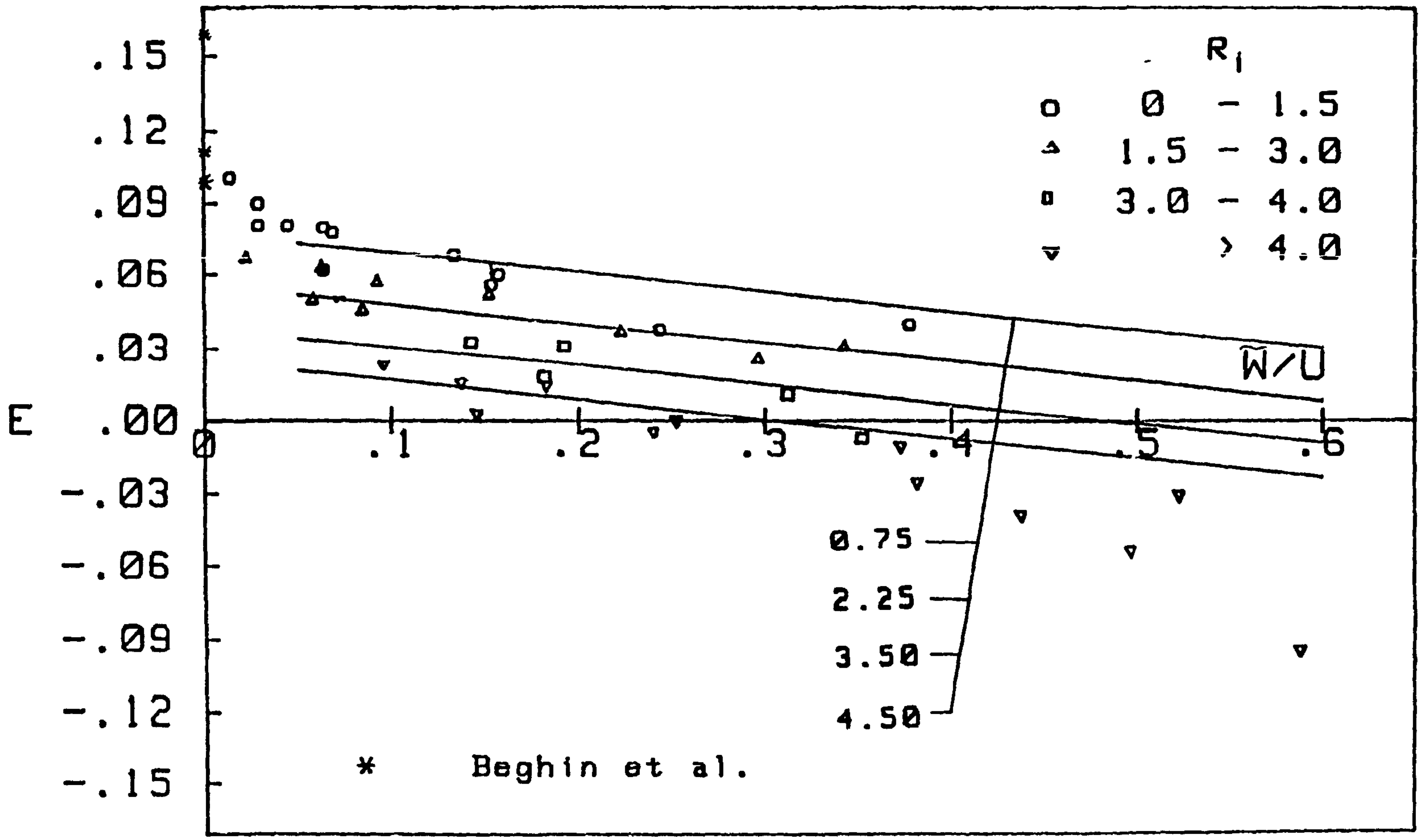

Fig.3.10 Entrainment coefficient versus velocity ratio $\tilde{W}/U$ for different values of Richardson number for combined data from sand and bead suspensions

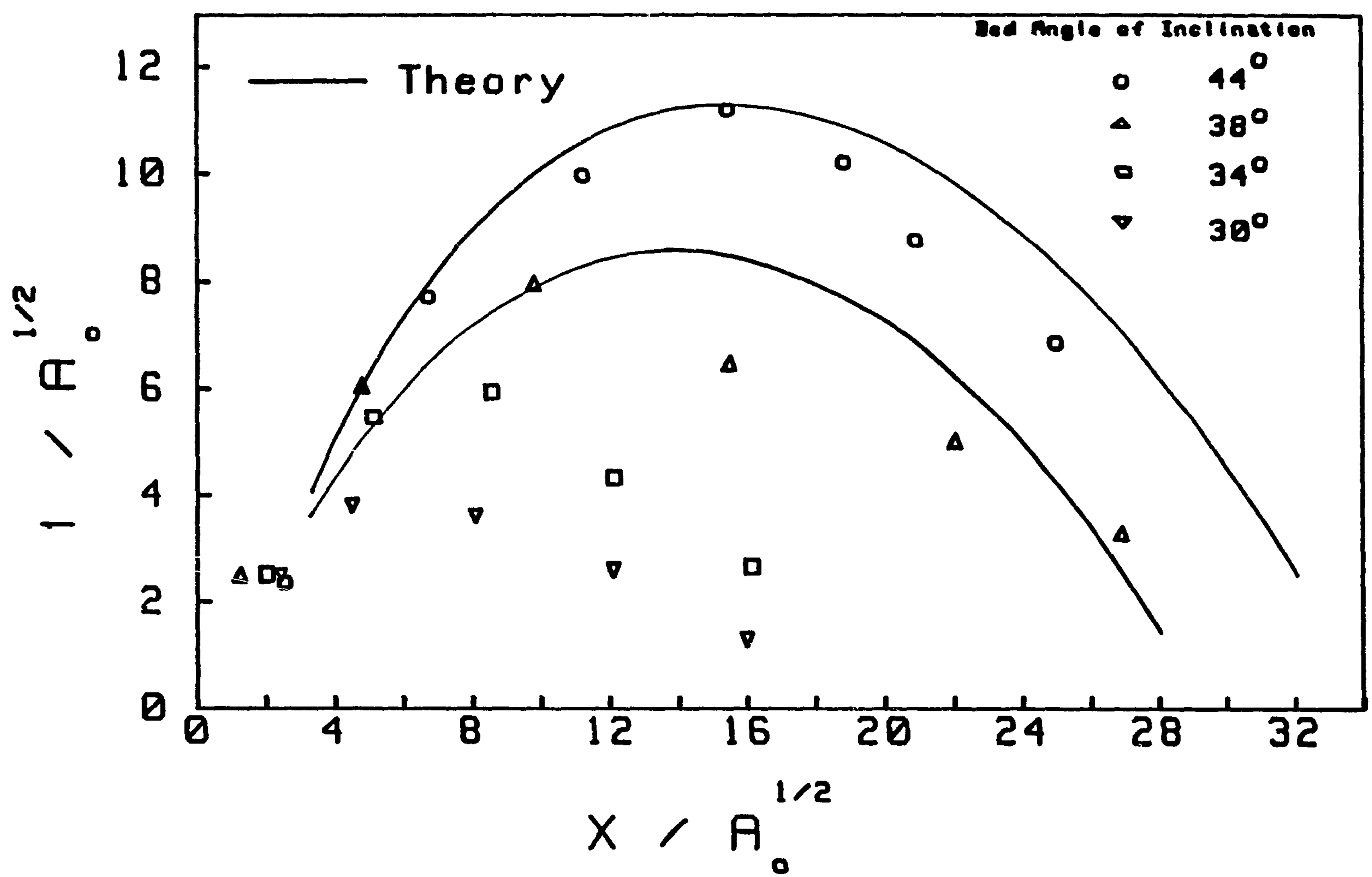

Fig.3.11 Length of the cloud versus traveling distance, both normalized by $A_o^{1/2}$ for sand suspension

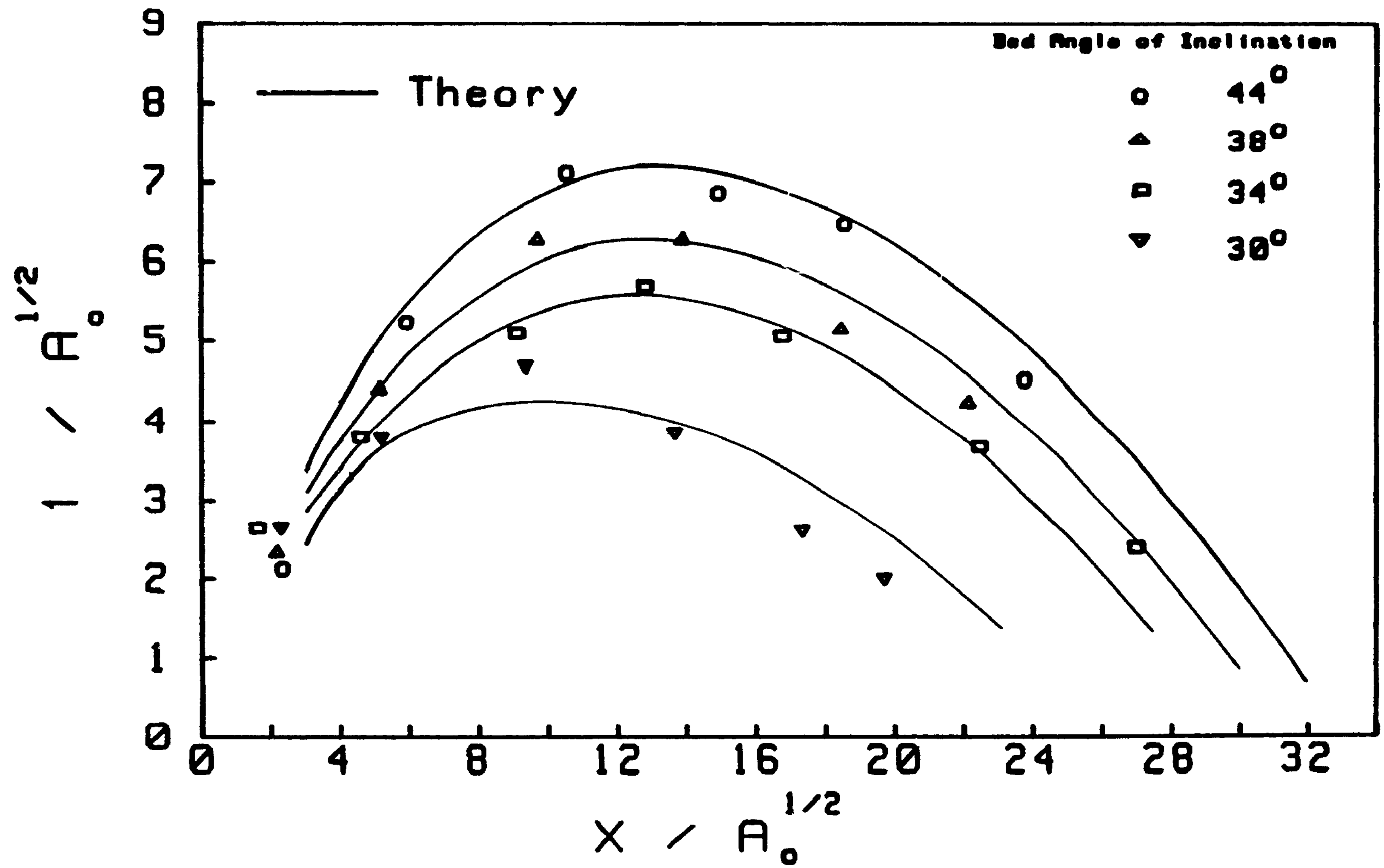

Fig.3.12 Length of the cloud versus traveling distance, both normalized by $A_o^{1/2}$ for bead suspension

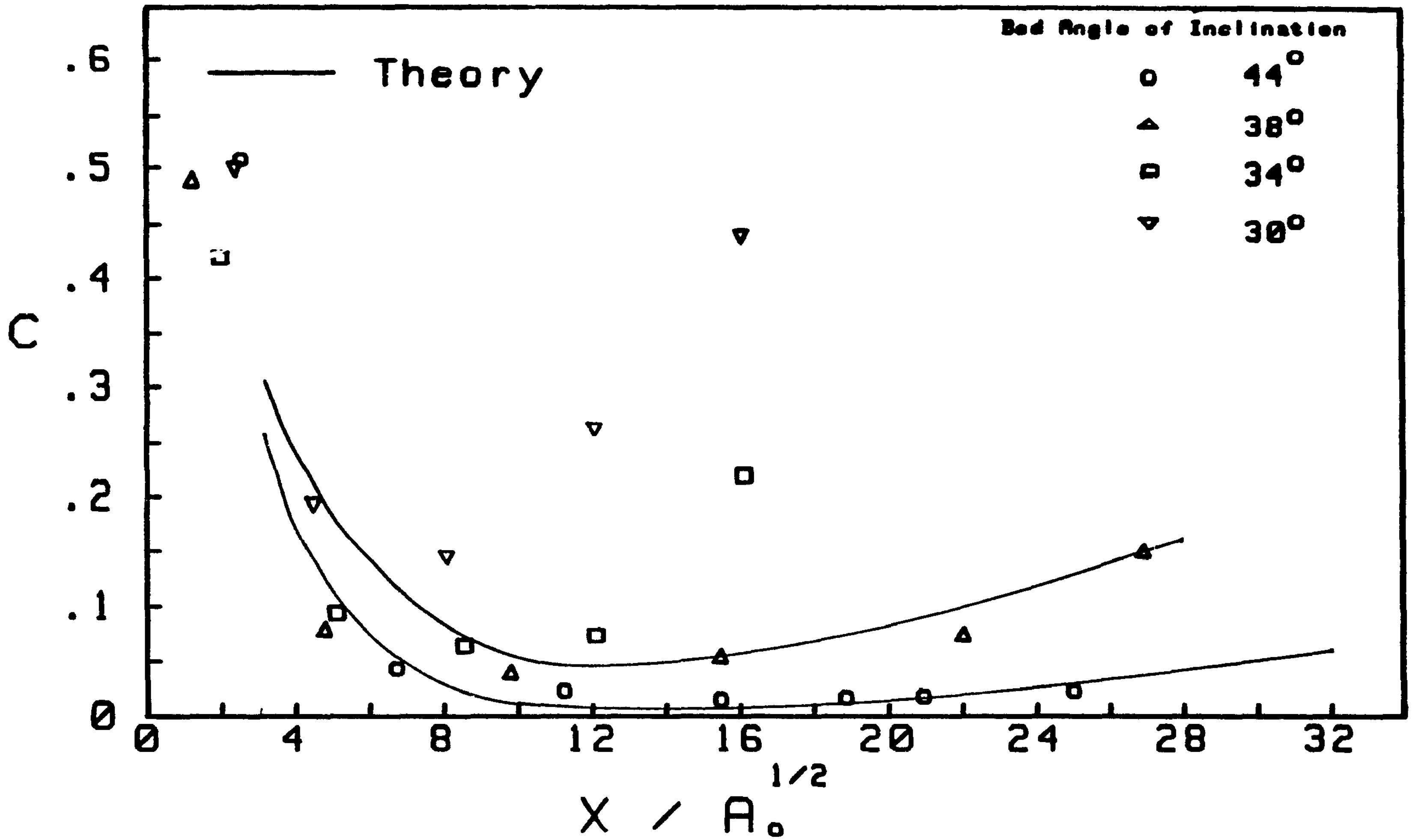

Fig.3.13 Cloud mean volumetric concentration versus traveling distance normalized by $A_o^{1/2}$ for sand suspension.

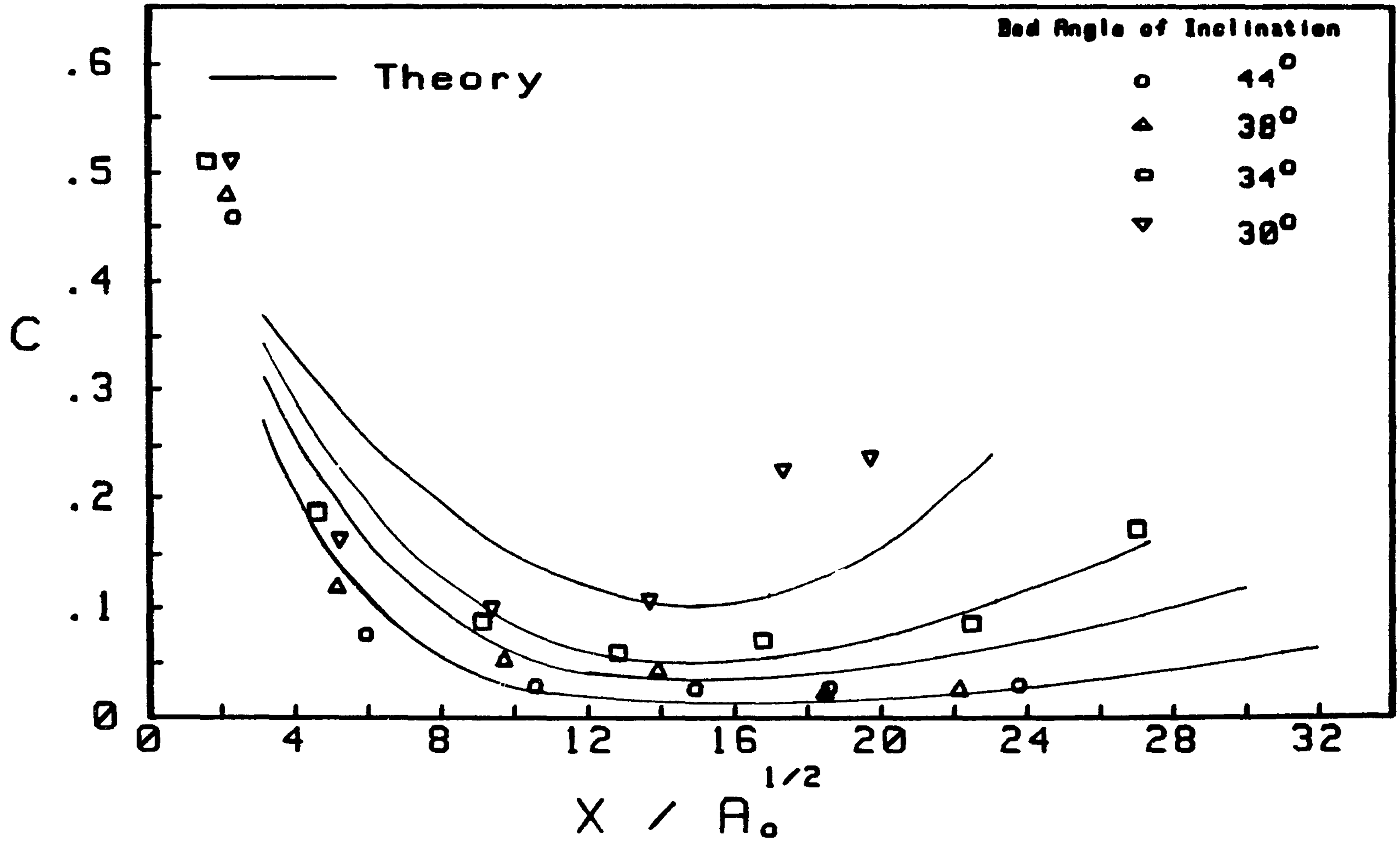

Fig.3.14 Cloud mean volumetric concentration versus traveling distance normalized by $A_o^{1/2}$ for bead suspension.

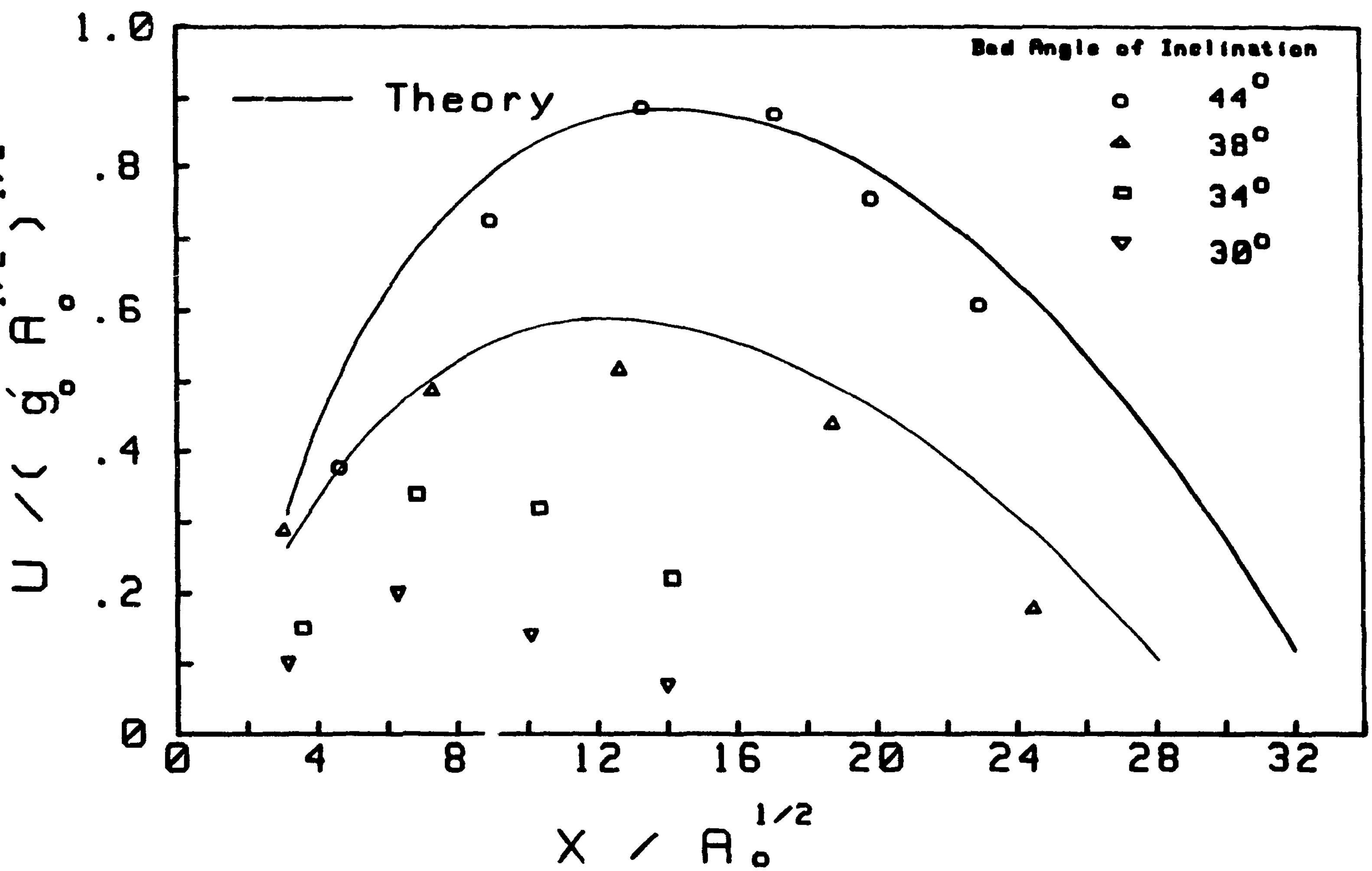

Fig.3.15 Non-dimensional center-of-mass velocity versus non-dimensional traveling distance for sand suspension

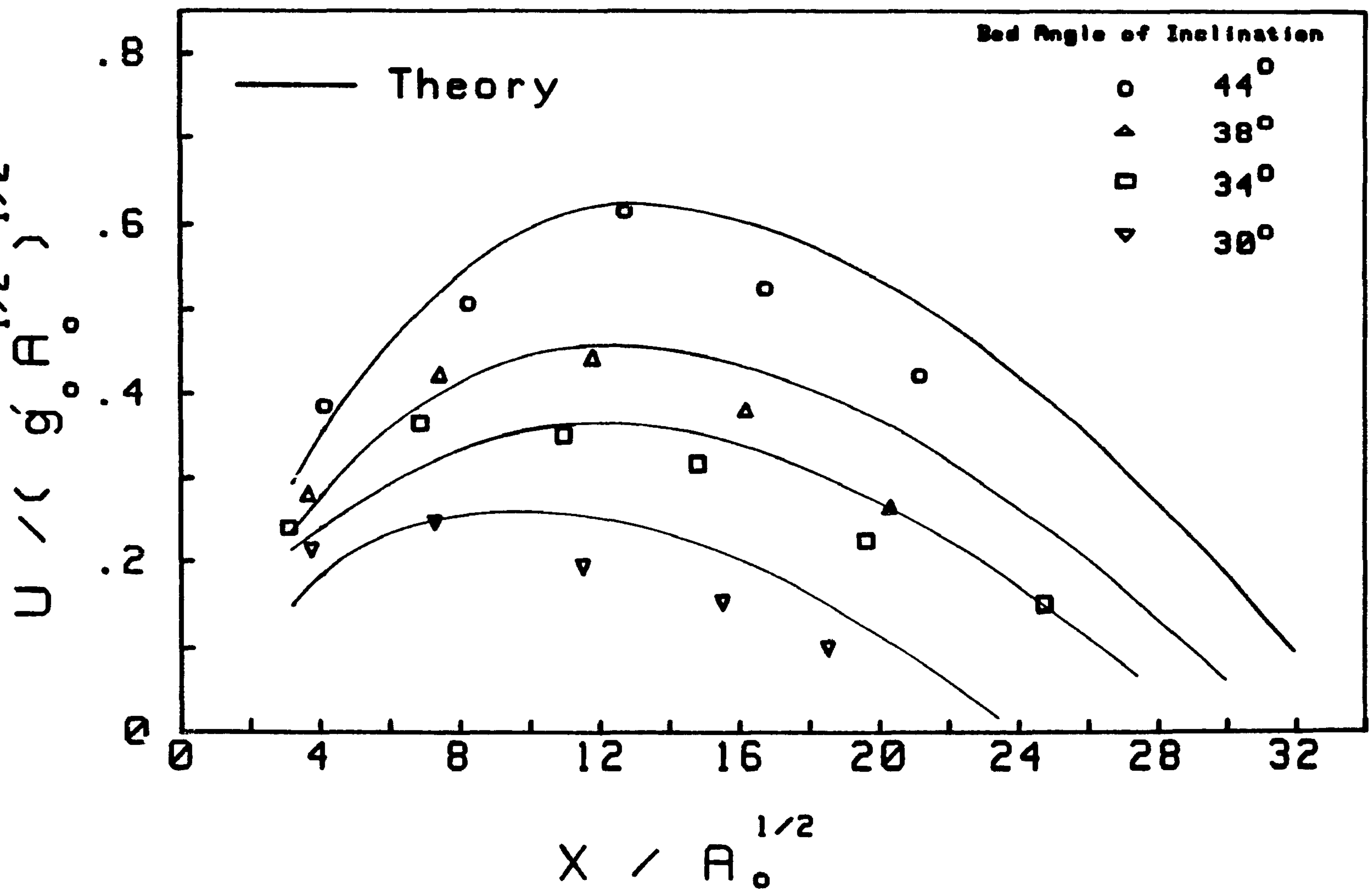

Fig.3.16 Non-dimensional center-of-mass velocity versus non-dimensional traveling distance for bead suspension

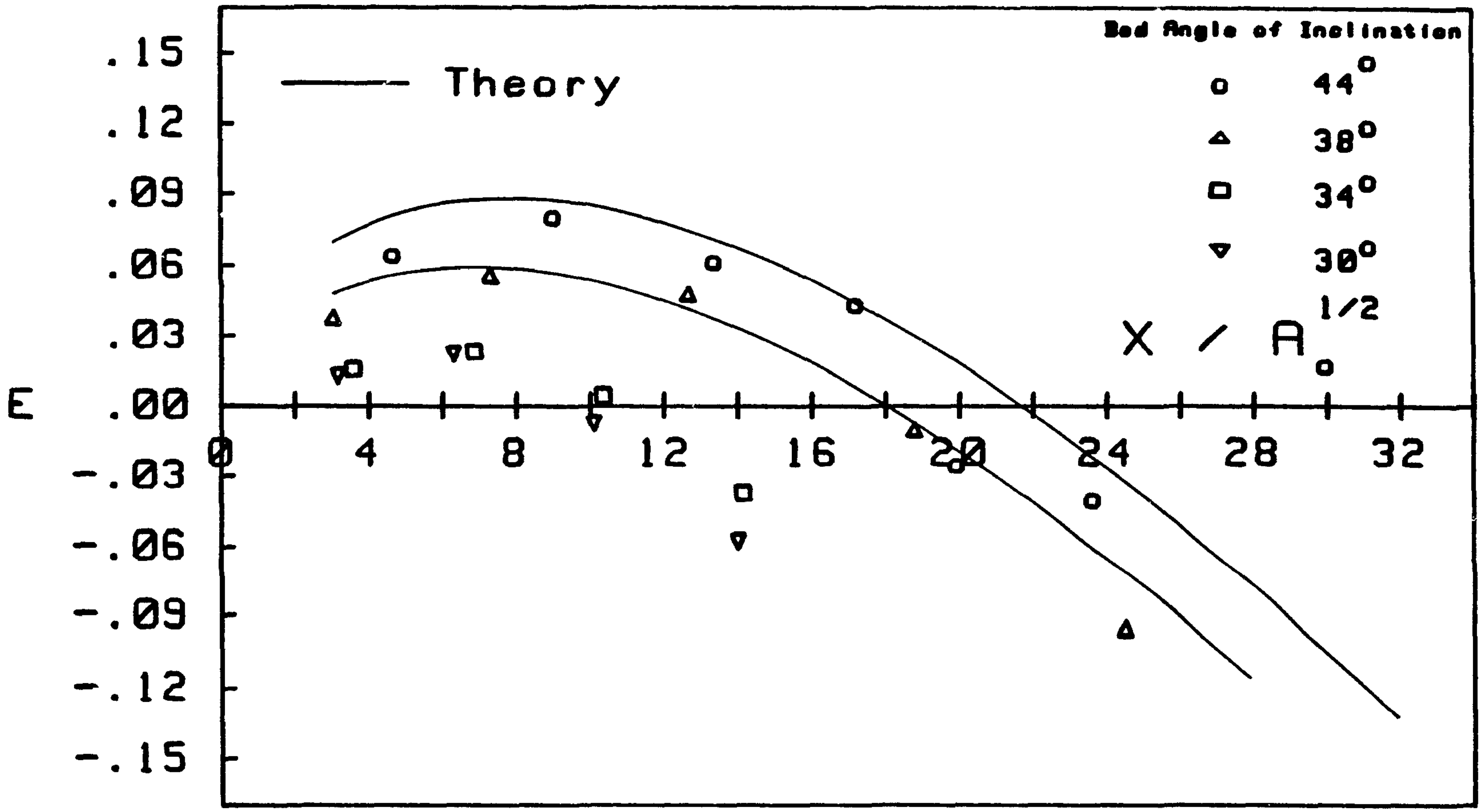

Fig.3.17 Entrainment coefficient versus traveling distance normalized by $A_o^{1/2}$ for sand suspension

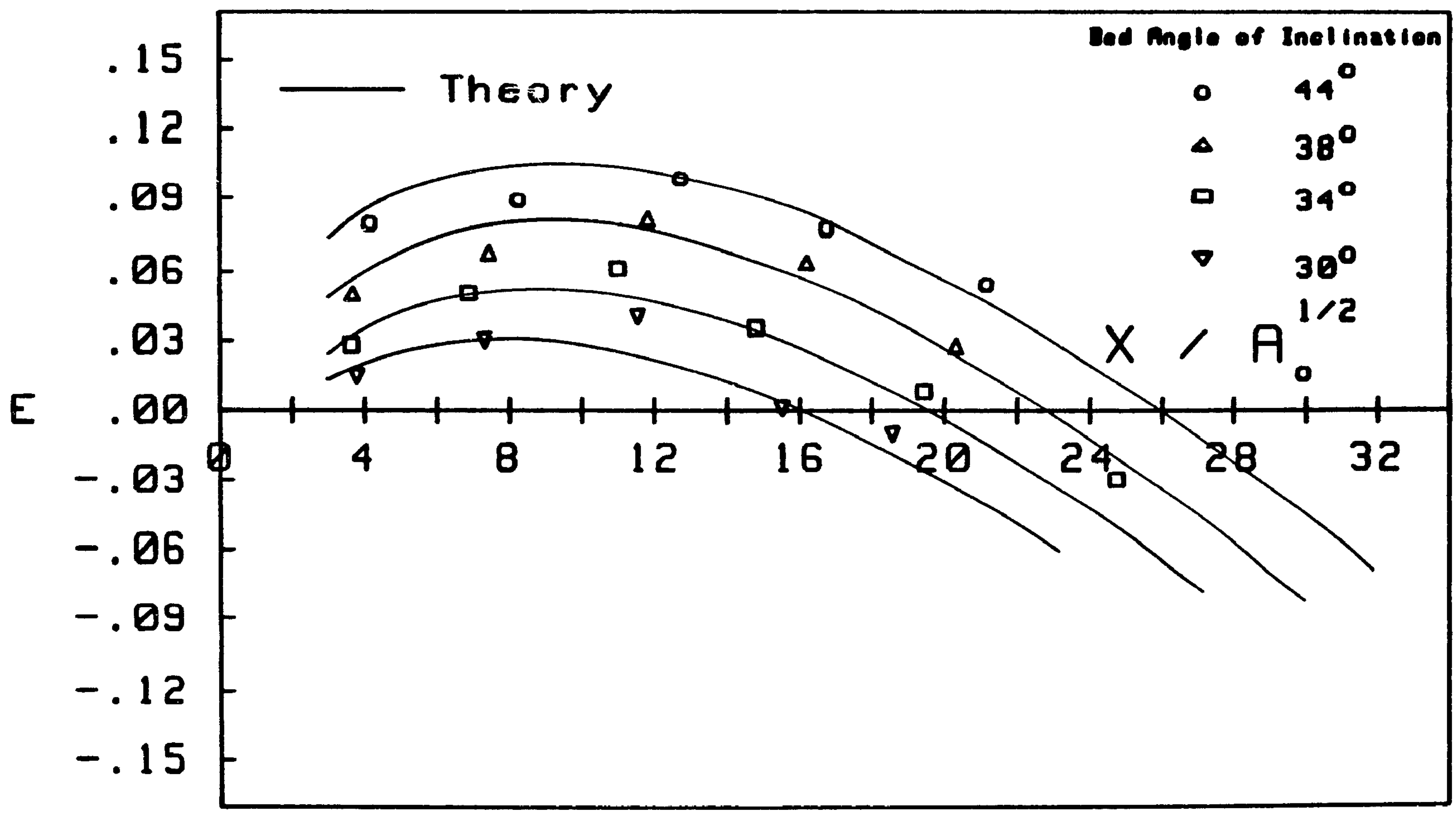

Fig.3.18 Entrainment coefficient versus traveling distance normalized by $A_o^{1/2}$ for bead suspension

REFERENCES

1. Hopfinger, E.J. and Tochon-Danguy, J.C. (1977) A model study of powder-snow avalanches. J. Glaciology , 19, No. 81, pp. 343-356.

2. Tochon-Danguy, J.C. and Hopfinger, E.J. (1975) Simulation of the dynamics of powder avalanches. IAHS-AISH , No. 114, pp. 369-380.

3. Krause, D.C., White, W.C., Piper, D.J.W. and Heezen, B.C. (1970) Turbidity currents and cable breaks in the western Britain Trench. Geol. Soc. Amer. Bull. , 81, pp. 2153-2160.

4. Daly, R.A. (1936) Origin of submarine canyons. Amer. J. Sci. , 31, pp. 410-420.

5. Kuenen, Ph.H. (1937) Experiments in connection with Daly's hypothesis on formation of submarine canyons. Leidsche Geol. Med. Dl. , 7, pp. 327-351.

6. Kuenen, Ph.H. (1950) Turbidity currents of high density. Int. Geol. Cong. London , 8, pp. 44-52.

7. Kuenen, Ph.H. and Migliorini, C.I. (1950) Turbidity currents as a cause of graded bedding. J. Geol. , 58, pp. 91-127.

8. Heezen, B.C. and Ewing, M. (1952) Turbidity current and submarine slumps, and the 1929 Grand Banks earthquake. Amer. J. Sci. , 250, pp. 849-873.

9. Middleton, G.V. (1966) Experiments on density and turbidity currents. I. Motion of the head. Can. J. Earth Sci. , 3, pp. 523-546.

10. Middleton, G.V. (1966) Experiments on density and turbidity currents. II. Uniform flow of density currents. Can. J. Earth Sci. , 3, pp. 627-637.

11. Middleton, G.V. (1967) Experiments on density and turbidity currents. III. Deposition of sediment. Can. J. Earth Sci. , 4, pp. 475-505.

12. Middleton, G.V. (1969) Turbidity currents, grain flows and other mass movements down slops. In D.J. Stanly ed. Amr. Geol. Inst. Short course notes, pp. GM-A-1 to GM-B-14.

13. Simpson, J.E. (1982) Gravity currents in the laboratory, atmosphere, and ocean. Ann. Rev. Fluid Mech. , 14, pp. 213-234.

14. Britter, R.E. and Simpson, J.E. (1978) Experiments on the dynamics of a gravity current head. J. Fluid Mech. ,

88, No. 2, pp. 223-240.

15. Simpson, J.E. and Britter, R.E. (1979) The dynamics of the head of a gravity current advancing over a horizontal surface. J. Fluid Mech. , 94, No. 3, pp. 477-495.

16. Britter, R.E. and Linden, P.F. (1980) The motion of the front of a gravity current travelling down an incline. J. Fluid Mech. , 99, No. 3, pp. 531-543.

17. Ellison, T.H. and Turner, J.S. (1959) Turbulent entrainment in stratified flows. J. Fluid Mech. , 6, pp. 423-448.

18. Benjamin, T.B. (1968) Gravity currents and related phenomena. J. Fluid Mech. , 31, No. 2, pp. 209-248.

19. Morton, B.R., Taylor, G.I. and Turner, J.S. (1956) Turbulent gravitational convection from maintained and instantaneous sources. Proc. Roy. Soc. London , 234A, pp. 1-23.

20. Lofquist, K. (1960) Flow and stress near an interface between stratified liquids. Phys. Fluids , 3, No. 2, pp. 158-175.

21. Turner, J.S. (1973) Buoyancy Effects in Fluids. Cambridge University Press.

22. Parker, G. (1982) Conditions for the ignition of catastrophically erosive turbidity currents. J. Marine Geol. , 46, pp. 307-327.

23. Beghin, P., Hopfinger, E.J. and Britter, R.E. (1981) Gravitational convection from instantaneous sources on inclined boundaries. J. Fluid Mech. , 107, pp. 407-422.

24. Bagnold, R.A. (1954) Experiments on a gravity-free dispersion of large solid spheres in a Newtonian fluid under shear. Proc. Roy. Soc. London , 225A, pp. 49-63.

25. Batchelor, G.K. (1967) An Introduction to Fluid Dynamics. Cambridge University Press.

26. Hoerner, S.F. (1958) Fluid Dynamic Drag.

27. Maude, A.D. and Whitmore, R.L. (1958) A generalized theory of sedimentation. British J. Applied Phys. , 9, pp. 477-482.

28. Daily, J.W. and Harleman, D.R.F. (1966) Fluid Dynamics. Addison-Wesley Co.

29. Vanoni, V. (1975) Sedimentation Engineering. ASCE Man., 54, New York.

30. Guitton, D.E. and Newman, B.G. (1977) Self-preserving turbulent wall jets over convex surfaces. J. Fluid Mech. 81, No. 1, pp. 155-185.

31. Hermann, F. and Scheiwiller, T. (1984) Measurement of particle velocities in suspension flow by an ultrasonic doppler-technique. Personal Communicatio..

32. Schlichting, H. (1979) Boundary Layer Theory. McGraw-Hill.

33. Bagnold, R.A. (1962) Auto-suspension of transport sediment; turbidity currents. Proc. Roy. Soc. London , 256A, pp. 315-319.

34. Allen, J.R.L. (1971) Mixing at turbidity current heads, and its geological implications. J. Sed. Pet. , 41, No. 1, pp. 97-113.

35. Carter, R.M. (1975) A discussion and classification of subaqueous mass-transport with particular application to grain-flow, slurry-flow and fluxoturbidities. Earth Sci. Rev. , 11, pp. 145-177.

36. Hampton, M.A. (1979) Buoyancy in debris flows. J. Sed. Pet. , 49, No. 3, pp. 753-758.

37. Gilmor, M.I. ed. Handbook of Steel Construction. Third edition, 1981.

38. Hauenstein, W. and Dracos, Th. (1984) Investigation of Plunging density currents generated by inflows in lakes. J. Hyd. Res. , 22, No. 3, pp. 157-179.

39. Ishii, M. and Zuber, N. (1979) Drag coefficient and relative velocity in bubbly, droplet or particulate flows. AIChE J. , 25, No. 5, pp. 843-855.

40. Kamis, A.S. and Savage, S.B. (1983) Subaqueous flow of a cloud of coarse particles down an inclined bed. Proc. of Can. Cong. Applied Mech. , pp. 537-538.

41. Kao, T.W., Park, C. and Pao, H. (1978) Inflows, density currents and fronts. Phys. Fluids , 21, No. 11, pp. 1912-1922.

42. Komar, P.D. (1972) Relative significance of head and body spill from a channelized turbidity current. Geol. Soc. Amer. Bull. , 83, pp. 1151-1156.

43. Middleton, G.V. and Hampton, M.A. (1976) Subaqueous sediment transport and deposition by gravity flow. In: Marine Sediment Transport and Environmental Management. Stanely, D.J. and Swift, D.J.P. editors. John Wiley&Sons.

44. Middleton, G.V. (1966) Small-scale models of turbidity currents and the criterion for auto-suspension. J. Sed. Pet. , 36, No. 1, pp. 202-208.

45. Middleton, G.V. (1966) The individuality and similarity of density and turbidity current heads. Can. J. Earth Sci. , 3, pp. 527-546.

46. Pykhov, N.V. (1973) The movement of sediments over an inclined sea floor after disturbance of their stability. Oceanology , 13, pp. 893-896.

47. Schwarz, W.H. and Cosart, W.P. (1961) The two-dimensional turbulent wall-jet. J. Fluid Mech. , 10, pp. 481-495.

48. Tam, C.K.W. (1969) The drag on a cloud of spherical particles in low Reynolds number flow. J. Fluid Mech. , 38, No. 3, pp. 537-546.

49. Wilkinson, D.L. and Wood, I.R. (1972) Some observations on the motion of the head of a gravity current. J. Hyd. Res. , 10, No. 3, pp. 305-324.

PART II

SPREADING OF ROCK AVALANCHES

SPREADING OF ROCK AVALANCHES

ABSTRACT

A study of the flow and spreading of a finite mass of dry cohesionless granular material released from rest on rough inclines is presented. Firstly, a two-dimensional depth-averaged model which describes both the longitudinal and the lateral spreading during flow down a rough inclined plane was developed. The relationship between the stress components was simply approximated by using a quasi-static Coulomb-like constitutive equation. A finite difference scheme applied on a staggered grid was employed to carry out the numerical integration of the governing partial differential equations. From the results of these numerical studies, it was concluded that the lateral spreading is insignificant relative to the longitudinal spreading. This suggested that a simple one-dimensional spreading model would be adequate for preliminary studies.

Therefore, a depth-averaged model which describes the one-dimensional longitudinal spreading down rough, curved beds was developed. Three rockfall events, Frank (24), Madison Canyon (25) and Medicine Lake (26) were analyzed and the predicted results agree reasonably well with the observed field data. It was concluded that, the traveling distance and velocity of the center of mass of a rock pile can be approximately predicted by a simple analysis of a point mass sliding down the same incline. The long runout distance of the leading edge of the slide debris can result from extreme spreading of the pile as it accelerates down the slope after initial release.

TABLE OF CONTENTS

LIST OF FIGURES

LIST OF SYMBOLS

A	aspect ratio (h_i / l_i)
AA, BB	coefficients of equation (3.30)
a, b	coefficients of equations (3.41) and (3.42)
B, C, E, G	coefficients of equations (3.7) and (3.8)
B', C', Dcos, E'	coefficients of equation (4.33)
CC	coefficient of equation (3.33)
DD, EE	coefficients of equation (3.35)
D_{ij}	rate of deformation tensor
Df(x), Df(y), Df(t)	differential operators
Dk(ξ), Dk(ξ)	differential operators (chapter 4)
DUR(ξ)	defined in equation (4.37)
d_t	non-dimensional time step
d_x	non-dimensional space step in x-direction
d_y	non-dimensional space step in y-direction
g	gravitational acceleration vector
H	instantaneous non-dimensional depth of the flow
h	instantaneous depth of the flow
h_i	initial maximum depth of a pile of granular material
i,j	position indices on finite difference grid
l_i	initial maximum length of a pile of granular material
$\vec{p}$	stress tensor
p_{xx} , p_{yy} , p_{zz}	normal stresses in the x,y and z-directions respectively

$p_{xy}, p_{xz} \cdots$	shear stresses
$\bar{p}_{xx}, \bar{p}_{yy}$	depth averaged normal stresses
$\bar{p}_{xy}, \bar{p}_{xz}, \bar{p}_{yz}$	depth averaged shear stresses
p	normal stress
p_o	mean normal stress (= .5 ($p_{11} + p_{22}$))
p_{11}	major normal stress
p_{22}	minor normal stress
$p_{\xi\xi}, p_{\eta\eta}$	normal stresses in the ξ and η direction
$p_{\xi\eta}, p_{\eta\xi}$	shear stresses
$\bar{p}_{\xi\xi}$	depth averaged normal stress
Q	non-dimensional velocity resultant (equation (2.44))
$\vec{\bar{q}}$	depth averaged velocity resultant (equation (2.32))
R	non-dimensional radius of curvature
r	radius of curvature
S	non-dimensional curvilinear coordinate (chapter 4)
T	non-dimensional time
t	time
U	non-dimensional velocity component in x - direction
UU1, UU2, VV1, VV2	intermediate values of the velocity components
$\vec{u}$	velocity vector
u	velocity component in x-direction
$\bar{u}$	depth averaged value of u
u_s	free surface value of u
V	non-dimensional velocity component in y - direction

v	velocity component in y-direction
$\bar{v}$	depth averaged value of v
v_s	free surface value of v
w	velocity component in z-direction
w_s	free surface value of w
X	non-dimensional longitudinal coordinate
x	cartesian longitudinal coordinate
Y	non-dimensional lateral coordinate
y	cartesian lateral coordinate
z	cartesian normal to the bed coordinate
α, β	real coefficients
$f(x)$, $f(y)$ $f(t)$	forward difference operators
$k(\xi)$, $k(\xi)$	forward difference operators (chapter 4)
δ	angle of bed friction
ζ	bed angle of inclination
η	normal to the bed curvilinear coordinate
θ, θ'	defined in equation (3.39)
ξ	streamwise curvilinear coordinate
ρ	mass density of granular material
τ	magnitude of shear stress
ϕ	angle of internal friction
ψ, ν, ϵ	complex quantities (function of t)
ψ', ν', ϵ'	new values of ψ , ν and ϵ at next time step

Superscripts and subscripts

$\rightarrow$	refers to vector quantity
$-$	refers to depth averaged value of the variable
i	refers to initial value
i,j	refers to coordinate system
n	refers to time cycle

CHAPTER 1
INTRODUCTION

Landslides or rockfalls that initiate on a steep slope eventually come to rest after flowing for some runout distance on a flat. Rockfalls of very large masses have been observed to exhibit unexpectedly long runout distances. Fig. 1.1 (data is quoted from Scheidegger (1)) shows the reduction in the so-called equivalent coefficient of friction (total fall height/total travel distance) as a function of the rockfall volume. It can be seen clearly that the total runout distance increases with the increase of the debris mass. Numerous hypotheses have been proposed to explain this puzzling phenomenon. However, none of these have been completely satisfactory or generally accepted. This study is concerned with the development of a simple model for the flow and spreading of a finite mass of cohesionless granular material released from rest on rough inclines. The purpose is to determine whether such a model can be used to predict the general features of at least some of the natural rockfall events.

1.1 Historical Review

As early as 1881, Albert Hiem noted the extraordinarily long travel distance that can occur in a large volume rockfall. Heim observed and described the Elm rockfall of Switzerland (see articles by Hsu (2,3)). This rockfall produced a debris which moved more than 2 Km along a nearly horizontal valley floor and one of its branches surged up the side of the valley to a height of 100 m. From the deposit of the Elm and the eyewitness accounts Heim concluded that the debris behaved as a flowing fluid rather than sliding solid blocks. A similar slide occurred in 1903 which destroyed the town of Frank, Alberta, in Canada. Such mobile debris flows which are called "sturzstroms" occur every year in different mountainous parts of the world (4).

The presence of small broken debris, fine stones, sand and dust is common and is believed to be present within the sturzstrom as interstitial material.

In an attempt to describe the fluidisation mechanism, Kent (5) suggested that the debris blocks were kept in a fluid-like state due to the rapid upward flow of air through the voids between the blocks. He proposed that this dilatation might reduce the frictional resistance and permit the debris to travel for a longer distance across a flat course. Shreve (4,6,7) postulated a similar mechanism, in which the air was also the mobilizing agent. He suggested that, as the debris mass rushes down the slope over an obstacle or hump, it leaves the ground and jumps into the air. As it does so it might confine a cushion of compressed air beneath it, permitting the debris to slide like a hovercraft. It is to be noticed that Shreve is one of the few to insist that the debris slides rather than flows, despite evidence of the fluid-like behaviour presented by, among others, Hsü (2,3). Another similar hypothesis by Goguel (8) was that high pressure steam would, in part, support the weight of the rock debris. This might reduce the frictional resistance thereby allowing the debris to flow for longer distances. The steam was assumed to be generated by the heat resulting from the sliding and colliding surfaces of the boulders. It is to be mentioned that, evidences of water presence in the rock debris were not found in many of the rockfalls.

The previous three hypotheses have been undermined by the observations of large volume landslides on the surface of the Moon and Mars (9,10). These observations suggest that neither air nor water is required for the mobility of the debris even though air or water may enhance the debris mobility.

Davies (11), among others, suggested that the excessive runout distance is volume dependent and the larger the volume of the debris, the longer the relative travel distance. From regression analysis Davies found that the final deposit extent of a sturzstrom depended mainly on its volume. The analysis also suggested that all struzstrom deposits were similar in shape and that the shape did not depend on the fall height. However, the analysis showed that the travel distance depends on the fall height. Davies suggested that the line connecting the initial and final center of mass positions of the debris makes an angle of inclination equal to the angle of normal friction of granular material and the long runout distance was due to the fluidlike spreading of the debris under the action of gravity. This spreading occurred due to mechanical fluidization caused by high basal shear rates as the debris moved rapidly across the ground. This mechanism was based on the grain flow theory of Bagnold (12,13). It should be mentioned that Bagnold's experiments provided information up to the edge of the grain-inertia region (moderate shear rates) and Davies used linear extrapolation of Bagnold's data points to suggest that the ratio of the shear stress to the normal stress which represents the angle of dynamic friction can be drastically reduced at high shear rates.

However, Savage and Sayed (14) in their recent experiments found that at high shear rates, the stress ratio either increases or decreases only slightly with the increase of the shear rates. In most of their experiments the particles were nearly uniform sized spheres (one series of tests was done with a bimodal mixture) and the tests were performed with dry material so that the effects of the interstitial fluid were not present. Lun et al. (15) found in their kinetic theory, for dry inelastic spherical particles of uniform diameter, that the stress ratio at high shear rates was independent of the shear rate and only weakly dependent upon solids concentration.

Hsü (2,3) recalled Heim's remarks about the kinetic energy associated with the collisions between the falling rocks. Based on Bagnold's theory (12,13) of the flow of cohesionless grains in a fluid, he proposed that the dispersion of fine debris particles between colliding blocks behaved in a manner similar to the interstitial fluid between the grains in Bagnold's theory. Hsü applied his hypothesis to the Elm event and he inferred that the interstitial materials were probably a mixture of one third dust and stones and two thirds air. This hypothesis, based on certain assumptions about the behaviour of the dust in a vacuum, was criticised by McSaveney (16). Moreover, it did not explain the runout distance dependency on the volume of the debris and it required prior knowledge of the reduction in the normal coefficient of friction (the tangent of the angle of repose of granular material).

Erismann (17) proposed a mechanism of self lubrication in which a thin layer of molten rock is generated at the base of the debris. The heat needed for such a process would result from the friction between the sliding surfaces under the weight of the debris. By a thermodynamic analysis, Erismann attempted to show the feasibility of this hypothesis. However, it requires the estimation of five parameters. These parameters may vary for the different events and, as Erismann mentioned, reliable figures are difficult to obtain.

Melosh (18,19) postulated a theory of acoustic fluidization. The proposed mechanism is a high frequency vibration which occurs either as a result of the impact of the debris rocks against the ground or naturally from an earthquake. This vibration may be capable of temporarily releasing the effective normal pressure in limited areas of the debris and hence reducing the frictional resistance considerably and allowing sliding to take place in the unloaded areas. However, the analysis is only qualitative and it is hard to see how it could be implemented in a physical model undergoing shearing deformation of discrete irregular blocks.

It is clear from above review that all the authors have merely offered hypotheses of physical mechanisms to explain debris mobility. Furthermore, there is still considerable controversy about the plausibility of all of these proposed mechanisms. Also it should be noted that no quantitative physical model explaining the flow and spreading of rockfalls and debris flows is currently available. This section of the thesis is concerned with development of such a physical model.

CHAPTER 2

TWO-DIMENSIONAL SPREADING MODEL

A continuum model of the flow and spreading of granular material down plane inclines is presented in this Chapter. Due to the lack of detailed and well proven constitutive equations relating the stresses and strain rates for the non-steady non-uniform flow of granular materials, we are forced to make several assumptions to simplify the constitutive relations. It is hoped that the present model will constitute the basis for a general model describing the mechanics of rockfalls as more refined constitutive equations become available.

2.1 Governing Equations

A simple model for the flow and spreading of a finite mass of cohesionless granular material released from rest down a rough inclined plane bed is now presented. The motion of the granular materials is referred to rectangular cartesian coordinates. The material point is denoted by x, y and z at time t. The x-coordinate is taken as positive in the streamwise direction, y is directed laterally and z is normal to the bed. For the analysis of a three-dimensional incompressible flow, the motion can be described by the continuity and momentum equations

$$\nabla \cdot \vec{u} = 0 \tag{2.1}$$

$$\rho \frac{D\vec{u}}{Dt} = - \nabla \vec{p} + \rho \vec{g} \tag{2.2}$$

where

∇ = gradient operator

$\vec{u}$ = material velocity vector

ρ = mass density of the granular material

$\frac{D}{Dt}$ = material derivative

$\vec{p}$ = stress tensor

$\vec{g}$ = gravitational acceleration vector

These equations can now be written out for the cartesian coordinate system (x, y, z) as follows

$$\frac{\partial u}{\partial x} + \frac{\partial v}{\partial y} + \frac{\partial w}{\partial z} = 0 \tag{2.3}$$

$$\rho \left[\frac{\partial u}{\partial t} + u \frac{\partial u}{\partial x} + v \frac{\partial u}{\partial y} + w \frac{\partial u}{\partial z} \right] = \rho g \sin \zeta - \frac{\partial p_{xx}}{\partial x} - \frac{\partial p_{xy}}{\partial y} - \frac{\partial p_{xz}}{\partial z} \tag{2.4}$$

$$\rho \left[\frac{\partial v}{\partial t} + u \frac{\partial v}{\partial x} + v \frac{\partial v}{\partial y} + w \frac{\partial v}{\partial z} \right] = - \frac{\partial p_{yx}}{\partial x} - \frac{\partial p_{yy}}{\partial y} - \frac{\partial p_{yz}}{\partial z} \tag{2.5}$$

$$\rho \left[\frac{\partial w}{\partial t} + u \frac{\partial w}{\partial x} + v \frac{\partial w}{\partial y} + w \frac{\partial w}{\partial z} \right] = - \rho g \cos \zeta - \frac{\partial p_{zx}}{\partial x} - \frac{\partial p_{zy}}{\partial y} - \frac{\partial p_{zz}}{\partial z} \tag{2.6}$$

where $u = u\,(x,y,z,t)$, $v = v\,(x,y,z,t)$ and $w = w\,(x,y,z,t)$ are the velocity components in the x, y and z directions respectively, ζ is the angle of inclination of the x-axis with the horizontal, p_{xx}, p_{yy} and p_{zz} are the normal stresses in the x, y and z directions respectively, and p_{xy}, p_{xz}, p_{yx}, p_{yz}, p_{zx} and p_{zy} are the shear stresses.

Multiplying equation (2.3) by ρu and adding it to equation (2.4) yields

$$\rho \left[\frac{\partial u}{\partial t} + \frac{\partial}{\partial x} (u^2) + \frac{\partial}{\partial y} (uv) + \frac{\partial}{\partial z} (uw) \right] = \rho g \sin \zeta$$

$$- \frac{\partial p_{xx}}{\partial x} - \frac{\partial p_{xy}}{\partial y} - \frac{\partial p_{xz}}{\partial z} \qquad (2.7)$$

In a similar manner equation (2.5) can be reduced to

$$\rho \left[\frac{\partial v}{\partial t} + \frac{\partial}{\partial x} (uv) + \frac{\partial}{\partial y} (v^2) + \frac{\partial}{\partial z} (vw) \right] = - \frac{\partial p_{yx}}{\partial x}$$

$$- \frac{\partial p_{yy}}{\partial y} - \frac{\partial p_{yz}}{\partial z} \qquad (2.8)$$

Several assumptions are now made in order to simplify the analysis. It was found from the available field data that, typical ratios of the height to the length of the debris were very small and of order 1/1000 for the final rest state. This suggests that it is acceptable to make use of what corresponds to the long wave approximation used in free surface hydrodynamics,

$$w \ll u \quad ; \quad w \ll v \qquad (2.9)$$

$$\frac{\partial}{\partial z} \gg \frac{\partial}{\partial x} \quad ; \quad \frac{\partial}{\partial z} \gg \frac{\partial}{\partial y} \qquad (2.10)$$

As a result the inertia effects in the z-direction are negligible and equation (2.6) simplifies to the hydrostatic equilibrium equation

$$\rho\ g\ \cos\zeta + \frac{\partial p_{zz}}{\partial z} = 0 \tag{2.11}$$

which can be integrated over the depth to give

$$p_{zz} = \rho\ g\ \cos\zeta\ (\ h - z\ ) \tag{2.12}$$

where h (x,y,t) is the instantaneous depth of the flow at any (x,y) position. Depth averaged x and y-momentum equations are derived in the next Section.

2.2 Depth Averaged Model

By integrating the momentum equations (2.7) and (2.8) over the depth of the flow, we obtain

$$\rho\ [\ \frac{\partial}{\partial t}\int_0^h u\ dz - u_s\frac{\partial h}{\partial t} + \frac{\partial}{\partial x}\int_0^h u^2\ dz - u_s^2\frac{\partial h}{\partial x} + \frac{\partial}{\partial y}\int_0^h uv\ dz$$

$$- u_s\ v_s\frac{\partial h}{\partial y} + u_s\ v_s\ ] = \rho\ g\ \sin\zeta\ h$$

$$- \frac{\partial}{\partial x}\int_0^h p_{xx}\ dz - \frac{\partial}{\partial y}\int_0^h p_{xy}\ dz - p_{xz}\ \Big|_0 \tag{2.13}$$

$$\rho\ [\ \frac{\partial}{\partial t}\int_0^h v\ dz - v_s\frac{\partial h}{\partial t} + \frac{\partial}{\partial x}\int_0^h uv\ dz - u_s\ v_s\frac{\partial h}{\partial x} + \frac{\partial}{\partial y}\int_0^h v^2\ dz$$

$$- v_s^2\frac{\partial h}{\partial y} + v_s\ w_s\ ] = - \frac{\partial}{\partial x}\int_0^h p_{yx}\ dz$$

$$- \frac{\partial}{\partial y}\int_0^h p_{yy}\ dz + p_{yz}\ \Big|_0 \tag{2.14}$$

Now at the upper boundary (free surface), we have the kinematic condition that

$$w_s = \frac{\partial h}{\partial t} + u_s \frac{\partial h}{\partial x} + v_s \frac{\partial h}{\partial y} \qquad (2.15)$$

where the subscript s refers to the surface value of the velocity component. Then, we can define the following depth average quantities,

$$\bar{u}\ (x,y,t) = \frac{1}{h} \int_0^h u\ (x,y,z,t)\ dz \qquad (2.16)$$

$$\bar{v}\ (x,y,t) = \frac{1}{h} \int_0^h v\ (x,y,z,t)\ dz \qquad (2.17)$$

$$\bar{p}_{xx} = \frac{1}{h} \int_0^h p_{xx}\ dz \qquad (2.18)$$

$$\bar{p}_{yy} = \frac{1}{h} \int_0^h p_{yy}\ dz \qquad (2.19)$$

$$\bar{p}_{xy} = \frac{1}{h} \int_0^h p_{xy}\ dz \qquad (2.20)$$

Moreover, it is assumed that,

$$\bar{u^2} \cong \frac{1}{h} \int_0^h u^2\ dz \cong \bar{u}^2 \qquad (2.21)$$

$$\bar{v^2} \cong \frac{1}{h} \int_0^h v^2\ dz \cong \bar{v}^2 \qquad (2.22)$$

$$\overline{uv} = \frac{1}{h}\int_0^h uv\ dz \cong \bar{u}\bar{v} \tag{2.23}$$

Then, by using equations (2.15) - (2.23), equations (2.13) and (2.14) can be reduced to

$$\rho\left[\frac{\partial}{\partial t}(\bar{u}h) + \frac{\partial}{\partial x}(\bar{u^2}h) + \frac{\partial}{\partial y}(\bar{u}\bar{v}h)\right] = \rho\ g\ h \sin\zeta$$

$$- \frac{\partial}{\partial x}(\bar{p}_{xx}h) - \frac{\partial}{\partial y}(\bar{p}_{xy}h) + p_{xz}\Big|_0 \tag{2.24}$$

$$\rho\left[\frac{\partial}{\partial t}(\bar{v}h) + \frac{\partial}{\partial x}(\bar{u}\bar{v}h) + \frac{\partial}{\partial y}(\bar{v^2})\right] = - \frac{\partial}{\partial x}(\bar{p}_{yx}h)$$

$$- \frac{\partial}{\partial y}(\bar{p}_{yy}h) - p_{yz}\Big|_0 \tag{2.25}$$

2.2.1 Constitutive Equations

A further assumption regarding the constitutive relation between the stress components is made. Since the appropriate relation for the type of flow of interest here is not available, it is proposed to consider a simple quasi-static constitutive relation (see reference (20)). For an ideal cohesionless granular material, the Mohr-Coulomb condition states that yield occurs on a plane element when

$$|T| = P \tan\phi \tag{2.26}$$

where T and P are the shear and normal stresses respectively acting on the element and ϕ is the quasi-static internal angle of friction. As a slight extension of this concept, the following constitutive relation for the stress components in plane deformations is now employed

$$p_{ij} = p_o\,\delta_{ij} - p_o \sin\phi \frac{D_{ij}}{[\frac{1}{2}\,\mathrm{tr}\,D_{ij}\,D_{ji}]^{\frac{1}{2}}} \tag{2.27}$$

where the subscripts i and j take the values 1,2 ,δ_{ij} is Kronecker delta, p_o is the mean quasi-static normal stress (see Fig. 2.1) and $\vec{D}$ is the strain rate tensor defined as

$$D_{ij} = \frac{1}{2}\left[\frac{\partial u_i}{\partial x_j} + \frac{\partial u_j}{\partial x_i} \right] \tag{2.28}$$

Equation (2.27) implies a coincidence between principal axes of stress and rate of deformation. In the present problem of the rockfall development, it is assumed that the shear planes are very nearly parallel to the plane of the bed such that $\frac{\partial u}{\partial z}$ is the dominant component of the rate of deformation tensor and that the plane x_1 ,x_2 coordinates are approximately lined up along the x,z axes. Hence we can write that,

$$\left| p_{xy} = p_{yx} \right| << p_{xx} \tag{2.29}$$

$$p_{xx} \cong p_{zz} \cong p_o \tag{2.30}$$

At the bed, it can be assumed that the friction force is colinear with the depth of averaged velocity vector $\vec{\bar{q}}$ = (u,v) (see Fig. 2.2) and opposes the motion such that

$$\frac{p_{xz}\,|_o}{T} = -\frac{\bar{u}}{\bar{q}} \quad , \quad \frac{p_{yz}\,|_o}{T} = -\frac{\bar{v}}{\bar{q}} \tag{2.31}$$

where $\bar{q}$ is the magnitude of the depth averaged velocity

$$\bar{q} = \left| \sqrt{\bar{u}^2 + \bar{v}^2} \right| \tag{2.32}$$

and τ is the magnitude of the total bed shear stress. From equation (2.27) we obtain

$$\tau = p_a \sin\phi = p_a \tan\delta \tag{2.33}$$

where δ is the bed angle of friction. In order for the deformation to be more general than planar, two of the principal stresses must be equal. For the problem under consideration, the flow of the material will tend to expand laterally in the y-direction and we take the normal stress in the y-direction to be the minor principal axis (rather than the major principal axis), hence

$$p_{yy} = p_a (1 - \sin \phi) \tag{2.34}$$

Then, from equation (2.11), (2.18) and (2.30), we obtain

$$\bar{p}_{xx} h = \bar{p}_{zz} h = \int_0^h p_{zz} \, dz$$

or

$$\bar{p}_{xx} h = \rho g \cos \zeta \frac{h^2}{2} \tag{2.35}$$

and

$$\bar{p}_{yy} = (1 - \sin \phi) \bar{p}_{zz} \tag{2.36}$$

Thus equations (2.24) and (2.25) can be rewritten as

$$\rho \left[\frac{\partial}{\partial t} (\bar{u}h) + \frac{\partial}{\partial x} (\bar{u}^2 h) + \frac{\partial}{\partial y} (\bar{u}\bar{v}h) \right] = \rho\, g\, h \sin \zeta$$

$$- \rho\, g\, h \cos \zeta \frac{\partial h}{\partial x} - \rho\, g\, h \cos \zeta \tan \delta \left(\frac{\bar{u}}{\bar{q}} \right) \qquad (2.37)$$

$$\rho \left[\frac{\partial}{\partial t} (\bar{v}h) + \frac{\partial}{\partial x} (\bar{u}\bar{v}h) + \frac{\partial}{\partial y} (\bar{v}^2 h) \right] =$$

$$- \rho\, g\, h (1 - \sin \phi) \cos \zeta \frac{\partial h}{\partial y}$$

$$- \rho\, g\, h \cos \zeta \tan \delta \left(\frac{\bar{v}}{\bar{q}} \right) \qquad (2.38)$$

Finally, the continuity equation (2.3) can be depth averaged in a similar manner using equation (2.15),the kinematic condition at the surface, to give

$$\frac{\partial h}{\partial t} + \frac{\partial}{\partial x} (\bar{u}h) + \frac{\partial}{\partial y} (\bar{v}h) = 0 \qquad (2.39)$$

Then using equation (2.39), equations (2.37) and (2.38) can be reduced to

$$\frac{\partial \bar{u}}{\partial t} + \bar{u} \frac{\partial \bar{u}}{\partial x} + \bar{v} \frac{\partial \bar{u}}{\partial y} = \rho \sin \zeta - g \cos \zeta \frac{\partial h}{\partial x}$$

$$- g \cos \zeta \tan \delta \left(\frac{\bar{u}}{\bar{q}} \right) \qquad (2.40)$$

$$\frac{\partial \bar{v}}{\partial t} + \bar{u}\,\frac{\bar{v}}{\partial x} + \bar{v}\,\frac{\partial \bar{v}}{\partial y} = -\,(\,1 - \sin\phi\,)\,g\cos\zeta\,\frac{\partial h}{\partial y}$$

$$-\,g\cos\zeta\,\tan\delta\,(\,\frac{\bar{v}}{\bar{q}}\,) \qquad (2.41)$$

The resulting equations (2.39) - (2.41) are sufficient to describe the longitudinal and lateral spreading of the flow.

2.3 Non-Dimensional Form of the Governing Equations

Let us introduce the following non-dimensional parameters (see Fig. 2.3)

$$H = \frac{h}{h_i} \quad ; \quad X = \frac{x}{l_i} \quad ; \quad Y = \frac{y}{l_i} \qquad (2.42)$$

$$U = \frac{\bar{u}}{\sqrt{g l_i}} \quad ; \quad V = \frac{\bar{v}}{\sqrt{g l_i}} \quad ; \quad T = \frac{t}{\sqrt{l_i / g}} \qquad (2.43)$$

$$A = \frac{h}{l_i} \quad , \quad Q = \frac{\bar{q}}{\sqrt{g l_i}} \qquad (2.44)$$

where h_i and l_i are the initial height and length of the pile of granular material. Substituting equations (2.42) - (2.44) in equations (2.39) - (2.41), we obtain the non-dimensional form of the proposed governing equations

$$\frac{\partial H}{\partial T} + \frac{\partial}{\partial X}\,(\,HU\,) + \frac{\partial}{\partial Y}\,(\,HV\,) = 0 \qquad (2.45)$$

$$\frac{\partial U}{\partial T} + U \frac{\partial U}{\partial X} + V \frac{\partial U}{\partial Y} = \sin \zeta - A \cos \zeta \frac{\partial H}{\partial X}$$

$$- \cos \zeta \tan \delta \left(\frac{U}{Q} \right) \qquad (2.46)$$

$$\frac{\partial V}{\partial T} + U \frac{\partial V}{\partial X} + V \frac{\partial V}{\partial Y} = - A \left(1 - \sin \phi \right) \cos \zeta \frac{\partial H}{\partial Y}$$

$$- \cos \zeta \tan \delta \left(\frac{V}{Q} \right) \qquad (2.47)$$

CHAPTER 3
THE STAGGERED GRID FINITE DIFFERENCE MODEL

A finite difference approximation to the governing partial differential equations proposed in the previous Chapter is now presented. A simple explicit scheme applied to a staggered grid will be used. In Section 3.3, a stability analysis will be performed to obtain the necessary stability condition for the proposed scheme. Computational results arising from the finite difference computer programs are discussed in Section 3.4.

3.1 Finite Difference Equations

Of all the methods of integrating a system of partial differential equations, the characteristics method is the most accurate one since the characteristic lines follow the true solution and tend to be closer together in areas of rapid changes. However, the chief disadvantage of this method is that the data at the intermediate points in the x-y-z space are difficult to obtain and a tedious interpolation is involved in obtaining the flow height and velocities on some line from the calculated points. Therefore, the finite difference method was selected because of its simplicity of formulation and the ease of interpreting the results that it yields. Furthermore, with the appropriate precautions, a high accuracy can be achieved as will be explained later.

This Section starts by defining some of the finite difference operators, and deriving some of the relations between them and the differential operators. Using these basic concepts, the finite difference approximation to the system of partial differential equations (2.45)-(2.47) is developed along with the appropriate approximations for the boundary condition.

Finite difference equations arise as approximations to partial differential equations whose solution cannot easily be found analytically. In order to develop these approximations, it is convenient to define various difference operators, and derive some of the relationships between them and the differential operators. Let d_x be the non-dimensional spacing between the abscissas in the x-direction, d_y be the non - dimensional spacing between ordinates in the y-direction and d_t be the non-dimensional time step. In addition to the space index, defined in Fig. 3.1, we use a superscript index n to number the time cycle. The U and V, and H computation are performed at different time levels. The U and V values are computed first and then used to obtain the H values as indicated in the flowchart diagram in Fig. 3.2. The forward difference operators are defined by

$$\Delta f(x) = f^n\,(x+d_x,y+d_y) - f^n\,(x,y+d_y) \tag{3.1}$$

$$\Delta f(y) = f^n\,(x+d_x,y+d_y) - f^n\,(x+d_x,y) \tag{3.2}$$

$$\Delta f(t) = f^{n+1}\,(x+d_x,y+d_y) - f^n\,(x+d_x,y+d_y) \tag{3.3}$$

where f represents any of the problem variables (U,V and H). The relations between the finite difference operators and the differential operators can be defined as follows

$$Df(x) = \frac{\Delta f(x)}{d_x} \tag{3.4}$$

$$Df(y) = \frac{\Delta f(y)}{d_y} \tag{3.5}$$

$$Df(t) = \frac{\Delta f(t)}{d_t} \tag{3.6}$$

The construction of a difference equation from a differential equation is not a unique process. Many approximations are possible for a given differential equation. The selection of a particular difference relation is usually determined by the nature of the truncation error associated with the approximation. The difference relations which will be used here were shown to have a minimum total error with the appropriate selection of the time step (22), as we will see in Section 3.4.

The grid used (see Fig. 3.1) consists of cells, with the continuity and the momentum equations expressed in terms of the velocities' values at the nodes and the flow height at the center of each cell (staggered grid). Equations (2.46) and (2.47) are approximated by means of the following difference equations; using equations (3.1)-(3.6)

$$DU(t) + U^{n-\frac{1}{2}}(i+1,j+1)\ DU(x) + V^{n-\frac{1}{2}}\ DU(y) = B - C\ DH(x) \tag{3.7}$$

$$DV(t) + U^{n-\frac{1}{2}}(i+1,j+1)\ DV(x) + V^{n-\frac{1}{2}}\ DV(y) = -\ E\ DH(y) - G \tag{3.8}$$

where

$$B = \sin \zeta(i+1) - R_1 \cos \zeta(i+1) \tan \delta \left(\frac{U}{Q} \right) \tag{3.9}$$

$$C = A \cos \zeta(i+1) \tag{3.10}$$

$$E = C\ (\ 1 - \sin \phi\ ) \tag{3.11}$$

$$G = \cos \zeta(i+1) \tan \delta \left(\frac{V}{Q} \right) \tag{3.12}$$

Furthermore, The Lax-Wendroff (45) type of approximation to the velocities $U^{n-1/2}(i+1,j+1)$ and $V^{n-1/2}(i+1,j+1)$ in equations (3.7) and (3.8) was employed to improve the accuracy of the scheme as follows

$$U^{n-\frac{1}{2}}(i+1,j+1) = \frac{1}{2} \left[U^{n+\frac{1}{2}}(i+1,j+1) + U^{n-\frac{1}{2}}(i+1,j+1) \right] \tag{3.13}$$

$$V^{n-\frac{1}{2}}(i+1,j+1) = \frac{1}{2} \left[V^{n+\frac{1}{2}}(i+1,j+1) + V^{n-\frac{1}{2}}(i+1,j+1) \right] \tag{3.14}$$

Substituting equations (3.13) and (3.14) in equations (3.7) and (3.8) and solving for $U^{n+1/2}(i+1,j+1)$ and $V^{n+1/2}(i+1,j+1)$ yields

$$\begin{aligned} U^{n+\frac{1}{2}}(i+1,j+1) = \Big[& U^{n-\frac{1}{2}}(i+1,j+1) - d_t \Big\{ \frac{1}{2} U^{n-\frac{1}{2}}(i+1,j+1)\, DU(x) \\ & + V^{n-\frac{1}{2}}(i+1,j+1)\, DU(y) - B + C\, DH(x) \Big\} \Big] \\ & / \left[1 + \frac{1}{2} d_t\, DU(x) \right] \end{aligned} \tag{3.15}$$

$$\begin{aligned} V^{n+\frac{1}{2}}(i+1,j+1) = \Big[& V^{n-\frac{1}{2}}(i+1,j+1) - d_t \Big\{ U^{n-\frac{1}{2}}(i+1,j+1)\, DV(x) \\ & + \frac{1}{2} V^{n-\frac{1}{2}}(i+1,j+1)\, DV(y) + E\, DH(x) + N \Big\} \Big] \\ & / \left[1 + \frac{1}{2} d_t\, DV(y) \right] \end{aligned} \tag{3.16}$$

The difference equation form of the continuity equation can be introduced in a way, such that it satisfies a physical representation of the continuity equation on the grid scheme in order to improve the accuracy of the solution. We start by introducing the following intermediate variables,

$$UU1 = \frac{1}{2} \left[U^{n+\frac{1}{2}} (i+1,j+1) + U^{n+\frac{1}{2}} (i+1,j+2) \right] \tag{3.17}$$

$$UU2 = \frac{1}{2} \left[U^{n+\frac{1}{2}} (i+2,j+1) + U^{n+\frac{1}{2}} (i+2,j+2) \right] \tag{3.18}$$

$$DUU(x) = \frac{UU1 - UU2}{d_x} \tag{3.19}$$

$$VV1 = \frac{1}{2} \left[V^{n+\frac{1}{2}} (i+1,j+1) + V^{n+\frac{1}{2}} (i+2,j+1) \right] \tag{3.20}$$

$$VV2 = \frac{1}{2} \left[V^{n+\frac{1}{2}} (i+1,j+2) + V^{n+\frac{1}{2}} (i+2,j+2) \right] \tag{3.21}$$

$$DVV(y) = \frac{VV1 - VV2}{d_y} \tag{3.22}$$

$$H^n (i+1,j+1) = \frac{1}{2} \left[H^n (i+1,j+1) + H^{n-1} (i+1,j+1) \right] \tag{3.23}$$

Finally equation (2.45) can be written as follows

$$H^n (i+1,j+1) = \Big[H^{n-1} (i+1,j+1) - d_t \Big\{ U^{n+\frac{1}{2}} (i+1,j+1)\, DH(x)$$

$$+ V^{n+\frac{1}{2}} (i+1,j+1)\, DH(y) + \frac{1}{2} H^{n-1} \big(DUU(x) + DVV(y) \big) \Big\} \Big]$$

$$/ \left[1 + \frac{1}{2} d_t \, (DUU(x) + DVV(y)) \right] \tag{3.24}$$

The solution of the system of equations (3.15), (3.16) and (3.24) proceeds in the following way. First all variables are initialized (the initial shape of the granular material pile is specified and all velocities are taken to be zero). Then, equations (3.15) and (3.16) and equation (3.24) can alternately be evaluated for all n.

3.2 Boundary Condition

The boundary condition for a rigid wall may be either of two types, no-slip or free- slip. The latter type may be considered to represent a plane of symmetry, rather than a true wall, or, in the case of modeling an idealized fluid, it may represent a non-adhering surface. Symmetry planes are restricted in orientation so that they lie along the boundaries of the scheme. Relaxation of this restriction could be accomplished only at the expense of considerable increase of complication.

For the case under consideration, the vertical x,z plane is considered to be a plane of symmetry. Therefore, calculations will be performed on only one half of the pile (see Fig. 2.1). A boundary condition has to be imposed at this vertical plane in order to accommodate this situation. For a free-slip wall, the normal velocity (in adjacent cells) reverses while the tangential velocity remains the same (22). The flow height h, also remains the same in adjacent cells, corresponding to $\frac{\partial H}{\partial Y} = 0$ at the center line. Fig. 3.3 schematically represents the no-slip boundary condition.

3.3 Stability Analysis

A finite difference procedure for calculating time - dependent phenomena is considered stable when small numerical truncation and round - off errors inevitably introduced at stage T = 0, are not amplified during successive applications of the procedure, and at subsequent time t have not grown so as to obscure the valid part of the solution. A method for investigating the stability aspects of the proposed finite difference scheme is outlined next.

A commonly used technique for investigating the stability of numerical schemes for partial differential equations involves the representation of pertinent functions in terms of the Fourier series. A rigorous mathematical presentation of this technique appears in the classic book by Robert Richtmyer (23). The basic approach to the problem is to postulate that at some time T_o of the calculations a distribution of small numerical errors has crept into the computed results such that the computed results have deviated from the true solution. The growth or decay of these errors during the repeated application of a particular finite difference scheme is investigated for a local linearized version of the scheme, with coefficients assumed constant. The error functions are assumed to be composed of the Fourier series, any component of which satisfies the modified difference scheme. An examination is made to see if the amplitude of any component increases during repeated application of the difference equations. If the amplitude of every component remains bounded, the scheme is judged to be stable.

The general term of the Fourier expansion for U, V and H at arbitrarily time $t = 0$ is $e^{i\alpha x} e^{i\beta y}$, apart from a constant . At a time t' later, these terms will become

$$U : \psi\, e^{i\alpha x} e^{i\beta y} \tag{3.25}$$

$$V : \nu\, e^{i\alpha x} e^{i\beta y} \tag{3.26}$$

$$H : \epsilon\, e^{i\alpha x} e^{i\beta y} \tag{3.27}$$

Substituting the above in equation (3.7) yields

$$\frac{\psi' - \psi}{d_t} e^{i\,\alpha\,x}\, e^{i\,\beta\,y} + U\, \frac{\psi[e^{i\,\alpha\,x}\, e^{i\,\beta\,y} - e^{i\,\alpha\,(x-d_x)}\, e^{i\,\beta\,y}]}{d_x}$$

$$+ V\, \frac{\psi[e^{i\,\alpha\,x}\, e^{i\,\beta\,y} - e^{i\,\alpha\,x}\, e^{i\,\beta\,(y-d_y)}]}{d_y} = B$$

$$- C\, \frac{\epsilon[e^{i\,\alpha\,x}\, e^{i\,\beta\,y} - e^{i\,\alpha\,(x-d_x)}\, e^{i\,\beta\,y}]}{d_x} \qquad (3.28)$$

which can be simplified to the form

$$\frac{\psi' - \psi}{d_t} + U\, \frac{\psi[1-e^{-i\,\alpha\,d_x}]}{d_x} + V\, \frac{\psi[1-e^{-i\,\beta\,d_y}]}{d_y} =$$

$$B\, e^{-i\,\alpha\,x}\, e^{-i\,\beta\,y} - C\, \frac{\epsilon[1-e^{-i\,\alpha\,d_x}]}{d_x} \qquad (3.29)$$

or

$$\psi' = AA\;\psi + BB\;\epsilon \qquad (3.30)$$

where

$$AA = 1 - d_t\; [\; U\, \frac{(1-e^{-i\,\alpha\,d_x})}{d_x} + V\, \frac{(1-e^{-i\,\beta\,d_y})}{d_y}\;] \qquad (3.31)$$

$$BB = B\; d_t\, \frac{e^{-i\,\alpha\,x}\, e^{-i\,\beta\,y}}{\epsilon} - C\; d_t\, \frac{(1-e^{-i\,\alpha\,d_x})}{d_x} \qquad (3.32)$$

Similarly equation (3.8) can be reduced to the following form

$$\nu' = AA\ \nu + CC\ \epsilon \tag{3.33}$$

where

$$CC = -E\ d_t \frac{(1-e^{-i\alpha d_x})}{d_x} - G\ d_t \frac{e^{-i\alpha x}\ e^{-i\beta y}}{\epsilon} \tag{3.34}$$

and finally equation (3.24) can be reduced in a similar manner to the form

$$\epsilon' = AA\ \epsilon - DD\ \psi - EE\ \nu \tag{3.35}$$

where

$$DD = H\ d_t \frac{1 - e^{i\alpha d_x}}{d_x} \tag{3.36}$$

$$EE = H\ d_t \frac{1 - e^{i\beta d_y}}{d_y} \tag{3.37}$$

Equations (3.33), (3.36) and (3.38) can be rewritten in a matrix form as follows

$$\begin{bmatrix} \psi' \\ \nu' \\ \epsilon' \end{bmatrix} = \begin{bmatrix} AA & 0 & BB \\ 0 & AA & CC \\ DD & EE & AA \end{bmatrix} \begin{bmatrix} \psi \\ \nu \\ \epsilon \end{bmatrix} \tag{3.38}$$

or

$$\theta' = F\ \theta \tag{3.39}$$

where F is the amplification factor. For stability each eigenvalue of F must not exceed unity

$$|AA| <= 1 \tag{3.40}$$

Let us define

$$a = \frac{U\ d_t}{d_x} \tag{3.41}$$

$$b = \frac{V\ d_t}{d_y} \tag{3.42}$$

hence,

$$AA = (1-a-b) + a\ e^{-i\ \alpha\ d_x}\ e^{-i\ \beta\ d_y} \tag{3.43}$$

The coefficients α and β are real and positive, and by representing AA on an Argand diagram (23); it can be shown that the maximum modulus of AA occurs when $\alpha\ d_x = m\pi$ and $\beta\ d_y = n\pi$ where m and n are integers and hence occur when AA is real. For d_t sufficiently large, the value of AA is greatest when m and n are odd integers; in which case

$$AA = 1 - 2\ (\ a + b\ ) \tag{3.44}$$

which becomes more negative as d_t increases. Now to satisfy $|AA| <= 1$, the most allowable value is AA = -1, therefore

$$a + b <= 1 \tag{3.45}$$

Thus the stability condition is

$$d_t \left[\frac{U}{d_x} + \frac{V}{d_y} \right] \leq 1 \tag{3.46}$$

which is equivalent to the well known Courant stability criterion (21) for the integration of the hyperbolic partial differential equations.

3.4 Results

3.4.1 Introduction

A computer code was developed for the two-dimensional spreading model to predict the shape and the velocity variations with time, of a finite mass of cohesionless granular material piled up at the top of a rough inclined plane. The code starts by declaring first, the constants such as the initial maximum height and length of the pile (h_i and l_i), angle of inclination of the bed plane, the internal angle of friction, the bed angle of friction, the maximum number of steps and the coefficients A,B, .. etc. of equations (3.15), (3.16) and (3.24). The spatial increments $d_x$and d_y and the time step d_t are then introduced. Finally, the variables H, U and V are initialized by establishing the initial shape of the pile and setting the velocities to zero. Following that, equations (3.15) and (3.16) are used to calculate new velocities at the first time step. After the computations of U and V are done for each node, the stability is checked by using equation (3.46) to assure the scheme stability. Equation (3.24) then is used to compute the new shape of the pile using the newly calculated velocities U and V. The number of time steps is checked and if that is less than the maximum, the program resumes the calculations by going back to compute the new velocities at the next time step and so on. Since the stability of the scheme was secured, the last concern was to insure that the scheme is conservative, that is to insure that the numerical diffusion is minimum. The numerical diffusion is defined as the dissipation of the initial function (the mass of the pile) with time, which is due to the difference between the solution constant speed of propagation (d_x / d_t) and the physical unsteady true solution (phase error). Therefore computer experimentation was carried out to select the best time step to insure the minimum numerical diffusion. The method used to check on the accuracy was to compute the volume of the new pile after each time step and compare it with the initial volume of the pile. The relative difference in volume was chosen as the measure of the scheme accuracy and it was called the 'Error - relative volume change'.

The programs were developed and run on a Hewlett Packard Series 200·HP9816 microcomputer with graphics capabilities. The program runs interactively and results can be displayed on both the screen and the plotter.

3.4.2 Results and Discussion

Initially, the program was tested on a simplified one-dimensional spreading version of the model to check whether the results predicted were correct for some very simple physical problems. For all the following cases, the angle of bed friction (DELTA) was taken to be 32^{o} .

The one-dimensional version of the governing equations can be written as follows

$$\frac{\partial H}{\partial T} + \frac{\partial}{\partial X}(UH) = 0 \tag{3.47}$$

$$\frac{\partial U}{\partial T} + U\frac{\partial U}{\partial X} = \sin\zeta - A\cos\zeta\frac{\partial H}{\partial X} - \cos\zeta\ \tan\delta\ \mathrm{sgn}(U) \tag{3.48}$$

In the first test the program was used to predict the timewise development of the shape of a finite volume of granular material piled on a horizontal plane. The pile was initially triangular in shape having free surface slopes of 60^o with the horizontal bed plane ($A = h_i / l_i = 1.154$). Fig. 3.4 shows the non-dimensional height of the pile versus the streamwise distance for both the initial and the final non-dimensional times. It was found that the free surface of the final shape of the pile made an angle equal to the angle of bed friction. This result is consistent with the physical situation of a simple test to determine the angle of repose of granular material.

A second test was made to predict the shape of a finite volume of granular material piled on an inclined plane which makes an angle of inclination (ZETA) of 20^o with the horizontal. The pile itself was of the form of an isosceles triangle whose equal sides are inclined at 40^o to the sloping bed plane ($A = 0.419$). Hence one leg was inclined at 20^o to the horizontal and the other was inclined at 60^o to the horizontal. Fig. 3.5 shows the spreading of the pile at different non-dimensional times. The flow stopped when the front free surface slope made an angle close to the angle of bed friction. This result is consistent with the stability condition which can be seen from equation (3.48) by setting the velocity to zero.

The last test was performed to check on the velocity prediction of the model. By canceling the second term in the right hand side of equation (3.48), the prediction of the model should correspond to a point mass sliding down a rough inclined plane. The lower graph in Fig. 3.6 represents a pile of granular material flowing down a plane having an angle of inclination (ZETA) of 60^o. The position of the pile at different non-dimensional times is presented and as expected, no spreading occurs. The upper graph of Fig. 3.6 shows the non-dimensional velocity of the pile which was found to match very closely the prediction of a point mass analysis. The difference between the two predictions is less than 1 %; this is due to the errors associated with the finite difference calculation.

The satisfactory results of the previous tests indicated that both the finite difference approximations to the governing equations and the developed program were ready to be generalized to handle the problem of spreading down general inclined surfaces.

The full governing equations (3.15), (3.16) and (3.24) were programed and used to predict the velocities and both the longitudinal and the lateral spreading of a finite volume of granular material released from rest down an inclined rough plane surface. The initial shape of the pile was taken to be a one half cycle of a sinusoidal curve. The selection of the initial aspect ratio ($A = h_i / l_i$) for the this investigation was based on the field data presented by, among others, Davies (10). The field data showed, from the deposit of the different rockfalls debris, that the ratio of the thickness to the length of the final deposit was of order O(1/1000). For example, the Sherman landslide debris deposit (4) was about 6 km in length and 3 to 6 m in thickness. Calculations showed that an initial shape having A of about 1/10 would spread to a final depth to length ratio of 1/1000 after going through the corresponding travel distance. Hence A = 1/10 was used for the calculations of this section. The bed angle of friction (DELTA) was selected to be equal to 32^o which corresponds to an angle of internal friction of 38.67^o (see Fig. 2.1). Three different inclinations were selected, a mild one close to the angle of bed friction (ZETA = 40^o), a medium one (ZETA= 60^o) and a steep one (ZETA = 80^o). The typical execution times for the three examples were about 30-45 minutes.

Fig. 3.7 shows both the longitudinal and the lateral spreading of the pile released down a bed having an angle of inclination of 40^o and the pile shapes at different non-dimensional times. The lower graph shows the non-dimensional height of the pile versus the non-dimensional streamwise distance and the upper graph shows the non-dimensional half width versus the non-dimensional distance. The space steps d_x and d_y were taken to be equal 0.1 and the time step was taken to be equal 0.1.

Fig. 3.7 clearly shows that the longitudinal spreading is much more significant than the lateral spreading. The net lateral force arising from the free surface slope is balanced by the bed friction, while in the longitudinal x-direction, bed friction is insufficient to prevent the spreading which is initiated as a result of free surface slopes. The final shape of the pile gave an aspect ratio of approximately 1/1500. Fig. 3.8 shows the non-dimensional center of mass velocity U versus the non-dimensional streamwise distance. It can be seen that, the velocity profile resembles the one presented in Fig. 3.6. At the center of mass of the pile, the second term on the right hand side of equation (2.46) approximately vanishes. Hence the center of mass velocity is very close to that predicted by the analysis of a point mass sliding down an inclined plane (the difference is less than 6%).

The upper graph of Fig. 3.7 indicates that the lateral velocity is very small; it may be seen that sides of the pile hardly move from their original lateral positions.

Fig. 3.9 shows the errors corresponding to the relative pile volume changes versus the computation time. The figure shows that the scheme is stable (no oscillations)and the numerical diffusion is well controlled.

The same calculations were repeated for bed angles of inclination ZETA = 60^o (Figs. 3.10 - 3.12) and for ZETA = 80^o(Figs. 3.13 - 3.15). The results were similar to those discussed earlier. As expected, higher accelerations and hence higher longitudinal velocities occurred. The aspect ratios for the final shape of the pile were approximately 1/2000 and 1/4500 respectively. However, the lateral spreading remained unnoticeable due to the balance between the net lateral force and the bed friction.

Fig. 3.15 shows a discontinuity in slope near the middle of the graph. Due to the high acceleration rate, the velocity increased in such a manner that the stability condition (equation (3.46)) was violated. An extrapolation of the first part of the graph at the point of inflection shows that the errors could have grown exponentially with time and the results would have been useless. This is taken care of in the computer program by resetting the time step to be half its value if the stability condition is not met. The 'kink' near the middle of the plot corresponds to this resetting of the time step.

3.5 Summary and Conclusions

In this Chapter, a simple continuum model was developed for the two-dimensional flow and spreading of a finite mass of granular material released from rest on rough inclined plane beds. The present model describes both the longitudinal and the lateral spreading of the pile. An explicit finite difference scheme applied on a staggered grid was employed for the numerical integration of the governing partial differential equations. The computation results seem to be stable and accurate. From these results, it was concluded that the lateral spreading is insignificant with respect to the longitudinal spreading. This result suggests that a simple one - dimensional spreading model is adequate for preliminary studies. It was also observed that the predicted center of mass velocity of the pile resembles very closely that predicted by the analysis of a point mass sliding down the same inclined plane surface.

In the next Chapter, a one-dimensional spreading model will be developed. The mathematical model will be derived for the flow and spreading of a finite mass of cohesionless granular material down rough curved beds. The governing equations will be written for a curvilinear coordinate system to accommodate the shape of the curved beds on which the material will flow. In this case, the normal to the bed stress will include the centrifugal force effects arising from curvature of the particle paths.

CHAPTER 4
ONE-DIMENSIONAL SPREADING MODEL

The results of the two-dimensional spreading model presented in Chapter 3 showed that the lateral spreading was insignificant and they suggested that, a one-dimensional spreading model would be adequate for the purpose of this study. A one-dimensional depth-averaged model is developed now for the flow and spreading of a finite mass of cohesionless granular material released from rest on rough curved beds. The governing partial differential equations for a curvilinear coordinate system are developed in Section 4.1. A finite difference approximation for the governing equations is presented in Section 4.2 along with the stability condition for the chosen scheme. Finally in Section 4.3, the results obtained from the computer programs are discussed.

4.1 Governing Equations

A simple continuum depth-averaged model for the flow of granular materials is now presented. The motion of the material is referred to a curvilinear coordinate system. The material point position is denoted by the coordinates ξ and η at time t. The ξ-coordinate is taken as positive in the streamwise direction following the bed curvature and the coordinate η is directed normal to the bed. Thus the curvilinear scheme consists of curves which are parallel to the bed and of straight lines perpendicular to the tangent to the bed at any point (Fig. 4.1).

For the analysis of the two-dimensional incompressible flow down a curved bed, the motion can be described by the continuity and momentum equations

$$\nabla \cdot \vec{u} = 0 \qquad (4.1)$$

$$\frac{D\vec{u}}{Dt} = - \nabla \vec{p} + \rho \vec{g} \tag{4.2}$$

The radius of curvature r (ξ) is to be taken to be positive for the concave shaped incline. Hence, these equations can be written for the curvilinear coordinate system (ξ , η) as follows

$$\frac{\partial u}{\partial \xi} + \frac{\partial v}{\partial \eta} - \frac{v}{r} = 0 \tag{4.3}$$

$$\rho \left[\frac{\partial u}{\partial t} + u \frac{\partial u}{\partial \xi} + v \frac{\partial u}{\partial \eta} \right] = \rho \, g \sin \zeta - \frac{\partial p_{\xi\xi}}{\partial \xi} - \frac{\partial p_{\xi\eta}}{\partial \eta} \tag{4.4}$$

$$\rho \left[\frac{\partial v}{\partial t} + u \frac{\partial v}{\partial \xi} + v \frac{\partial v}{\partial \eta} + \frac{u^2}{r} \right] = - \rho \, g \cos \zeta - \frac{\partial p_{\eta\xi}}{\partial \xi} - \frac{\partial p_{\eta\eta}}{\partial \eta} \tag{4.5}$$

where $p_{\xi\xi}$ and $p_{\eta\eta}$ are the normal stresses, $p_{\xi\eta}$ and $p_{\eta\xi}$ are the shear stresses and ζ is the local bed inclination angle (see Fig. 4.1).

Multiplying equation (4.3) by ρu and adding it to equation (4.4) yields

$$\rho \left[\frac{\partial u}{\partial t} + \frac{\partial}{\partial \xi} (u^2) + \frac{\partial}{\partial \eta} (uv) + \frac{uv}{r} \right] = \rho \, g \sin \zeta - \frac{\partial p_{\xi\xi}}{\partial \xi} - \frac{\partial p_{\xi\eta}}{\partial \eta} \tag{4.6}$$

The model can be simplified further by employing the long wave approximation. This approximation can be written out as

$$v \ll u \tag{4.7}$$

$$\frac{\partial}{\partial \eta} >> \frac{\partial}{\partial \xi} \tag{4.8}$$

$$r >> \eta \tag{4.9}$$

Hence, equation (4.5) can be simplified, using equations (4.7) - (4.9), to the hydrostatic equilibrium equation, including the centrifugal force effects arising from the curved particle paths.

$$\frac{\partial p_{\eta\eta}}{\partial \eta} + \rho\ g \cos \zeta + \frac{\rho\ u^2}{r} = 0 \tag{4.10}$$

or

$$p_{\eta\eta} = \rho\ g \cos \zeta\ (h-\eta) + \frac{\rho}{r} \int_\eta^h u^2\ d\eta \tag{4.11}$$

where h is the depth of the pile at any position. Integrating equation (4.6) over the depth yields

$$\rho\ [\ \frac{\partial}{\partial t} \int_0^h u\ d\eta + u_s \frac{\partial h}{\partial t} + \frac{\partial}{\partial \xi} \int_0^h u^2\ d\eta - u_s^2 \frac{\partial h}{\partial \xi} + u_s v_s\ ]$$

$$= \rho\ g \sin \zeta - \frac{\partial}{\partial \xi} \int_0^h p_{\xi\xi}\ d\xi + p_{\xi\eta} \Big|_0 \tag{4.12}$$

where the subscript s refers to the free surface value of the velocity component. At the free surface, we have the kinematic condition,

$$v_s = \frac{\partial h}{\partial t} + u_s \frac{\partial h}{\partial \xi} \tag{4.13}$$

Then, we define the following depth averaged quantities,

$$\bar{u} = \frac{1}{h} \int_0^h u \, d\eta \tag{4.14}$$

$$\bar{p}_{\xi\xi} = \frac{1}{h} \int_0^h p_{\xi\xi} \, d\eta \tag{4.15}$$

Also, we assume that

$$\overline{u^2} = \frac{1}{h} \int_0^h u^2 \, d\eta \cong (\bar{u})^2 \tag{4.16}$$

By using equation (4.13) - (4.16), equation (4.12) can be reduced to

$$\rho \left[\frac{\partial}{\partial t} (h\bar{u}) + \frac{\partial}{\partial \xi} (h\bar{u}^2) \right] = \rho \, g \, h \sin \zeta -$$

$$\frac{\partial}{\partial \xi} (h \, \bar{p}_{\xi\xi}) - p_{\xi\eta} \Big|_0 \tag{4.17}$$

The constitutive relation between the stress components is assumed to be the same relation introduced earlier in Section 2.2.1 (Fig. 2.1). Hence, we write

$$p_{\xi\xi} \cong p_{\eta\eta} \cong p_o \tag{4.18}$$

$$p_{\xi\eta} = - \tau \frac{\bar{u}}{|\bar{u}|} = - \tau \, \mathrm{sgn}(\bar{u})$$

$$\tau = p_o \sin\phi = p_o \tan\delta \tag{4.19}$$

Using equation (4.16), equation (4.11) can be reduced to

$$p_{\eta\eta} = \rho\ g\ \cos\zeta\ (h-\eta) + \frac{\rho\ \bar{u}^2}{r}\ (h-\eta) \tag{4.20}$$

From equations (4.20) and (4.15), we obtain

$$\bar{p}_{\eta\eta}\ h = \int_0^h p_{\eta\eta}\ d\eta$$

$$= [\ \rho\ g\ \cos\zeta\ \frac{h^2}{2} + \frac{\rho\ \bar{u}^2}{r}\ \frac{h^2}{2}\ ] \tag{4.21}$$

Finally, equation (4.17) can be rewritten using equations (4.21) and equation (4.19) as

$$\rho\ [\ \frac{\partial}{\partial t}\ (\ h\bar{u}\ ) + \frac{\partial}{\partial \xi}\ (\ h\bar{u}^2\ )\ ] = \rho\ g\ h\ \sin\zeta\ - \frac{\partial}{\partial \xi}\ [\ \rho\ g\ \cos\zeta\ \frac{h^2}{2} +$$

$$\frac{\rho\ \bar{u}^2}{r}\ \frac{h^2}{2}\ ] + [\ \rho\ g\ h\ \cos\zeta\ \tan\delta$$

$$+ \frac{\rho\ \bar{u}^2}{r}\ h\ \tan\delta\ ]\ \ \mathrm{sgn}(\bar{u}) \tag{4.22}$$

Integrating equation (4.3) over the depth and using the free surface kinematic condition, equation (4.13), yields

$$\frac{\partial h}{\partial t} + \frac{\partial}{\partial \xi}\ (\ h\bar{u}\ ) = 0 \tag{4.23}$$

Using equation (4.23), equation (4.22) can be reduced to

$$\rho \left[\frac{\partial \bar{u}}{\partial t} + \bar{u} \frac{\partial \bar{u}}{\partial \xi} \right] = \rho \; g \sin \zeta - g \left[\cos \zeta \frac{\partial h}{\partial \xi} + \frac{h}{2} \frac{\partial \cos \zeta}{\partial \xi} \right]$$

$$- \left[\frac{\bar{u}^2}{r} \frac{\partial h}{\partial \xi} + \frac{h}{2} \frac{\partial}{\partial \xi} \left(\frac{\bar{u}^2}{r} \right) \right]$$

$$- \left[g \cos \zeta \tan \delta + \frac{\bar{u}^2}{r} \tan \delta \right] \operatorname{sgn}(\bar{u}) \qquad (4.24)$$

The resulting equations (4.23) and (4.24) are sufficient to describe the longitudinal spreading of the flow. The above depth-averaged equations can now be expressed in non - dimensional form following the same procedure which was used in Section 2.4. Let us start by introducing the following non-dimensional parameters

$$H = \frac{h}{h_i} \quad ; \quad S = \frac{\xi}{l_i} \quad ; \quad R = \frac{r}{l_i} \qquad (4.25)$$

$$U = \frac{\bar{u}}{\sqrt{g \; l_i}} \quad ; \quad T = \frac{t}{\sqrt{l_i / g}} \quad ; \quad A = \frac{h_i}{l_i} \qquad (4.26)$$

where h_i and l_i are the maximum height and length of the debris mass before release. Then, by substituting equations (4.25) and (4.26) in equations (4.23) and (4.24), the non-dimensional form of the model can be written as

$$\frac{\partial H}{\partial T} + \frac{\partial}{\partial S} \left(HU \right) = 0 \qquad (4.27)$$

$$\frac{\partial U}{\partial T} + U \frac{\partial U}{\partial S} = \sin \zeta - A \left[\cos \zeta \frac{\partial H}{\partial S} + \frac{H}{2} \frac{\partial \cos \zeta}{\partial S} \right]$$

$$- A \left[\frac{U^2}{R} \frac{\partial H}{\partial S} + \frac{H}{2} \frac{\partial}{\partial S} \left(\frac{U^2}{R} \right) \right]$$

$$- [\cos \zeta \tan \delta + A \frac{U^2}{R} \tan \delta] \operatorname{sgn} (U) \tag{4.28}$$

4.2 Finite Difference Equations

A simple explicit scheme applied to a staggered grid is presented. Fig. 4.2 shows the proposed grid with the space index i. The superscript n is used to number the time cycle. The U values are computed first and used to obtain the H values as indicated in the flowchart diagram in Fig. 4.3. Computational results arising from the finite difference programs are discussed later in Section 4.3.

We start by defining various difference operators and their relationship with the differential operators. Let d_ξ be the non-dimensional spacing between abscissas in the s-direction and d_t be the non-dimensional time step. The forward difference operators are defined by

$$\Delta k(\xi) = k^n (\xi+d_\xi) - k^n (\xi) \tag{4.29}$$

$$\Delta k(t) = k^{n+1} (\xi+d_\xi) - k^n (\xi+d_\xi) \tag{4.30}$$

where k represents either dependent variable H or U. The differential operators are defined by

$$Dk(\xi) = \frac{\Delta k(\xi)}{d_\xi} \tag{4.31}$$

$$Dk(t) = \frac{\Delta k(t)}{d_t} \tag{4.32}$$

The difference equations, approximating the continuity and the momentum equations (4.27) and (4.28) can be written in terms of the velocity values at the nodes of the scheme and the flow height at the center of each cell. Starting with the momentum equation (4.28), the following difference approximation was used

$$DU(t) + U^{n-\frac{1}{2}}(i+1)\,DU(\xi) = B' - C'\,DH(\xi) - \frac{1}{2}H^{n}(i+1)\,D\cos$$

$$- \frac{1}{2}H^{n}(i+1)\,DUR(\xi) - E' \tag{4.33}$$

where

$$B' = \sin\zeta(i+1) - \cos\zeta(i+1)\tan\delta\ \mathrm{sgn}\,(U) \tag{4.34}$$

$$C' = A\left[\cos\zeta(i+1) + \frac{U^2}{R}\right] \tag{4.35}$$

$$D\cos = A\left[\cos\zeta(i+1) - \cos\zeta(i)\right] \tag{4.36}$$

$$DUR\,(\xi) = A\left[\frac{\{U^{n-\frac{1}{2}}(i+1)\}^2}{R(i+1)} - \frac{\{U^{n-\frac{1}{2}}(i)\}^2}{R(i)}\right] \tag{4.37}$$

$$E' = A\tan\delta\,\frac{\{U^{n-\frac{1}{2}}(i+1)\}^2}{R(i+1)}\,\mathrm{sgn}\,(U) \tag{4.38}$$

A Lax-Wendroff (45) type of approximation to the velocity $U^{n-1/2}(i+1)$ in equation (4.33) was used as follows

$$U^{n-\frac{1}{2}}(i+1) = \frac{1}{2}\left[U^{n+\frac{1}{2}}(i+1) + U^{n-\frac{1}{2}}(i+1)\right] \tag{4.39}$$

Substituting equation (4.39) in equation (4.33) and solving for $U^{n+1/2}(i+1)$ yields

$$U^{n+\frac{1}{2}}(i+1) = [\, U^{n-\frac{1}{2}}(i+1) - d_t \{ \frac{1}{2} U^{n-\frac{1}{2}}(i+1)\, DU(\xi) - B'$$

$$+ C'\, DH(\xi) + \frac{1}{2} H^n (i+1)\, Dcos + \frac{1}{2} H^n (i+1)\, DUR(\xi)$$

$$+ E' \} \,] \,/\, [\, 1 + \frac{1}{2} d_t\, DU(\xi) \,] \qquad (4.40)$$

Similarly, equation (4.27) can be approximated by the following finite difference equation

$$DH(t) + H^n (i+1)\, DU(\xi) + U^{n+\frac{1}{2}}(i+1)\, DH(\xi) = 0 \qquad (4.41)$$

By using the Lax-Wendroff approximation, equation (4.41) can be rearranged and solved for $H^{n+1}(i+1)$ to yield

$$H^{n+\frac{1}{2}}(i+1) = [\, H^n (i+1) - d_t \{ \frac{1}{2} H^n (i+1)\, DU(\xi) +$$

$$U^{n+\frac{1}{2}}(i+1)\, DH(\xi) \} \,] \,/\, [\, 1 + \frac{1}{2} d_t\, DU(\xi) \,] \qquad (4.42)$$

The solution of the system of equations (4.40) and (4.42) proceeds in a manner similar to that described earlier for the two-dimensional spreading model. First all variables are initialized and then equations (4.40) and (4.42) can alternately be evaluated for all n.

A stability analysis was worked out following the same procedures explained previously in Section 3.3 and the stability condition obtained was

$$\frac{U\ d_t}{d_\xi} \leq 1 \qquad (4.43)$$

4.3 Results and Discussion

A computer code similar in logic to the one presented in Section 3.4 was constructed. It was necessary to add a segment which is used to generate the desired curved bed shape and to calculate the radius of curvature. The program was used to predict the longitudinal spreading and velocity of three different rockslides. The selection of these particular cases was based on the availability of the required data for the computations, namely, a cross section of the bed along the slide path and an estimation of the dislodged mass dimensions before the slide occurred. The angle of bed friction (DELTA) was chosen to be 35°.

4.3.1 Frank Rockslide

The Frank rockslide which occurred in 1903 is one of several rockslides that have taken place in the Canadian Rockies. This particular slide is one of the most studied events because of the destruction it caused to the town of Frank in the southern part of Alberta, Canada (25). The volume of the rock mass which was estimated to be $3 \times 10^7 m^3$. The extent of the final deposit was about 1600 m with an average thickness of 13.7 m. The total fall height was estimated to be 775 m. Fig 4.4, shows a longitudinal cross section which was constructed from both a topographic map and a cross section through the path of the slide which were given in reference (25).

An analytical expression to simulate the shape of the bed was constructed as follows. The initial position of the shape was a plane surface inclined at 50° to the horizontal. At station x = 500 m (see Fig. 4.4) this was joined with a smooth exponential curve which approached horizontal surface at large x, i.e.

$$y = 180\, e^{-0.0066\,(x-500)} \quad , x >= 500 \tag{4.44}$$

The radius of curvature of the incline is defined by

$$\frac{1}{r} = \frac{\frac{d^2y}{dx^2}}{\left[1 + \left(\frac{dy}{dx} \right)^2 \right]^{\frac{3}{2}}} \tag{4.45}$$

The initial maximum height and length of the rock mass before the slide occurred were estimated to be 150 m and 625 m respectively which give an initial aspect ratio A = 1 / 4. The initial shape of the rock mass was approximated by a sine curve shape. Fig. 4.5 shows the non-dimensional shape of the debris versus the non-dimensional travel distance along the slide path at different non dimensional times. The calculated final deposit length was found to be 1600 m and the averaged thickness was 40 m. These dimensions (especially the thickness) are larger than the observed dimensions of the Frank slide debris. The difference can be attributed to three-dimensional effects since both the topographic map and the oblique aerial photograph of the slide site (25) show that lateral spreading of the debris occurred because of a slight lateral bed inclination.

Fig. 4.4 shows the initial rock mass before release and the calculated final shape of the debris. It was found that the line connecting the initial and final center of mass positions makes an angle of inclination equal to 35.5^{o} which is close to the assumed angle of bed friction of 35^{o} . The difference is no doubt due to the finite size of the debris mass whose shape is changing and to errors associated with the finite difference computations. The predicted total travel distance of the farthest point of the debris (at x = 1950 m) was found to be consistent with the observed runout distance (25).

It was found that the line connecting the highest point in the slide path with the farthest point of the debris makes an angle of inclination of 21.6° which gives an equivalent coefficient of friction of 0.396. Fig. 4.6 shows the non-dimensional center of mass velocity versus the non-dimensional traveling distance along the slide path. Fig. 4.7 shows the 'Error' expressed in terms of the relative volume change versus the computation time. The figure shows four points of discontinuity in slope which correspond to changes in the time step.

Computations were performed for two other slide volumes of 10 % and 50 % of the Frank slide. The results of these computations are shown in Figs. 4.8 and 4.9 . Two interesting things may be observed. First the angles of inclination of the line connecting the initial and final centers of mass are all much the same and very close to the bed friction angle of 35°. In addition, the angles of inclination of the line connecting the aft end of the initial position of the debris with the nose of the final shape of the debris pile are seen to decrease moderately with the increasing debris volume. A similar computation was performed for a slide volume of 350 % of the Frank slide. The result of this computation is shown in Fig. 4.10. It was observed that the line connecting the initial and final centers of mass are very close to the bed friction angle, however, the angle of inclination of the line connecting the aft end of the initial position with the nose of the final shape is larger than that of the Frank slide. The reason of this behaviour is that after its initial acceleration the front of the pile decelerates more rapidly than the rest of the pile since it flows on the flat part of the incline earlier than the rest of the debris. This behaviour is consistent with the field data of the Medicine lake rockslide as will be seen later in Section 4.3.3.

4.3.2 Madison Canyon Rockslide

In 1959, a large rockslide took place in a steep walled canyor of the Madison River (24) in Montana, U.S.A. The slide was a direct result of a strong earthquake. A volume of approximately $2x10^7$ m^3 was dislodged and rushed down the steep slope of the canyo.ı to an almost flat valley. The total fall height was about 575 m. The debris traveled about 1200 m across the flat valley. The final deposit was 1380 m in length, an average of 7.5 m in thickness and an average of 2000 m in width.

The shape of the slide path cross section was constructed from the topographic map given by Hadley (Fig. 6 of reference (24)). This shape was approximated by the following exponential function (Fig. 4.12)

$$y = 575 \quad e^{-0.01\ x} \tag{4.46}$$

The initial maximum height and length of the debris pile before the slide was estimated to be 75 m and 150 m which gives an initial aspect ratio A of 0.5. The shape of the initial pile was approximated by a sine curve shape.

In the computer program, the governing equations (4.27) and (4.28) were used throughout the curved part of the bed up to station x = 600 m and then equation (4.28) was simplified by canceling out the terms involving R, the radius of curvature, since R has the value of infinity in the flat part of the bed.

Fig. 4.12 shows the non-dimensional shape of the pile versus the non-dimensional traveling distance aıong the incline at different non-dimensional times. The graph shows that the rock mass spread to a final physical aspect ratio of 1 / 400. The calculated final deposit length was found to be 1490 m and the average thickness was found to be approximately 3.25 m. These results are considered to be satisfactory considering both the errors associated with the estimation of the geometry of the actual slide debris, three-dimensional flow effects and the approximations made in the computation.

Fig. 4.12 shows the initial shape of the rock mass and the calculated final shape of the debris. Note that the thickness shown in this graph is distorted to permit a representation of the depth variations with distance along the slide path. The graph shows that the line connecting the initial and final center of mass positions makes an angle of inclination of 36° which is approximately equal to the angle of bed friction which was assumed to be 35°. This result agrees with the simple analysis of a point mass sliding down the same incline. The graph also shows that the line connecting the highest point of the incline with the farthest point of the debris makes an angle of 21° . This line gives an equivalent coefficient of friction of 0.384.

Fig. 4.14 shows the non-dimensional center of mass velocity versus the non-dimensional traveling distance along the slide path. Again the calculated profile resembles the one which might be obtained from the point mass analysis and the velocity reaches a maximum at the point where the bed angle of inclination is equal to the angle of bed friction.

A few remarks about how the debris comes to rest are in order. Fig. 4.13a shows the non-dimensional longitudinal velocity profile versus the non-dimensional traveling distance along the incline at different non-dimensional times just before the motion ceased. The graph shows that the front part of the slide is moving faster than the rear end of the debris which results in the spreading behaviour. Just prior to the end of the motion, portions at the rear end of the debris come to rest while the front part continues to move. As time progresses more and more material at the back end comes to rest until finally all motion ceases. During this process the center of mass of the complete debris mass continued to move in the downstream direction and the center of mass velocity became zero at the same time that all the material came to rest.

4.3.7 Medicine Lake Rockslide

The Medicine Lake slide occurred in the same general area of the Frank rockslide in the Rocky Mountains. It was estimated that the dislodged volume was about 8.6×10^7 m^3. A cross-section along the path of slide was given by Cruden in Fig 11 of reference (26). This graph also showed the estimated initial profile before the slide occurred as well as the shape of the final debris deposit. The total fall height was was about 600 m.

The shape of the incline (see Fig. 4.15) was approximated by a straight line having an angle of inclination equal to 45^o followed after station x = 500 by an exponential curve of the form

$$y = 100\, e^{-\,0.01\,(x-500)}\,,\quad x >= 500 \qquad (4.47)$$

The initial height and length of the rock mass were taken to be 110 m and 860 m respectively. Fig. 4.16 shows that the front of the pile accelerates and then slows down more rapidly than the rest of the pile since it flows on the flat part of the incline earlier than the rest of the debris. Fig. 4.17 shows a comparison of the calculated final profile of the debris and the profile observed in the field. The computed profile in the final state was found to be somewhat lower than the observed deposit of the rockfall. Notice that the final 'center line' cross-sectional area of the observed debris is less than that before the slide occurred. This anomaly is evidently due to lateral convergence of the flow that occurred in the actual slide.

Fig. 4.18 shows the non-dimensional velocity profile which again resembles the profile which might be obtained from an analysis of a point mass sliding down the same incline.

4.3.4 Other Rockslides

The rest of the available data on rockslides events from the literature can be divided into two categories. First, there are events that could not be analyzed by the present model because no detailed information about the shape of the cross-section along the slide path was found in the literature. For the second group of events, the required data for the computation was available but the bed angle of inclination at the starting zone was less than the angle of bed friction. These cases can not be handled by the present model and the mobility of these events is no doubt due to factors not considered in the present model. Such factors might be the occurrence of a strong earthquake which could supply the debris with the enough vibrational energy to mobilize the flow. Another might be the presence of water and or mud within the discrete rock material which could change the constitutive behaviour to that of a non-Newtonian fluid, thereby allowing the debris to travel for extended distances over a nearly flat course.

4.4 Summary and Conclusions

In this Chapter, a one dimensional spreading model was developed for the prediction of the flow and spreading of a finite mass of dry cohesionless granular material released from rest on a rough curved beds. The computational results agree reasonably well with the field data of three rockslides which were selected because of the availability of the required data for the calculations. The main conclusions of these results are as follows. The movement of the center of mass of the rock debris resembles the simple motion of a point mass sliding down the same incline. The long runout distance of the leading edge of the debris can be attributed to the spreading of the material which occurs as the debris traverses the slide path.

One of the problems which arose during the selection of the three cases presented here was the lack of correspondence between the data published in the original sources and the data which appeared in subsequent publications describing the same event. Also, it seems that the estimation of the dislodged rock volume varies widely and hence no accurate figure can be obtained. For example, the estimated volumes of the Sherman rockslide (16) were found to vary between 1.2×10^7 m^3 and 10.1×10^7 m^3 which is a factor of about 8. Shreve (4) estimated the equivalent coefficient of friction for this rockslide to be 0.22; it was subsequently quoted by Scheidegger (1) to be 0.19 and by Lucchitta (10) to be 0.18. Other cases of a similar nature can be found in the literature. More accurate data would be helpful for any further investigations into the mechanics of rockfalls.

CHAPTER 5
SUMMARY AND CONCLUSIONS

Landslides and rockfalls that initiate on steep slopes eventually come to rest after flowing for some runout distance on a horizontal bed. It has been observed that the granular material making up the slide can be deposited in a very long and thin layer such that the nose of the slide moves through a surprisingly long distance. To those familiar with soil mechanics and geology or even someone aware that the angle of repose (surface slope of a static pile of material) of typical geological materials is around 35^{o}- 50^{o}, these long runout distances seem extraordinary. For over 100 years, since Albert Hiem observed and described the Elm rockfall in Switzerland in 1881, attempts have been made to explain the apparent fluid-like behaviour of these slides. Various proposals have involved upward flow of air as a fluidizing mechanism, hovercraft action, generation of high pressure steam, lubrication by molten rock, etc. All of these hypotheses have been at best controversial and none have been universally accepted. It also appears that none of the proposals have been accompanied by a detailed computation of the flow development for a typical field event in an effort to establish the validity of the proposed fluidizing mechanism. In view of this in addition to the questionable nature of the fluidization hypotheses, it seemed worthwhile at the outset of this investigation to attempt to predict the gross flow features of a typical rockfall by a numerical computer simulation based upon the assumption of simple and common-place constitutive behaviour. The idea was that the extreme spreading might be a consequence merely of the flow dynamics for a very ordinary Coulomb-like material and that nothing extraordinary such as an external fluidization of the granular material was required.

The investigation began with the development of the governing equations for the somewhat idealized problem of the two-dimensional flow and spreading of a pile of granular material down rough inclined plane beds. The equations of motion were simplified by depth averaging and by making use of approximations analogous to the long wave approximation used in hydraulics. The granular material was treated as a continuum and the stresses were simply approximated by using a quasi-static constitutive relation based upon the Mohr-Coulomb yield criterion. Numerical solutions of the governing partial differential equations were obtained by using a finite difference approximation applied on a staggered grid scheme. A stability analysis was performed to obtain the necessary stability condition to assure the accuracy and stability of the computation. The analysis predicts both the longitudinal and the lateral spreading of the pile as well as the velocities. It was concluded from the results of the two-dimensional spreading computations that the lateral spreading is insignificant relative to the longitudinal spreading and that a one-dimensional spreading model would be adequate for preliminary studies.

Based upon this work, a depth - averaged model was developed to describe the one-dimensional spreading of a finite mass of cohesionless granular material released from rest on a rough curved bed. The governing equations were expressed in terms of a curvilinear coordinate system and the centrifugal force effects arising from the curvature of the particle paths were included. A finite difference scheme for the numerical integration of the governing equations was used to predict the longitudinal spreading and the flow velocities.

Of all the available information on rockfalls, there are only three events, the Frank, Madison Canyon and Medicine Lake slides, for which sufficient data exist to make a detailed simulation using the present model. The basis of the selection of these three events was the availability of a cross section along the slide path and the condition that the bed angle of inclination at the original position of the dislodged mass was larger than typical values of the bed friction angle. The results obtained from the simulation of the three selected cases were found to agree satisfactorily with the field data. It was found that extreme spreading could indeed occur without introducing any unusual fluidization mechanisms. For the case of the Madison Canyon rockslide the final length to depth ratio of the debris was 400 whereas the initial length to depth ratio of the pile was 2. Additional computations for fictitious slides having volumes of 10 % and 50 % of the Frank event and flowing down the same curved bed showed that the angle of inclination of the line connecting the aft end of the initial position of the debris with the nose of the final shape of the debris pile decreased moderately with increase in slide volume.

It was concluded that the motion of the center of mass of a rock pile resembles the motion of a point mass sliding down the same incline. Also, the long runout distance of the leading edge of the debris can be due to the spreading of the pile under gravity during its travel down the slope. Nevertheless, several other rockfalls have shown extreme mobility over mild inclines. In these cases the bed slopes over the whole slide travel distance was less than bed friction angles for typical geological materials. It is believed that other factors such as continued vibration from earthquakes or the presence of mud within the debris might have contributed to the mobility of the debris in these instances.

The present analysis has used a very simple model of the constitutive behaviour and further work is needed to develop improved and more detailed constitutive theories. The effects of the interstitial fluid such as mud would be of considerable interest in connection with further investigations into the large rockfalls.

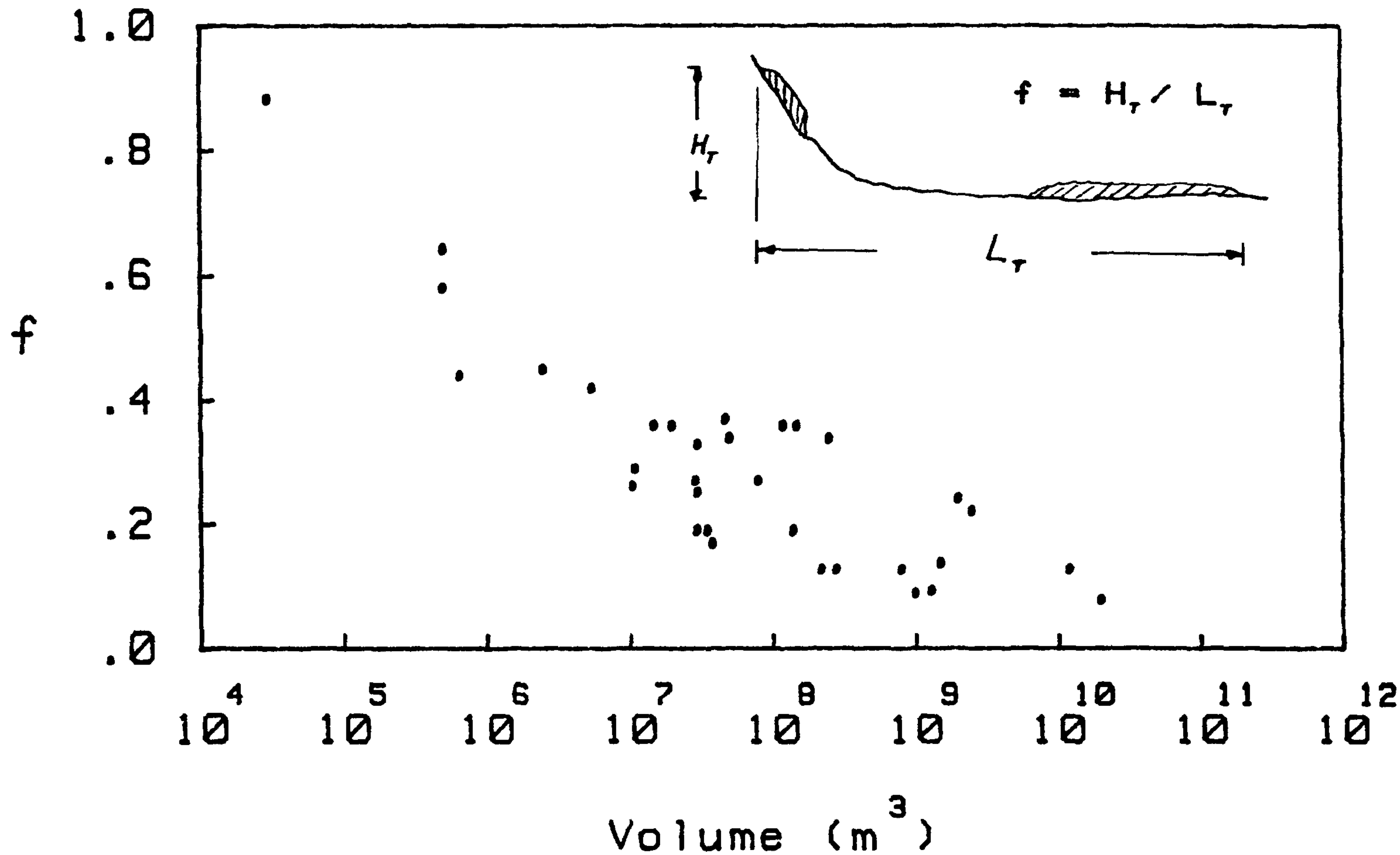

Fig. 1.1 'Equivalent coefficient' of friction, f, versus the volume of rockfall

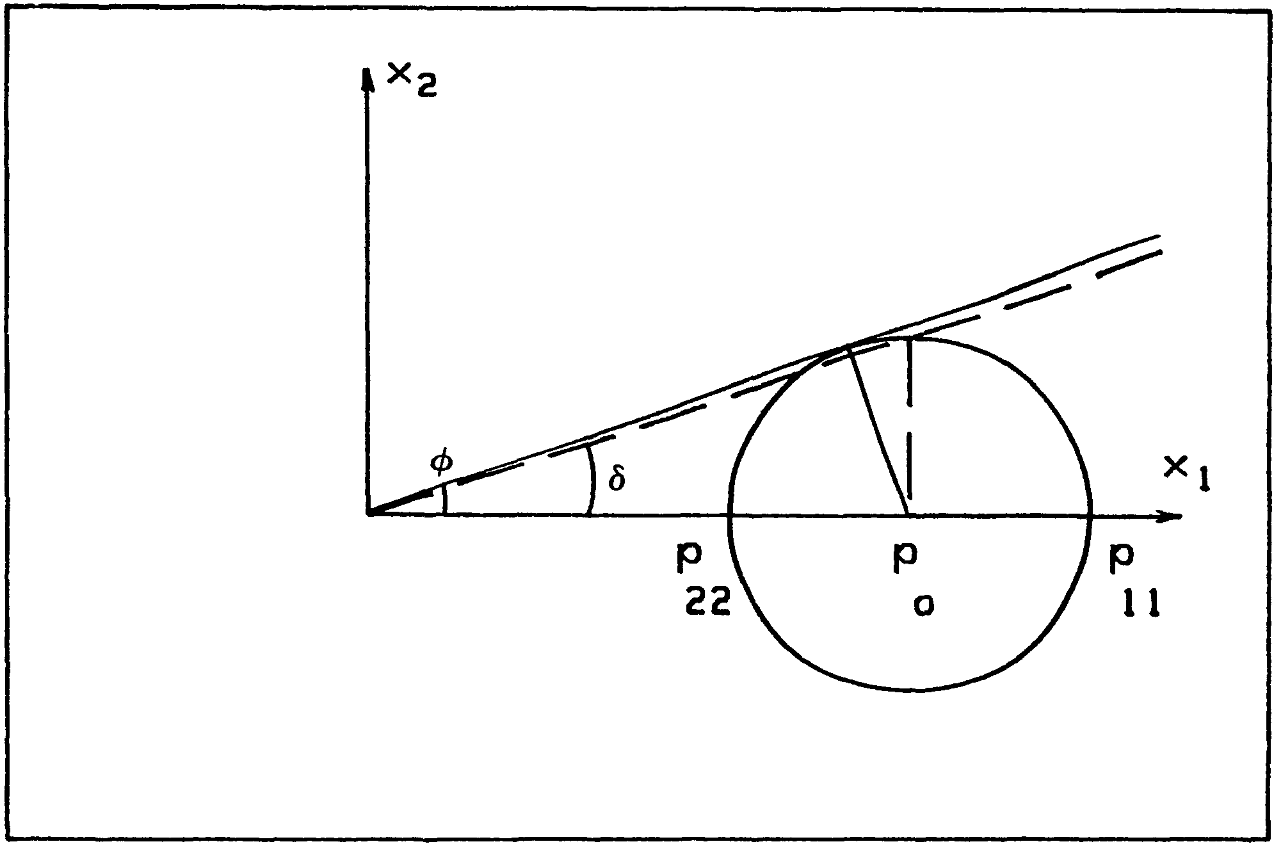

Fig. 2.1 Definition sketch of the proposed approximation of the Coulomb-like yield and flow criterion

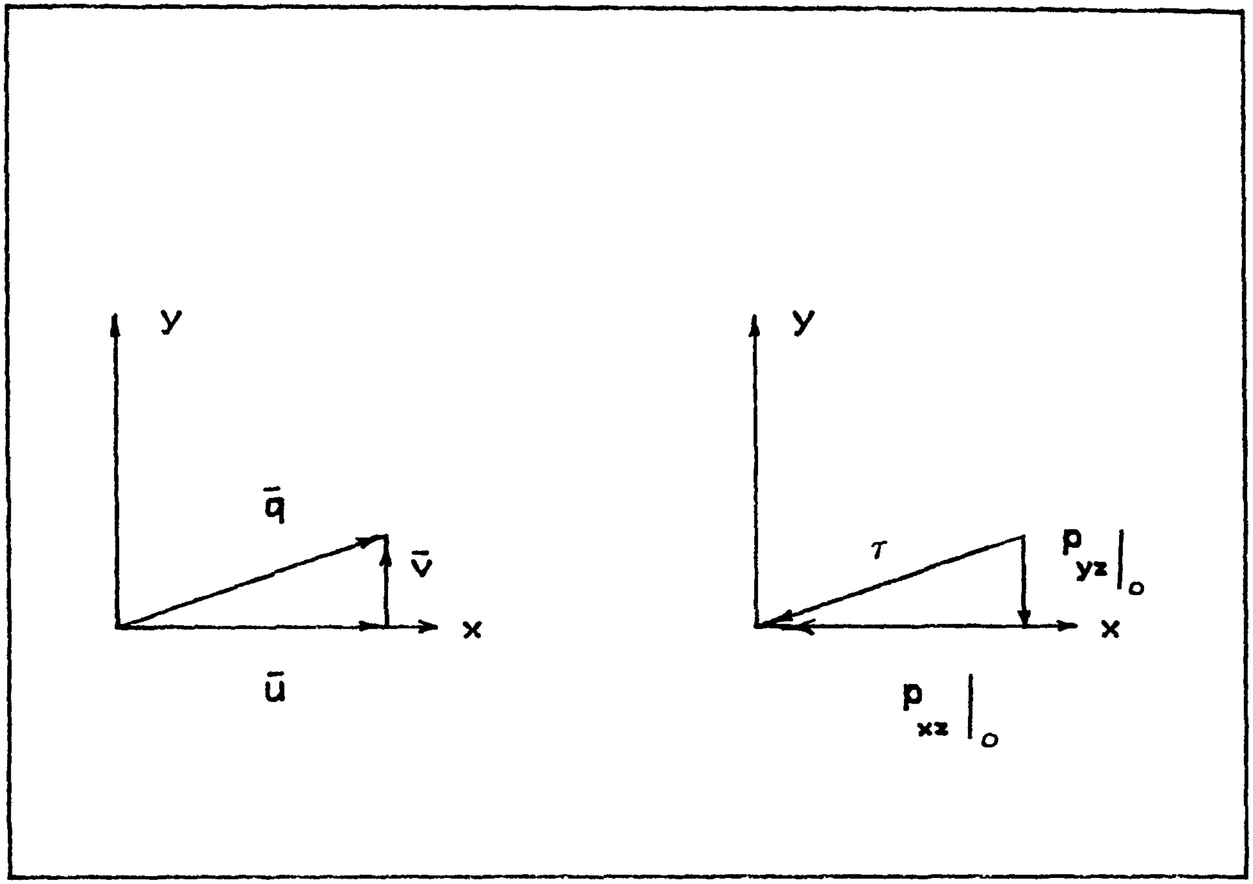

Fig. 2.2 Definition sketch of the assumed colinearity between the friction force and the velocity vector

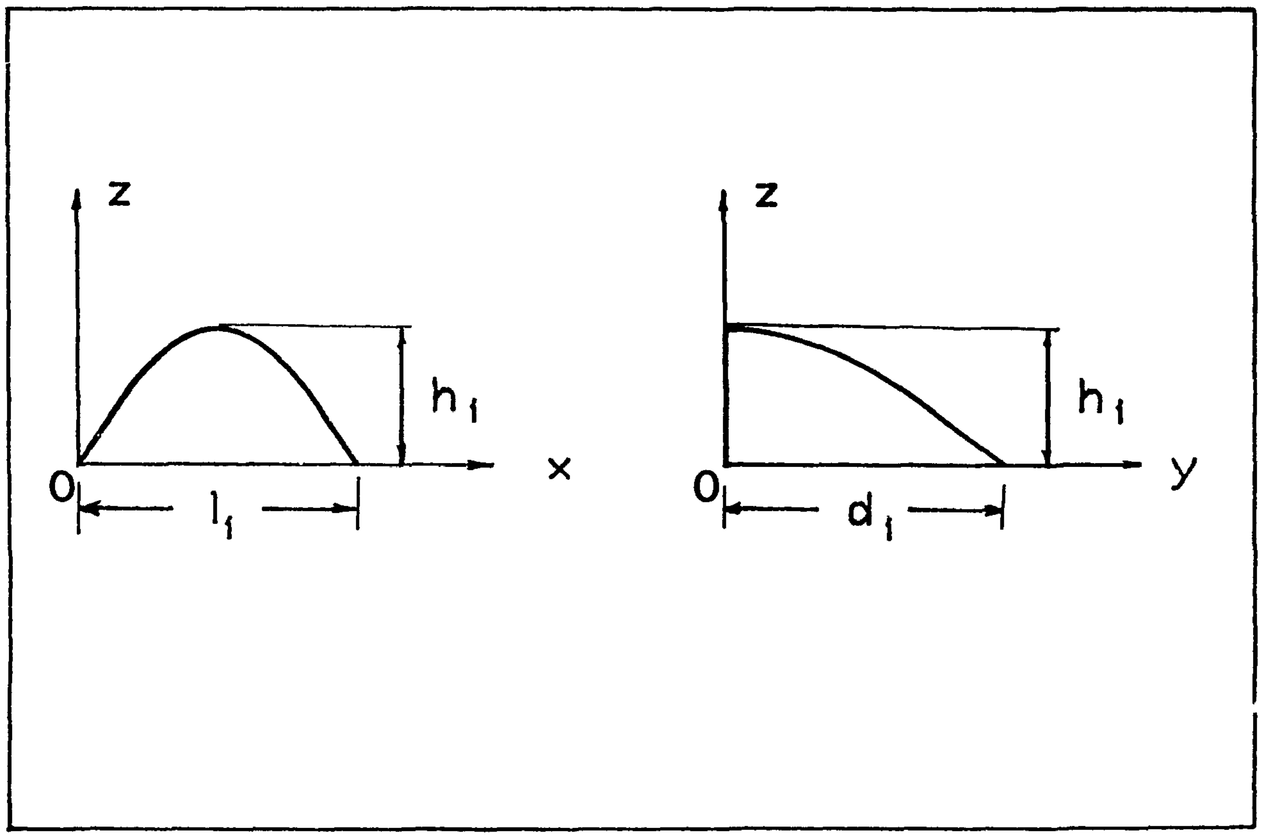

Fig. 2.3 Definition sketch of the initial dimensions of the pile of granular material

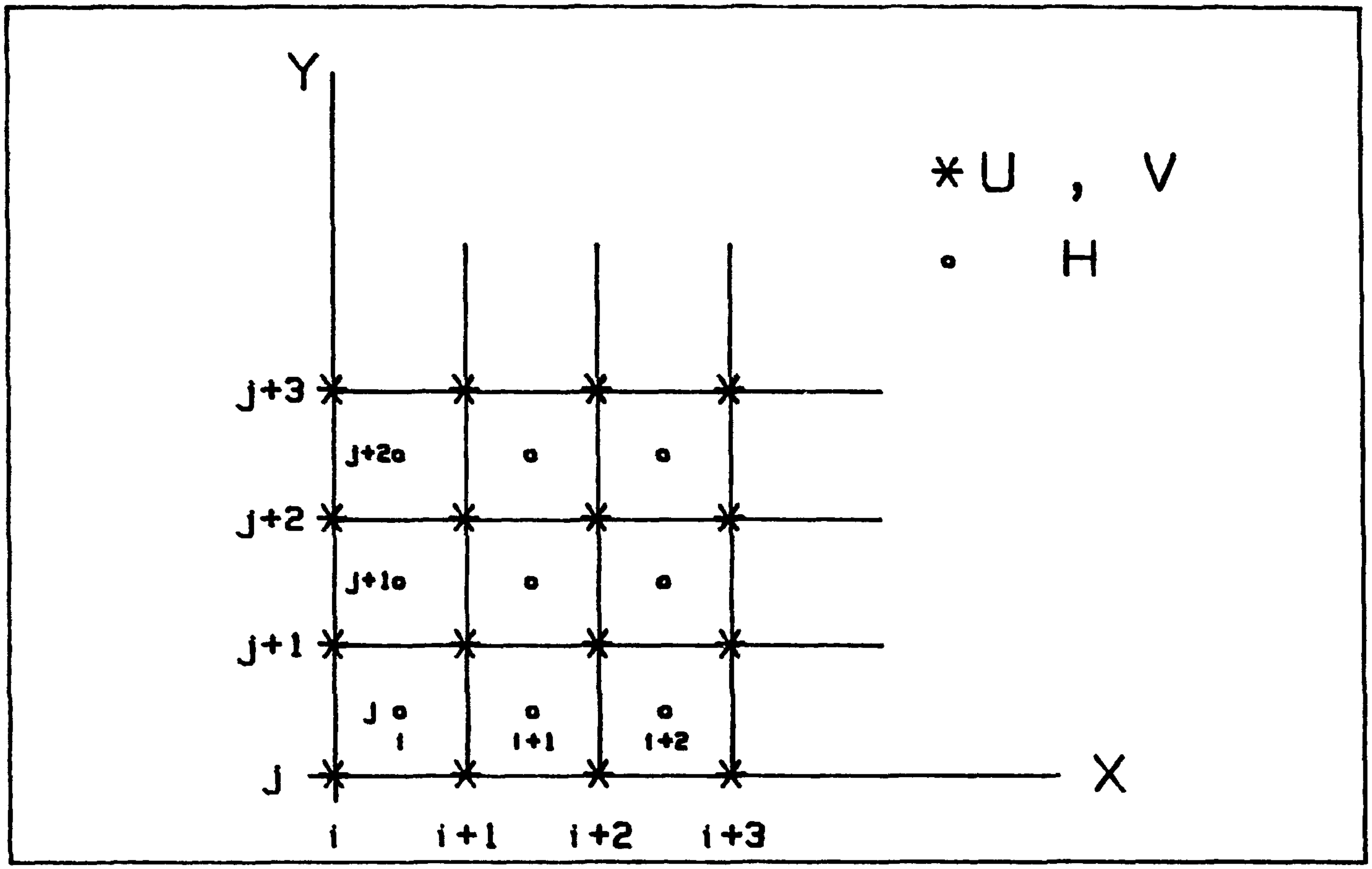

Fig. 3.1 Sketch of the staggered grid scheme

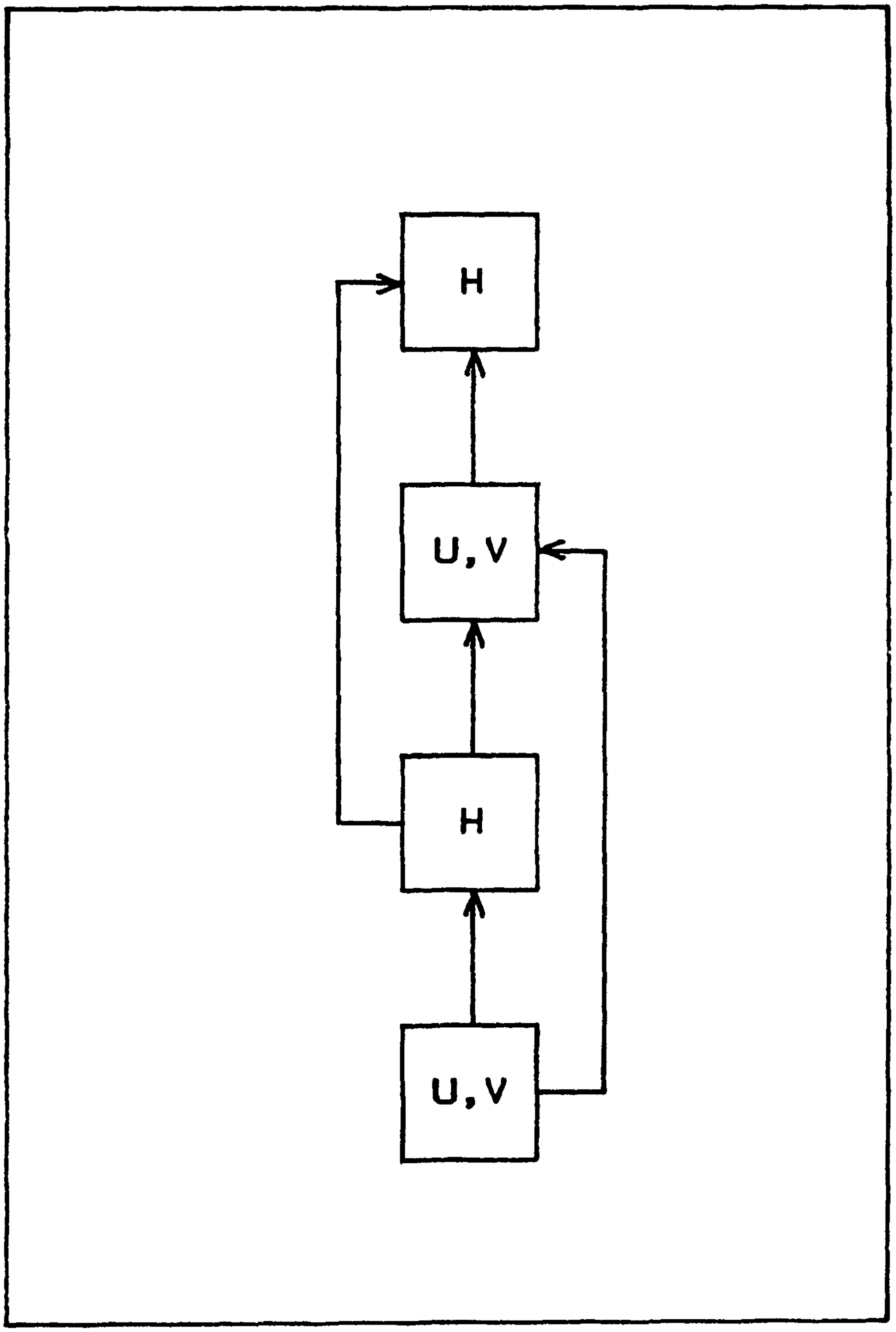

Fig. 3.2 Flowchart of the computation procedure

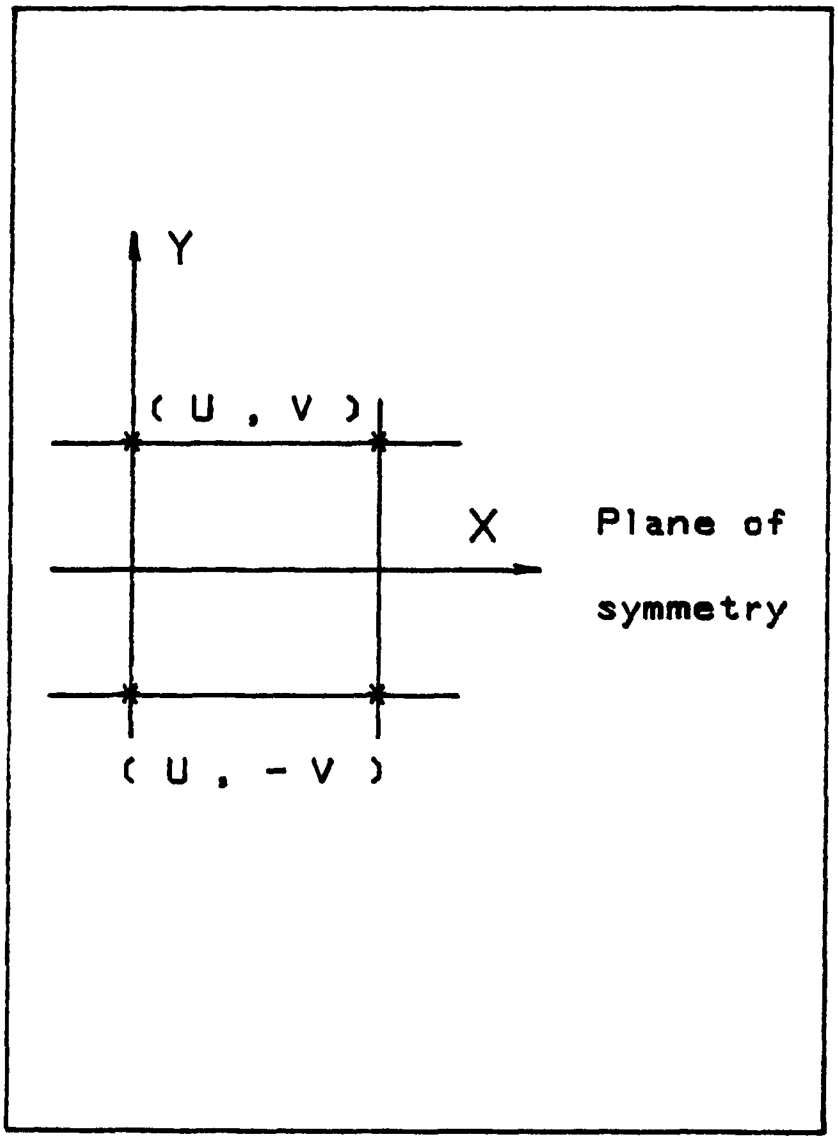

Fig. 3.5 Definition sketch of the boundary condition at a
a plane of symmetry

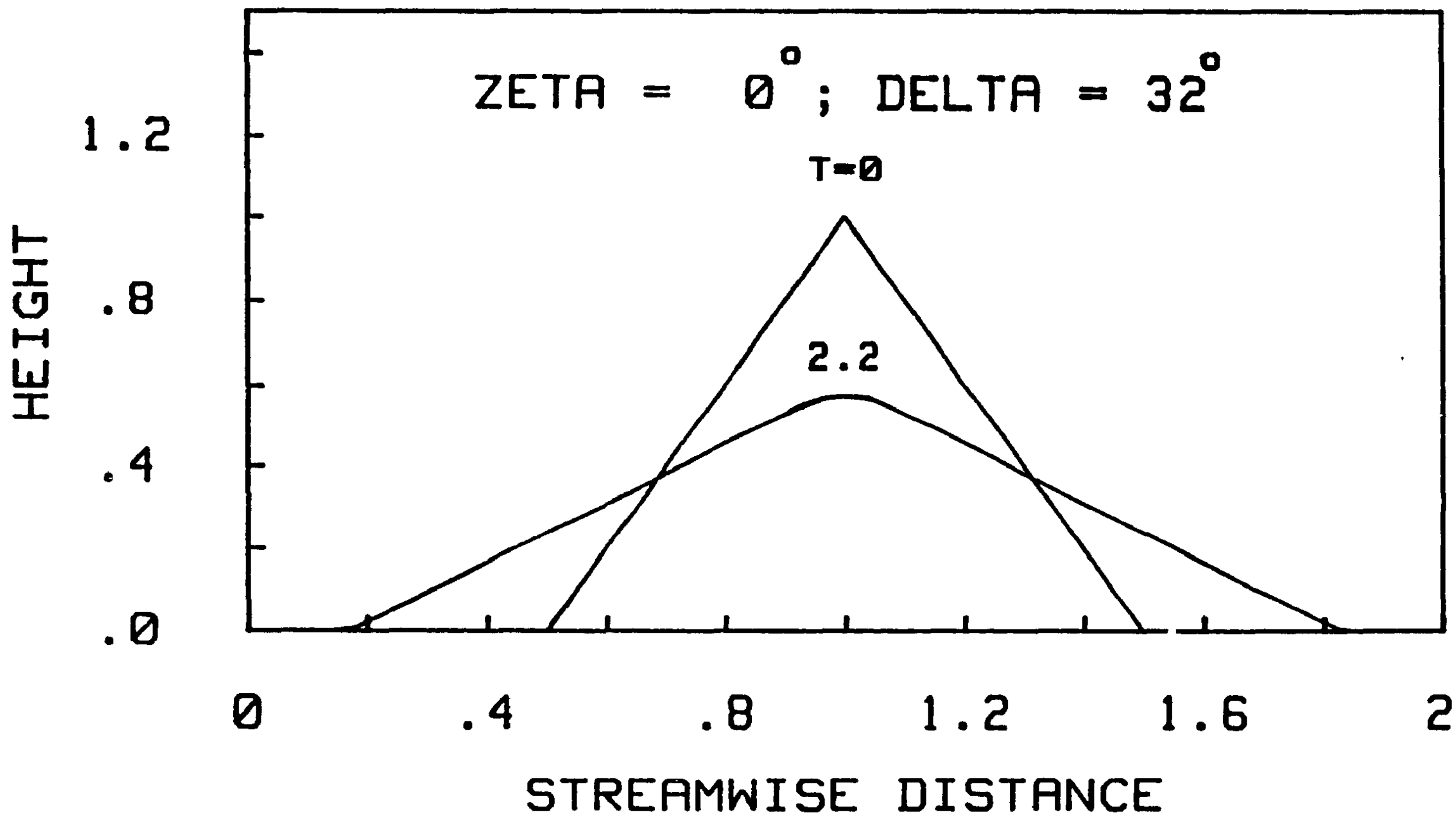

Fig. 3.4 Non-dimensional height versus non-dimensional traveling distance of the initial and final non-dimensional times

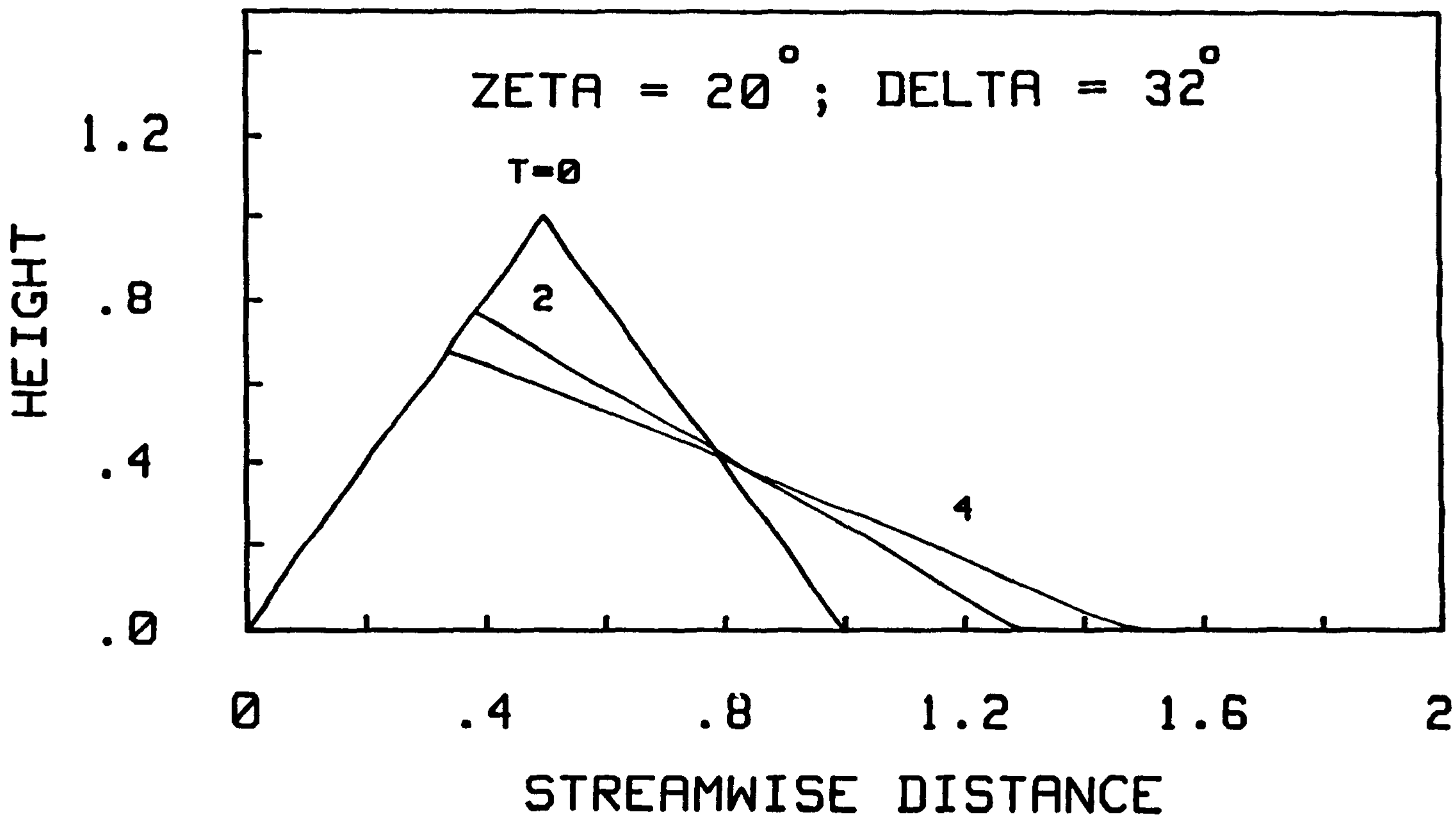

Fig.3.5 Non-dimensional height versus non-dimensional traveling distance at different non-dimensional times

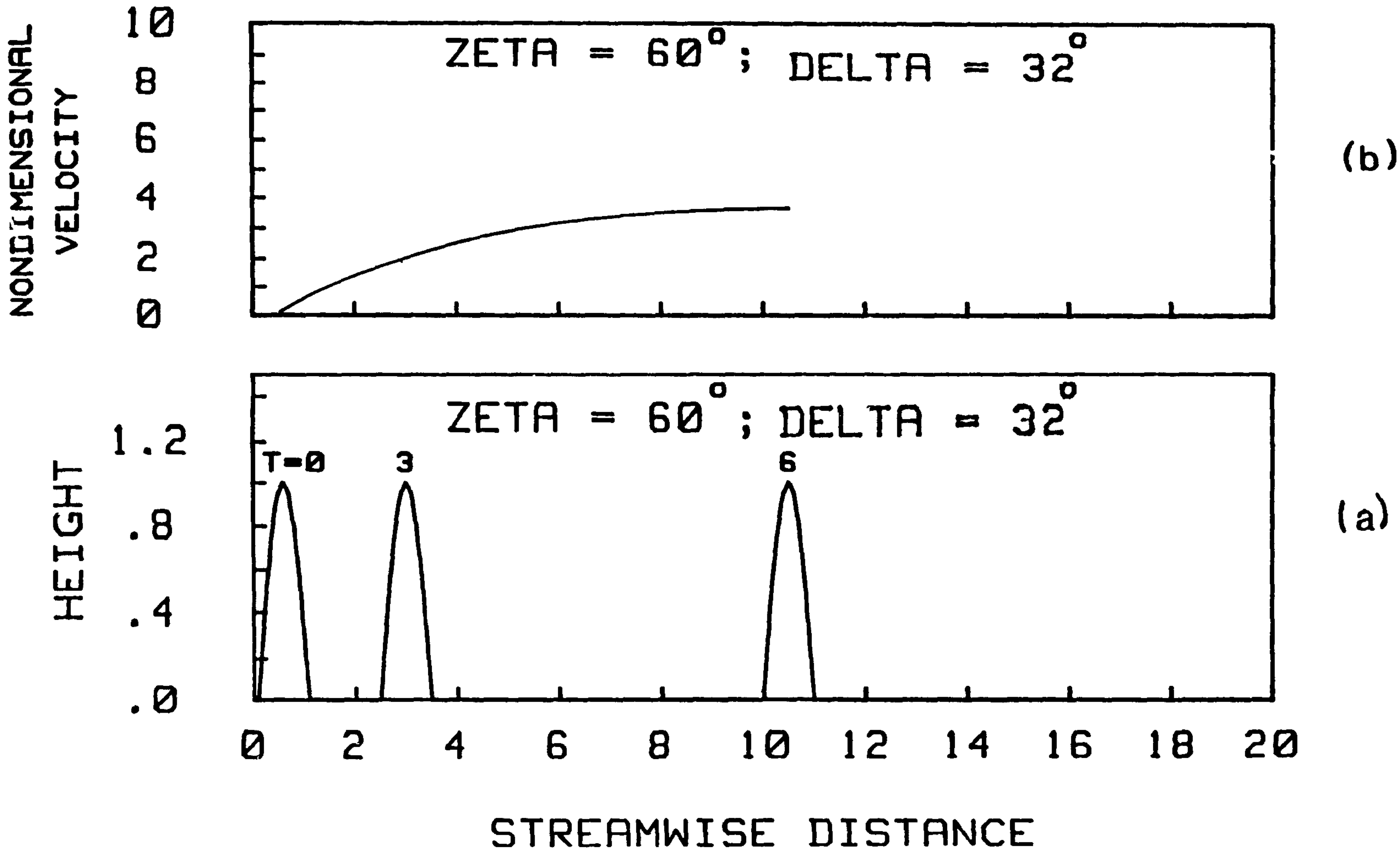

Fig. 3.6 Non-dimensional shape (a) and non-dimensional velocity (b) versus non-dimensional traveling distance at different non-dimensional times

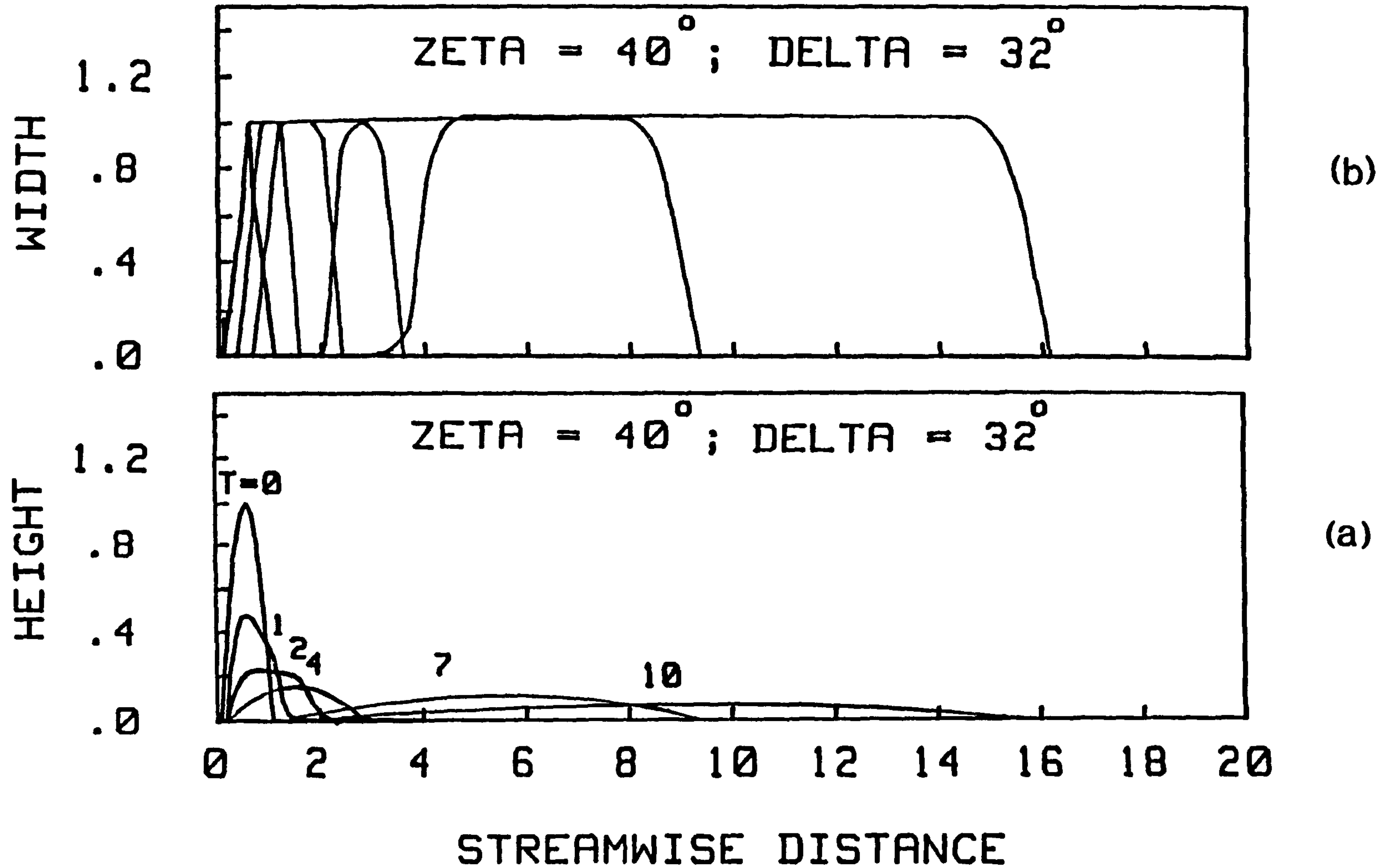

Fig. 3.7 Non-dimensional height (a) and non-dimensional half (b) width versus non-dimensional traveling distance at different non-dimensional times

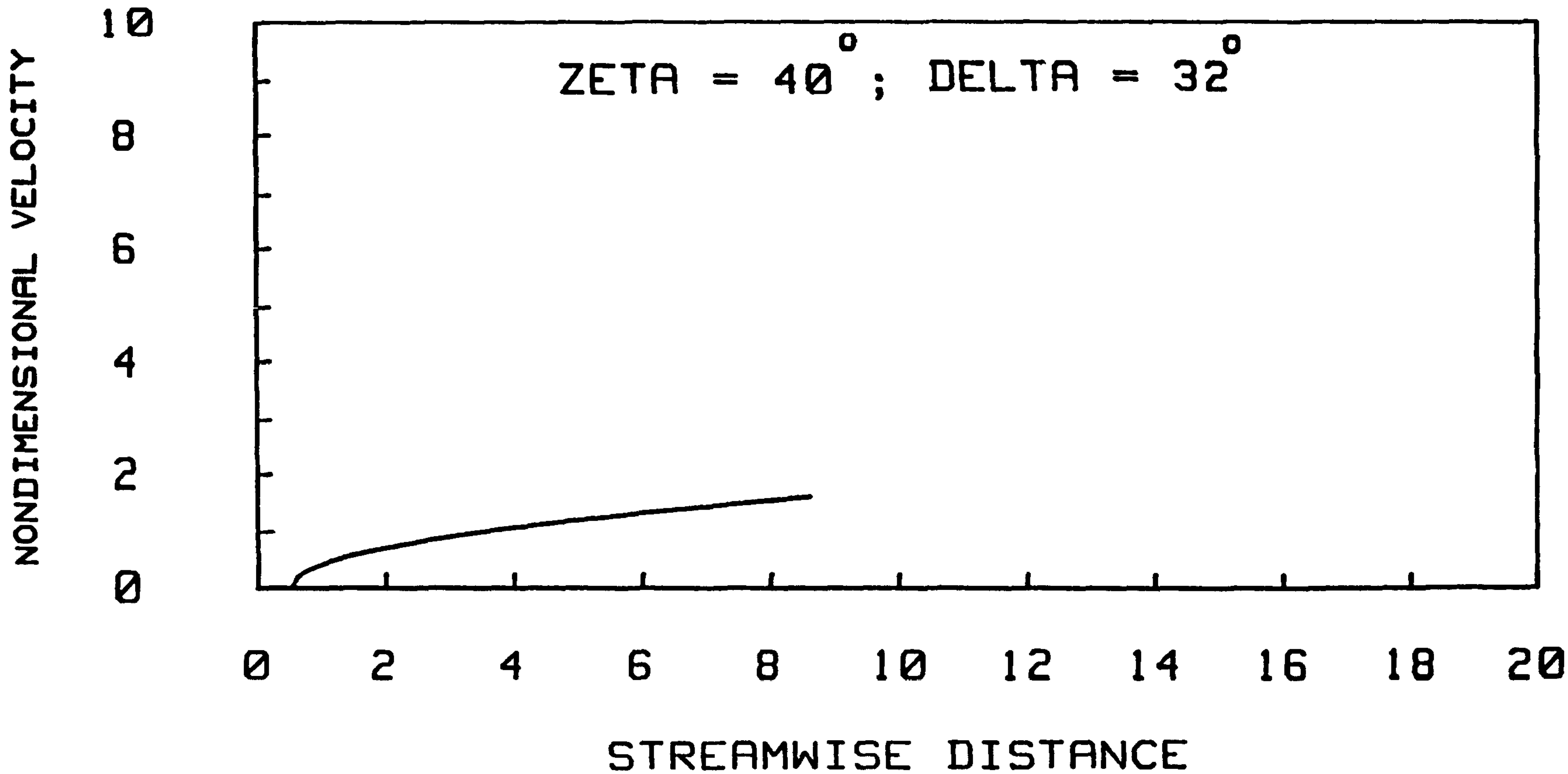

Fig. 3.8 Non-dimensional center of mass velocity versus non-dimensional traveling distance

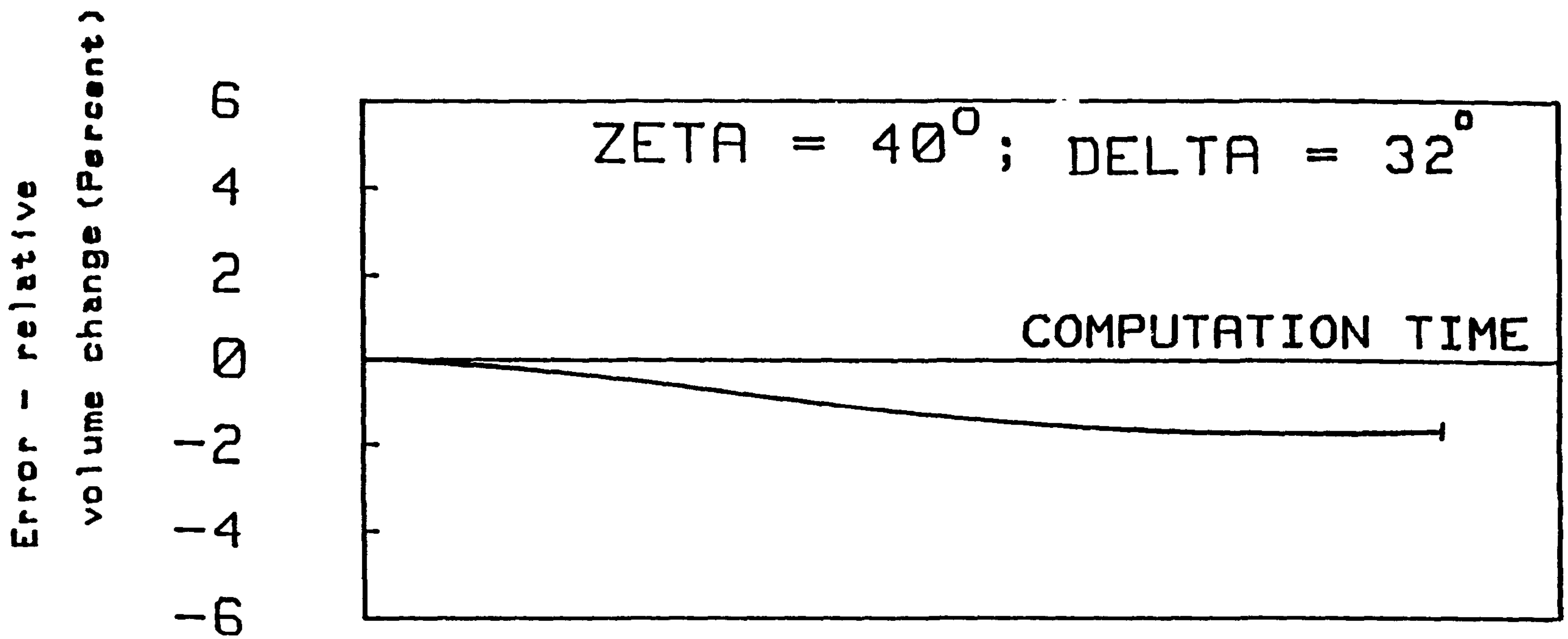

Fig. 3.9 Error expressed in terms of relative volume change versus computation time

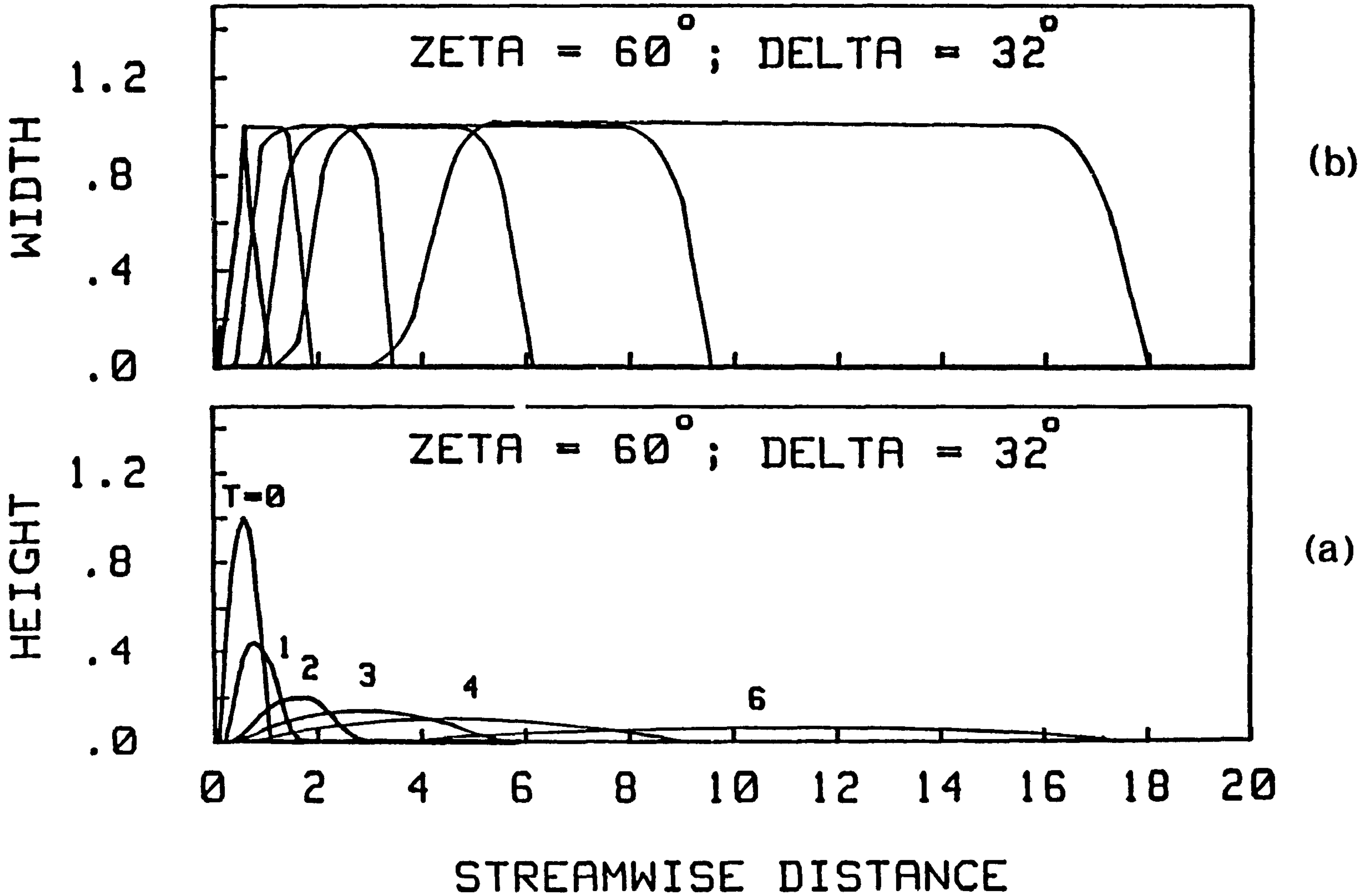

Fig. 3.10 Non-dimensional height (a) and half width (b) versus non-dimensional traveling distance

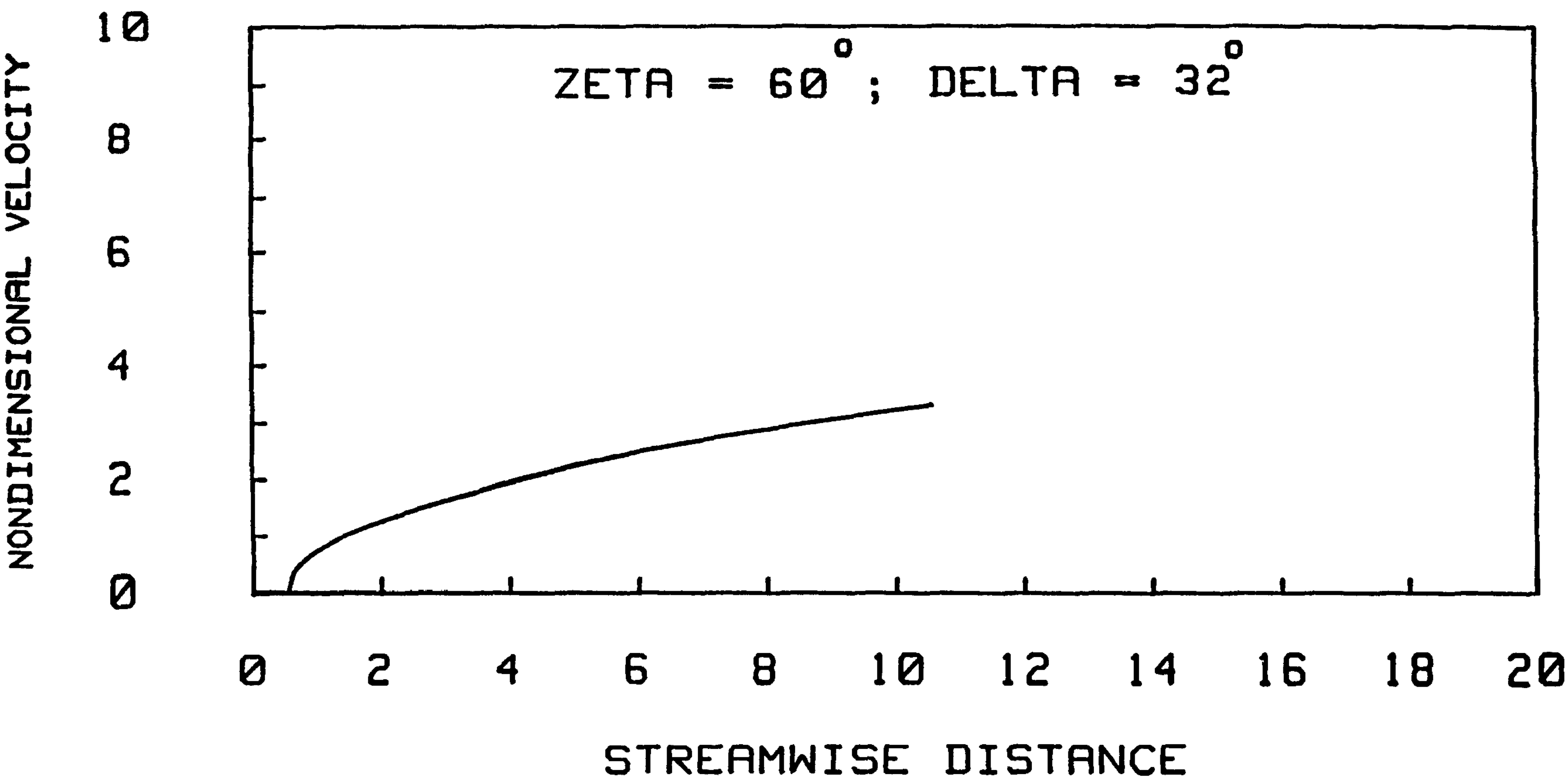

Fig. 3.11 Non-dimensional center of mass velocity versus non-dimensional traveling distance

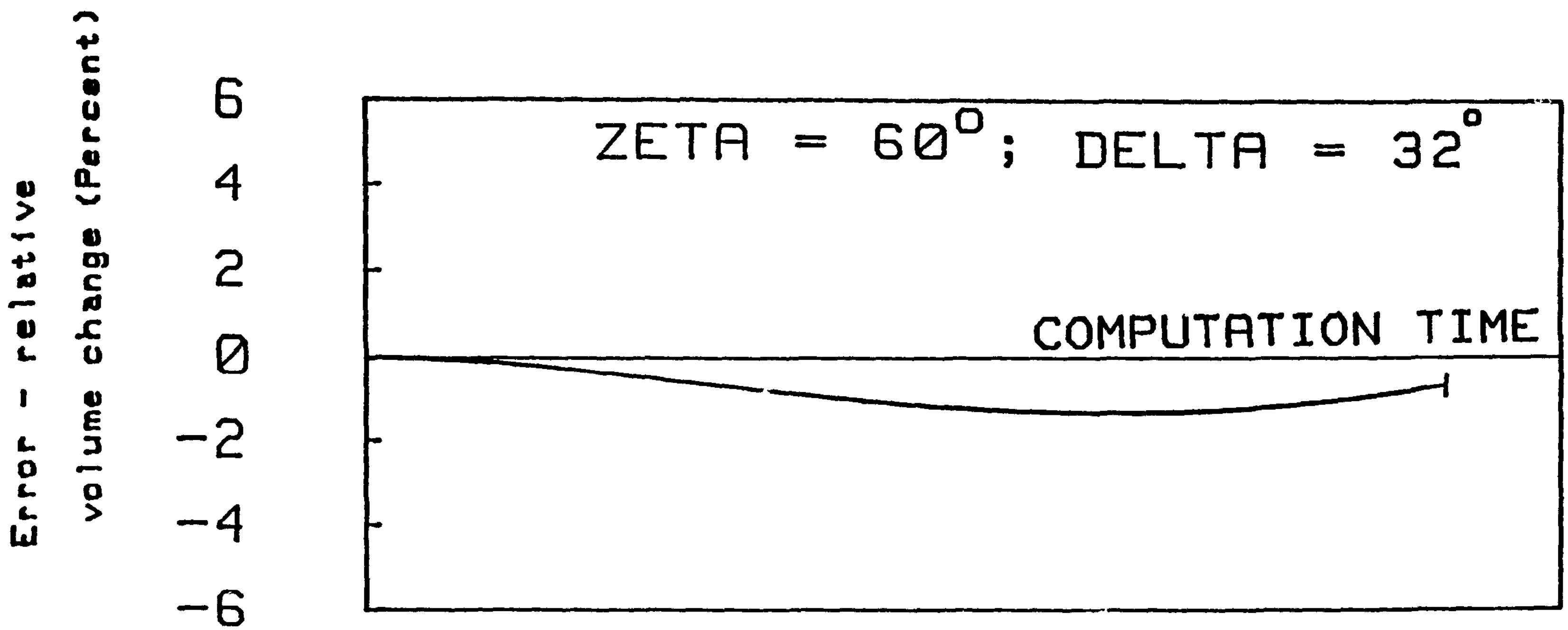

Fig. 3.12 Error expressed in relative volume change versus computation time

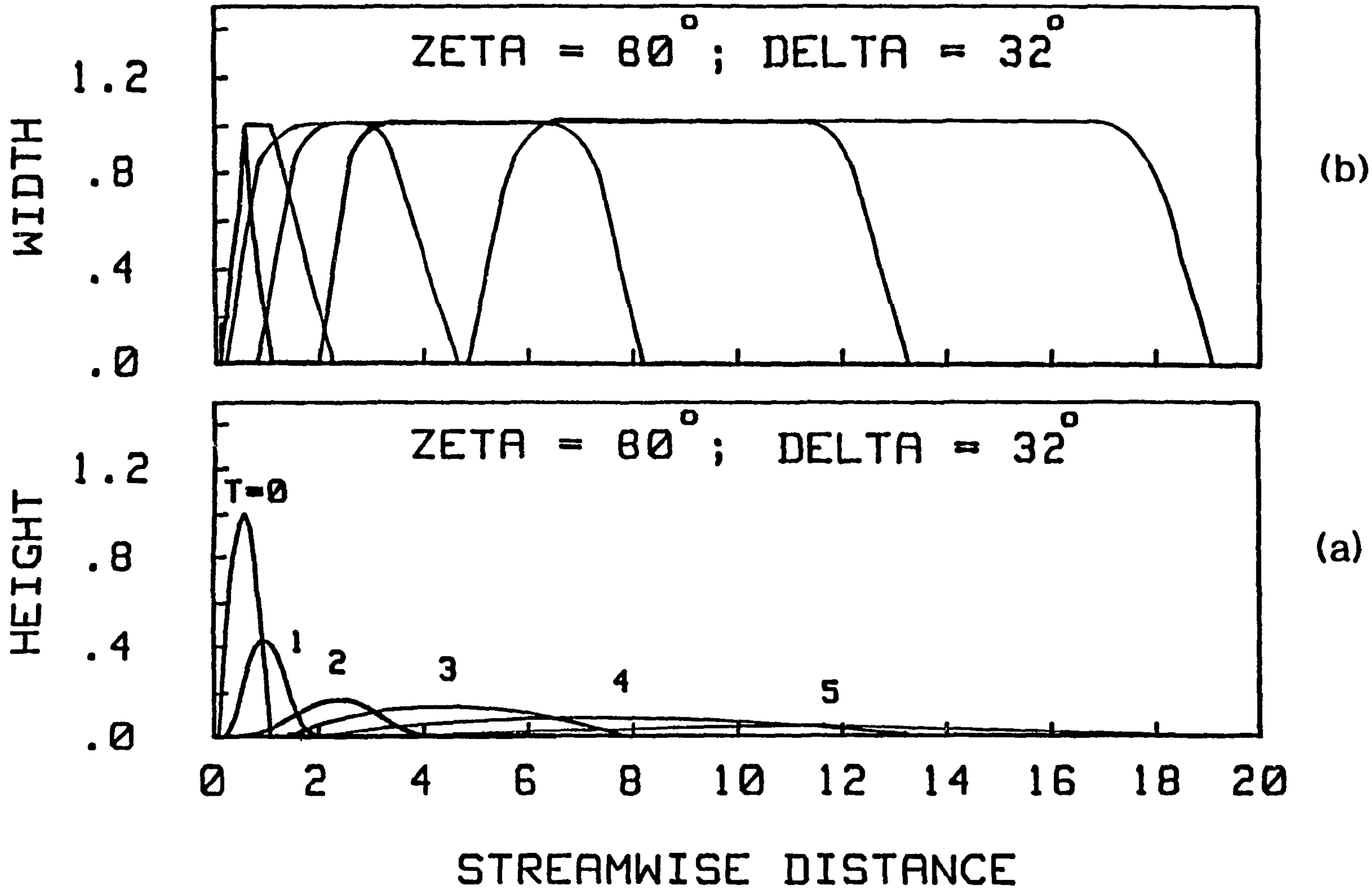

Fig. 3.13 Non-dimensional height (a) and half width (b) versus non-dimensional traveling distance

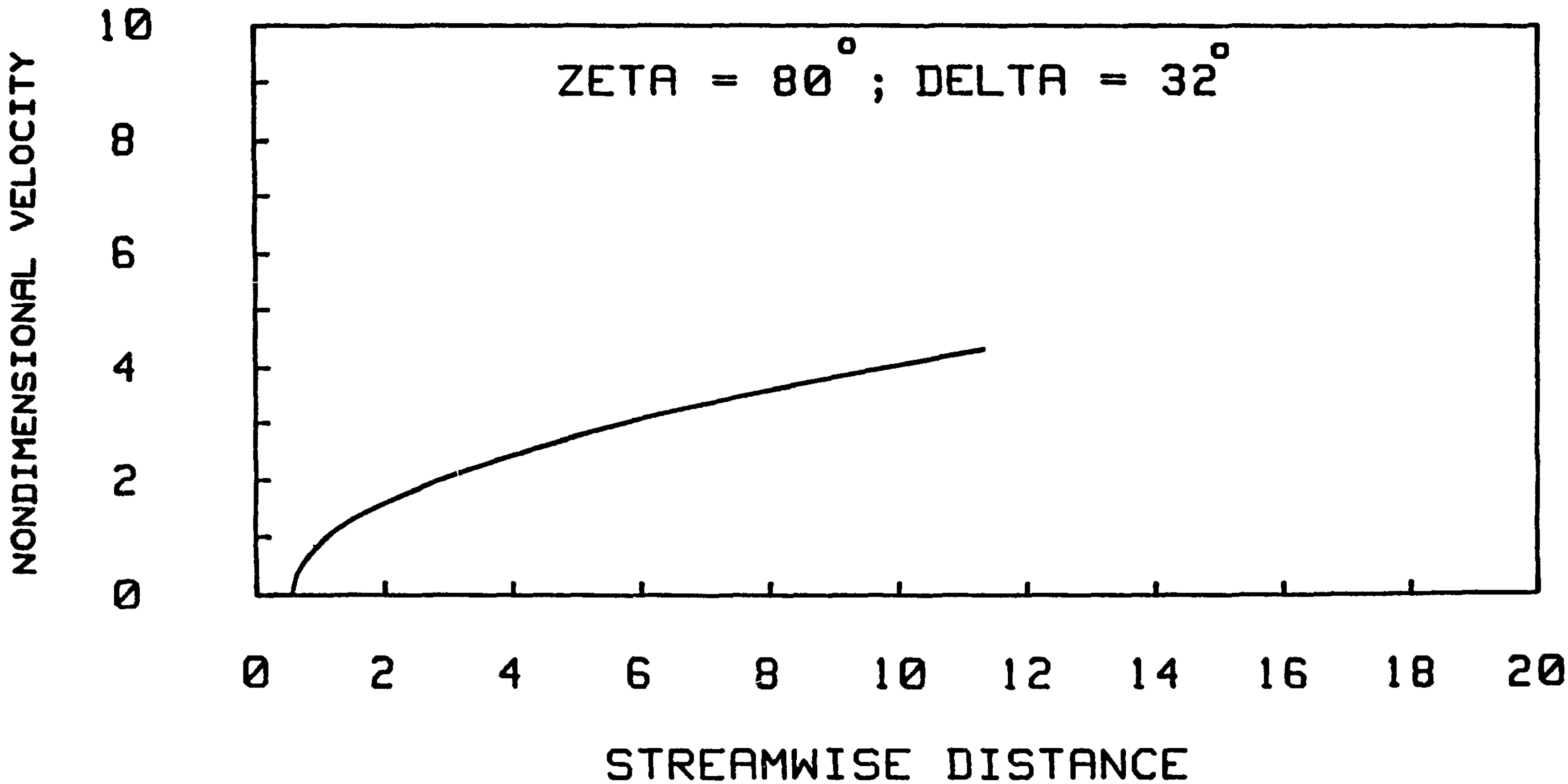

Fig. 3.14 Non-dimensional center of mass velocity versus non-dimensional traveling distance

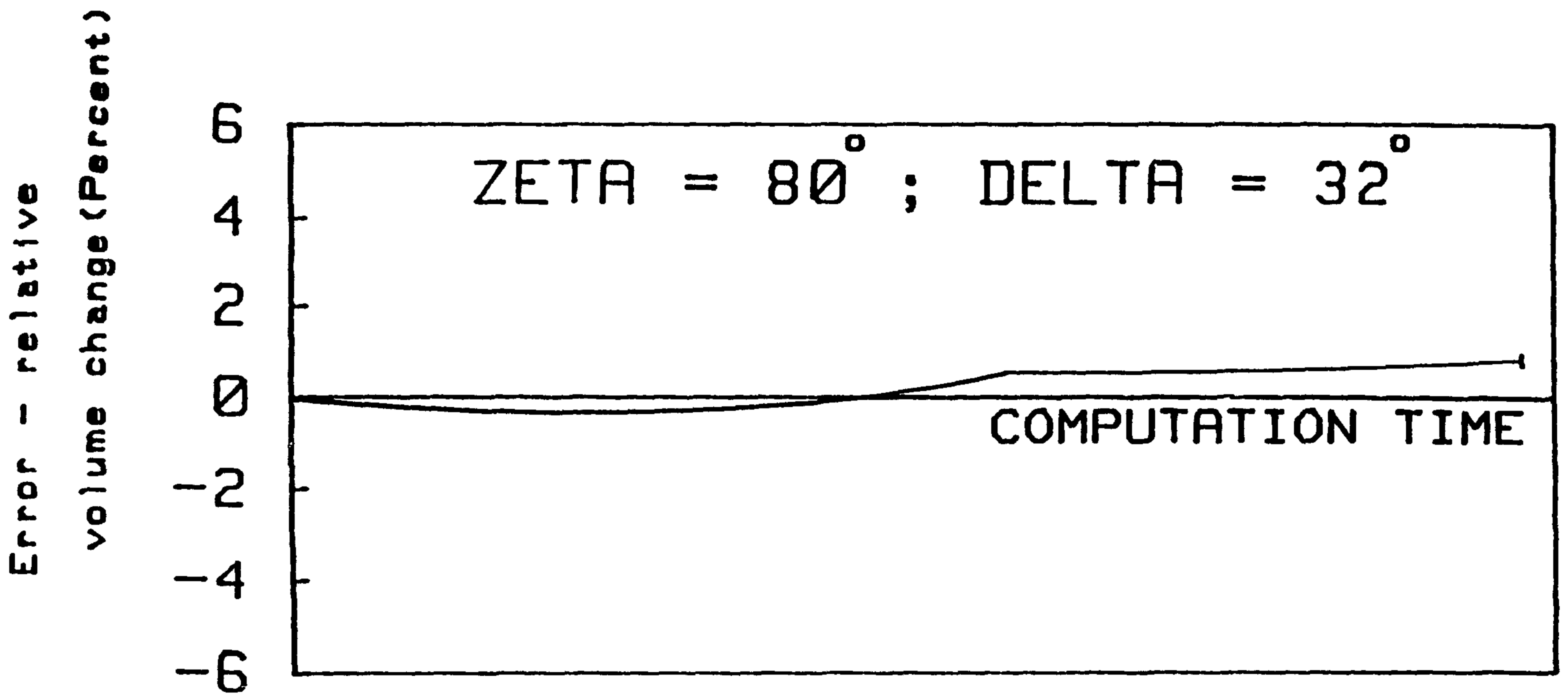

Fig. 3.15 Error expressed in terms of relative volume change versus computation time

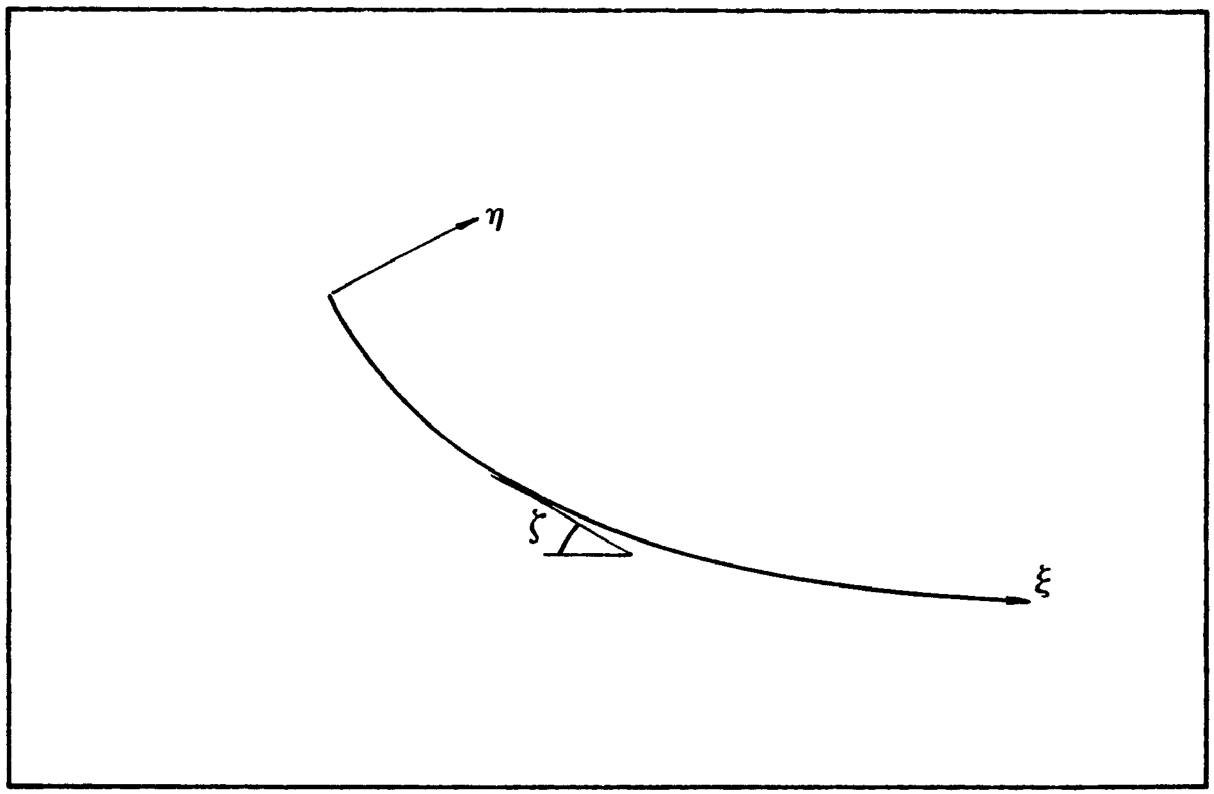

Fig. 4.1 Definition sketch of the curvilinear coordinate system

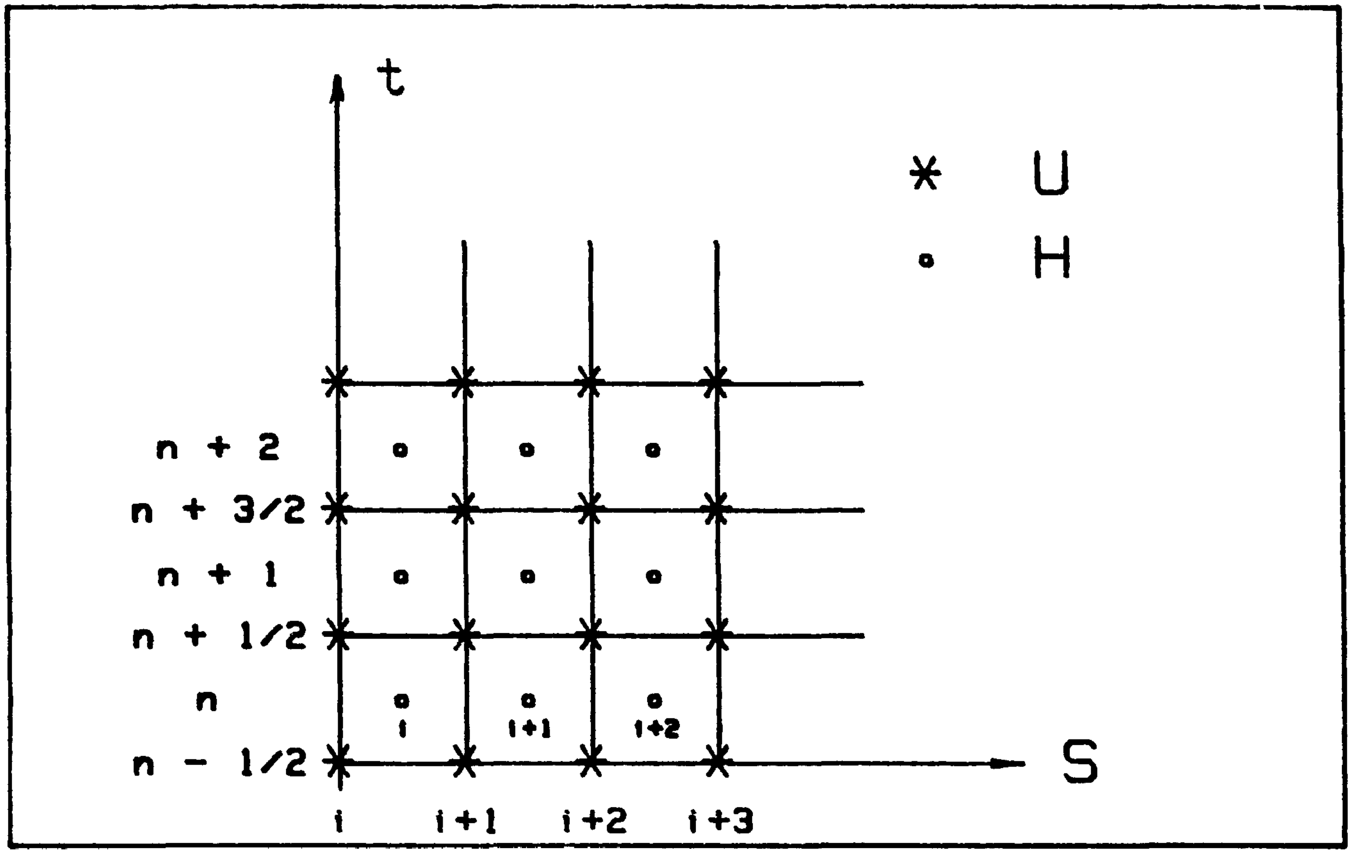

Fig. 4.2 Sketch of the staggered grid scheme

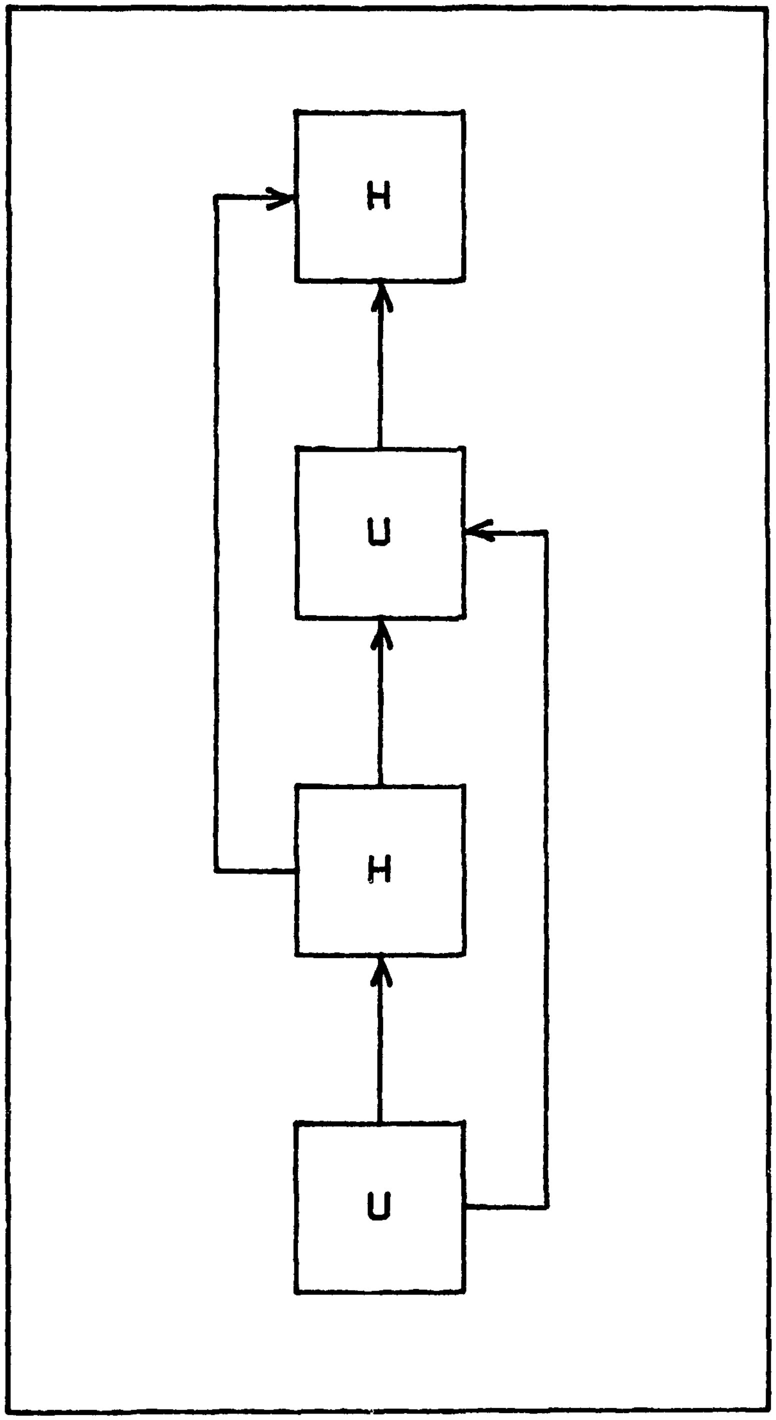

Fig. 4.3 Flowchart of the computation procedure

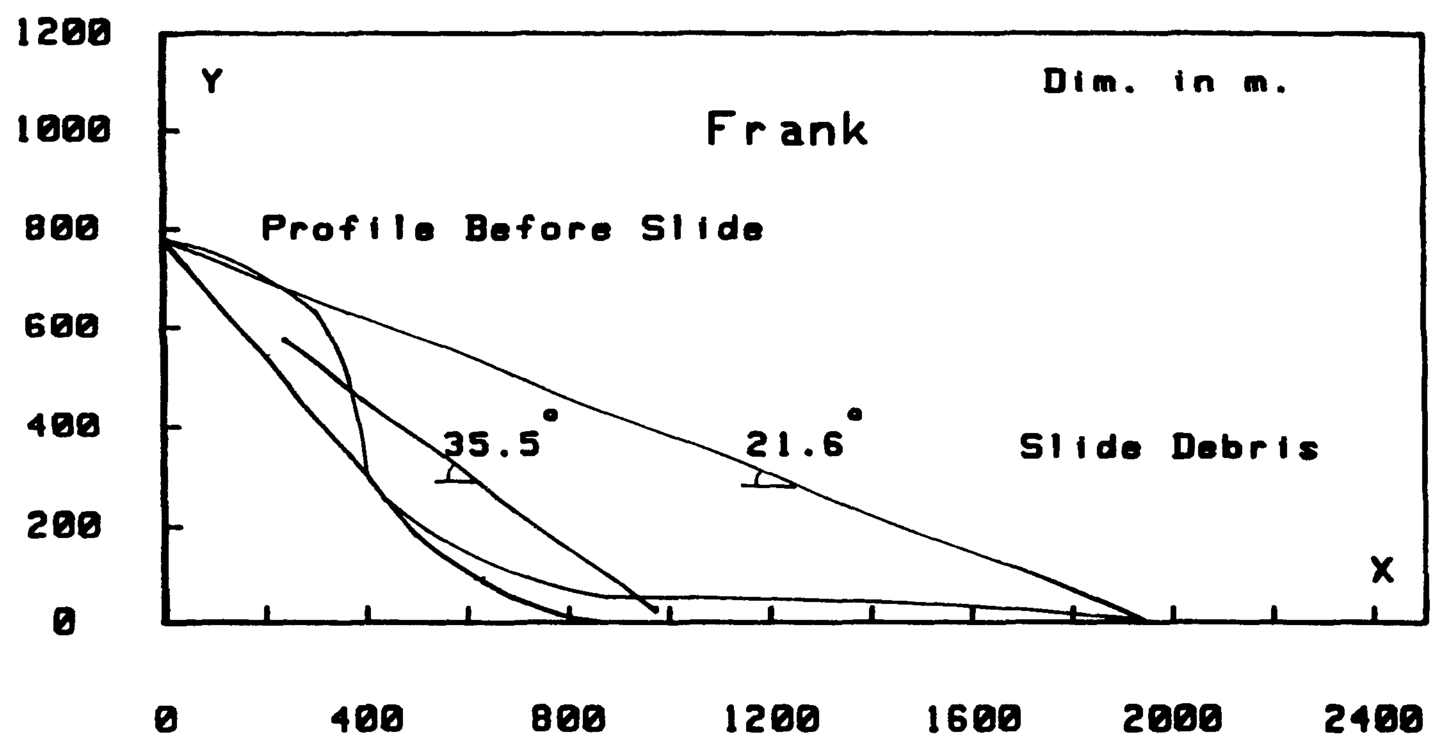

Fig. 4.4 Initial and final shapes and positions of the slide debris

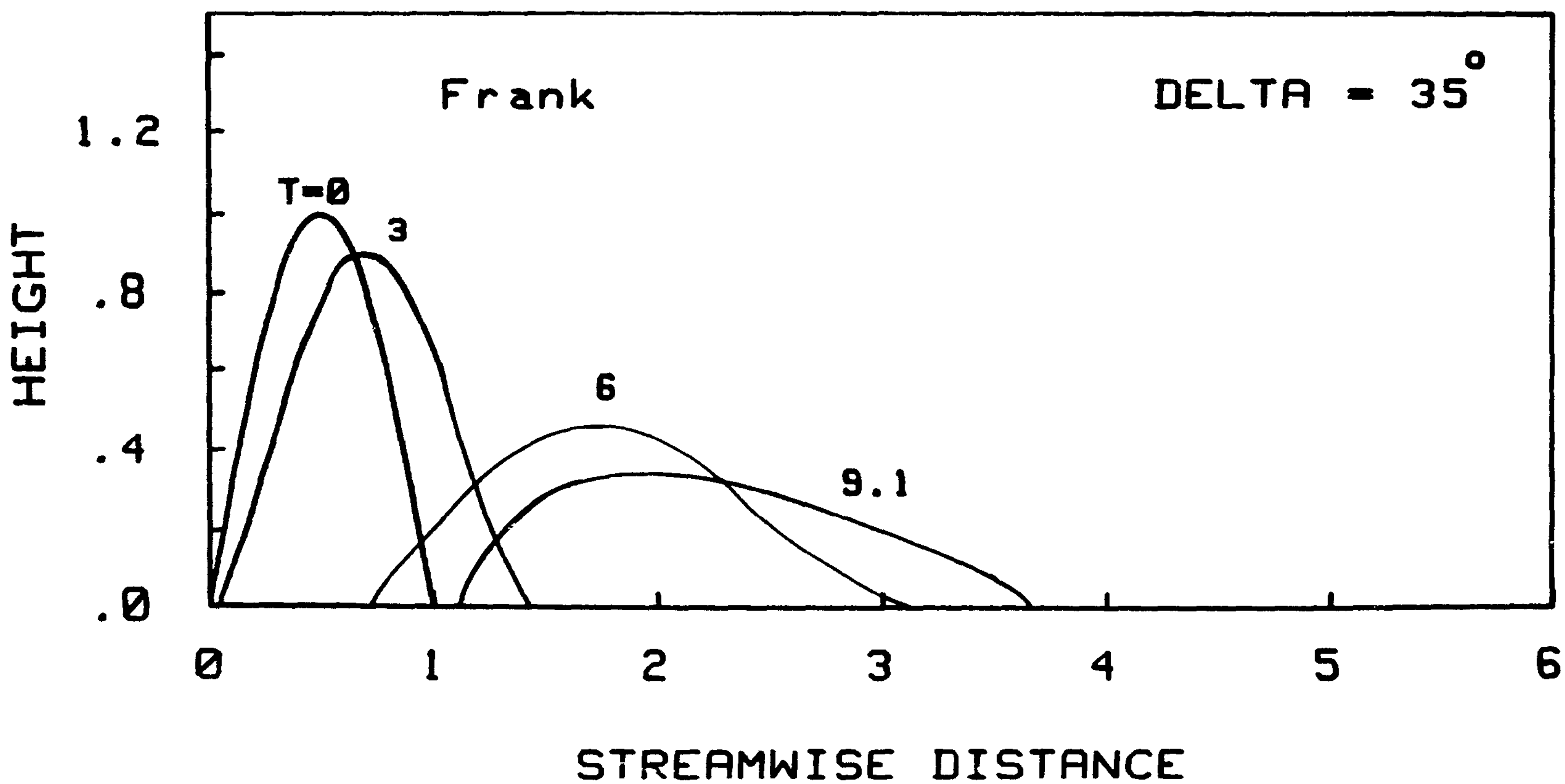

Fig. 4.5 Non-dimensional height of the rock mass versus non-dimensional traveling distance along the path of the slide at different non-dimensional times

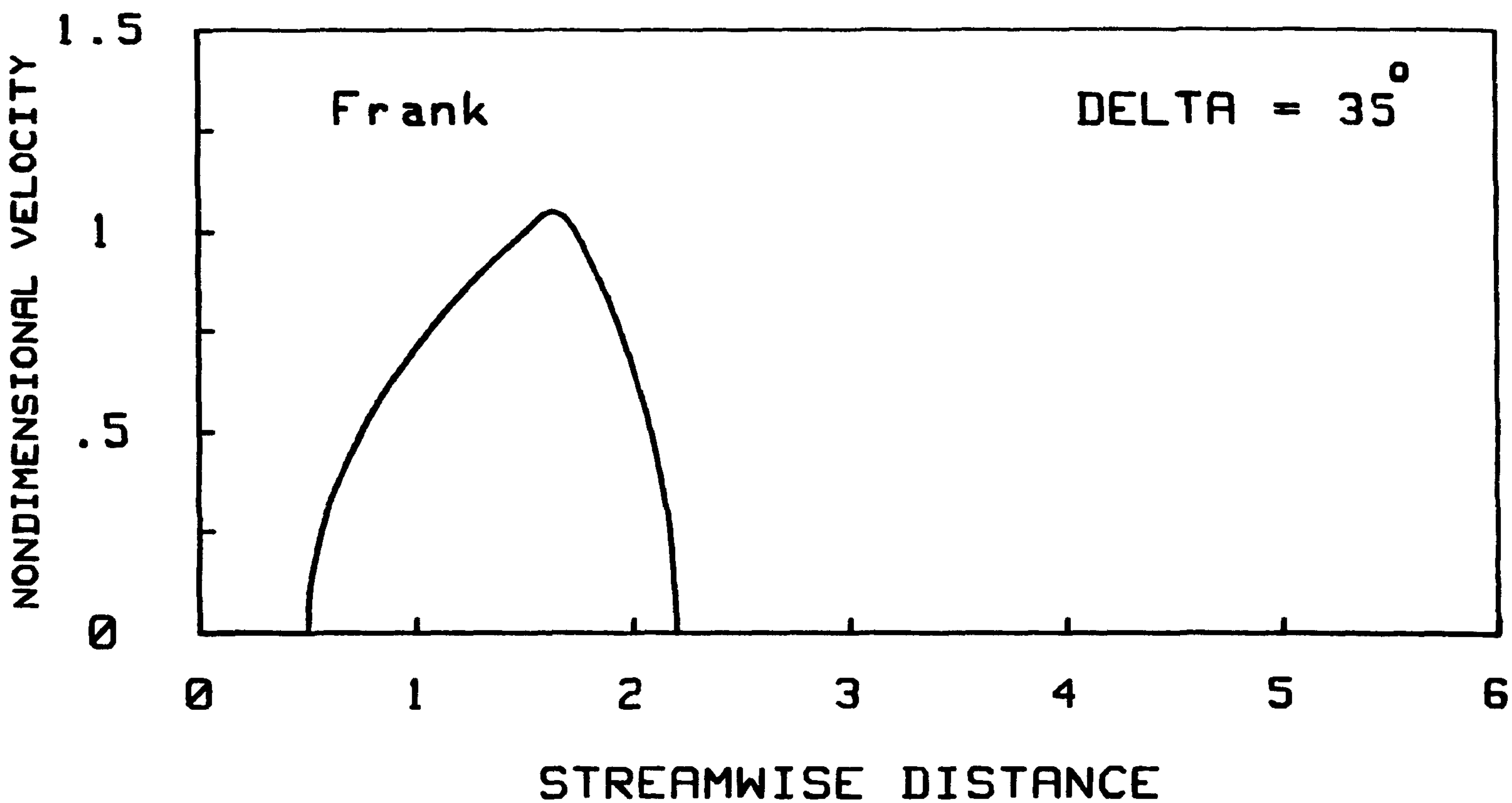

Fig. 4.6 Non-dimensional center-of-mass velocity versus non-dimensional traveling distance along the slide path

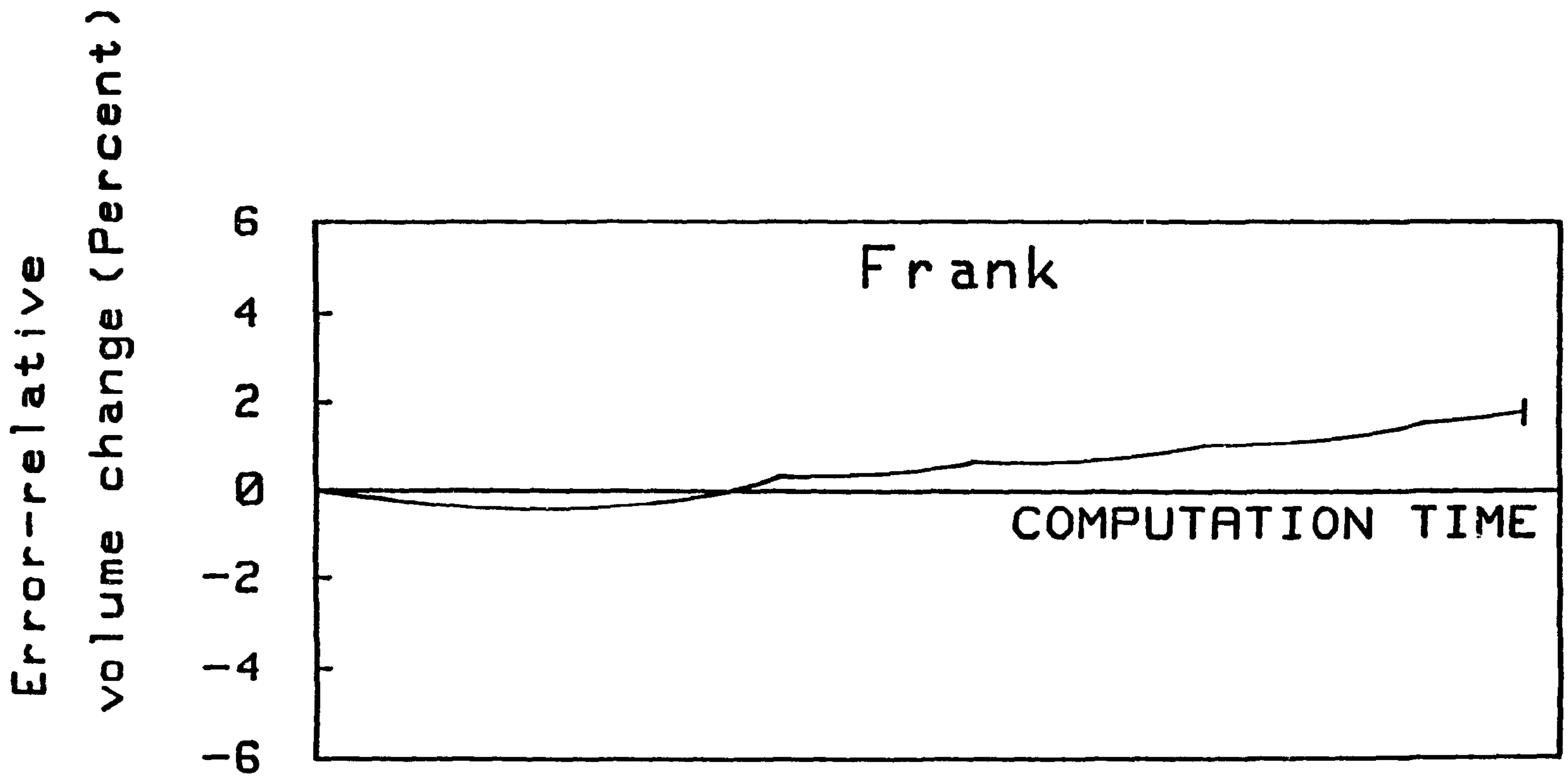

Fig. 4.7 Error expressed in terms of relative volume change versus computation time

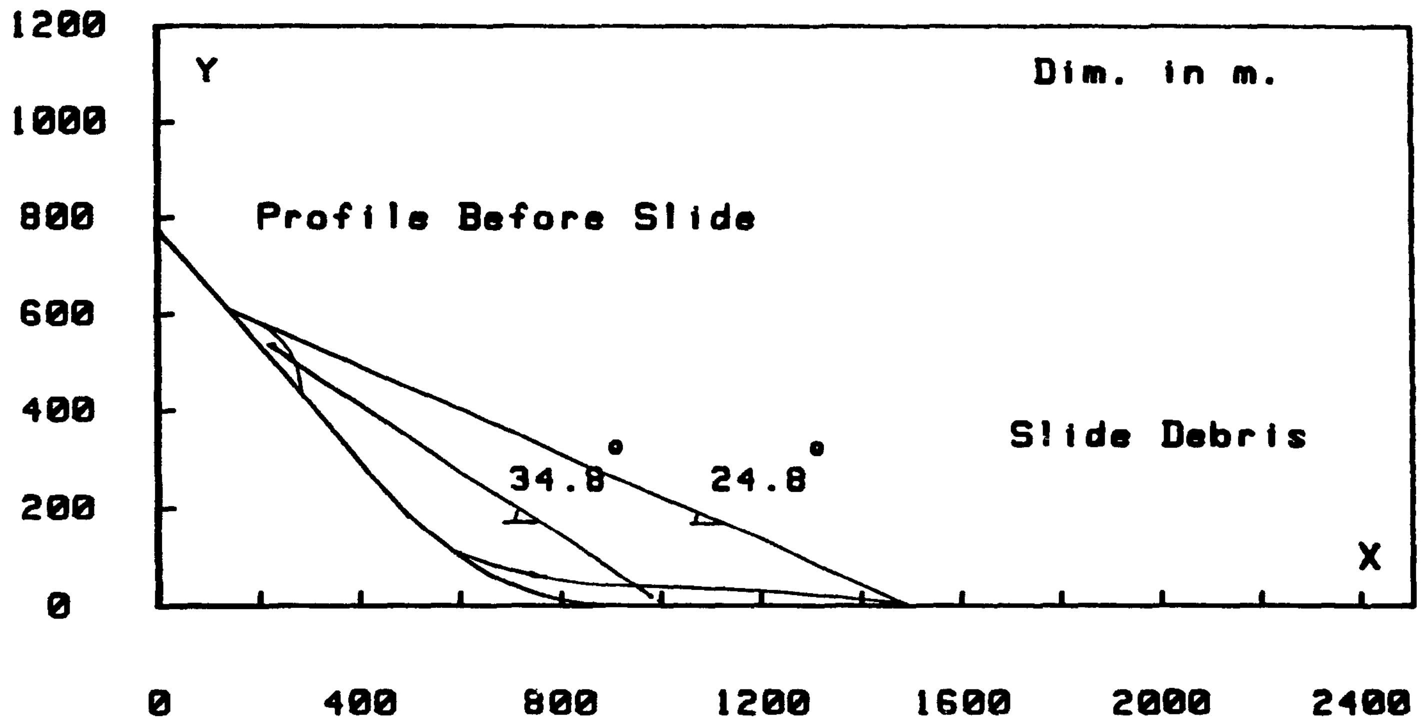

Fig. 4.8 Initial and final shapes of a rockslide having a volume of 10 % of Frank slide

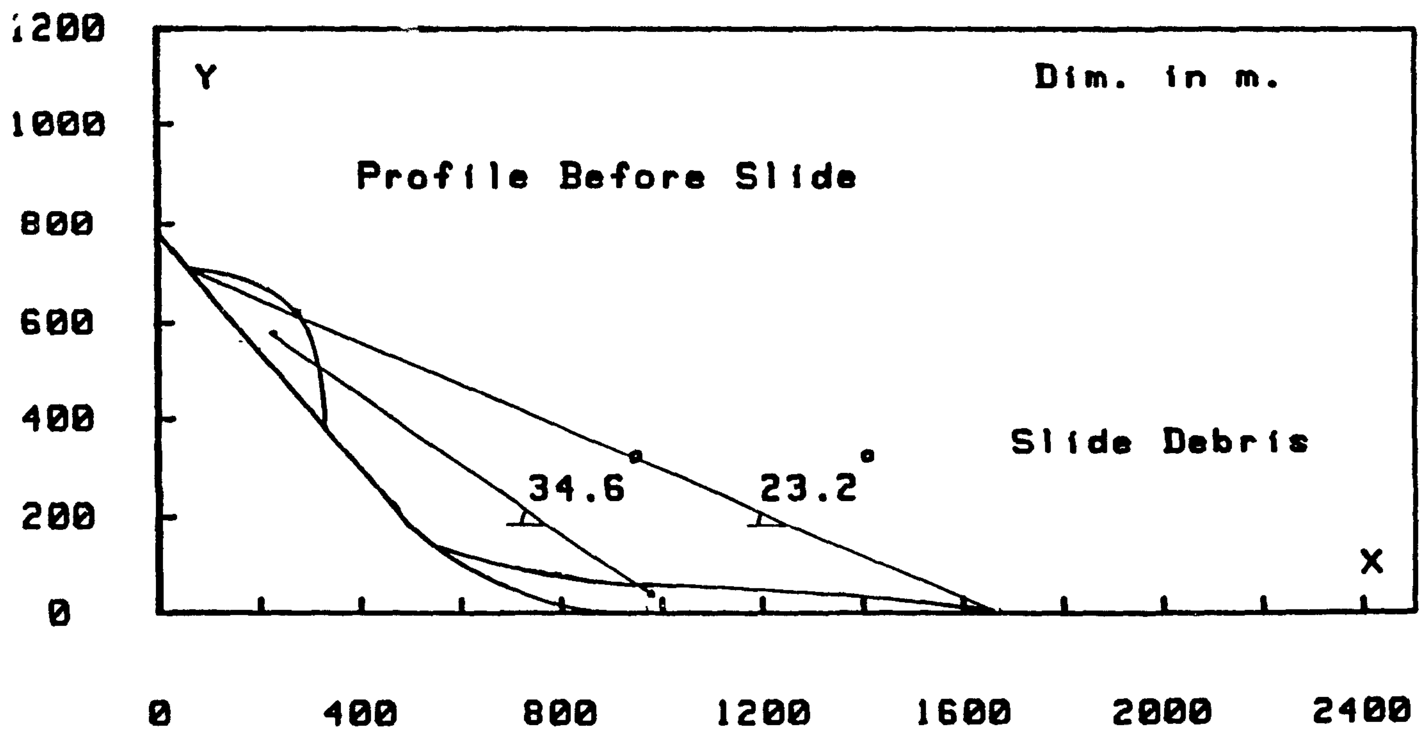

Fig. 4.9 Initial and final shapes of a rockslide having a volume of 50 % of Frank slide

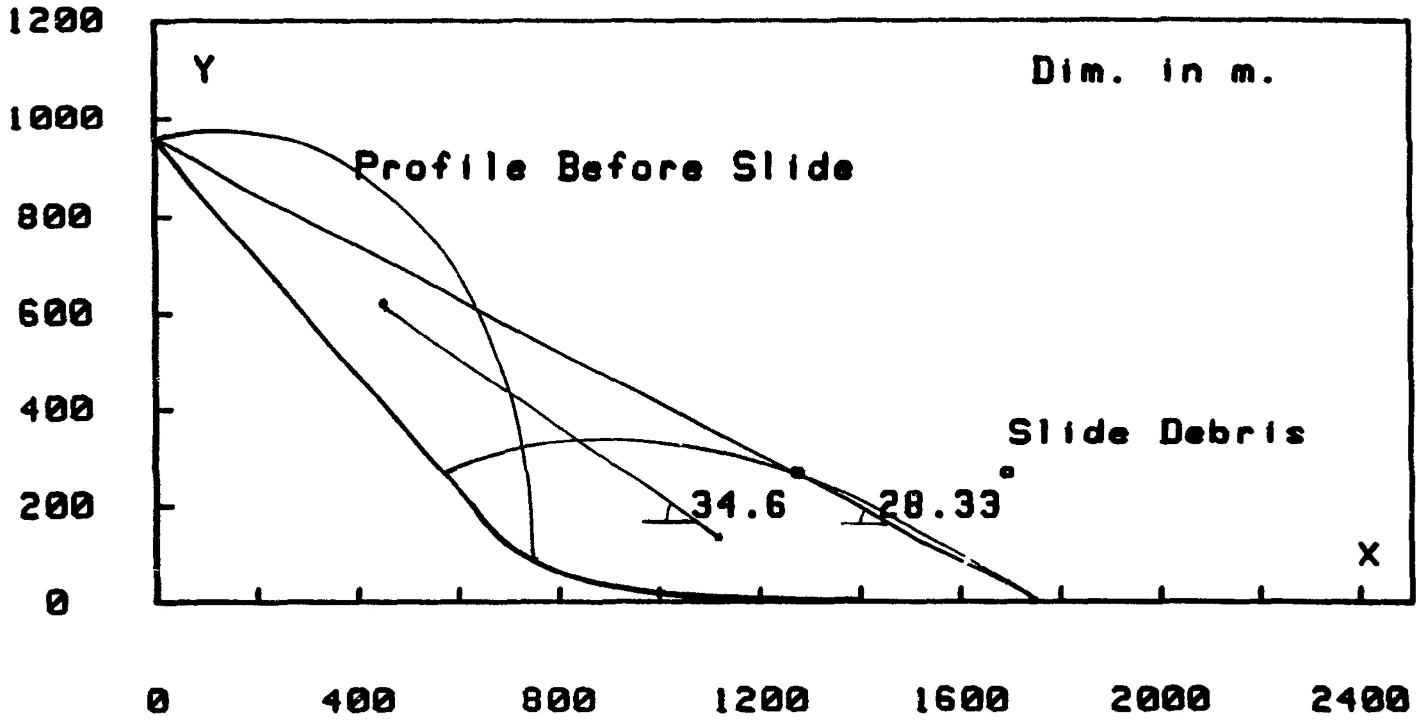

Fig. 4.10 Initial and final shapes of a rockslide having a volume of 350 % of Frank slide

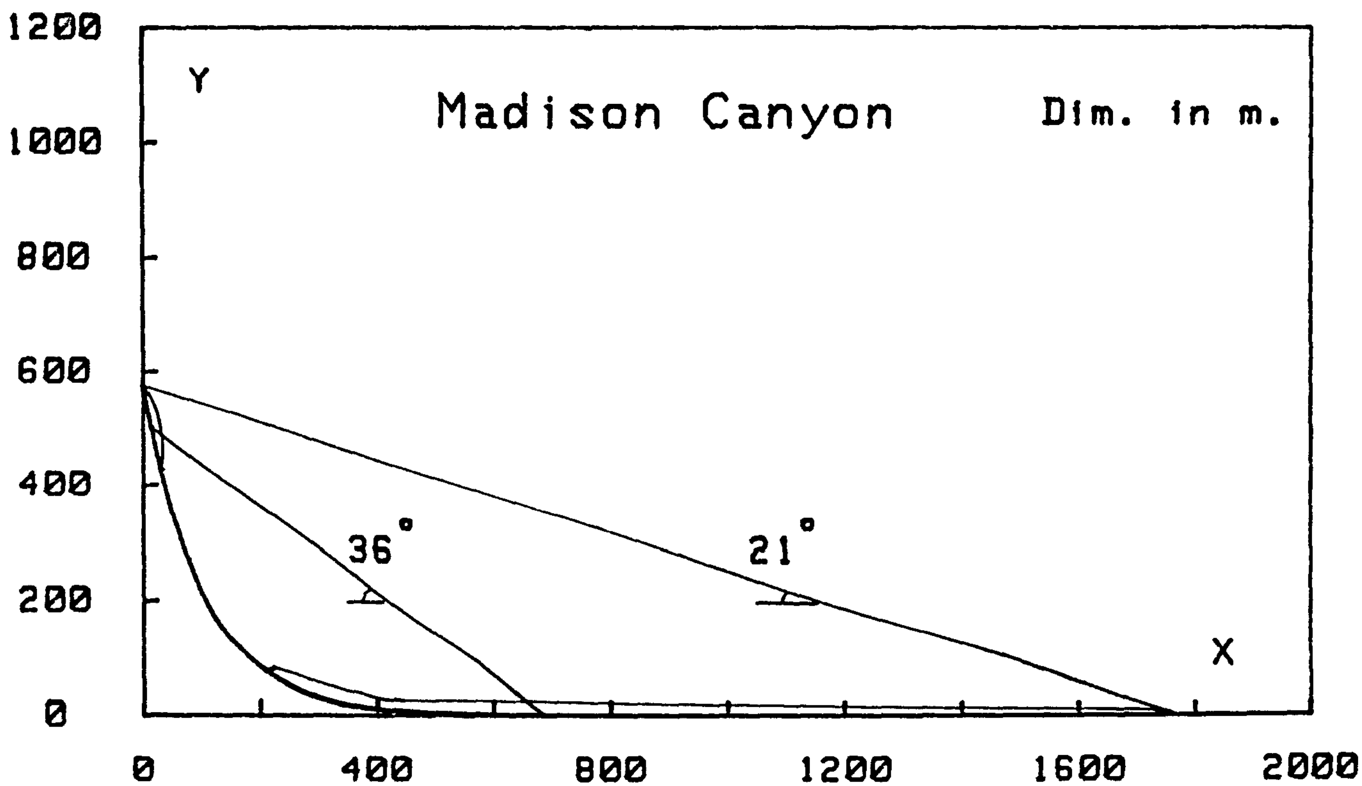

Fig. 4.11 Initial and final shapes and positions of the rock mass. Thickness of the debris in final state is distorted to indicate profile of rock mass

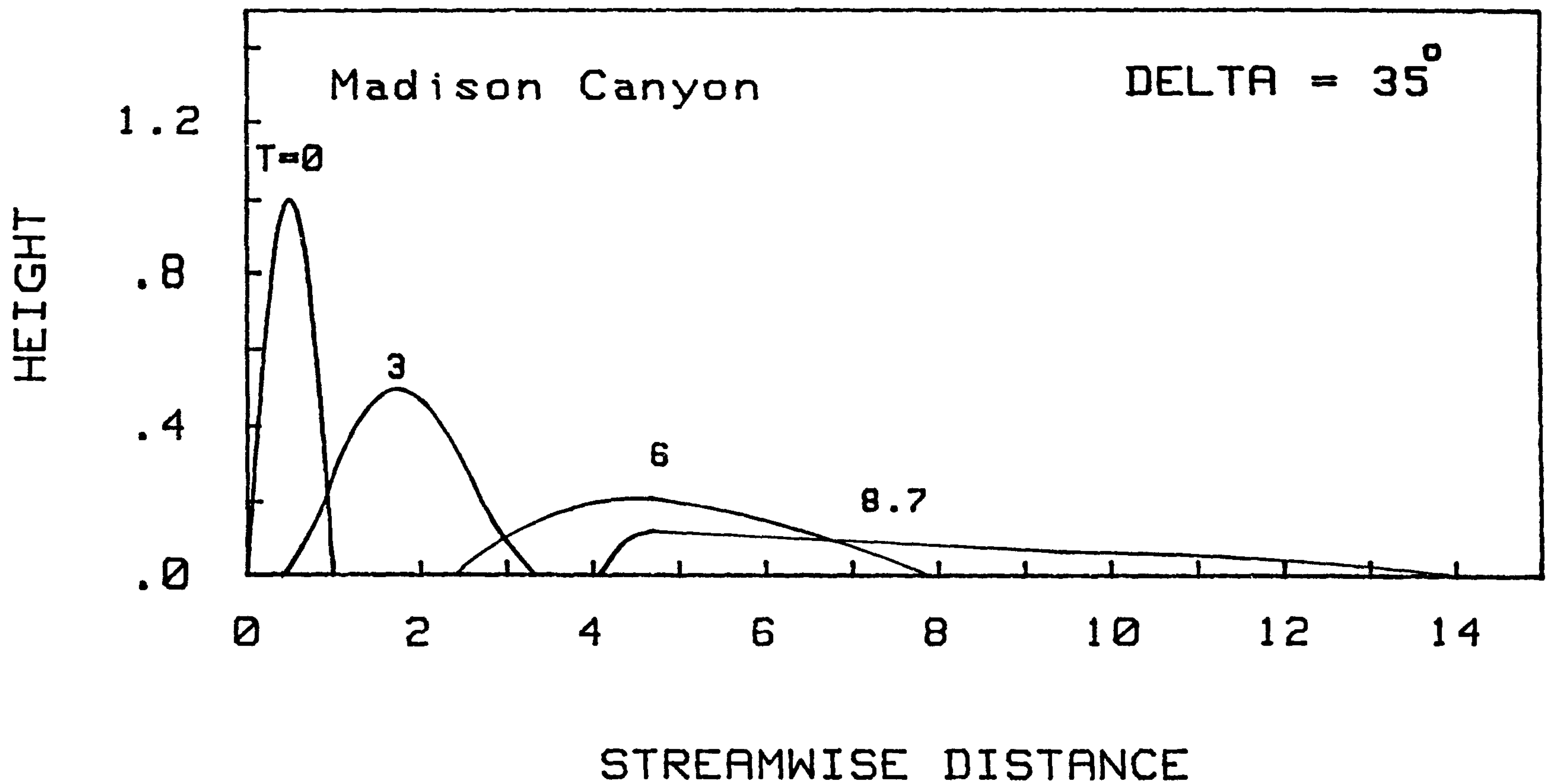

Fig. 4.12 Non-dimensional shape of the rock mass versus the non-dimensional traveling distance along the slide path at different non-dimensional times

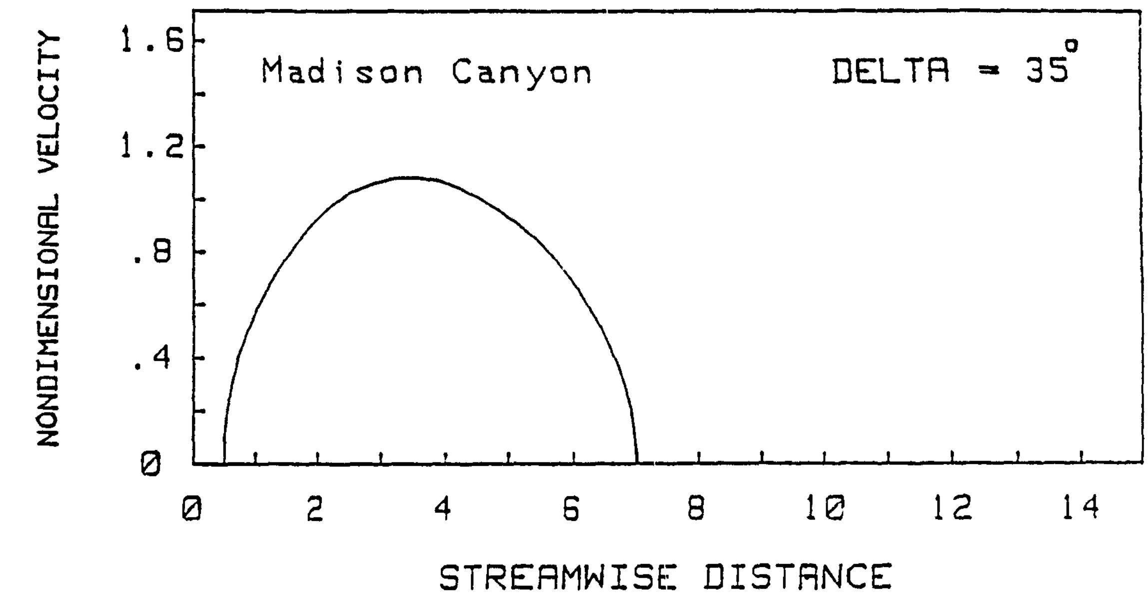

Fig. 4.13 Non-dimensional center-of-mass velocity versus non-dimensional traveling distance

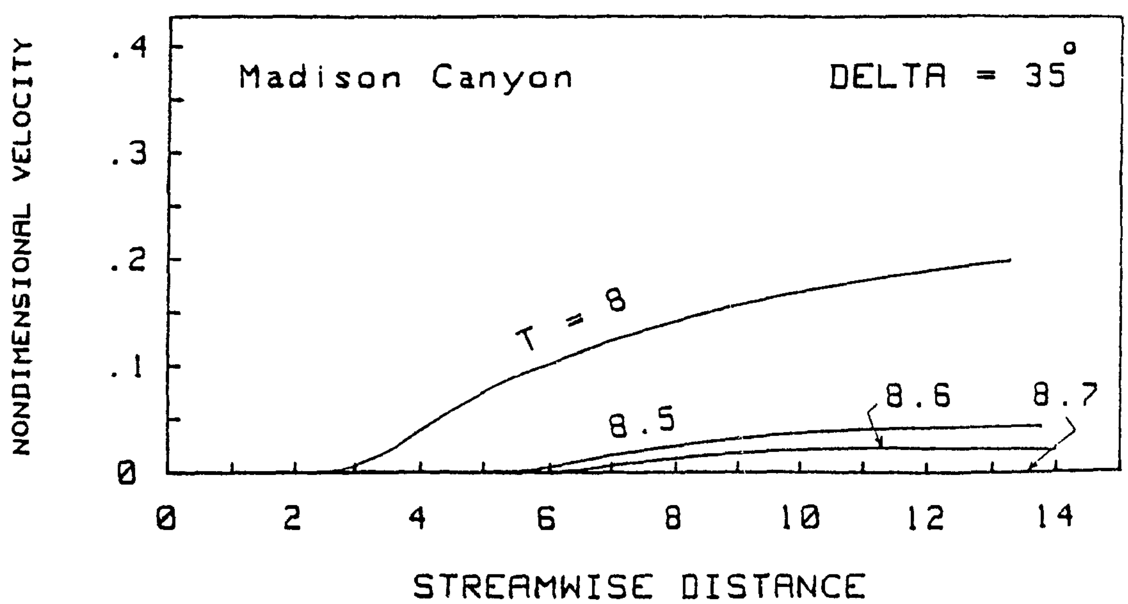

Fig. 4.13a Non-dimensional longitudinal velocity profile vesus non-dimensional traveling distance at different non-dimensional times

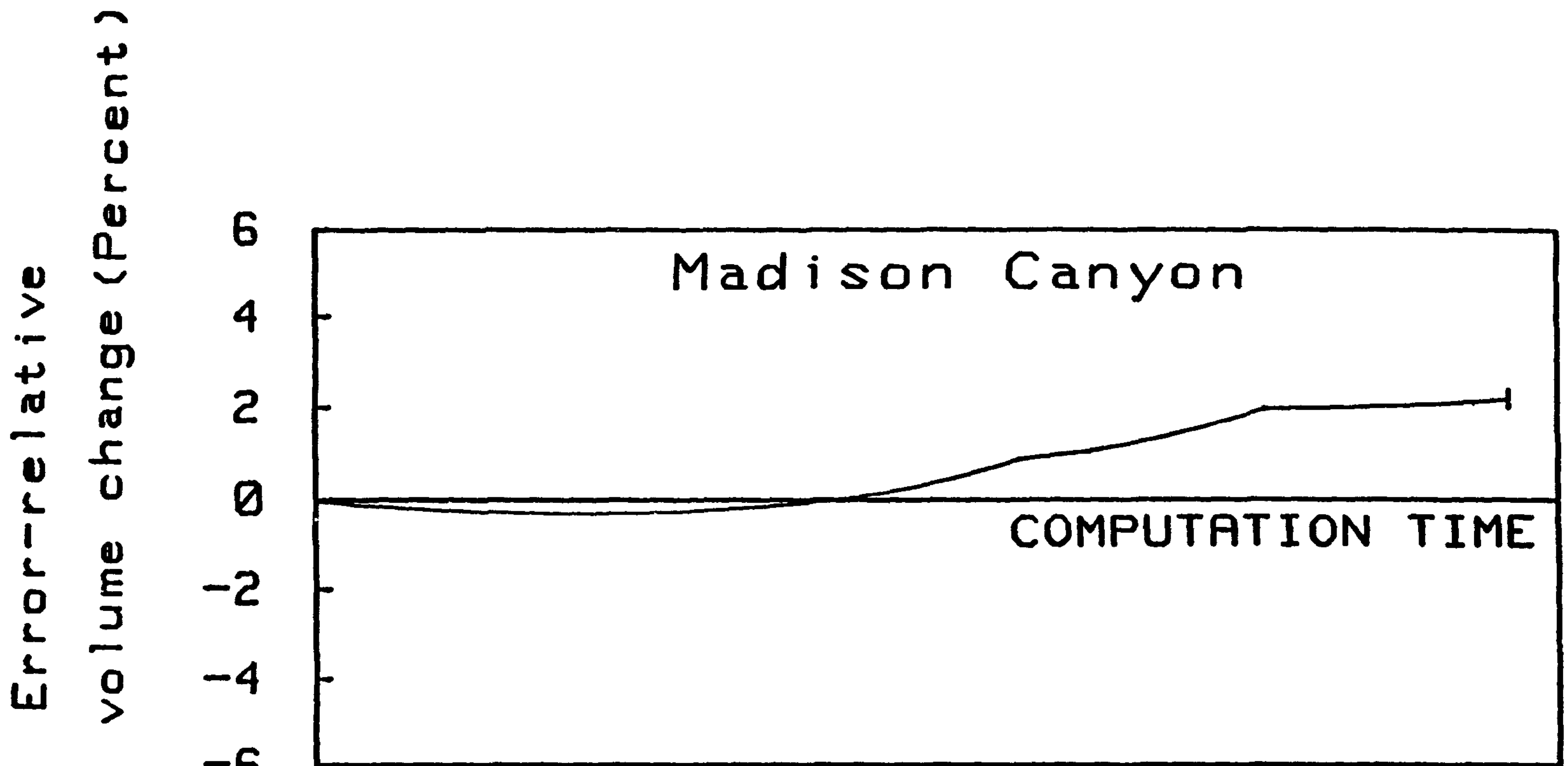

Fig. 4.14 Error expressed in terms of volume change versus computation time

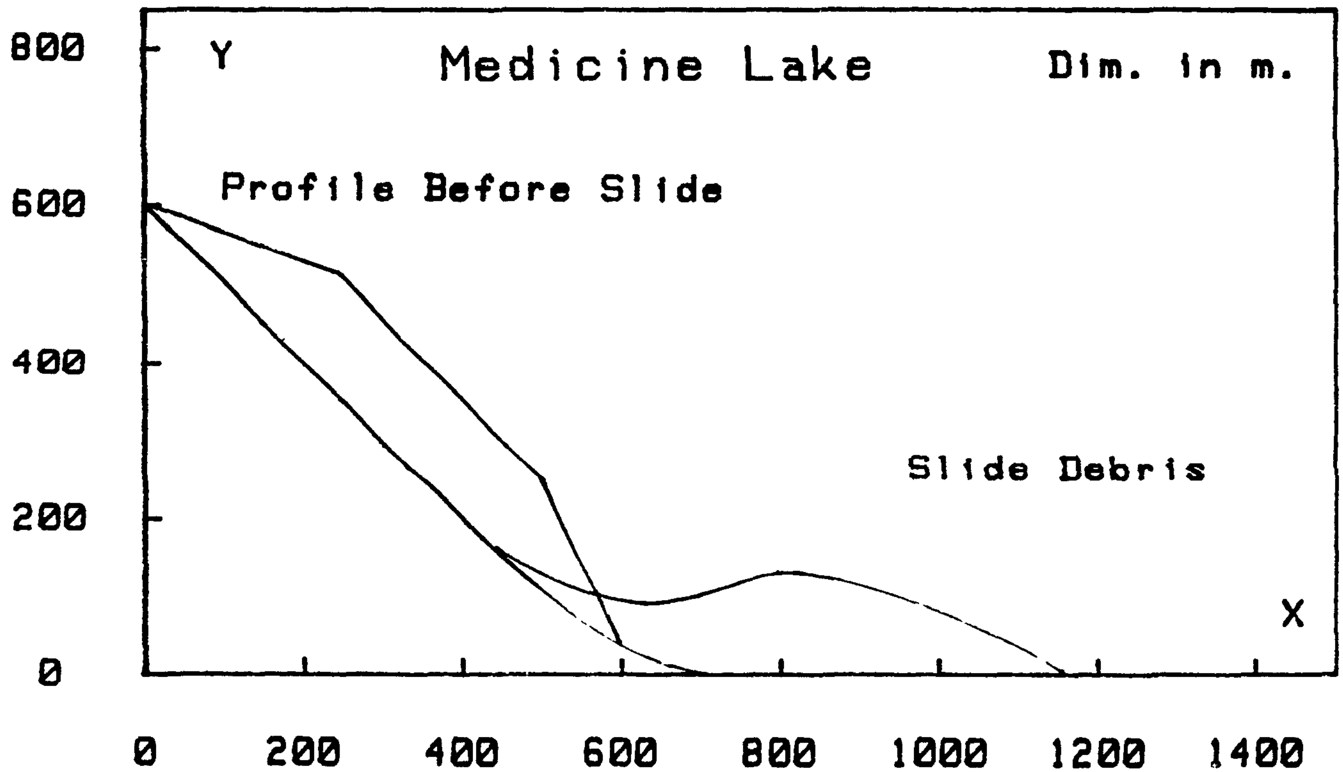

Fig. 4.15 Initial and final shapes and positions of rock mass

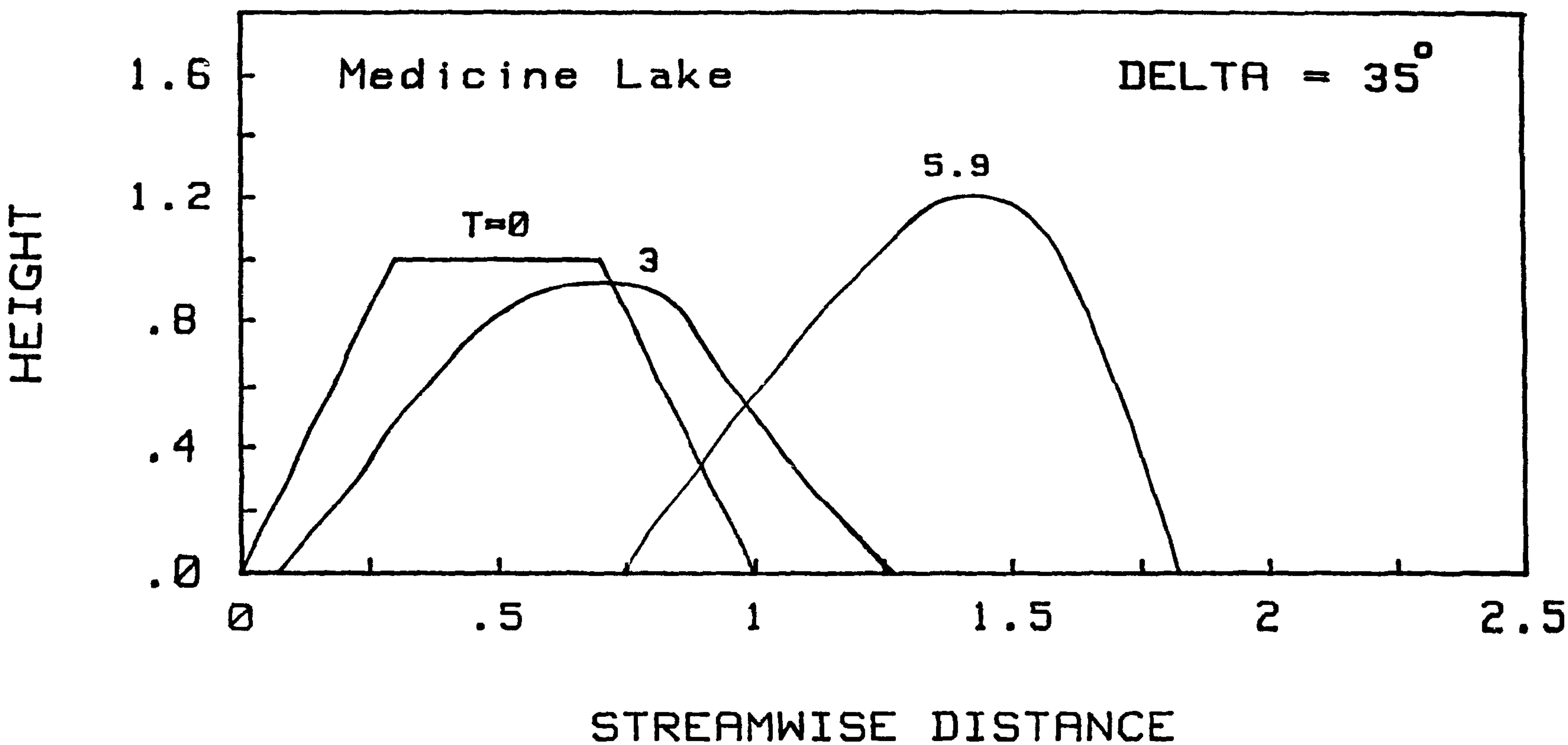

Fig. 4.16 Non-dimensional shape of the rock mass versus the non-dimensional traveling distance along the slide path at different non-dimensional times

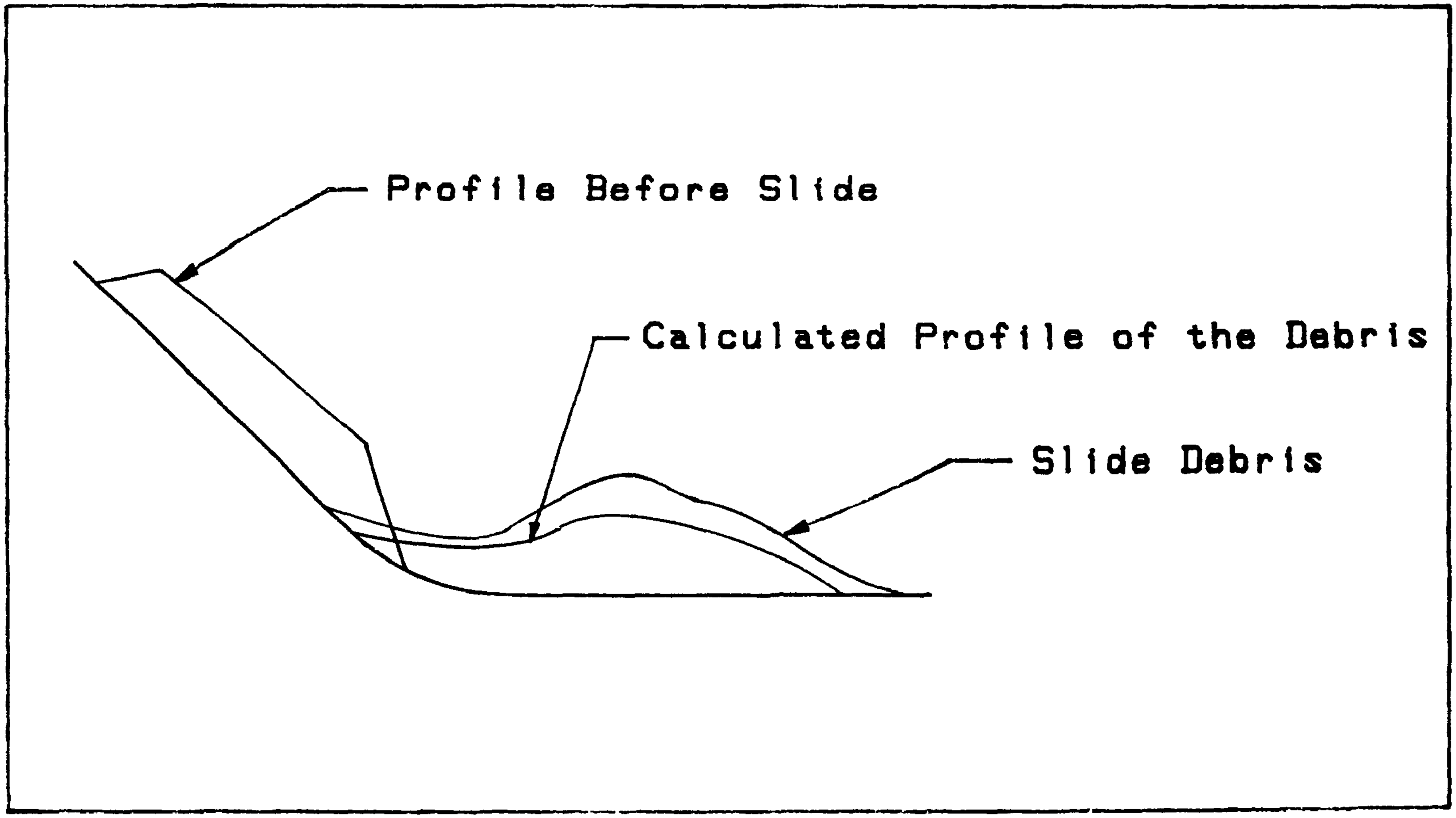

Fig. 4.17 Comparison between the calculated final shape of the rock mass and the observed slide debris

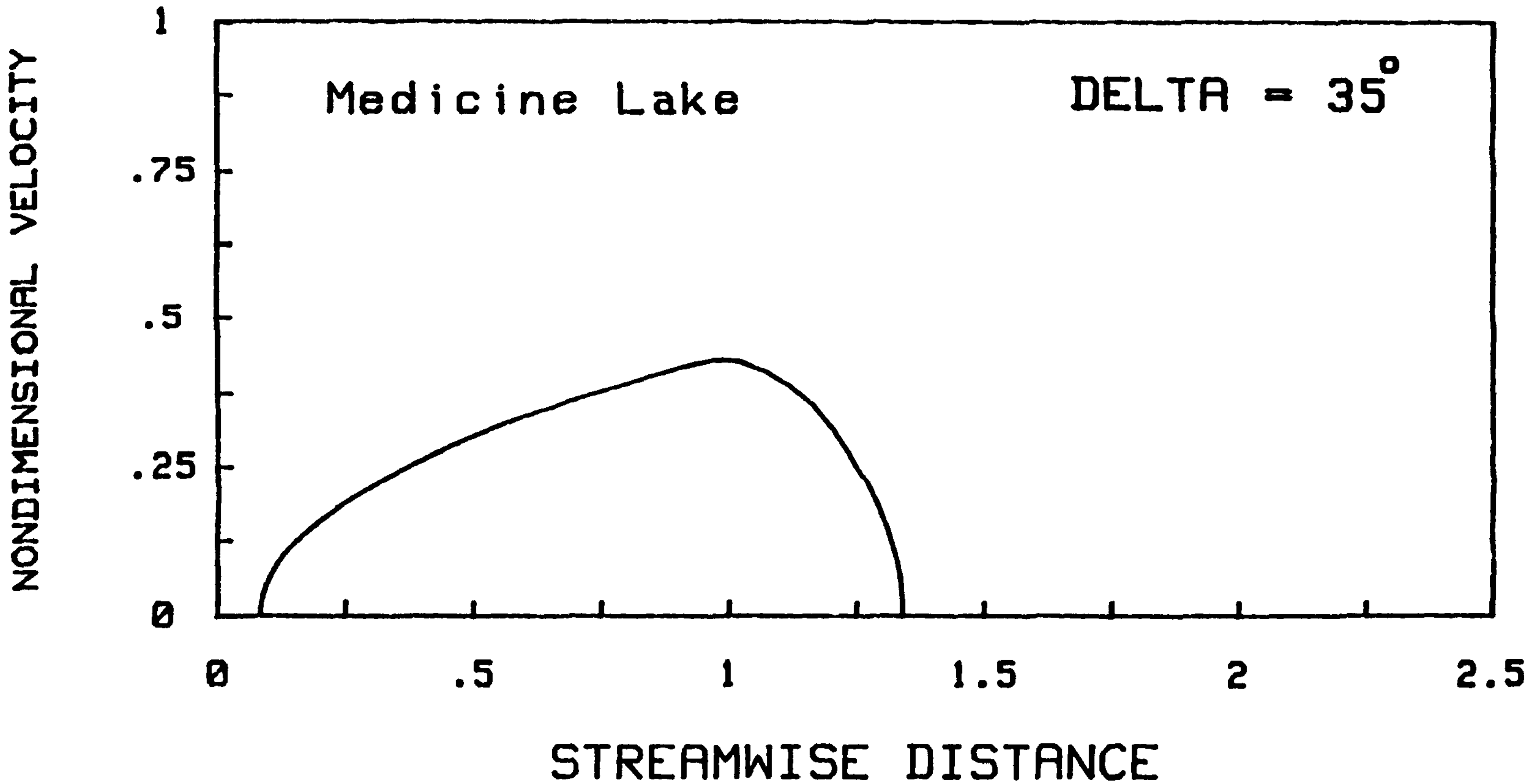

Fig. 4.18 Non-dimensional center-of-mass velocity versus non-dimensional traveling distance

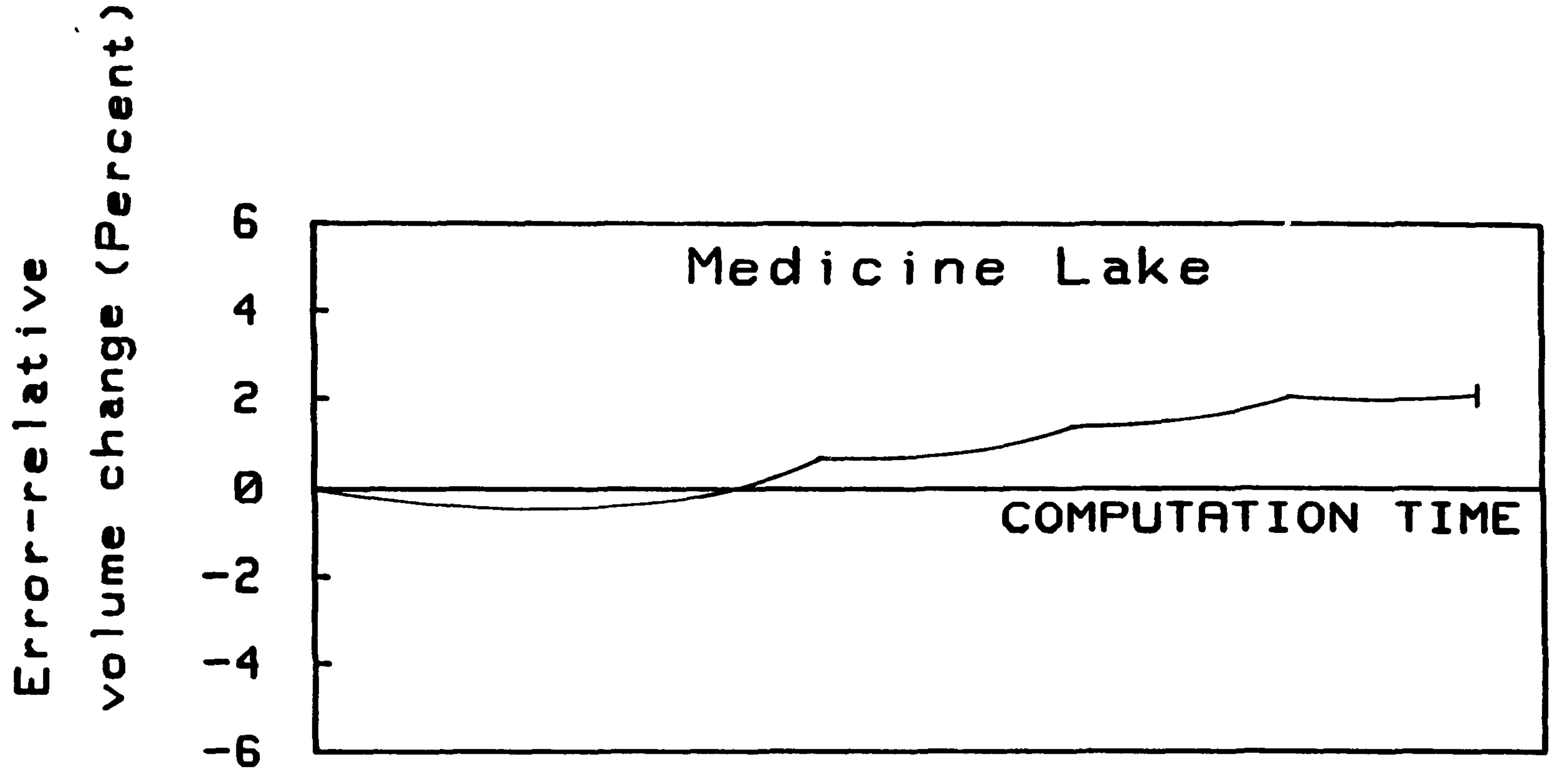

Fig. 4.19 Error expressed in terms of volume change versus non-dimensional time

Appendix .

Typical computer program listing
(Madison Canyon Rockslide)

```
10                    !***********************************!
20                    !    Madison Canyon Rockslide    !
30                    !***********************************!
40    OPTION BASE 1
50    SET TIME TIME("00:00:00")
60    GINIT
70    DIM U(151),H(151),U_u(501),Vol(1500),Chg(1500)
80    DIM Hh(151,25),Ze(151),Cm(501),R(151)
90    DEG
100   Dt=.005             !    TIME STEP
110   Tmax=8.7
120   T=0
130   Dx=.1               !    SPACE STEP
140   L1=150
150   Ah=75
160   !
170      Xi=0
180      Xx=0
190      Ze(1)=ATN(575*.01)
200      PRINT "     ZETA       XX        XI         S         R "
210      Dxi=L1/10                                ! equivalent to Dx
220      S=1
230      Sum1=0
240      Hhh=2
250      Xi=Xi+Dxi
260      CALL Zeta(Xi,Xx,Sum1,Hhh,Zeta,Rr,L1)
270      Ze(S)=Zeta
280      R(S)=Rr
290   PRINT USING "5X,K,15X,K,15X,K,12X,K";Ze(S),Xx,Xi,S+1,Rr
300      IF Ze(S)<.5 THEN
310      Ze(S)=0
320      GOTO 370
330      END IF
340      !
350      S=S+1
360      GOTO 250
370         FOR I=S TO 150
380         Ze(I)=0
390         NEXT I
400   Phy=35.
410   Z1=TAN(Phy)
420   A=Ah/L1
430   !
440   FOR I=1 TO 151
450     H(I)=0
460     U(I)=0
470   NEXT I
480   !
490   FOR I=1 TO 11               ! Initial shape of the slide
500      H(I)=SIN((I-1)*18)
510   NEXT I
520   !
530   N=15                          !  Initial Number of Steps
540   K=1
550   Kkk=1
```

```
560   PRINT "     I                  H                  U "
570   !
580   FOR I=1 TO N
590     Z2=SIN(Ze(I+1))
600     Z3=COS(Ze(I+1))
610     B=Z2-Z3*Z1
620       Dux=(U(I+1)-U(I))/Dx
630       Dhx=(H(I+1)-H(I))/Dx
640                             IF Ze(I)<.5 THEN 810
650           C=A*(Z3+(U(I+1))^2/R(I+1))
660           Dcos=Z3-COS(Ze(I))
670           E=A*Z1*(U(I+1))^2/R(I+1)
680           Dur=((U(I+1)^2/R(I+1))-(U(I)^2/R(I)))
690           Ft=.5*U(I+1)*Dux
700           Td=C*Dhx
710           Fh=.5*H(I+1)*Dcos*A
720           Sh=.5*H(I+1)*Dur*A
730           La=1+.5*Dt*Dux
740    U(I+1)=(U(I+1)-Dt*(Ft-B+Td+Fh+Sh+E))/La
750   !
760   Chk=Z5*(ABS(U(I+1)))*Dt/Dx       !  Stability Condition
770   IF Chk<.90 THEN GOTO 870
780   Dt=Dt*.5
790   PRINT "                       REDUCED TIME STEP "
800        GOTO 880
810           C=A*Z3
820           Ft=.5*U(I+1)*Dux
830           Td=C*Dhx
840           La=1+.5*Dt*Dux
850  U(I+1)=(U(I+1)-Dt*(Ft-B+Td))/La
860           GOTO 760
870          !
880   NEXT I
890   FOR I=1 TO N
900   !
910      Dux2=(U(I+2)-U(I+1))/Dx
920      Dhx=(H(I+1)-H(I))/Dx
930   !
940      H(I+1)=(H(I+1)-Dt*(U(I+1)*Dhx+.5*H(I+1)*Dux2))
950      H(I+1)=H(I+1)/(1+.5*Dt*Dux2)
960   !
970   NEXT I
980   !
990   FOR I=1 TO N
1000     IF H(I)<.0000001 THEN GOTO 1020
1010  PRINT USING "4X,DD,13X,DD.DDDD,8X,DD.DDDD";I,H(I),U(I)
1020  NEXT I
1030    !
1040    Volume=0
1050  FOR I=1 TO N-1
1060    Volume=Volume+(H(I)+H(I+1))/2*Dx
1070  NEXT I
1080  !
1090  PRINT USING """VOLUME = "",DD.DDD";Volume
1100  Vol(K)=Volume
1110  Vol_ref=Vol(1)
1120  Chg(K)=(Vol(K)/Vol_ref)*100-100
```

```
1130  T=T+Dt
1140  PRINT USING """          TIME = "",DD.DDD";T
1150  PRINT USING """   % OF ERROR    = "",K";Chg(K)
1160  K=K+1
1170  !
1180      CALL C_m(I,H(*),N,C_m,Dx,Volume)
1190      Uu=U(C_m)
1200      CALL U_x(I,T,C_m,Uu)
1210      Cm(Kkk)=C_m
1220      U_u(Kkk)=Uu
1230      Kkk=Kkk+1
1240      !
1250  SELECT T
1260  !
1270    CASE =Dt
1280      Kk=1
1290      CALL H_x(I,H(*),T,N)
1300      FOR I=1 TO N
1310      Hh(I+1,Kk)=H(I+1)
1320      NEXT I
1330    CASE .50
1340      Kk=2
1350      CALL H_x(I,H(*),T,N)
1360      FOR I=1 TO N
1370      Hh(I+1,Kk)=H(I+1)
1380      NEXT I
1390    CASE 6.00
1400      Kk=3
1410      CALL H_x(I,H(*),T,N)
1420      FOR I=1 TO N
1430      Hh(I+1,Kk)=H(I+1)
1440      NEXT I
1450    CASE Tmax
1460      Kk=4
1470      CALL H_x(I,H(*),T,N)
1480      FOR I=1 TO N
1490      Hh(I+1,Kk)=H(I+1)
1500      NEXT I
1510    CASE ELSE
1520      GOTO 1550
1530  END SELECT
1540  !
1550  IF T>Tmax THEN GOTO 1680
1560  Total=0
1570  FOR I=1 TO N
1580      IF T>1 THEN
1590        Total=(Total+U(I))
1600      ELSE
1610        Total=Total+U(I)+1
1620      END IF
1630  NEXT I
1640     Average=Total/N*3
1650     L=INT(Average)
1660     N=N+L
1670  GOTO 580
```

```
1680  BEEP
1690  PRINT
1700  PRINT TIME$(TIMEDATE)
1710  !
1720  PRINT "PRESS CONTINUE"
1730     PAUSE
1740     GCLEAR   !    Error Plot
1750     GINIT
1760      GRAPHICS ON
1770      VIEWPORT 20,120,30,70
1780      WINDOW 0,K+2,-6,6
1790      FRAME
1800      AXES 0,2
1810      VIEWPORT 0,120,0,100
1820      MOVE K/2,5.
1830      LORG 5
1840      LABEL " Madison Canyon "
1850      MOVE K-15,.65
1860      LABEL "COMPUTATION TIME"
1870      MOVE -11,0
1880      LDIR 90
1890      LABEL "'Error-relative"
1900      MOVE -9,0
1910      LABEL "volume change'"
1920      LDIR 0
1930      FOR I=-6 TO 6 STEP 2
1940      MOVE -4.5,I
1950      LABEL I
1960      NEXT I
1970      MOVE 0,0
1980      FOR I=1 TO K-1
1990        DRAW I,Chg(I)
2000      NEXT I
2010      !
2020  PRINT "DO YOU WANT TO PLOT THE GRAPHS (ERROR GRAPH) ?"
2030  PRINT "RELAY (Y/N)"
2040  PRINT " PRESS CONTINUE "
2050      PAUSE
2060      LINPUT Ans$
2070        IF Ans$="Y" THEN
2080        GINIT
2090    PLOTTER IS 705,"HPGL"
2100        GOTO 1750
2110     ELSE
2120     GOTO 2150
2130     END IF
2140     !          ****
2150  PRINT "DO YOU WANT TO PLOT THE GRAPHS ?  REPLAY (Y/N)"
2160  PRINT " PRESS CONTINUE "
2170      PAUSE
2180      LINPUT Ans$
2190        IF Ans$="Y" THEN
2200        GOTO 2240
2210        ELSE
2220        GOTO 3030
2230        END IF
```

```
2240        GINIT
2250        PLOTTER IS 705,"HPGL"
2260        VIEWPORT 20,120,40,80
2270        WINDOW 0,15,0,1.5
2280        FRAME                    !   H vs. X Plot
2290        AXES 1,.2
2300  VIEWPORT 0,130,0,100
2310  MOVE 12,1.4
2320  LORG 5
2330  LABEL "DELTA = 35  "
2340  MOVE 14.5,1.43
2350  CSIZE 2
2360  LABEL "        o "
2370  CSIZE 5
2380  MOVE 3,1.3
2390  LABEL "Madison Canyon"
2400  MOVE -2,.75
2410  LDIR 90
2420  LABEL "HIGHT"
2430  LDIR 0
2440  MOVE 7.5,-.45
2450  LABEL "STREAMWISE DISTANCE"
2460  MOVE 0,-.2
2470  FOR I=0 TO 15
2480  MOVE I,-.2
2490  LABEL I/2
2500  NEXT I
2510  MOVE -1,0
2520  FOR I=0 TO 1.3 STEP .4
2530  IF I=0 THEN
2540  LABEL ".0"
2550  GOTO 2640
2560  END IF
2570  IF I=1 THEN
2580  MOVE -1.1,1.2
2590  LABEL "1.2"
2600  ELSE
2610  MOVE -1,I
2620  LABEL I
2630  END IF
2640  NEXT I
2650  MOVE 0,0
2660        FOR Kk=1 TO Kk
2670          FOR I=1 TO N
2680            DRAW (I+1)/10,Hh(I+1,Kk)
2690          NEXT I
2700          MOVE 0,0
2710        NEXT Kk
2730       BEEP
2740       !
```

```
2750  VIEWPORT 20,120,60,100
2760  WINDOW 0,15,1,1.8
2770  AXES 1,.2
2780  FRAME                  ! U vs. X Plot
2790  VIEWPORT 0,120,60,100
2800  MOVE 4,1.5
2810  LORG 5
2820  LABEL "Madison Canyon"
2830  MOVE 12,1.5
2840  LABEL "DELTA = 35"
2850  MOVE 12,1.55
2860  CSIZE 3
2870  LABEL "           o"
2880  MOVE -2.5,.9
2890  LDIR 90
2900  CSIZE 3
2910  LABEL "NONDIMENSIONAL VELOCITY"
2920  LDIR 0
2930  MOVE -1.0,0
2940  FOR I=0 TO 1.8 STEP .4
2950  MOVE -1,I
2960  LABEL I
2970  NEXT I
2980       Nn=Tmax/Dt
2990       FOR I=1 TO Nn
3000         DRAW Cm(I),U_u(I)
3010       NEXT I
3020       BEEP
3030  PRINT "END OF NORMAL PROGRAM"
3040        BEEP
3050  END
```

```
3060  !
3070  !                    SCREEN PLOT
3080  !          **********************************
3090  !          ******  PLOT H VS. X  ***********
3100  !          **********************************
3110  !
3120   SUB H_x(I,H(*),T,N)
3130   BEEP
3140  IF T>.16 THEN GOTO 3520
3150  GRAPHICS ON
3160  VIEWPORT 20,120,20,50
3170  WINDOW 0,15,0,1.5
3180  FRAME
3190  AXES 1,.2
3200  VIEWPORT 0,130,0,100
3210  MOVE 7.5,1.3
3220  LORG 5
3230  LABEL "PHY = 35  "
3240  MOVE 8.5,1.43
3250  CSIZE 2
3260  LABEL "        o "
3270  CSIZE 5
3280  MOVE -2,.75
3290  LABEL "H"
3300  MOVE 7.5,-.45
3310  LABEL "X"
3320  MOVE 0,-.2
3330  FOR I=0 TO 15 STEP 2
3340  MOVE I,-.2
3350  LABEL I
3360  NEXT I
3370  MOVE -1,0
3380  FOR I=0 TO 1.5 STEP .4
3390  IF I=0 THEN
3400  MOVE -1,0
3410  LABEL ".0"
3420  GOTO 3510
3430  END IF
3440  IF I=1 THEN
3450  MOVE -1.1,1
3460  LABEL "1.0"
3470  ELSE
3480  MOVE -1,I
3490  LABEL I
3500  END IF
3510  NEXT I
3520  MOVE 0,0
3530  !
3540  FOR I=1 TO N
3550    DRAW I/10,H(I+1)
3560  NEXT I
3570   !
3580   SUBEND
```

```
3590   !
3600   !                      SCREEN PLOT
3610   !             *********************************
3620   !             ******** PLOT U VS. X  **********
3630   !             *********************************
3640   !
3650   SUB U_x(I,T,C_m,Uu)
3660   Dt=.005
3670  IF T>(Dt+.002) THEN GOTO 3870
3680  GRAPHICS ON
3690  VIEWPORT 20,120,60,100
3700  WINDOW 0,15,0,1.8
3710  AXES 1,.2
3720  FRAME
3730  VIEWPORT 0,120,0,100
3740  MOVE 25,8.5
3750  LORG 5
3760  MOVE -2.0,.9
3770  LABEL "U"
3780  MOVE -1,0
3790  FOR I=0 TO 1.8 STEP .4
3800  MOVE -1,I
3810  LABEL I
3820  NEXT I
3830  !
3840        Cc=C_m
3850        Uuu=Uu
3860        PRINT Cc,Uuu
3870        MOVE Cc,Uuu
3880     DRAW C_m,Uu
3890      !
3900   SUBEND
```

```
3910   !        ****************************************
3920   !        ******  angle of inclination and  *******
3930   !        ******  radius of curvature        *******
3940   !        ****************************************
3950   !
3960   SUB Zeta(Xi,Xx,Sum1,Hhh,Zeta,Rr,L1)
3970   INTEGER Jjj
3980     C=(-.01)
3990     Hs=Hhh/5
4000     Sum0=0
4010     Sum0=Sum0+(1+(C*C)*EXP(2*C*Xx))^.5
4020     M=6
4030     H1=Hs/M
4040     FOR Jjj=1 TO M
4050       Xx=Xx+H1
4060       IF Jjj=M THEN GOTO 4120
4070       IF Jj=Jj/2*2 THEN GOTO 4100
4080     Sum0=Sum0+4*(1+575^2*(C*C)*EXP(2*C*Xx))^.5
4090     GOTO 4130
4100     Sum0=Sum0+2*(1+575^2*(C*C)*EXP(2*C*Xx))^.5
4110     GOTO 4130
4120     Sum0=Sum0+(1+575^2*(C*C)*EXP(2*C*Xx))^.5
4130     NEXT Jjj
4140     Simps=Sum0*H1/3
4150     Sum1=Sum1+Simps
4160     IF Sum1>Xi THEN GOTO 4180
4170     GOTO 4000
4180     Zeta=ATN(575*ABS(C)*EXP(C*Xx))
4190     Up=C^2*575*EXP(C*Xx)
4200     Bo=(1+575^2*C^2*EXP(2*C*Xx))^1.5
4210     Rr=(Bo/Up)/L1                       ! Non-dimensional
4220     SUBEND
4230     !
4240     !              ***************************
4250     !              *****  center of mass  *****
4260     !              ***************************
4270     !
4280     SUB C_m(I,H(*),N,C_m,Dx,Volume)
4290     !
4300       M=0
4310       FOR I=1 TO N-1
4320         L=(H(I)+H(I+1))/2*Dx
4330         M=M+L*(I+I+1)/2
4340       NEXT I
4350       C_m=M/Volume
4360   SUBEND
```

REFERENCES

1. Scheidegger, A.E. (1973) On the prediction of the reach and velocity of catastrophic landslides. Rock Mech. , 5, pp. 231-236.

2. Hsü, K.J. (1975) Catastrophic debris streams generated by rockfalls. Geol. Soc. Amer. Bull. , 86, pp. 129-140.

3. Hsü, K.J. (1978) Albert Hiem: Observations on landslides and relevance to modern interpretations. In: Rockslides and Avalanches, 1 (Voight, B. ed.), pp. 71-93. Elsevier.

4. Shreve, R.L. (1966) The Sherman landslide, Alaska. Science , 154, pp. 1639-1643.

5. Kent, P.E. (1965) The transport mechanism in catastrophic rock falls. J. Geol. , 74, pp. 79-83.

6. Shreve, R.L. (1968a) The Blackhawk landslide. Geol. soc. Amer. Sepc. Paper , 108, pp. 47.

7. Shreve, R.L. (1968b) Leakage and fluidization in air layer lubricated avalanches. Geol. Soc. Amer. Bull. , 79, pp. 653-658.

8. Goguel, J. (1978) Scale-dependent rockslide mechanisms In: Rockslides and Avalanches, 1 (Voight, B. ed.) pp. 693-705. Elsevier.

9. Howard, K. (1973) Avalanche mode of motion: Implications from lunar examples. Science , 180, pp. 1052-1055.

10. Lucchitta, B.K. (1978) A large landslide on Mars. Geol. Soc. Amer. Bull. , 89, pp. 1601-1609.

11. Davies, T.R.H. (1982) Spreading of rock avalanche debris by mechanical fluidization. Rock Mech. , 15, pp. 9-24.

12. Bagnold, R.A. (1954) Experiments on a gravity-free dispersion of large solid spheres in a Newtonian fluid under shear. Proc. Roy. Soc. London , 225A, pp. 49-63.

13. Bagnold, R.A. (1966) The shearing and dilatation of dry sand. Proc. Roy. Soc. London , 295A, pp. 219-232.

14. Savage, S.B. and Sayed, M. (1984) Stresses developed by dry cohesionless granular materials sheared in an annular shear cell. J. Fluid Mech. , 142, pp. 391-430.

15. Lun, C.K.K. ,Savage, S.B. ,Jeffrey, D.J. and Chepurniy, N. (1984) Kinetic theories for granular flow: inelastic particles in Couette flow and slightly inelastic particles in a general flowfield. J. Fluid Mech. , 140. pp. 223-256.

16. McSaveney, M.J. (1978) Sherman glacier rock avalanche. In: Rockslides and Avalanches,1 (Voight, B. ed.), pp. 197-258. Elsevier.

17. Erismann, T.H. (1979) Mechanisms of large landslides. Rock Mech. , 12, pp. 15-46.

18. Melosh, H.J. (1979) Acoustic fluidization: A new geologic process?. J. Geophys. Res. , 84, pp. 7513 - 7520.

19. Melosh, H.J. (1982) A schematic model of crater modification by gravity. J. Geophys. Res. , 87, pp. 371-380.

20. Savage, S.B. (1983) Granular flows down rough inclines. In: Mechanics of Granular Material (Jenkins, J.T. and Satake, M. eds.), pp. 261-282. Elsevier.

21. Strelkoff, T. (1970) Numerical solution of Saint - Venant equations. ASCE , 96, HY1, pp. 223-252.

22. Koutitas, C.G. (1983) Elements of Computational Hydraulics. Pentch Press.

23. Richtmyer, R.D. (1957) Difference Methods for Initial Value Problems. Interscience N.Y.

24. Hadley, J.B. (1978) Madison canyon rockslide, Montana U.S.A. In: Rockslides and Avalanches, 1(Voight, B., ed.), pp. 167-180. Elsevier.

25. Cruden, D.M. and Krahn, J. (1978) Frank rockslide, Alberta, Canada. In: Rockslides and Avalanches, 1 (Voight, B. ed.), pp. 97-112. Elsevier.

26. Cruden, D.M. (1976) Major rock slides of the Rockies. Can. Geotech. J. , 13, pp. 8-20.

27. Kamis, A.S. and Savage, S.B. (1985) Spreading of rock avalanches. Proc. of Canadian Congress of Applied Mechanics , University of Western Ontario, Abstract (accepted).

28. Hungr, O. and Morgenstern, N.R. (1984) Experiments on the flow behaviour of granular materials at high velocity in an open channel. Ge technique , 34, No. 3, pp. 405-413.

29. Jeyapalan, J.K., Duncan, J.M. and Seed, H.B. (1983) Analysis of flow failures of mine tailings dams. ASCE, J. Geotch. Eng. , 109, No. 2, pp. 150-171.

30. Jeyapalan, J.K., Duncan, J.M. and Seed, H.B. (1983) Investigation of flow failures of tailings dams. ASCE, J. Geotch. Eng. , 109, No. 2, pp. 172-189.

31. Lang, T.E. and Dent, J.D. (1982) Review of surface friction, surface resistance and flow of snow. Reviews of Geophys. and Space Phys. , 20, No. 1, pp. 21-37.

32. Melosh, H.J. (1977) Crater modification by gravity: A mechanical analysis of slumping. In: Impact and Explosion Cratering, Pergamon Press., pp. 1245-1260.

33. Melosh, H.J. (1983) Acoustic fluidization. Amer. Scientist , 71, pp. 158-165.

34. Melosh, H.J. and Gaffney, E.S. (1983) Acoustic fluidization and scale dependence of impact crater morphology. J. Geophy. Res. , 88, pp. A830-A834.

35. Takahashi, T. (1981) Debris flow. Ann. Rev. Fluid mech., 13, pp. 57-77.

36. Tsubaki, T. ,Hashimoto, H. and Suetsugi, T. (1983) Interparticle stresses and characteristics of debris flow. J. Hydroscience and Hydraulic Eng. , 1, No. 2, pp. 67-82.

37. Vallejo, L.E. (1979) An explanation of mudflows. Geotechnique , 29, No. 3, pp. 351-358.

38. Voight, B. (ed.) (1978) Rockslides and Avalanches. Vol. 1, Elsevier.

39. Voight, B. (ed.) (1978) Rockslides and Avalanches. Vol. 2, Elsevier.

40. Bauer, S.W. and Schmidt, K.D. (1984) Irregular-grid finite-difference simulation of lake Geneva surge. ASCE , 109, HY10, pp. 1285-1297.

41. Gourlay, A.R. and Morris, J.Ll. (1968) Finite difference methods for nonlinear hyperbolic systems. Math. Comp. , 22, pp. 28-39.

42. Gourlay, A.R. and Morris, J.Ll. (1968) Finite difference methods for nonlinear hyperbolic systems II. Math. Comp. , 22, pp. 549-556.

43. Harlow, F.H. and Welch, J.E. (1965) Numerical calculation of time-dependent viscous incompressible flow of fluid with free surface. Phys. of Fluids , 8, No. 12, pp. 2182-2189.

44. Hirt, C.W. (1968) Heuristic stability theory for finite-difference equations. J. Comp. Phys. , 2, No. 4, pp. 339-355.

45. Lapidus, L. and Pinder, G.F. (1982) Numerical Solution of Partial Differential Equations in Science and Engineering. Wiley-interscience.

46. Liggett, J.A. and Woolhiser, D.A. (1967) Difference solutions of shallow-water equation. ASCE , 93, EM2, pp. 39-71.

47. Dressler, R.F. (1952) Hydraulic resistance effect upon the dam-break functions. J. Research, National Bureau of standerds , 49, No. 3, pp. 217-225.

48. Dressler, R.F. (1954) Comparison of theories and experiments for hydraulic dam-break wave. International Association of Scientific Hydrology , 38, pp. 319-328.

49. Sakkas, J.G. and Strekloff, T. (1974) Dam-break flood in a prismatic dry channel. ASCE , 99, HY12, pp. 2195 -2216.

50. Whitham, G.B. (1955) The effects of hydraulic resistance on the dam-break problem. Proc. Roy. Soc. London , 227, pp. 399-407.

GENERAL CONCLUSIONS

The main conclusions of the two studies described in this thesis are given below.

Part I: Subaqueous Flow of a Cloud of Coarse Particles Down an Inclined Bed.

Based upon the two series of laboratory experiments and the theoretical analysis, it may be concluded that:

1. The flow behaviour of a density current involving sedimenting particles can be very different from that of one involving miscible fluids. The previous experiments and the analysis of Beghin, et al. involving the release of salt water into fresh water on a sloping bed showed that the ensuing (negatively buoyant) cloud continued to grow without bound as it moved down the bed. In the present experiments the cloud of particles initially grew but then collapsed at some downstream position.

2. The aspect ratio (the height to length) of the cloud was found to be approximately constant for each bed inclination and did not vary greatly for different inclinations. This is similar to results found previously for miscible fluids.

3. The entrainment coefficient for turbulent density currents has commonly been expressed as a function of the Richardson number. This is inadequate for flows involving sedimenting particles, and on the basis of dimensional analysis it is proposed that the entrainment coefficient be expressed as a function of both the Richardson number and the ratio of the particle net fall velocity to the cloud center-of-mass velocity. The proposed functional form agrees well with the present set

of experiments and roughly predicts the previous results for miscible fluids as the particle fall velocity tends to zero.

4. The effects of the cloud form drag and the bed friction arising from particle interactions were found to be very significant in the present work. Both have been regarded as negligible in the previous investigations.

5. The present analysis based upon the three overall conservation equations; the sediment balance equation, the ambient fluid entrainment equation and the linear momentum equation along the bed, was found to give reasonably good predictions of the observed flow behaviour for cloud size and shape, mean velocity and mean particle concentration and cloud collapse location.

6. The above effects which have previously been neglected, but which were found to be important in the present investigation, should be included in further investigations of gravity currents involving sedimenting particles.

Part II: <u>Spreading of Rock Avalanches</u>

The second part of the thesis considered a related problem of flow of particles down an inclined bed, but in this instance the interstitial fluid effects were taken to be negligible. The development of numerical computer codes to simulate rockfalls was undertaken in an attempt to investigate the surprisingly long runout distances that have been observed in some field events involving very large volumes. The codes were based upon the use of continuum depth-averaged equations of motion and a simple quasi-static form of the constitutive equation for the granular rock material. The conclusions derived from the numerical studies of the rockfall problem are as follows:

1. From the results of computer simulations which involved two-dimensional spreading of granular material down an inclined rough plane, it was found that lateral spreading of the material was small compared to longitudinal spreading in the streamwise direction.

2. As a result of these studies, a two-dimensional flow model which considered only one-dimensional spreading was regarded as sufficiently accurate for the present investigation. This one-dimensional spreading model showed that extreme spreading of the granular material could occur without introducing any unusual fluidizing mechanisms such as have been deemed necessary in the past.

3. There were only three rockfall events, the Frank, Madison Canyon and Medicine Lake slides, for which sufficient data existed to perform detailed numerical simulations using the present model. The predictions for the overall flow features for these events were in good agreement with the field observations and the behaviour inferred from these observations.

4. It was concluded that the motion of the center of mass of the rockfall resembled the motion of a point mass moving down the same incline.

5. The long runout distance of the leading edge of the debris can be due to the spreading of the pile under gravity during its travel down the slope.

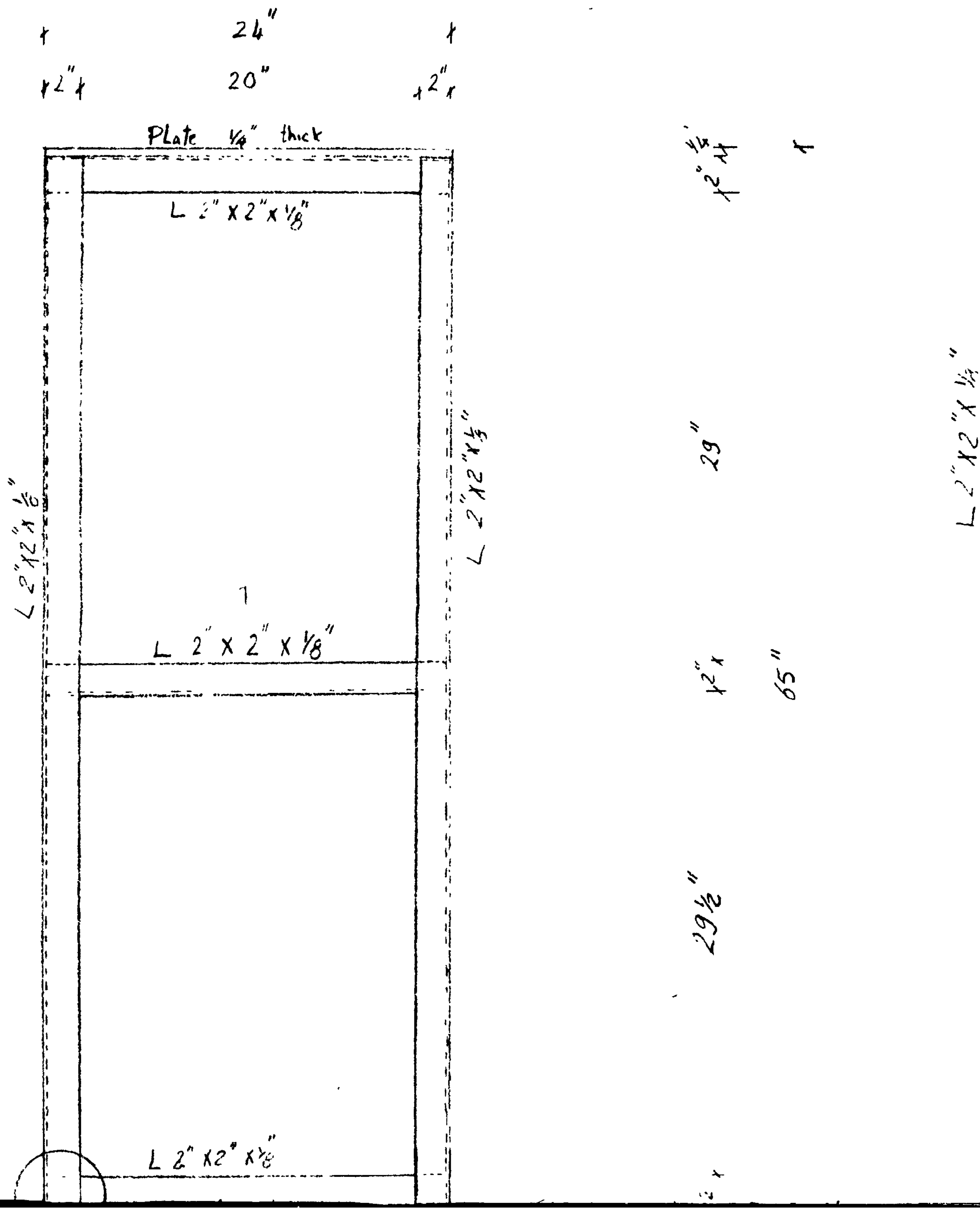
24"
2"
20"
2"
Plate 1/4" thick
L 2" X 2" X 1/8"
L 2" X 2" X 1/8"
L 2" X 2" X 1/8"
1
L 2" X 2" X 1/8"
L 2" X 2" X 1/8"
L 2" X 2" X 1/8"
2" 1/4"
29"
2"
65"
29 1/2"
L 2" X 2" X 1/8"

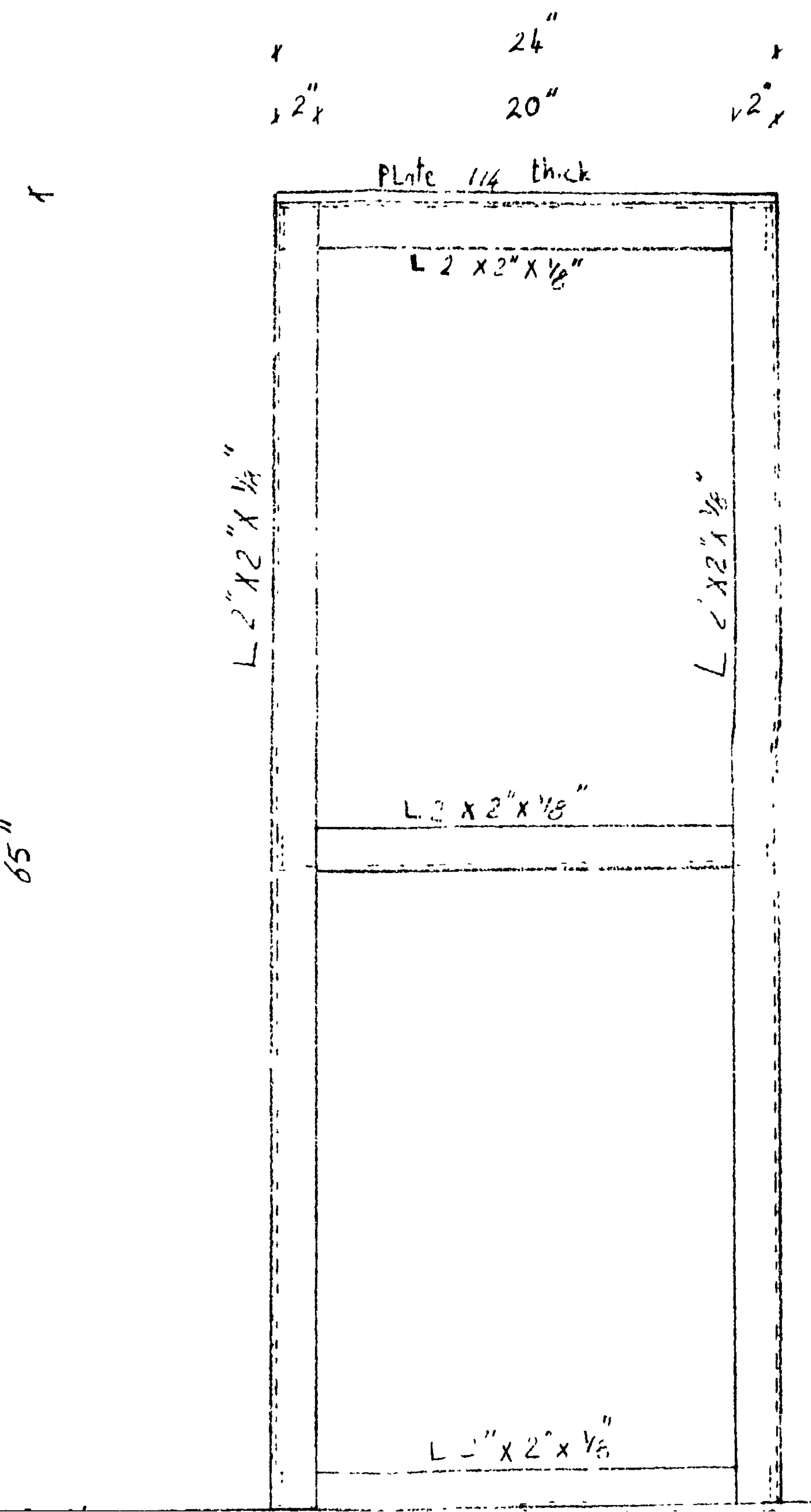

24"
2"
20"
2"
Plate 1/4 thick
L 2 x 2" x 1/8"
L 2" x 2" x 1/8"
L 2" x 2" x 1/8"
L 2 x 2" x 1/8"
L 2" x 2" x 1/8"
65"

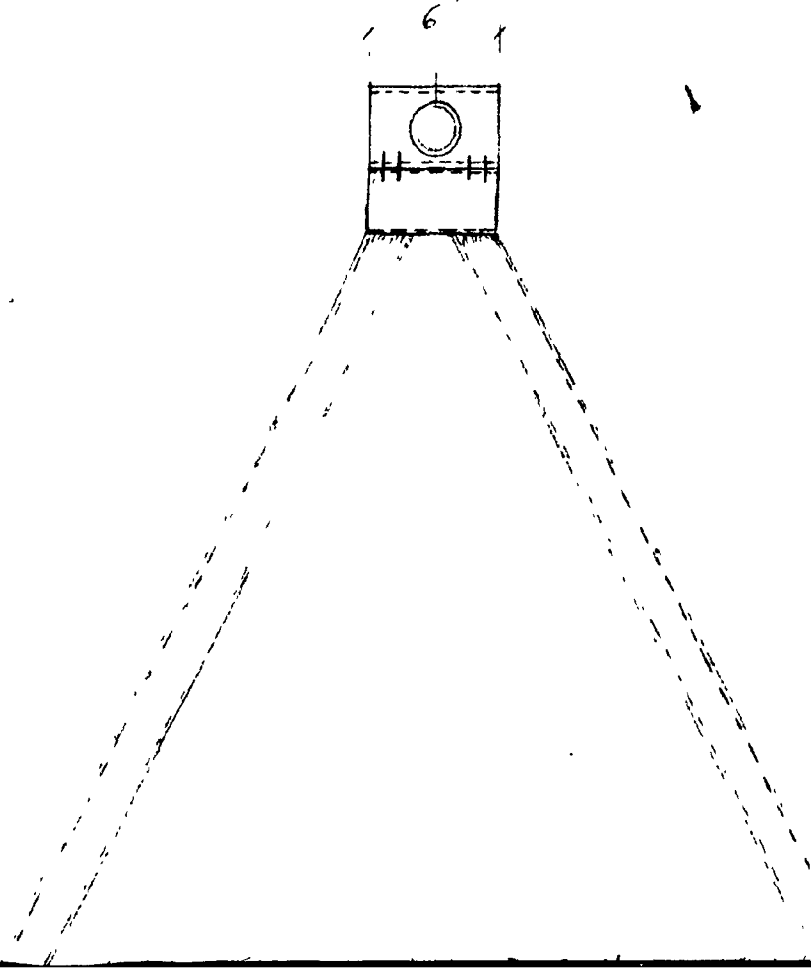
6"

3

75

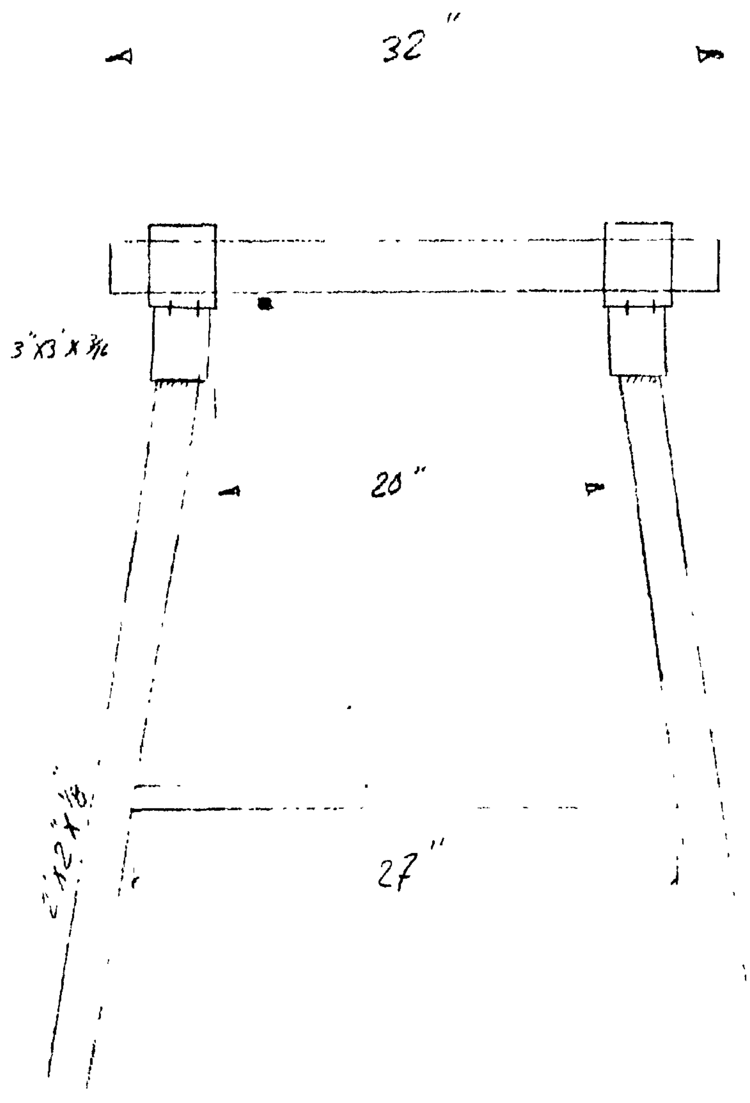
32"
3"X3"X3/16
20"
2"X2"X1/8
27"

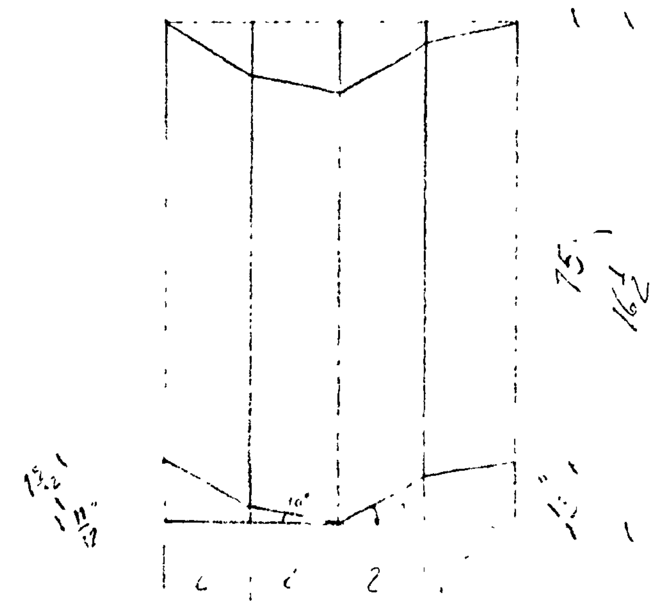

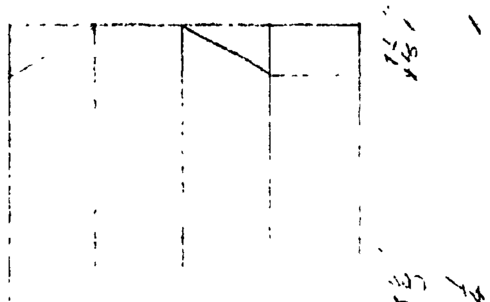

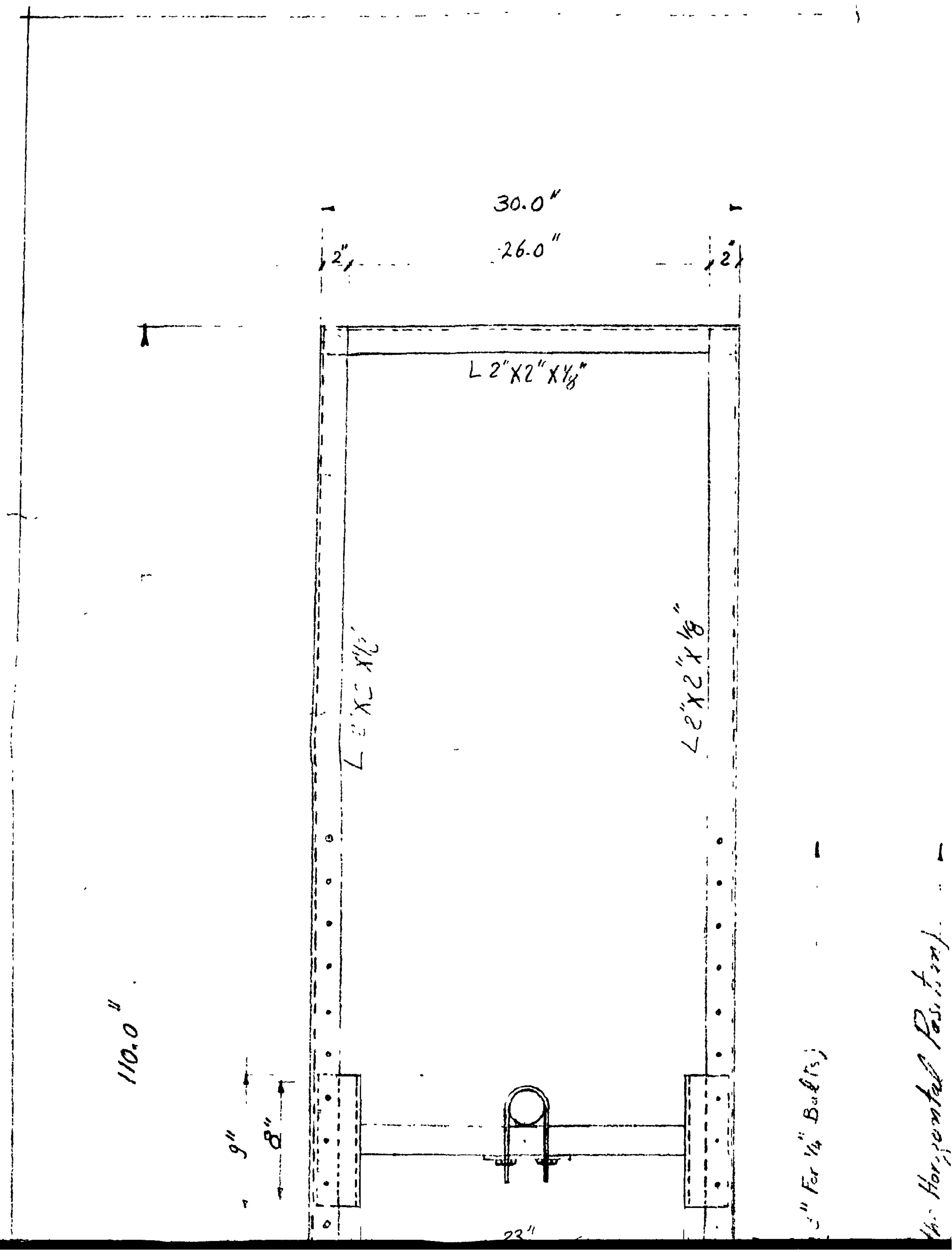
30.0"
26.0"
2"
2"
L 2"X2"X1/8"
L 2"X2"X1/8"
110.0"
9"
8"

" For 1/4" Bolts)

Horizontal Position)

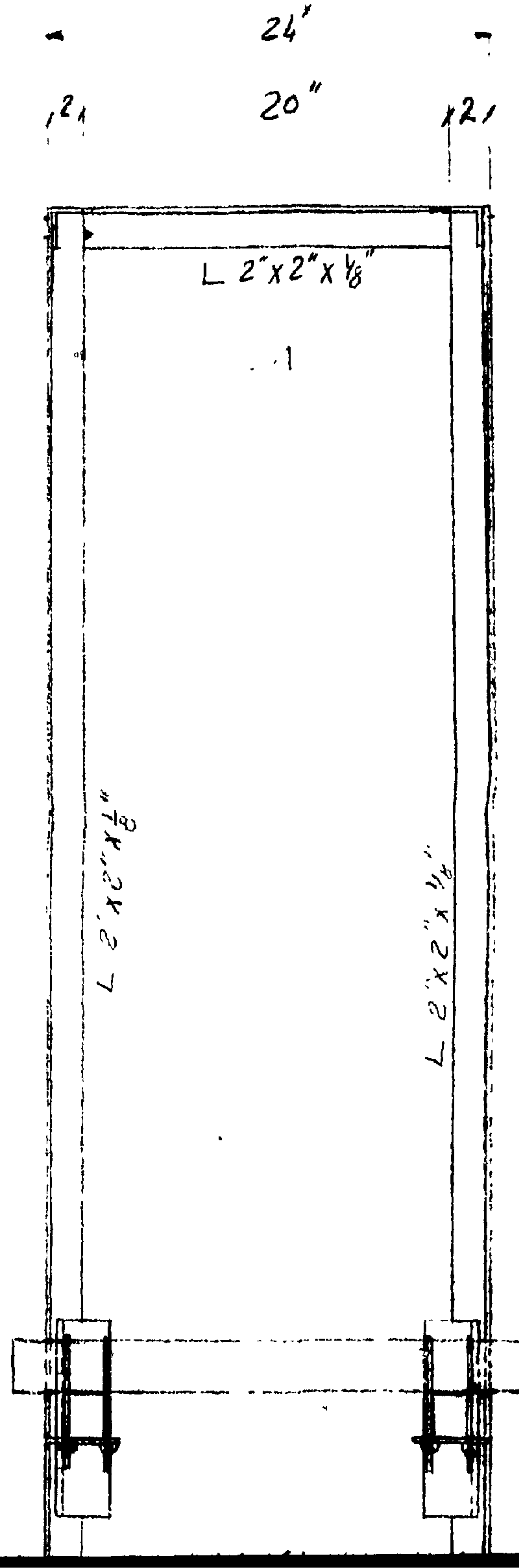

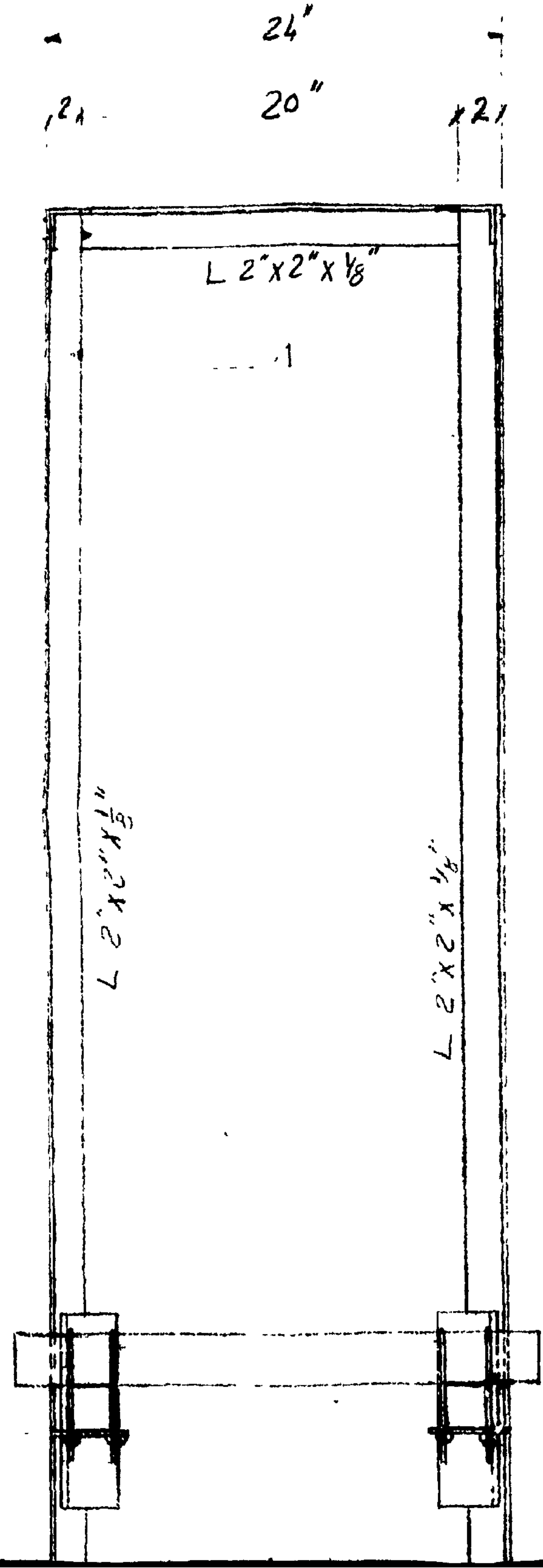

24"
20"
2
2
L 2"x2"x1/8"
1
L 2"x2"x1/8"
L 2"x2"x1/8"

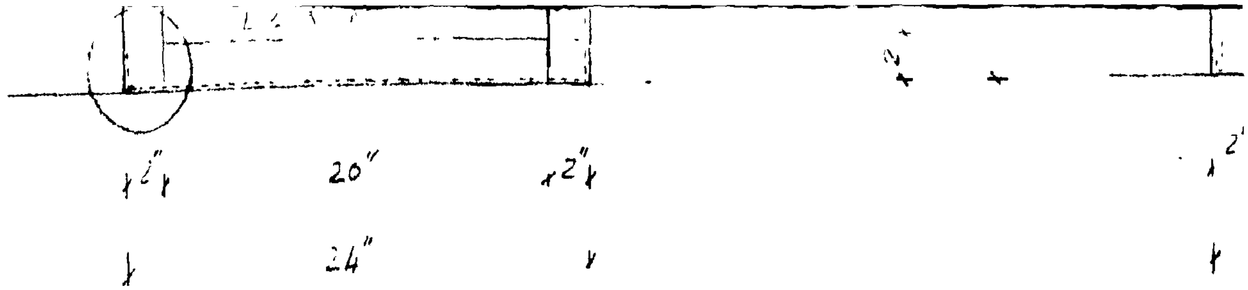

ELEVATION

Scale 1:8

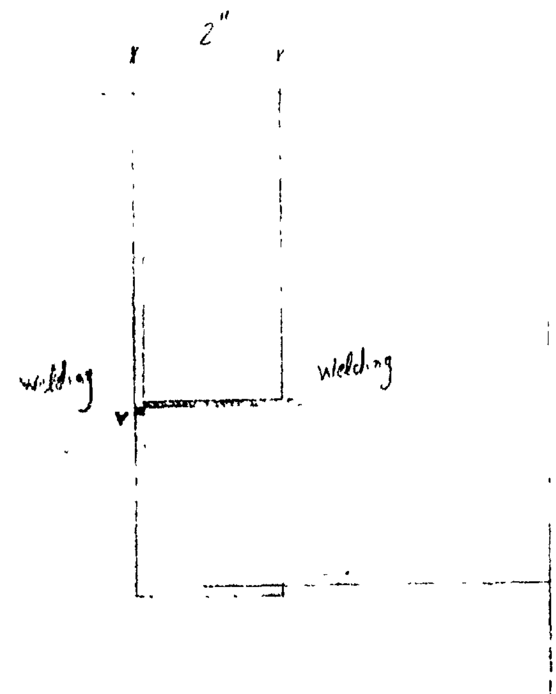

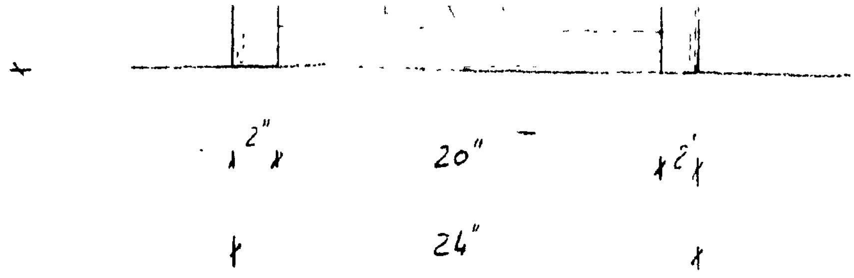

8

SIDE VIEW

U.S. SUPPORT

SCALE 1:2

Fig. 2.11

a)

1

70

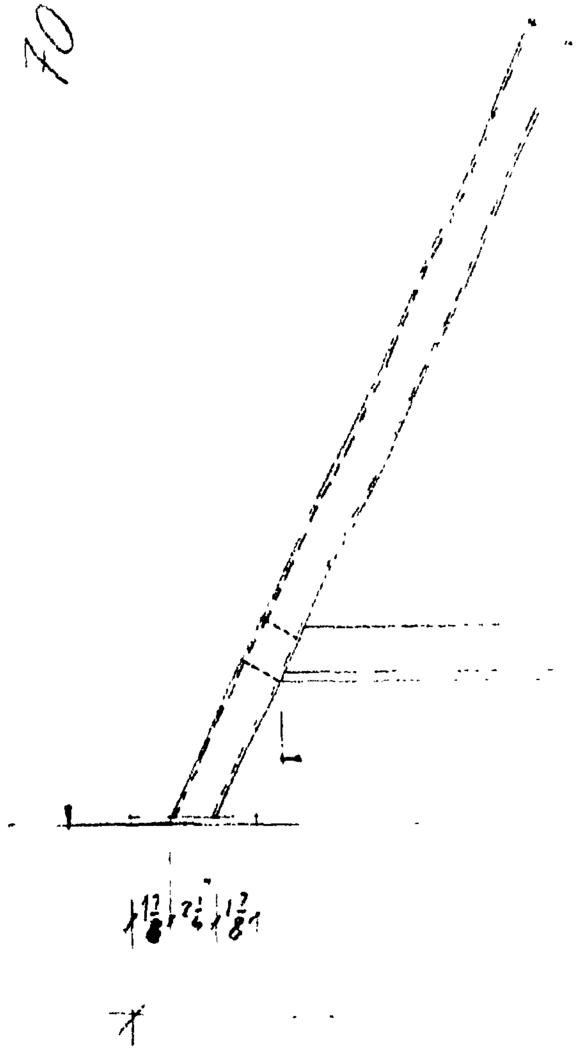

70 1/4"

73"

88 1/4

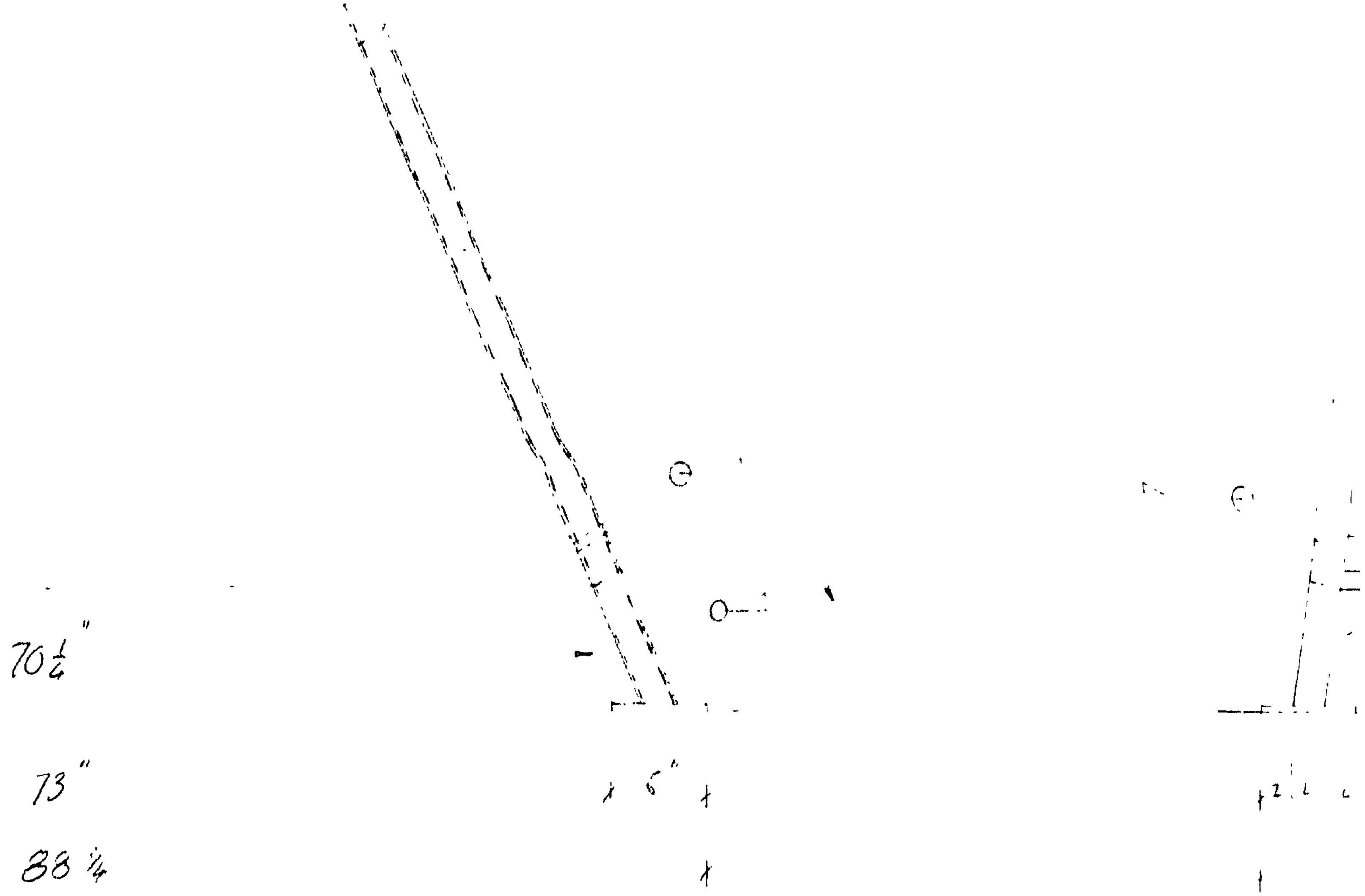

Scale 1:8

ALL WELDS:

1/2" FILLET WELD
E7XXX

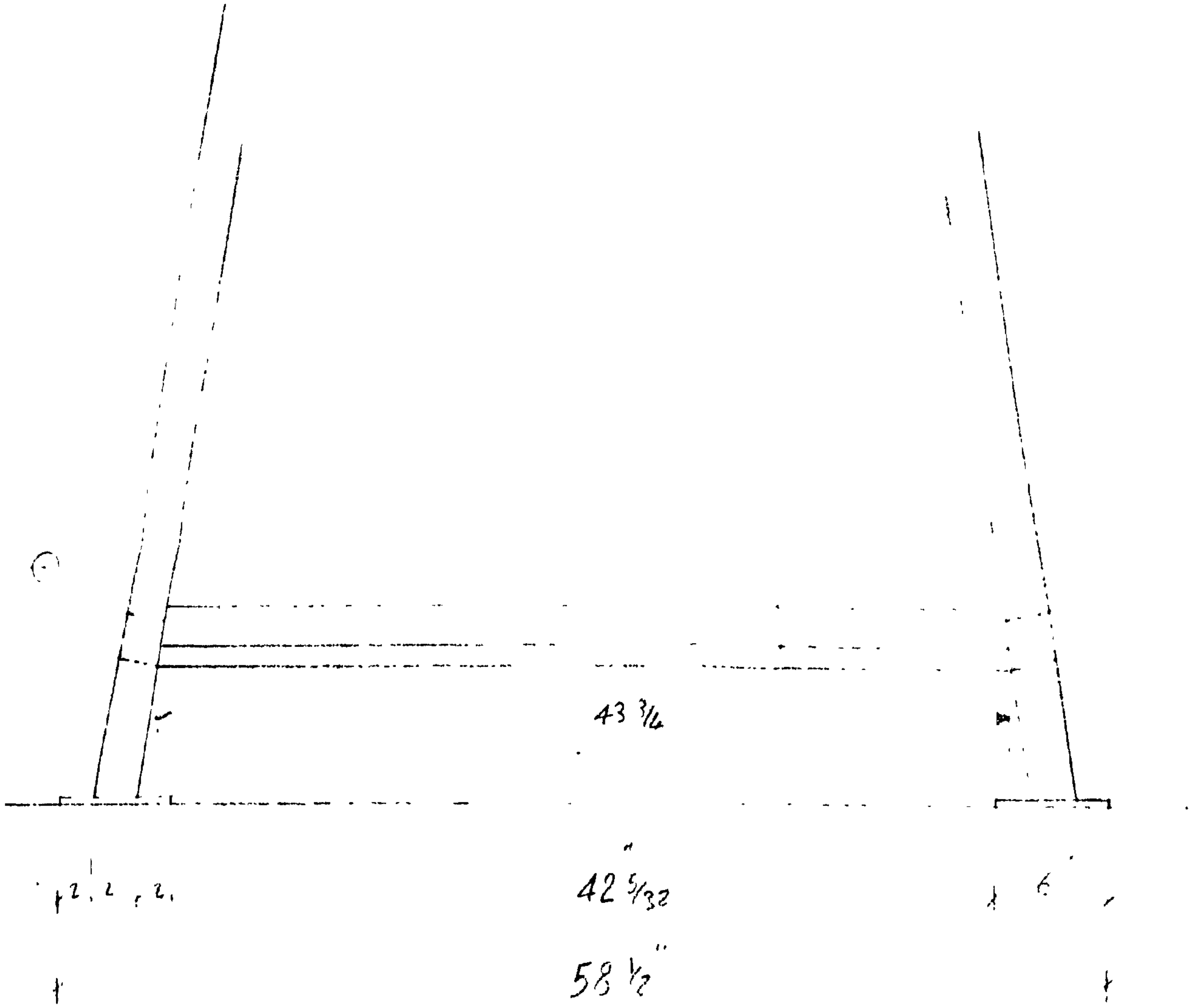

43 3/4
42 5/32"
58 1/2"

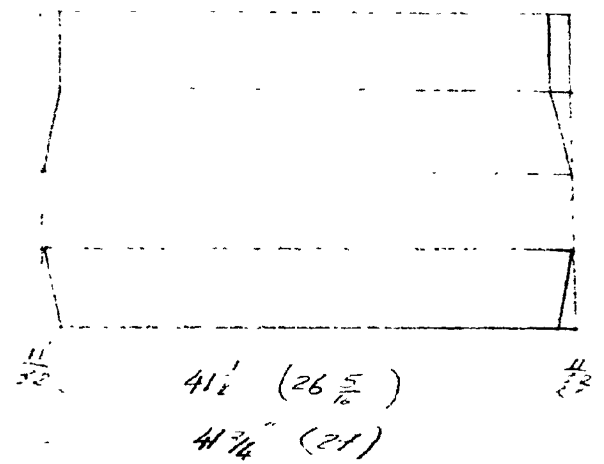
41½' (26 5/16)
41¾" (27)

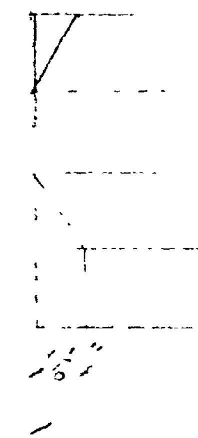

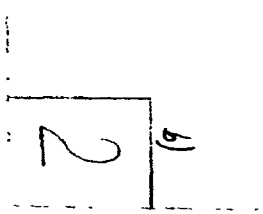
b)
2

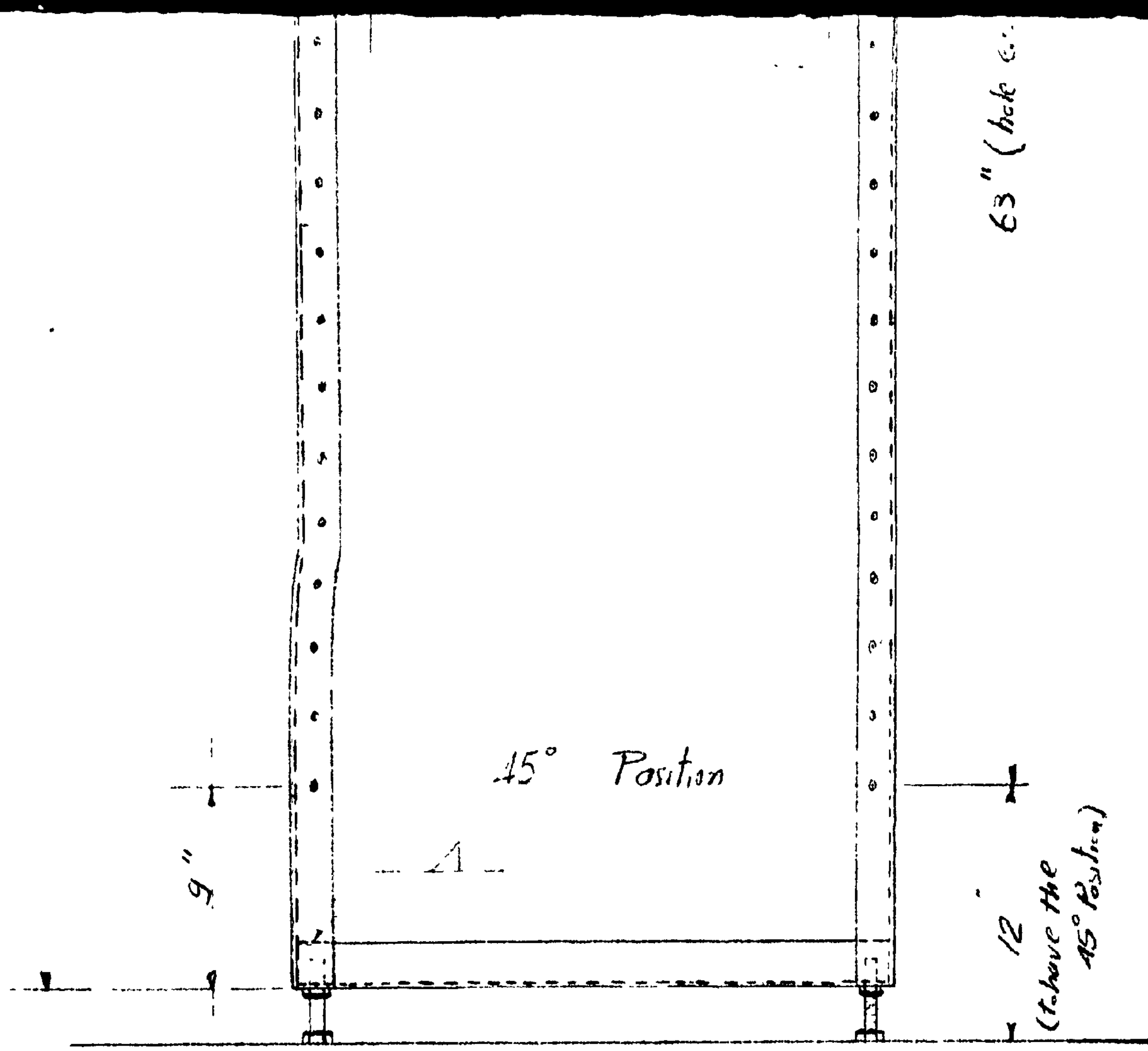

ELEVATION

D.S. SUPPORT

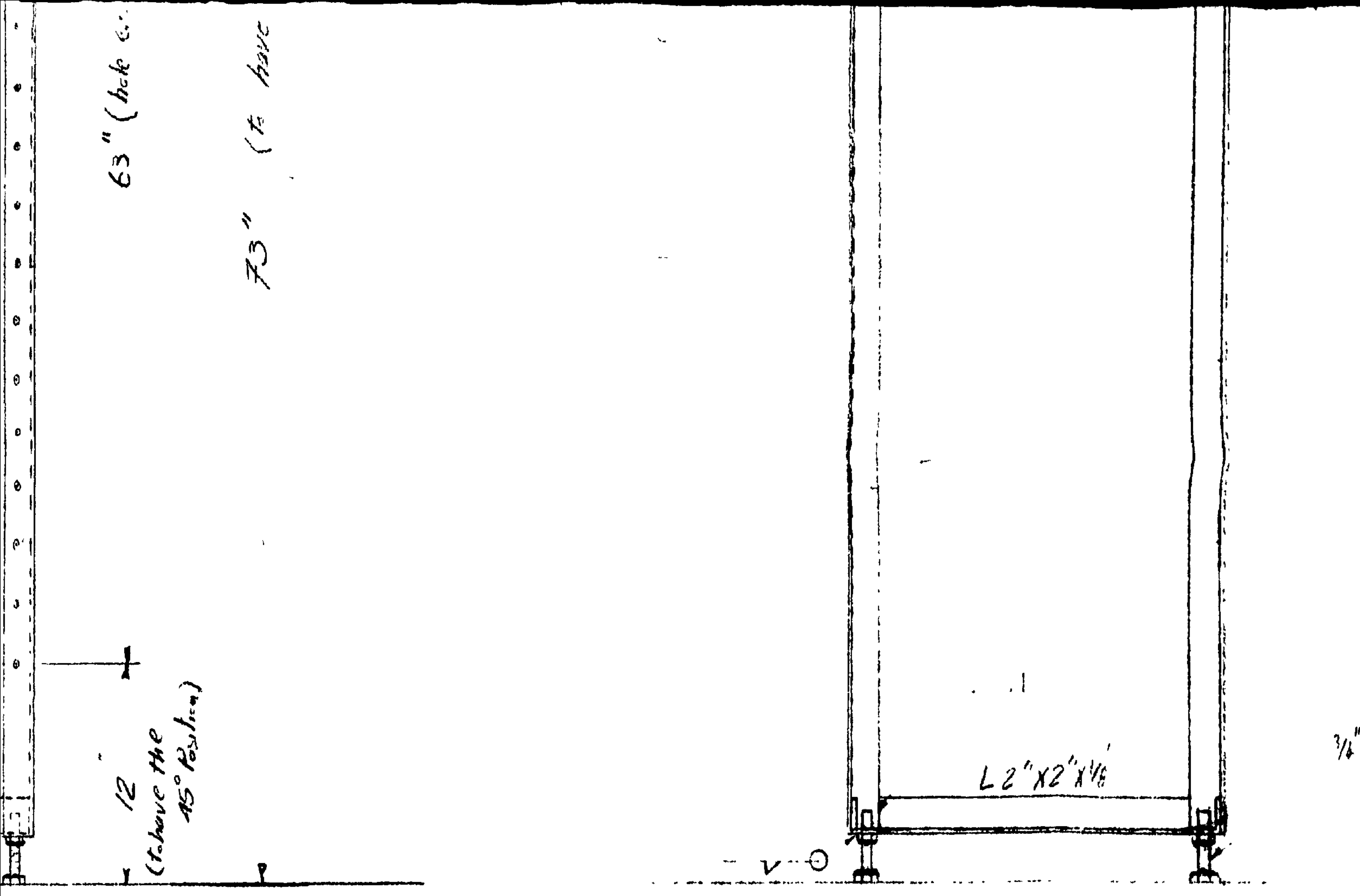

SECTION

Scale 1:8

ALL WELDS:
1/8" FILLET WELD
E70XX

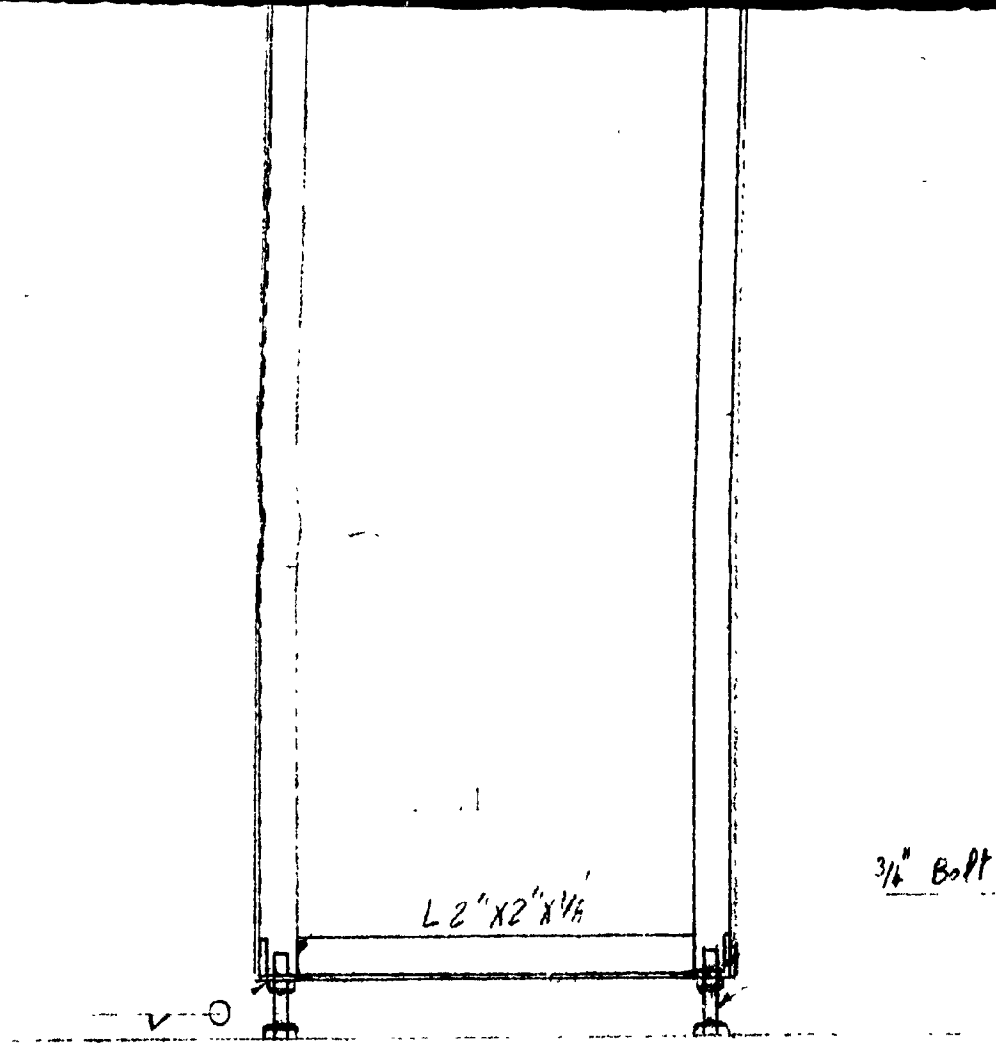

SECTION

ALL WELDS:
1/8" FILLET WELD
E70XX

3

c)

3

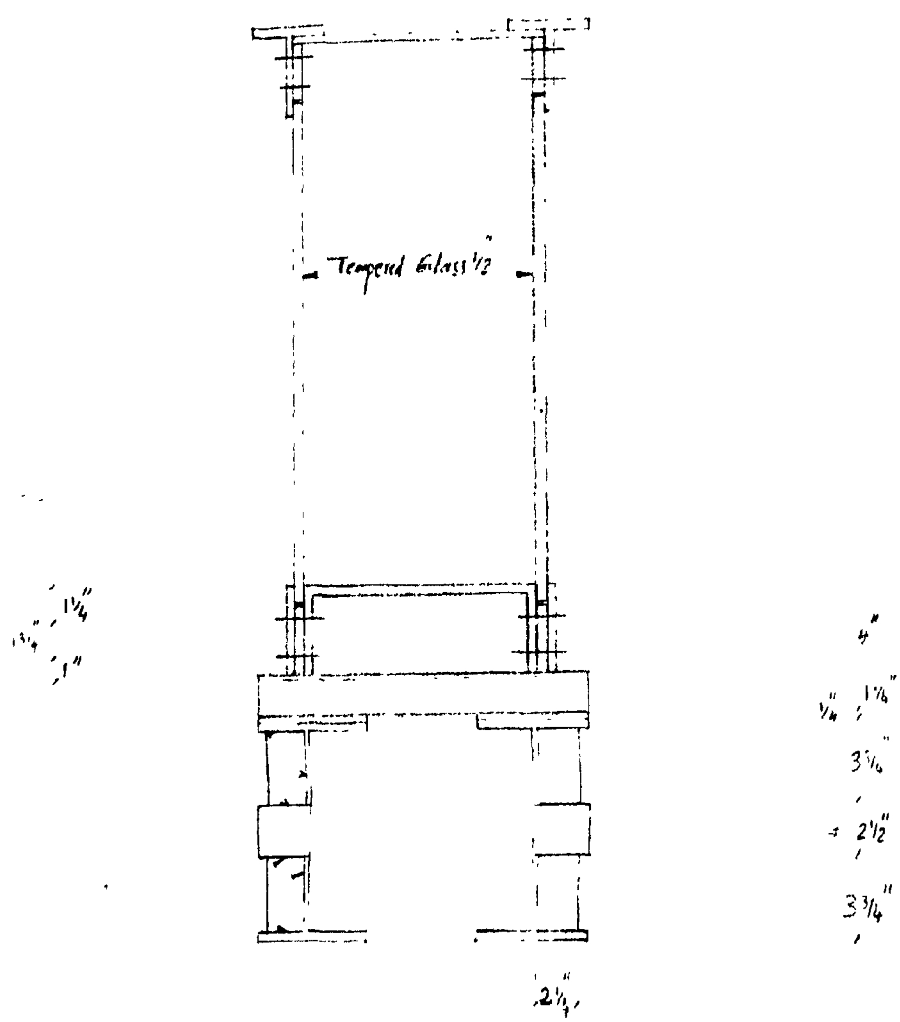

SECTION 6

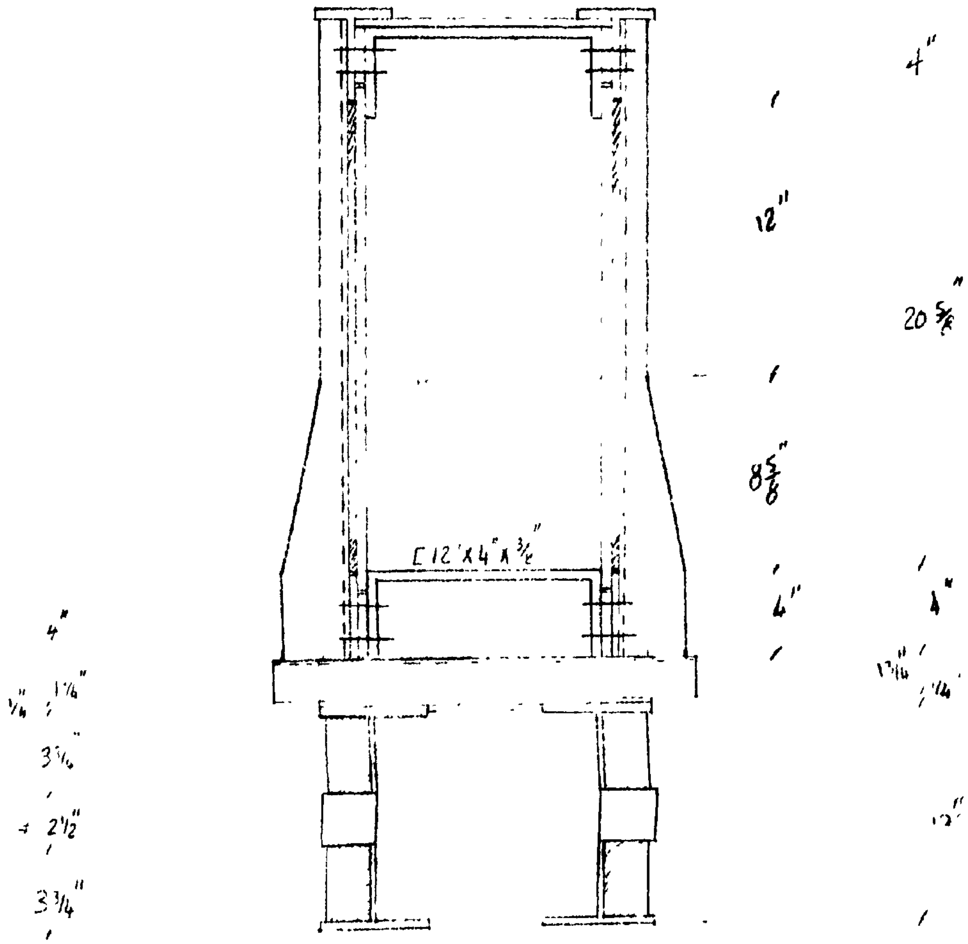

SECTION 7

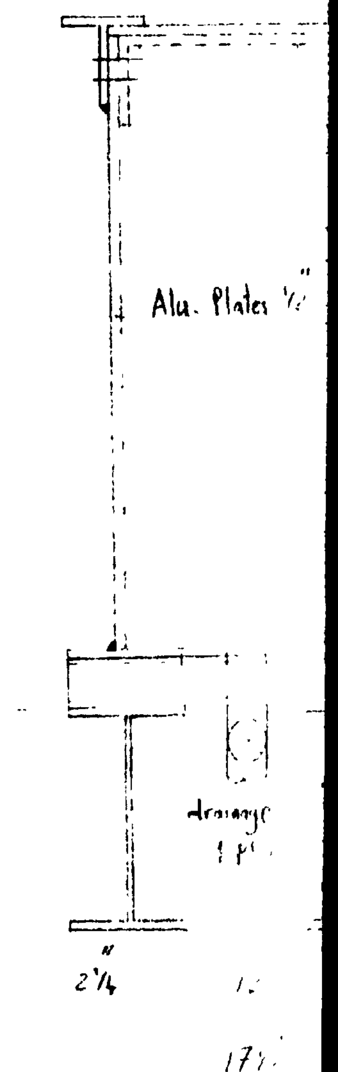

SECTION

Scale 1:8

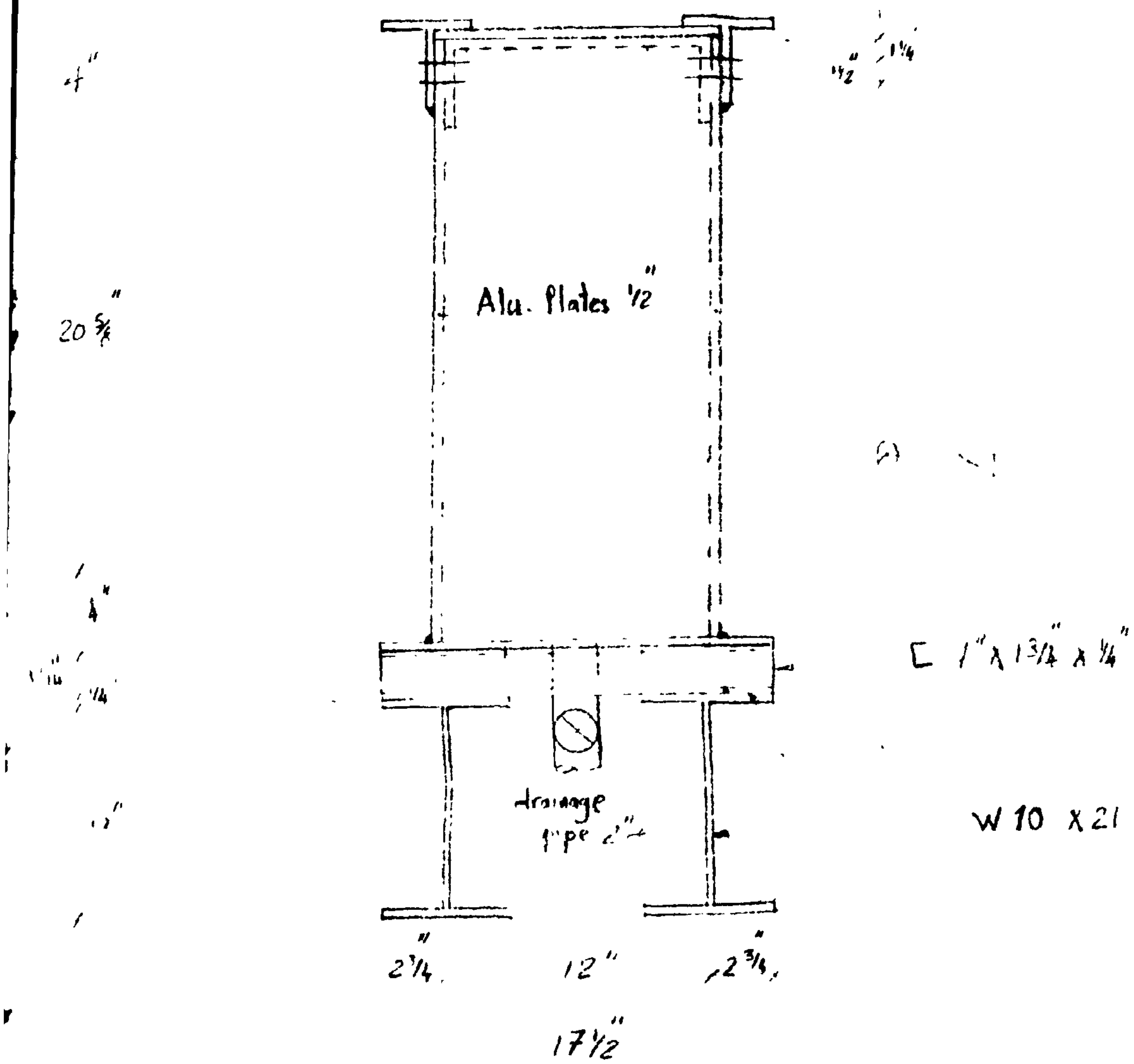

SECTION 8

Scale 1:8

e)

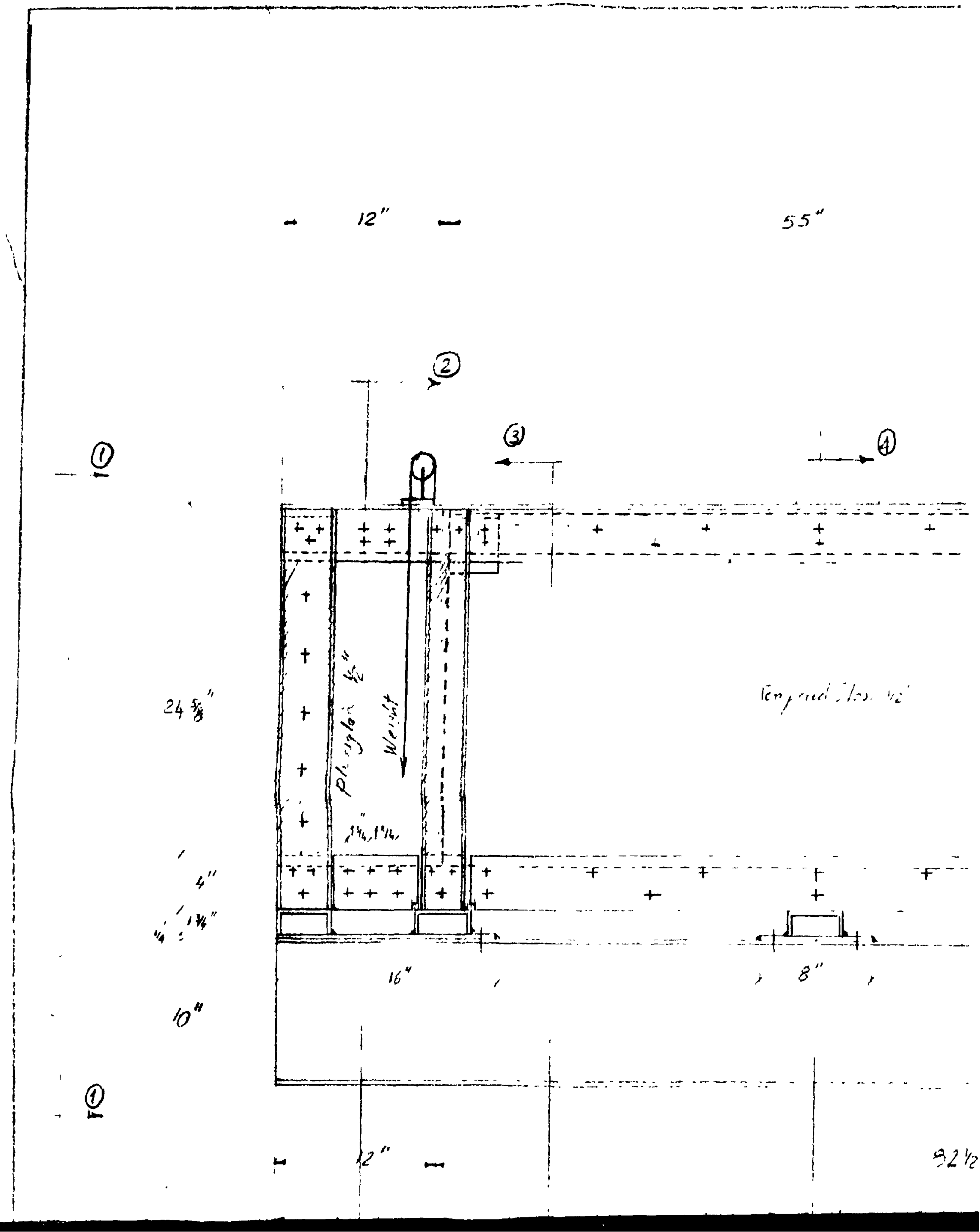

12"
55"
②
③
④
①
24 5/8"
Plexiglas 1/2"
Weight
Tempered Glass 1/2"
1¼, 1¼
4"
1¼"
16"
8"
10"
①
12"
32½

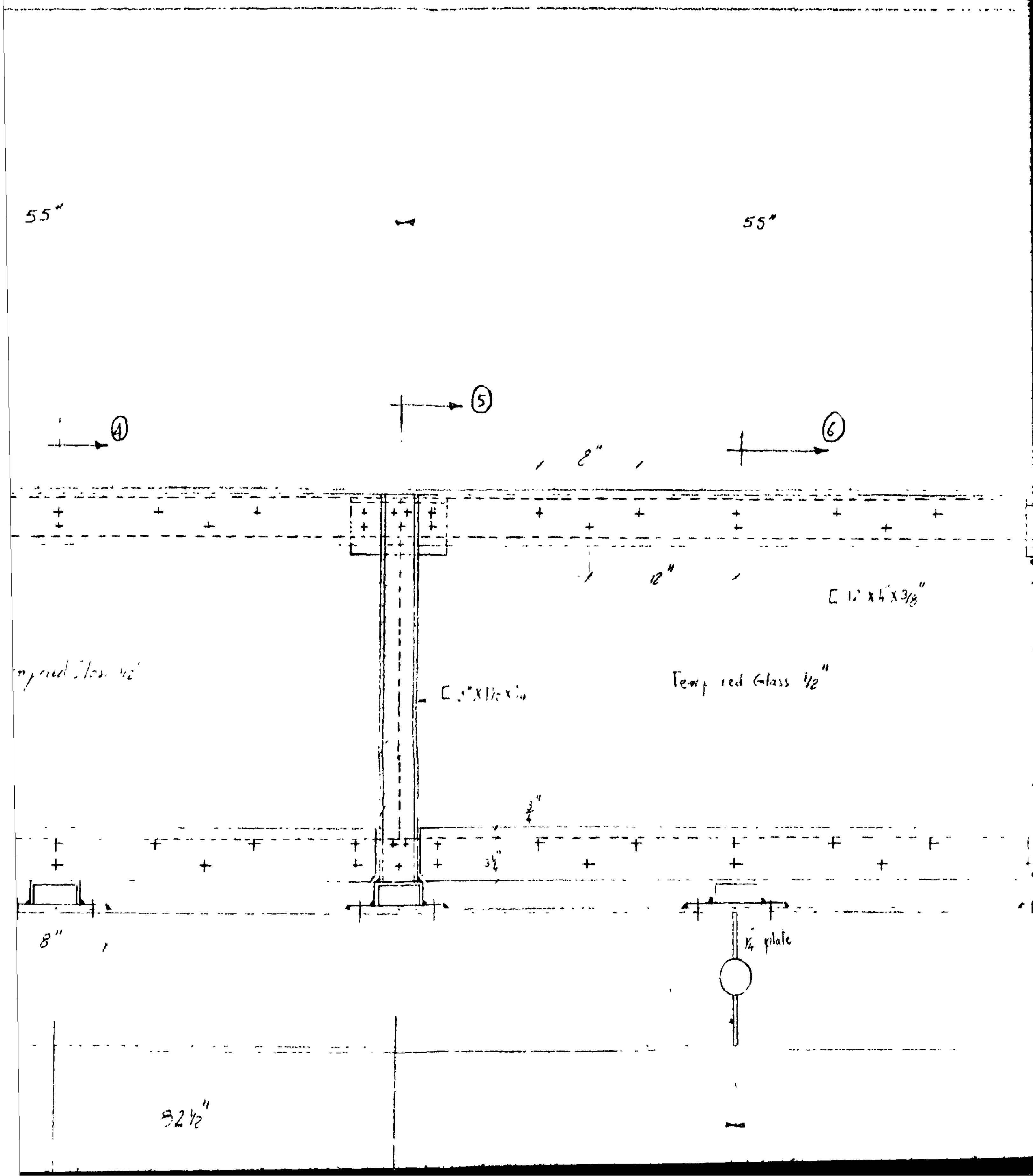
55"
55"
4
5
6
8"
12"
C 12" x 4" x 3/8"
Temp red Glass 1/2"
3/4"
3¼"
8"
¼ plate
32½"

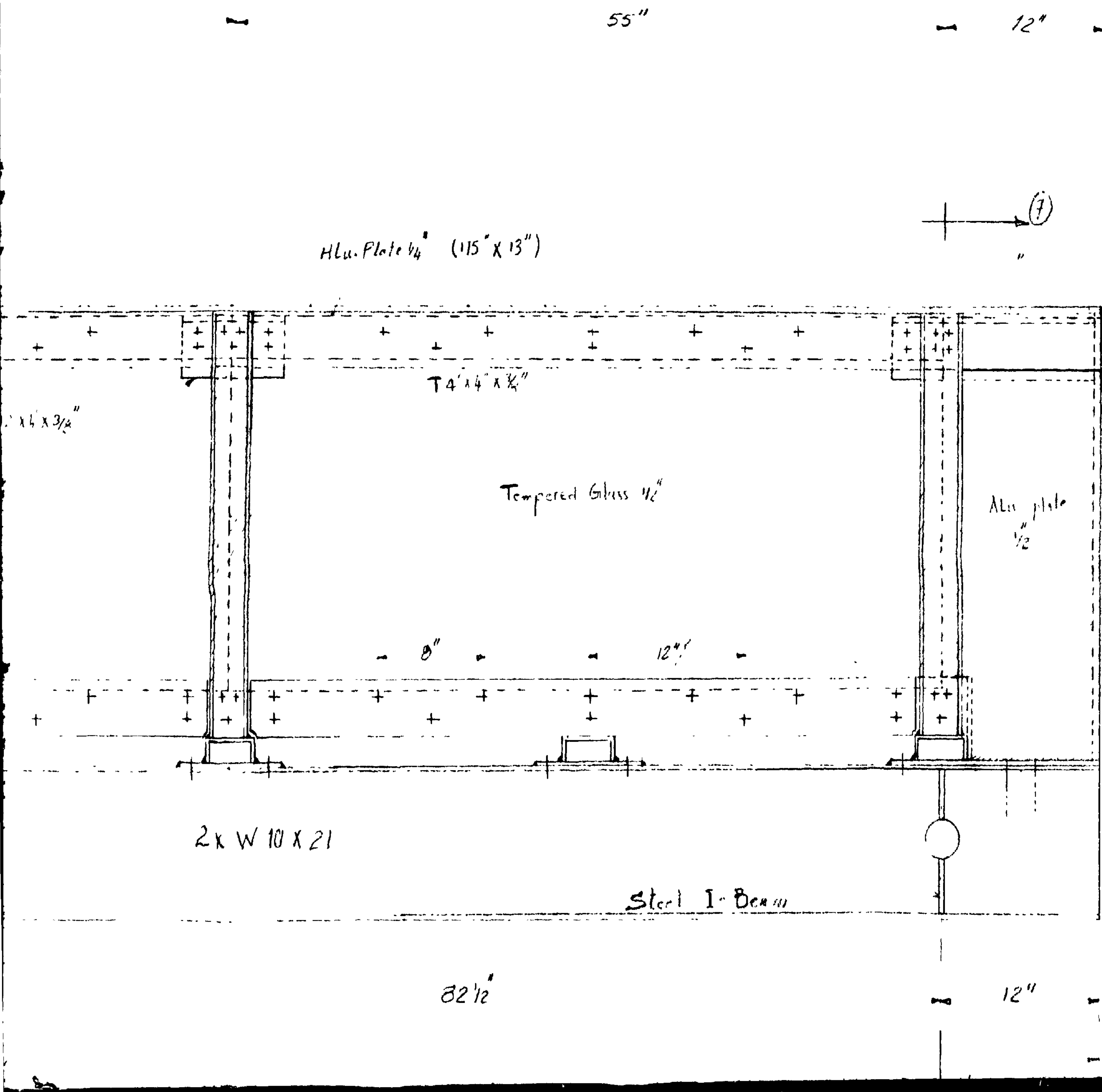

55"
12"
7
Alu. Plate 1/4" (115" X 13")
T 4"x4"x 1/4"
Tempered Glass 1/2"
Alu plate 1/2"
8"
12"
2x W 10 X 21
Steel I-Beam
82 1/2"
12"

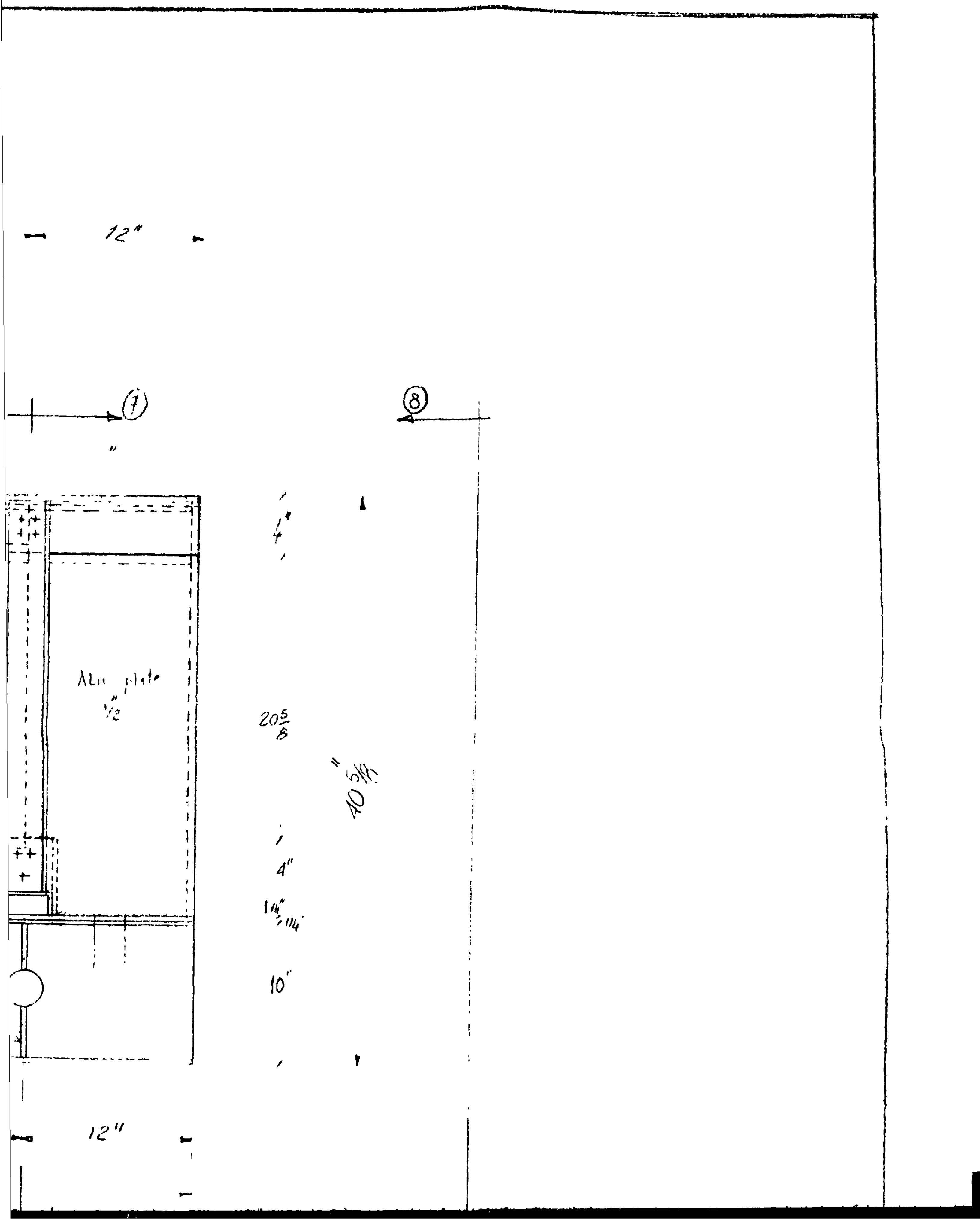
12"
7
8
4"
Alu plate
1/2"
20 5/8
40 5/8"
4"
10"
12"

.2¼.

SECTION 6

SECTION 7

SECTION 8

Scale 1:8

ALL [illegible] are 1/4"

¼ 12 ¾

17½"

SECTION 8

Scale 1:8

e)

5

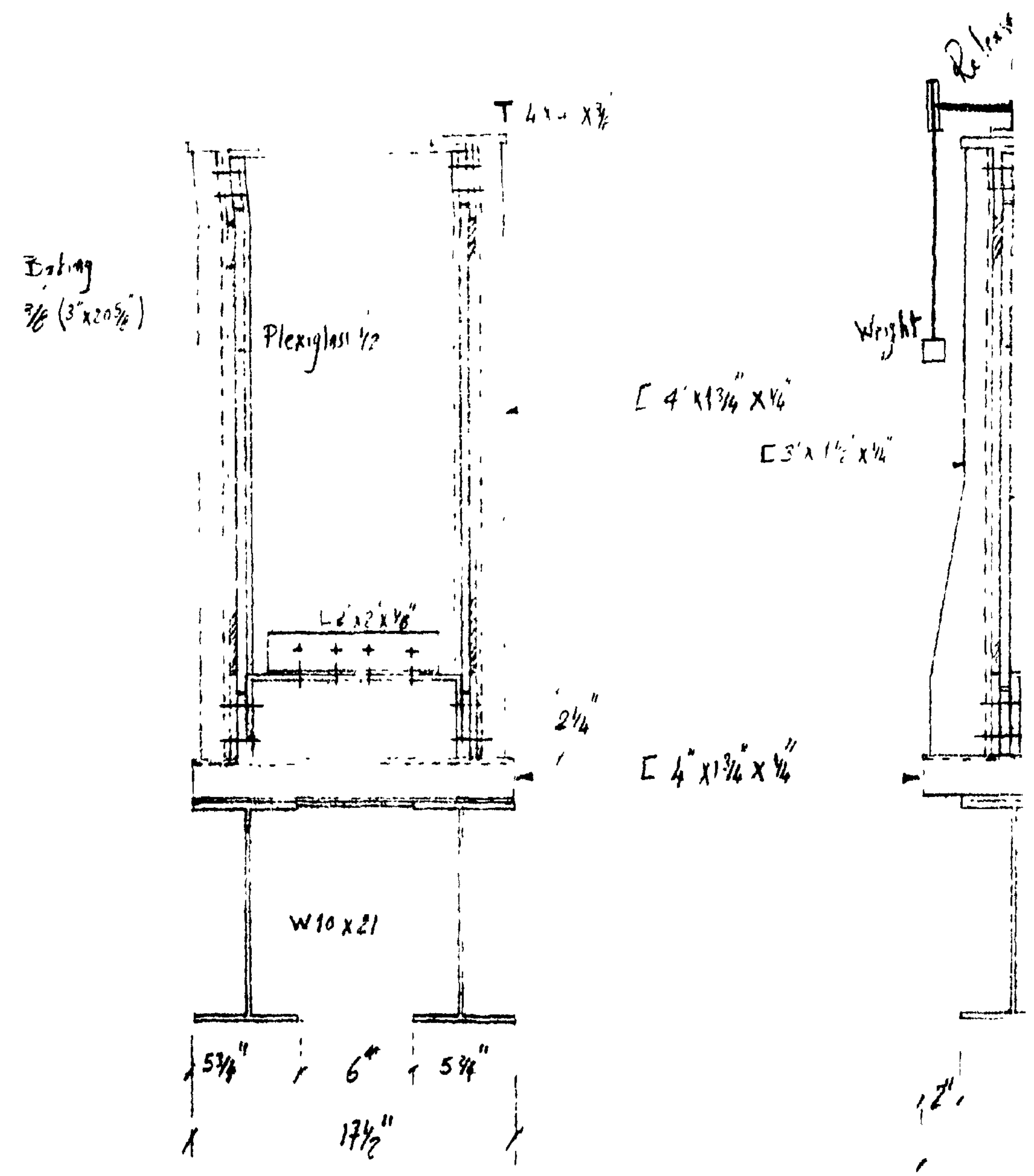

T 4x- x3/4
Bolting
3/8 (3"x20 5/8")
Plexiglass 1/2
Weight
[4"x1 3/4"x1/4"
[3"x1 1/2"x1/4"
L 2"x2"x1/8"
2 1/4"
[4"x1 3/4"x1/4"
W10x21
5 3/4"
6"
5 3/4"
17 1/2"
12"

SECTION 1

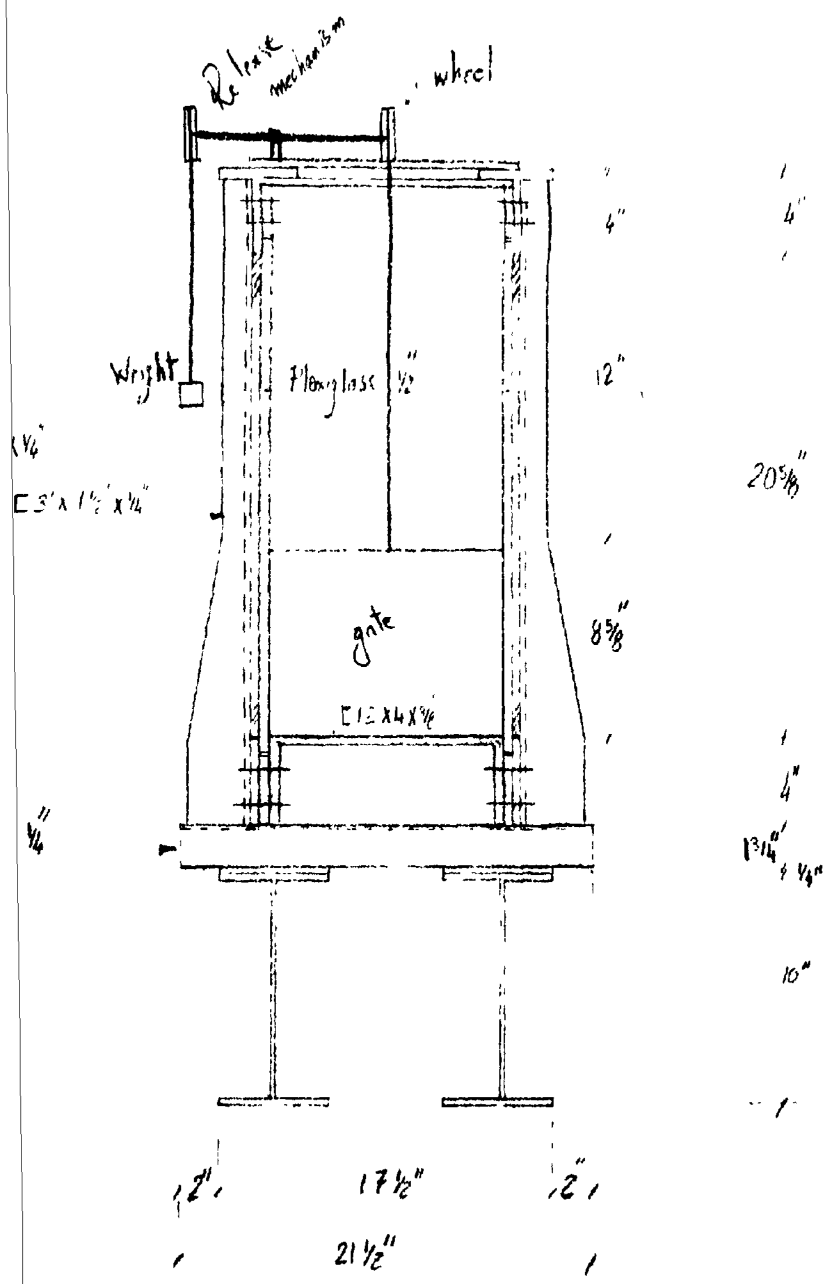

SECTION 2

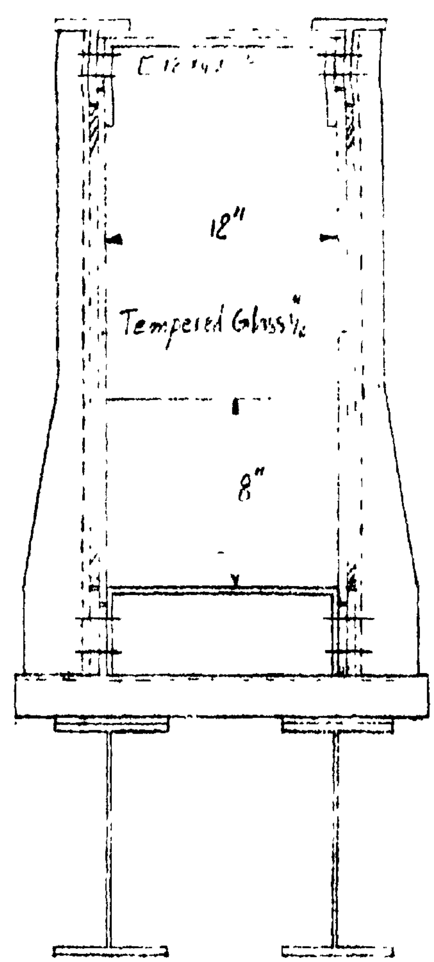

SECTION 3

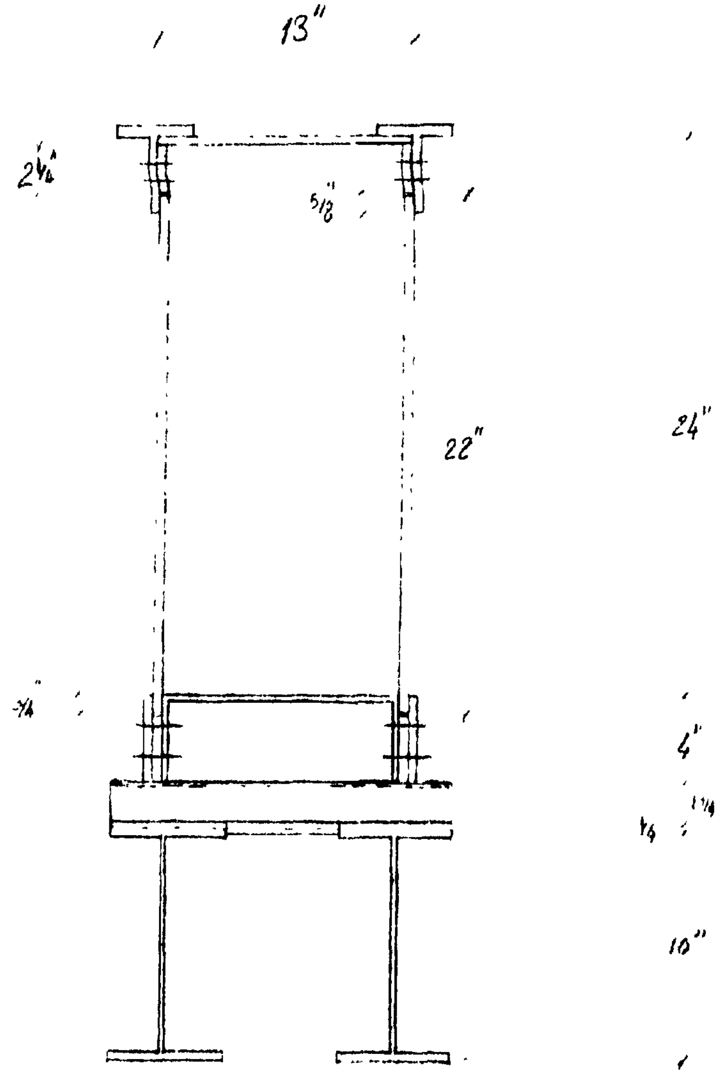

SECTION 4

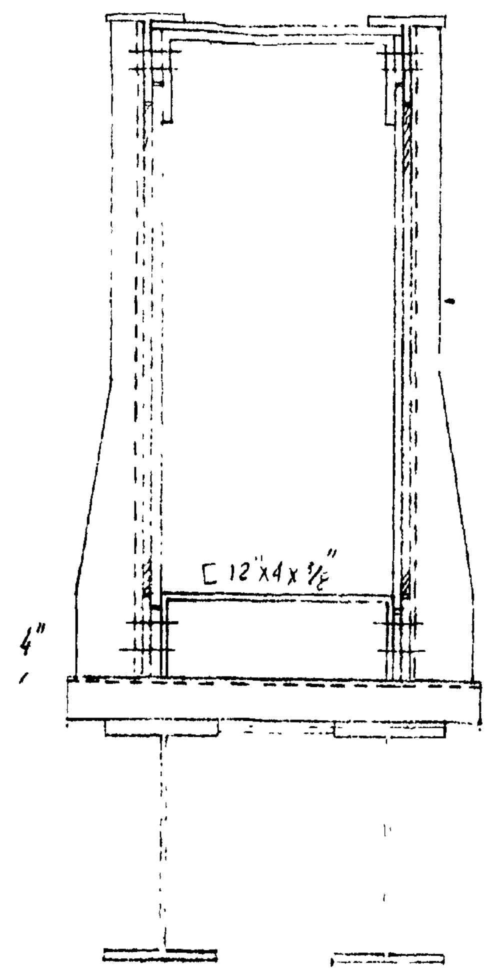

SECTION 5

(5)

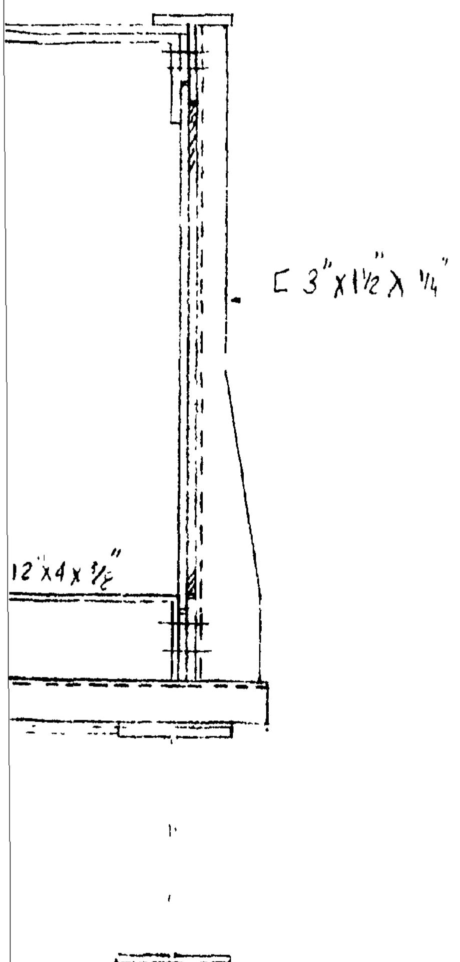

Scale 1:8

All Rivet ¼"

TION 5

2)

4